Wireless Sensor System for Infrastructure Health Monitoring

Abeysing Jayawardana Yapa Devaka Manoj

A thesis submitted for degree of
Doctor of Philosophy in Engineering

CENTRE FOR INFRASTRUCTURE ENGINEERING
SCHOOL OF COMPUTING, ENGINEERING AND MATHEMATICS
WESTERN SYDNEY UNIVERSITY
SYDNEY, AUSTRALIA

January 2017

©Abeysing Jayawardana Yapa Devaka Manoj, 2017

To my dearest wife, son, sister, parents, and teachers…

DECLARATION

Date: January 2017

Author: Abeysing Jayawardana Yapa Devaka Manoj

Title: Wireless Sensor System for Infrastructure Health Monitoring

Degree: Ph.D.

I certify that the work presented in this thesis is, to the best of my knowledge and belief, original except as acknowledged in the text, and the material has not been submitted, either in full or in part, for a degree at this or any other institution.

I certify that I have complied with the rules, requirements, procedures and policy relating to my higher degree research award of Western Sydney University.

[redacted]

Author's Signature

Acknowledgements

Primarily I offer my sincere gratitude to my principle supervisor, Associate Professor Sergey Kharkovsky for supporting me throughout my candidature with his insightful expert knowledge and continuous guidance. His vision, motivation, enthusiasm and patience encouraged me immensely in my research achievements during last three years.

I extend my earnest gratitude for my co-supervisor Dr. Ranjith Liyanapathirana for his constant encouragement and support. His expert ideas, continuous advice, and mentorship had been immensely helpful in the process towards research goals.

I express my genuine gratitude for my co-supervisor Associate Professor Xinqun Zhu for supporting me with his expert knowledge, constant advice and guidance. I greatly appreciate the support provided by him with imperative measurement equipment throughout my research candidature.

I gratefully appreciate the Centre for Infrastructure Engineering (CIE, erstwhile Institute for Infrastructure Engineering), Western Sydney University for granting me the Institute for Infrastructure Engineering Postgraduate Research Award (IIEPRA) which was highly important in this research achievement. Furthermore, I greatly appreciate the financial support provided by CIE in the procurement of imperative design components and equipment for my research. Furthermore, the travel grants provided by CIE to attend international conferences are also highly appreciated.

My sincere thanks go to both current and previous staff (Administration and Technical) of CIE who directly or indirectly had an influence on the success my research efforts. Especially, I would like to thank Dr. Mithra Fernando and Mr. Ranjith Ratnayake for their expert technical support and guidance in laboratory experiments. Furthermore, I express my gratitude for fellow colleagues of CIE who were kind and always prepared to help even in non-research related issues.

I would like to extend my thanks to the academic staff of University of Moratuwa, Sri Lanka, for supporting and inspiring me to pursue my research interests. My special thanks go to Professor Rohan Munasinghe for his expert advice and mentorship in my honors and postgraduate diploma theses.

I would like to express my heartfelt gratitude for my parents who had done immense in bringing up me and providing me with the freedom to pursue my dreams. Especial thanks go to my sister Achini, brother-in-law Udaya and other relatives who have supported me to date.

Finally, I would like to extend my heartfelt gratitude to my wife Chani who always provided the encouragement, support, and strength throughout this journey. I would like to thank my son Niven who brought me joy and happiness. Furthermore, I would like to extend my thanks to my parents-in-law for their immense help and dedication in support throughout this journey. Finally, I would like to thank my in-laws Ishan, Sujani, Paul and Leenika for their valuable support during last three years.

Abstract

In this thesis, radio frequency identification (RFID)-based wireless sensor system for infrastructure health monitoring (IHM) is designed and developed. It includes mountable semi-passive tag antenna integrated sensors capable of measuring critical responses of infrastructure such as dynamic acceleration and strain. Furthermore, the system is capable of measuring structural displacement. One of the most important parts of this system is the relatively small, tunable, construction material mountable RFID tag antenna. The tag antenna is electronically integrated with the sensors. Leading to the process of developing tag antenna integrated sensors having satisfactory wireless performance (sensitivity and read range) when mounted on concrete and metal structural members, the electromagnetic performance of the tag antenna is analyzed and optimized using both numerical and experimental procedures. Subsequently, it is shown that both the simulation and the experimental measurement results are in good agreement.

The semi-passive RFID-based system is implemented in a wireless IHM system with multiple sensor points to measure dynamic acceleration and strain. The developed system can determine the natural frequencies of infrastructure and identify any state changes of infrastructure by measuring natural frequency shifts. Enhancement of the spectral bandwidth of the system has been performed under the constraints of the RFID hardware. The influence of the orientation and shape of the structural members on wireless power flow in the vicinity of those members is also investigated with the RFID reader-tag antenna system in both simulation and experiments. The antenna system simulations with a full-scale structural member have shown that both the orientation and the shape of the structural member influence the wireless power flow towards and in the vicinity of the member, respectively. The measurement results of the conducted laboratory experiments using the RFID antenna

system in passive mode have shown good agreement with simulation results. Furthermore, the system's ability to measure structural displacement is also investigated by conducting phase angle of arrival measurements. It is shown that the system in its passive mode is capable of measuring small structural displacements within a short wireless distance.

The benchmarking of the developed system with independent, commercial, wired and wireless measurement systems has confirmed the ability of the RFID-based system to measure dynamic acceleration and strain. Furthermore, it has confirmed the system's ability to determine the natural frequency of an infrastructure accurately. Therefore, the developed system with wireless sensors that do not consume battery power in data transmission and with the capability of dynamic response measurement is highly applicable in IHM.

Contents

Abbreviations

ADC	analog to digital conversion
BAP	battery assisted passive
CWA	commercial wired accelerometer
CWLA	commercial wireless accelerometer
CWLSS	commercial wireless strain sensor
DAQ	data acquisition
DC	direct current
DSM	digital strain meter
EIRP	effective isotropic radiated power
EPC	electronic product code
FIFO	first-in first-out
HF	high frequency
ICSP	in-circuit serial programming
IDE	integrated development environment
IHM	infrastructure health monitoring
I^2C	inter-integrated circuit
ISM	industrial scientific and medical
LF	low frequency
MEMS	microelectromechanical systems
MSITA	multi-sensor integrated tag antenna
NVM	non-volatile memory
ODR	output data rate

PCB	printed circuit board
PGA	programmable gain amplifier
PNA	performance network analyser
PWM	pulse width modulation
RF	radio frequency
RFID	radio frequency identification
RMSE	root mean square error
RSSI	received signal strength indicator
SA	signal analyser
SDK	software development kit
SNR	signal to noise ratio
SPI	serial peripheral interface
TAIAS	tag antenna integrated acceleration sensor
UHF	ultra-high frequency
USB	universal serial bus

List of Figures

List of Tables

Chapter 1 Introduction

1.1 Infrastructure Health Monitoring

Infrastructure Health Monitoring (IHM) is defined as the use of non-structure sensing systems to monitor the performance of the structures and evaluate their health [1]. The integrity of critical civil infrastructures such as bridges, buildings, and tunnels is extremely important as they are being built by investing millions of dollars, and for the safety of their users. However, infrastructure integrity is being challenged throughout their lifetime by various environmental and accidental causes which may lead to catastrophes [2-4]. IHM targets monitoring structural conditions to prevent such catastrophic failures and to provide quantitative data for engineers and infrastructure owners to design reliable and economical asset management plans [1].

1.2 Infrastructure Health Monitoring Methods

According to the literature, IHM methods can be divided into three main categories: First one includes the conventional methods such as *visual inspection* and *tap-testing* [5]. With a higher percentage of human factors involved, the efficiency of the conventional methods and their ability to detect alarming conditions are low. The accidental crack detection of Oakland Bay Bridge, USA, which was unforeseen by utilizing conventional methods [6] is one of the major incidents which highlights this fact as the facility had to be closed down until proper repair. Therefore, the next two categories include automated data acquisition of various measurable quantities of infrastructure (e.g., acceleration, strain, displacement) through sensory systems [7-9]. Predominantly the dynamic responses of infrastructure are acquired in these methods as those responses carry rich diagnostic information (e.g., natural frequencies, mode shapes) [10-14].

Implementing *wired* automated sensor systems has negated the drawbacks of conventional methods such as low efficiency and the inability of tracking alarming conditions. The sensors can be either wired electrical [15-17] or optical fiber [18-22] systems. However, higher installation costs and installation durations inherent to them have become a major drawback to cater for a higher population of sensors needed in IHM [7, 16, 17, 23-25]. Furthermore, the limitations of the amount of wiring or cabling that can be done without disturbing the operation of the infrastructure also limit the number of sensors that the system can occupy [11].

Therefore, *wireless* sensors and sensor systems for IHM are extremely important and their usage and implementation are under continuous research to address the operational and economic issues inherent to previously mentioned categories [26-30]. However, cost-effective wireless sensors and power efficient wireless communication have always been a problem in wireless IHM. The amount of data transferred in a system depends upon the number of sensors in the wireless system and the type of measurement that sensors carry out (i.e., dynamic versus static). In particular measuring dynamic responses leads to higher power consumption in the sensor nodes due to increased data transfers to support high sampling rates. According to [31, 32], the power consumption of one bit of active wireless data transfer is equal to the power consumption of executing several thousands of instructions in a processor.

1.3 Motivation and Research Objectives

1.3.1 Motivation

The application of wireless sensor systems for IHM is attractive due to convenience that they provide in installation time, cost and operation. Most importantly, they possess the ability to measure dynamic responses of infrastructure (e.g., vibration induced dynamic acceleration, strain, etc.) which are required to extract the health monitoring indicators such as natural frequencies and mode shapes [33]. However, most of the commercially available systems and those used in research consist of active wireless nodes which consume power to data transfer. Consequently, frequent servicing of sensor nodes (i.e., battery replacement) may be necessary depending upon the amount of data transfers that take place in the system. Due to the large number of sensor nodes which is necessary for IHM, frequent servicing each of them is an extra effort and burden, especially in the infrastructure in operation. In addressing this problem, research has been expanded in investigating compressive sensing [34, 35] and power harvesting techniques for active wireless sensor nodes [28, 36]. However, there is a research gap in developing system solutions for dynamic response measurements of infrastructure with wireless sensors that do not consume power in data transmission.

Even though some alternative *passive* wireless sensors [37-39] and *radio frequency identification (RFID) technology-based passive* wireless sensors [40-44] for IHM have been developed; they lack the ability of implementation in systems for field applications. This is mostly due to low communication ranges, their inability to measure dynamic responses and possible peculiarities of their indirect raw measurement techniques (e.g., the resonant frequency, backscatter signal power, transmit power) in complex infrastructure environments [45]. Integration of modern ultra-high frequency (UHF) RFID technology into wireless IHM may provide extended communication ranges [46, 47]. However, when implemented in passive sensing the communication range gets curtailed and the ability of dynamic response measurement diminishes [44, 48]. Furthermore, the majority of passive RFID-based sensors realized in research of wireless IHM are capable of acquiring only a single measurand (e.g., either strain or displacement) which is disadvantageous when considering the developing area of IHM research with multimetric sensing [49].

Usage of UHF RFID technology in *semi-passive* wireless sensing of infrastructure still have the possible underperformance issues of RFID tag antennas due to the adverse influence from electromagnetically harsh environments (containing concrete and metal structural members) on its passive backscatter communication. Furthermore, the semi-passive RFID tag antenna-based sensors which can measure critical dynamic responses (e.g., dynamic acceleration, dynamic strain) are limited. However, if the above issues are solved, the semi-passive RFID tag antenna-based sensors have great potential for serving as low power substitutes for active sensor nodes in the lowest tier (tier in which multiple active sensor nodes operate with single hop communication covering the specific spatial area) of modern wireless sensor system architectures of IHM.

The study of this thesis is motivated by aforementioned prevailing issues of wireless IHM and the possibility of a semi-passive RFID-based wireless system solution.

1.3.2 Research Objectives

The main aim of this research is the development and application of an RFID-based wireless measurement system with semi-passive tag antenna integrated sensors for IHM with both dynamic and static measurements. The research objectives formulated to fill the research gap are as follows:

- Propose the concept of an RFID-based wireless measurement system for IHM capable of acquiring the natural frequency information of infrastructure by dynamic acceleration measurement and detecting state changes in infrastructure.
- Develop construction material mountable UHF RFID tag antenna with sensor integration capabilities and analyze its electromagnetic performance when mounted on concrete and metal structural members.
- Enhance the RFID-based wireless measurement system to monitor full-scale structural members with multiple mountable semi-passive tag antenna integrated acceleration sensors possessing higher spectral bandwidth and benchmark the system against independent commercial measurement systems.
- Design an RFID-based wireless measurement system to monitor simultaneous dynamic acceleration and strain of infrastructure and benchmark the system against commercial wireless measurement system.
- Demonstrate the influence of orientation and shape of structural elements on wireless power delivery to mounted RFID tag antennas to optimize their placement on the structure and antenna system with respect to the orientation of the structure.
- Investigate passive mode RFID-based wireless system application on static structural displacement measurement.

1.4 Major Contributions

In this thesis, a semi-passive RFID-based wireless sensor system is designed predominantly to measure dynamic acceleration and strain of infrastructure. Additionally, the system ability in passive mode structural displacement measurement has also been investigated. In achieving these, novel structure mountable RFID tag antenna integrated sensors are developed and applied. The developed system's ability to measure dynamic responses from mounted sensors with enhanced communication range is experimentally proven.

The major contributions and their brief descriptions are as follows:

- Prototype RFID-based wireless dynamic acceleration system with tag antenna integrated acceleration sensor for natural frequency shift-based IHM.

  Specific firmware design to achieve the capability of measuring dynamic acceleration using tag antenna integrated acceleration sensor is developed. It is shown that the prototype system is capable of acquiring natural frequency information of a rectangular steel beam; a part of a bridge model. Furthermore, it has also been shown that the system is capable of identifying the loaded and unloaded states of the beam.

- Tuneable construction material mountable UHF RFID tag antenna which can be used as I^2C slave component for the creation of tag antenna integrated sensors.

  It is shown that slit-based miniaturization method can be simultaneously used for impedance matching and parametric optimization of the tag antenna to acquire higher performance in several UHF RFID frequency bands. It has also been shown that mounting material of concrete and metal has a minor negative influence on the maximum gain, and the size of the metal mounts has no influence upon reflection characteristics of the antenna. The usage of local mesh properties around tiny features of the antenna to retain similar accuracy with increased simulation volume is performed. In addition, the essential laboratory measurements of the resonant frequency, maximum gain and read range of the fabricated tag antenna are conducted. Furthermore, the influence of surface currents generated on metal mounts upon antenna gain pattern is proved by the measurement of received signal strength indicator (RSSI).

- The RFID-based dynamic acceleration measurement system with multiple tag antenna integrated acceleration sensors and wide spectral bandwidth.

  A miniaturized acceleration sensor circuit which can be integrated with the developed construction material mountable tag antenna is designed. The spectral bandwidth of the system is enhanced to 50-Hz in 3-axis dynamic acceleration measurement with improved firmware and data acquisition. The feasibility of the system to handle multiple tag antenna integrated acceleration sensors is shown by conducting measurements upon full-scale steel I-beam. The ability of the system in determining the natural frequency of the I-beam and the acceleration sensitivity is benchmarked with independent commercial wired and wireless measurement systems.

- The RFID-based measurement system for simultaneous measurement of dynamic acceleration and strain.

  A miniaturized multi-sensor circuit which can be integrated with the developed construction material mountable tag antenna is designed. The firmware is improved to measure 3-axis acceleration and strain with spectral bandwidths of 40 Hz and 26.5

Hz, respectively. The strain interface is calibrated against a standard strain measurement instrument by conducting static train measurements upon a cantilever steel beam. The feasibility of the system to acquire natural frequency information of the beam from both dynamic acceleration and strain measurements (simultaneous measurements) is shown. The ability of the system in determining the natural frequency of the cantilever beam and the strain sensitivity is benchmarked with the commercial wireless strain measurement system.

- The methodology and results of the investigation of wireless power flow in the vicinity of a steel I-beam using RFID reader-tag antenna system.

  Model of a reader antenna and tag antennas with lumped elements in transmitting and receiving mode, respectively, are developed. It is shown that the power flow towards the I-beam is influenced by its orientation with respect to reader antenna and the power flow in the vicinity of the beam is influenced by the shape. It is also been shown that in some orientation of the I-beam, the line-of-sight location has less incident power influenced by shape. The experimental method is formulated using wireless link budget to relate minimum reader transmit power to incident power.

- The results of an investigation into the ability of the passive mode RFID system to measure structural displacement using the acquisition of phase angle of arrival.

  It is shown that displacement of 1 mm can be measured directly by the phase angle of arrival or frequency domain phase difference of arrival within starting distance of a single wavelength (λ) related to Australian UHF RFID frequencies. It is also shown that 5-mm displacement can be measured directly by the phase angle of arrival within a 6λ initial distance under the performance of RFID reader equipment.

1.5 Publications

Following research papers are published in peer-reviewed journals or conference proceedings.

Journal papers

1. D. Jayawardana, S. Kharkovsky, and R. Liyanapathirana, "Construction material mountable UHF RFID tag antenna," *Microwave and Optical Technology Letters*, vol. 58, no. 9, pp. 2231-2237, September 2016.

2. D. Jayawardana, S. Kharkovsky, R. Liyanapathirana, and X. Zhu, "Measurement system with accelerometer integrated RFID tag for infrastructure health monitoring," *IEEE Transactions on. Instrumentation and Measurement*, vol. 65, no. 5, pp. 1163-1171, May 2016.

Conference papers

1. D. Jayawardana, S. Kharkovsky, and R. Liyanapathirana, "Investigation of UHF power flow in the vicinity of a steel I-beam for optimization of its health monitoring using wireless sensor integrated RFID tag antenna system," in *IEEE-APS Tropical Conference on Antennas and Propagation in Wireless Communications (APWC)*, 2016, pp. 138-141.

2. D. Jayawardana, S. Kharkovsky, and R. Liyanapathirana, " Wireless system with a RFID tag antenna for infrastructure health monitoring," in *Proceedings of Third Conference on Smart Monitoring, Assessment and Rehabilitation of Civil Structures (SMAR 2015)*, September 2015, Antalya, Turkey.

3. D. Jayawardana, S. Kharkovsky, and R. Liyanapathirana, "Measurement system with a RFID tag antenna mounted on structural members for infrastructure health

monitoring," in *Proceedings of IEEE International Instrumentation and Measurement Technology Conference (I2MTC)*, May 2015, pp. 7-12.

1.6 Thesis Organisation

The remainder of the thesis is organized as follows:

- Chapter 2 provides a comprehensive review of wireless sensors and sensory systems for IHM. The active, passive, RFID-based passive and RFID-based semi-passive wireless sensing methods developed for IHM are considered. The popularity of active nodes in wireless IHM system implementation due to their ability to measure dynamic responses is highlighted. The issues preventing the use of passive and RFID-based passive sensing in multi-point wireless IHM systems are foregrounded. The possibilities of the use of RFID-based semi-passive sensing in wireless IHM systems are highlighted by reviewing already implemented active wireless system architectures. Then, the research gap related to underdeveloped semi-passive RFID tag antenna integrated sensors capable of measuring dynamic responses and proper wireless performance when mounted on structural members is identified. Finally, the methodology which will be followed in the thesis in filling the identified research gap is discussed.

- In Chapter 3, the concept of an RFID-based wireless measurement system for remote monitoring of infrastructure is proposed. The RFID part of the proposed monitoring system is developed with a custom designed semi-passive tag antenna integrated acceleration sensor. The firmware for the tag antenna integrated acceleration sensor to perform dynamic acceleration measurements is developed. The laboratory dynamic acceleration measurement results of the system upon a simply supported rectangular beam are presented. The beam's natural frequency determination from the system measurements are compared with measurements from independent commercial systems for loaded and unloaded states.

- A novel design of a construction material mountable UHF RFID tag antenna which is capable of integrating sensors is presented in Chapter 4. CST-based design, impedance matching, and electromagnetic simulation are detailed. The electromagnetic simulation results (e.g., reflection characteristics, gain, and gain patterns) of the tag antenna in free space and mounted on large scale concrete and metal blocks are presented. The laboratory measurement results of the resonant frequency, maximum gain and read range of the fabricated tag antenna are also presented in order to corroborate simulation results. The comparison of the performance of the designed tag antenna with two other commercially available tag antennas is performed. Finally, the ability to modify the tag antenna for other UHF RFID frequency bands is discussed.

- In Chapter 5, the RFID-based dynamic acceleration system is further enhanced by introducing a novel tag antenna integrated acceleration sensor (consisting of construction material mountable tag antenna and custom designed acceleration sensor circuit) and a new commercial UHF RFID reader. The firmware of tag antenna integrated acceleration sensor and the data acquisition are enhanced to achieve higher spectral bandwidth in 3-axis dynamic acceleration measurements. Both hardware and firmware design enhancements are detailed. The enhanced system is tested upon a simply supported full-scale steel I-beam with multiple tag antenna integrated acceleration sensors. A comprehensive analysis of measurement results is presented with system benchmarking with independent wired and wireless commercial acceleration measurement systems for its ability to determine the natural frequency and the acceleration sensitivity.

- Chapter 6 presents the developed RFID-based multi-sensor system for simultaneous measurement of dynamic acceleration and strain of infrastructure. The hardware and firmware enhancement needed for multi-sensor integrated tag antenna are detailed. The strain interface of the tag antenna integrated multi-sensor is calibrated against standard strain measurement equipment by conducting static strain measurements upon a cantilever steel beam. Then, the system is tested for simultaneous dynamic acceleration and strain measurements upon the same cantilever beam and the results are presented. A comprehensive analysis of measurement results is presented with system benchmarking using commercial strain measurement system for its ability to determine the natural frequency and the strain sensitivity.

- Chapter 7 presents the methodology and the results of an investigation into wireless power flow in the vicinity of a full-scale steel I-beam using the RFID antenna system in passive mode. The simulation and experimental parts of this investigation are detailed. Initially, the reader antenna is adapted in simulation and the performances are presented. Then, the power flow simulations for two I-beam orientations with respect to reader antenna are performed. Consequently, the simulation results are justified with the laboratory measurement results. Additionally, phase angle-of-arrival-based passive mode structural displacement measurement is introduced. The displacement measurements from the raw phase angle of arrival and frequency domain phase difference of arrival are presented for two initial distances between reader and mounted tag antennas.

- Investigation summary and conclusions based on the research outcome of the thesis is provided in Chapter 8. Furthermore, recommendations for future work related to continuation of the research and development are also presented.

Chapter 2 Literature Review

2.1 Introduction

In this chapter, the implemented wireless IHM systems with active sensor nodes are reviewed and their advantages and disadvantages are identified. Then the issues in applying passive wireless sensing methods in IHM systems are identified with a comprehensive overview. Subsequently, the potential of incorporating semi-passive RFID-based sensing in wireless IHM systems is highlighted with its advantages over active nodes and passive sensing methods. The lack of research in RFID-based wireless systems with semi-passive sensors suitable to operate with infrastructure and measure necessary dynamic responses is identified. Consequently, the research methodology for developing a novel RFID-based semi-passive wireless sensor system for IHM is formulated to fill the identified research gaps. Finally, the conclusions of the chapter are presented.

2.2 Active Sensing for Wireless IHM

Incorporation of active sensor nodes is the most common and established practice when applying wireless sensor systems for IHM. Most of these systems with active sensor nodes utilize industrial scientific and medical (ISM) band of frequencies in wireless communication [25]. Apart from the ability of wireless communication, these nodes basically possess capabilities of data processing and sensor integration to acquire different measurands. The flexibility of deploying arrays in wireless IHM systems to acquire information covering large scale infrastructure is one of the major advantages of active sensor nodes [50, 51]**.** Some of these active nodes were research prototypes which were custom designed for specific wireless IHM tasks [26, 27, 52-57]. Inexpensive strain gauge loaded nodes were used in a wireless IHM system and the results were compared with the results from wired measurement system [9]. A wireless IHM system with 15 nodes was used to acquire 2-axis acceleration measurements implementing time division multiple access method to reduce data packet collision in [58]. A wireless system with 30 number of sensor nodes working in star network topology was studied with integrated accelerometers for condition assessment of highway bridges in [59]. Sixty four acceleration sensor nodes were employed in [60] as a multi-hop wireless bridge monitoring system. Both temporal and special jitter analysis were performed in the process to synchronize the system. The bridge health monitoring study performed in [27] had a wireless system with 20 capacitive vertical accelerometer integrated sensor nodes installed on the bridge.

Development of microelectromechanical systems (MEMS)-based onboard accelerometer hardware, improvements of dynamic acceleration and strain data interpretation techniques and damage detection algorithms have also increased the use of active nodes in wireless IHM systems. Consequently, the successful wireless nodes such as "*Imote2*", "*Stanford WiMMS*" and "*MICA*" were introduced [61-63]. These nodes possess the ability to integrate different sensors with specific interface circuit boards [64-67]. An autonomous decentralized IHM system had been realized using the *Imote2* nodes incorporating damage detection algorithms with dynamic strain measurements [68]. Usage of the same for wireless IHM has been validated by implementing them to monitor cable-stayed bridges in [28, 30] by conducting dynamic acceleration measurements. The *Stanford WiMMS* node was used by several researchers and validated for wireless IHM [69-72]. It was used in a wireless system to study wind loading on a steel tower of a wind turbine in [73] by dynamic acceleration measurements. The nodes integrated with capacitive accelerometers were used in a wireless system to monitor bridge health in [72]. A wireless system consisted of *Stanford WiMMS* nodes was implemented to investigate an excessive vibration issue of a cantilever theater balcony in [71]. Dynamic acceleration measurements were conducted using a wireless system consisted of *MICA* nodes in [74, 75] for risk assessment of buildings. A two-story building model upon a shake table was used in the experimental testing. Ambient structural vibrations were reliably monitored in a bridge health monitoring study with a wireless system consisted of accelerometer interfaced *MICAz* nodes [60]. A prototype wireless system using "*AEPod*" wireless nodes was proposed to real-time detection of active fatigue cracks in railway bridges in [76]. In addition to the research described above, several other commercial wireless sensor systems with active wireless nodes are currently available for IHM [77-80] and have been used in research [29, 81, 82].

As a whole, all of the above efforts involving active sensor nodes highlight the advantage of them being used in multiple numbers in wireless IHM systems to monitor large scale infrastructure. Furthermore, they highlight the advantage of active nodes being useful in the measurement of dynamic responses of infrastructure. However, these active sensor nodes consume power in wireless data transfer. Depending on the number of sensors in the wireless system and the sampling rates, the amount of data transfers in the system increases and therefore the power consumption in active sensor nodes. This high power consumption adds considerable system maintenance overhead as the batteries of multiple sensor nodes deployed in different locations of the infrastructure have to be frequently replaced. Energy harvesting was attempted to support the power consumption of active wireless nodes as a hardware-based approach [28, 36, 57, 83]. However, the consumed power portion in the active sensor nodes for data transfer still prevails.

2.2.1 System Architectures

It is important to consider wireless sensor system architectures implemented for IHM predominantly to identify their spatial coverage and how sensor nodes communicate between each other. Widely implemented wireless network architectures comprising active sensor nodes are homogeneous. Although some of the nodes in the system are assigned with different tasks, hardware of the nodes remains the same. According to the system architecture discussed in [68], the assigned tasks define whether the node is a "*Base station*", a "*Manager*", a "*Cluster head*" or a "*Leaf node*". *Leaf nodes* function as relevant local data collectors which are spread within a cluster which covers a specific spatial area of the infrastructure. The *Cluster head* collects the total data of *Leaf nodes* in a cluster. *Manager nodes* control the inter-cluster communication between *Cluster heads*. The *Base station* acts as the human interface providing observation and control functionalities of the whole system. However, when it comes to large-scale infrastructure the number of *Leaf nodes* are highly increased with the appropriate expansion of the system. Most of the time the clusters are localized and the communication between *Leaf nodes* and the *Cluster head* is point-to-point (i.e. single hop). The Same type of cluster-based architecture for wireless IHM has also been proposed in [84] where the whole wireless network is partitioned into single hop clusters. Two level cluster tree architecture proposed in [54] has a "*Super node*" which fulfills the functions of *Manager node* and was a single level reduced version of the one discussed in [68].

The multi-tiered architecture introduced in [85] was predominantly for heterogeneous wireless sensor networks. It had two tiers known as "*micro-net*" and "*meso-net*". The *micro-net* consists of a single active wireless node which collects data from wired sensors spread around a specific spatial area of the structure. The *meso-net* is the upper tier which interconnects all *micro-nets* through the wireless nodes. An extended version of the aforementioned architecture with three tiers was presented in [86] with introduced "*macro node*" which controls the whole network. The two-tier architecture detailed in [25] has wireless sensors in the lower tier in addition to the central wireless nodes consisting the upper tier. The wireless sensors in lower tier have point-to-point communication with upper tier central nodes.

Overall, it can be highlighted that the lowest tier of almost all of the aforementioned architectures covers a specific spatial area of the infrastructure. Additionally, the communication between lowest tier wireless nodes and immediate upper tier wireless nodes are point-to-point. Furthermore, the system architectures can be both homogeneous and heterogeneous.

2.2.2 Vibration-Based Method for IHM

Another important reason for the usage of active nodes in wireless IHM in addition to the economical and convenience advantages is their ability to support the measurement of dynamic responses of infrastructure. The measurements of dynamic responses (e.g., vibration induced dynamic acceleration, strain, etc.) are used to extract important indicators such as natural frequencies and mode shapes related to infrastructure [11, 33, 87-89]. In particular, the natural frequency can be taken as an indicator of the state (e.g., loading, damage) of the structure as it is sensitive to mass and stiffness changes. The natural frequency of a simply supported beam is given by [90],

$$f_n = \frac{\kappa^2}{2\pi}\sqrt{\frac{EI}{\rho A}} \qquad 2.1$$

where, f_n is the natural frequency of the n^{th} mode (Hz), $\kappa \approx n\pi/l$ (m^{-1}), E is Young's modulus (Nm^{-2}), I is the moment of inertia given by $bh^3/12$ (m^4) where b and h are width and height of the cross-section, respectively, ρ is weight density (kgm^{-3}) and A is the area of cross-section given by bh (m^2). The value of κ depends upon the boundary conditions (e.g., simply supported, cantilever, clamped-clamped).

The health monitoring study conducted in a cable-stayed bridge with installed active wireless accelerometers has provided a comparison of acquired natural frequencies with the same previously acquired from a wired system [28]. Most of the considered natural frequency values were in good agreement with the ones acquired from wired measurements. Three-axis acceleration was measured in induced vibration testing of a concrete bridge in [91]. The frequency response analysis was performed upon the measurements where lowest natural frequencies detected were used to interpret different mode shapes and damaged scenarios. IHM study of a bridge in [88] has shown that stiffness degradation produced damage could be identified if the frequency shifts are more than 1%, provided that the environmental influences (e.g., the effect of temperature, humidity, wind, etc.) are pre-filtered. Natural frequencies of five modes in different damage scenarios were analyzed using the data acquired from force balanced 3-axis accelerometers. A three-story building model was equipped with wireless accelerometer nodes under free vibration conditions in [69] to investigate the performance of the wireless measurement system. The natural frequencies obtained by the prominent peaks of the amplitude spectrum for third-floor measurements were in good agreement with simulated values. Wireless health monitoring of a wind turbine steel tower has been done in [70] with wireless accelerometers attached to four discrete levels. The first three natural frequencies obtained were in good agreement with those acquired from wired measurements and simulated values. The health monitoring performed on a bridge with active wireless accelerometers has validated that the frequencies first four modes against simultaneously measured data from wired accelerometers [92]. Vibration-based IHM was performed in [71] of a instrumented theater balcony with active wireless accelerometers by acquiring natural frequencies from the frequency analysis. The natural frequencies of the first four modes were used in the bridge health monitoring study conducted in [60] with active wireless accelerometers. A study in [93] has presented vibration-based health monitoring of a footbridge. The study which spanned for five years has shown shifts in the natural frequencies of first nine modes of the footbridge.

The natural frequency shifts were found to be reliable in simple damage identification of graphite/epoxy composite plates in [94] with conducted vibration measurements of the plates. The shifts in three lowest natural frequencies of a beam with varying depth have been used to propose a numerical method to determine the location of a crack in [95]. The shifts in first three natural frequencies were used to identify damage of a simulated simply supported beam in [96] with a different form of damage modeling. An analytical and simulation-based method to detect damage of an edge-hinged circular arch was presented in [97] based on shifts in natural frequencies of lowest four modes. The study was experimentally supported in [12] with a steel arch consisted of a damage at random location. It has been identified that the maximum shifts of the frequency response function of an aircraft wing model affected by damage occurred at two distinct prominent peaks [13]. A method to predict the fatigue life of concrete structures has been presented in [98] using the shifts of first natural frequency acquired from a concrete beam. Conventional strain gauges were used in [99] for vibration-based damage detection of an aircraft wing. In the process of justifying the method, the extracted natural frequencies of different modes were compared with simulation results. When considering the aforementioned research studies, it is evident that the natural frequency shift in structures can provide descriptive information about their health.

2.3 Passive Sensing for Wireless IHM

Passive wireless sensing methods were introduced for IHM to overcome the disadvantage of battery power supply of active sensor nodes. These methods can be predominantly categorized into antenna-based sensing and sense with inductive coupling principle.

In antenna-based sensing, the antenna dimension perturbations driven resonant frequency shifts are correlated with strain or expansion of cracks in infrastructure. Different types of antennas including rectangular microstrip patch antennas [37, 100-102], circular microstrip patch antennas [38, 103, 104], slotted circular microstrip patch antennas [105] and dipole antennas [106, 107] were exploited in this approach. Furthermore, A cylindrical coaxial cavity resonator studied in [108] was another antenna-based solution. This was a potential embeddable wireless strain sensor for IHM applications. The resonant frequency shift influenced by longitudinal dimension change of the cavity encased in the structure under test was taken as the indirect measurement of strain.

A wireless strain sensor was introduced in [109] using inductive coupling principle. The sensor was a core-less multi-turn inductor coil of which ends are terminated with a capacitor. The changes of the cross-sectional area of the coil sensor due to stress were detected by the resonant frequency shifts. Another inductively coupled coil sensor/interrogator system to measure corrosion of reinforcement of concrete is presented in [39]. The resonant frequency shifts of the sensor were correlated with corrosion voltage perturbations. The near-field corrosion sensor developed in [110] operated with inductive coupling. The sensor followed the principle of transient resistance measurement and the measured resistance values were in good agreement with those from laboratory measurement equipment. A mountable planner inductor with series connected capacitor was studied as a passive wireless strain sensor in [111]. The capacitive element was used as strain transducer while inductor acted as the coupling element. The interrogation was done by a ring antenna in the close vicinity where the resonant frequency shift was the indirect indicator of strain.

Even though aforementioned efforts are promising for wireless IHM predominantly due to the passive operation of the sensors, their field usage to date is limited. This is due to several inherent practical issues. The shorter wireless interrogation distances and less sensitivity (e.g., strain to the resonant frequency shift) are some of those issues as detailed in [45]. In particular, high precision measurement equipment is necessary to measure the resonant frequency shifts related to structural strain changes in $\mu\epsilon$ levels. Furthermore, jitter is always possible in reflection characteristic measurements ($|S_{11}|$ in dB) in electromagnetically harsh structural environments with the presence of concrete and metal structural members. The other approaches apart from patch antenna-based sensors may not perform well with metal structures. Especially, the approaches involving inductive coupling principle may need tight coil antenna alignment to function properly. More importantly, the ability of these sensors to perform much desired dynamic measurements of infrastructure has not also been proven.

2.4 RFID Technology-Based Wireless Sensing

RFID systems, in general, comprise a radio scanner unit called as "*reader*" and remote transponders termed as "*tag antennas*". These systems can be different according to reader transmit frequencies, physical coupling method and read ranges they possess [47]. The reader transmit frequencies can be in the bands of low frequency (LF, 30 kHz – 300 kHz), high frequency/radio frequency (HF/RF, 3 MHz – 30 MHz), ultra-high frequency (UHF, 300 MHz – 3 GHz) and microwave (> 3 GHz) [47]. The systems which have read ranges up to 1 cm are known as "*close coupling systems*". These systems are coupled using electric and magnetic fields and they operate with frequencies up to 30 MHz. The "*remote coupling systems*" can possess read ranges up to 1 m. The majority of these systems operate with inductive coupling between reader and tag antennas and use frequencies below 135 kHz or 13.56 MHz. The systems that possess read ranges beyond 1 m are known as "*long-range systems*" [47]. They operate with backscatter principle and use 860 MHz – 960 MHz UHF frequencies and 2.5 GHz and 5.8 GHz microwave frequencies [47, 112]. The UHF RFID frequency band usage is regulated in different parts of the world where 920 MHz – 926 MHz range is allowed with 4-W effective isotropic radiated power (EIRP) for Australia [113].

Figure 2.1 depicts a UHF system with a single tag antenna. The tag antenna normally consists of a miniaturized antenna and a RFID tag chip. The RFID tag chip has a read/write memory which keeps the identification information [114]. The transmitted interrogation signal by the reader received by the miniature antenna is used to power up the RFID tag chip which modulates the identification information on to the backscattering signal. This modulated backscatter signal is then acquired by the reader in reverse and unravels the identification information. In the modulation process, tag chip employs two impedance states which include a "*matched state*" and "*high impedance state*" [114]. Normally the matched state is where the antenna impedance is conjugately matched with the complex impedance of the tag chip to achieve maximum power transfer to the chip. High impedance state is normally shorted where the chip offers maximum impedance mismatch to achieve maximum signal reflection.

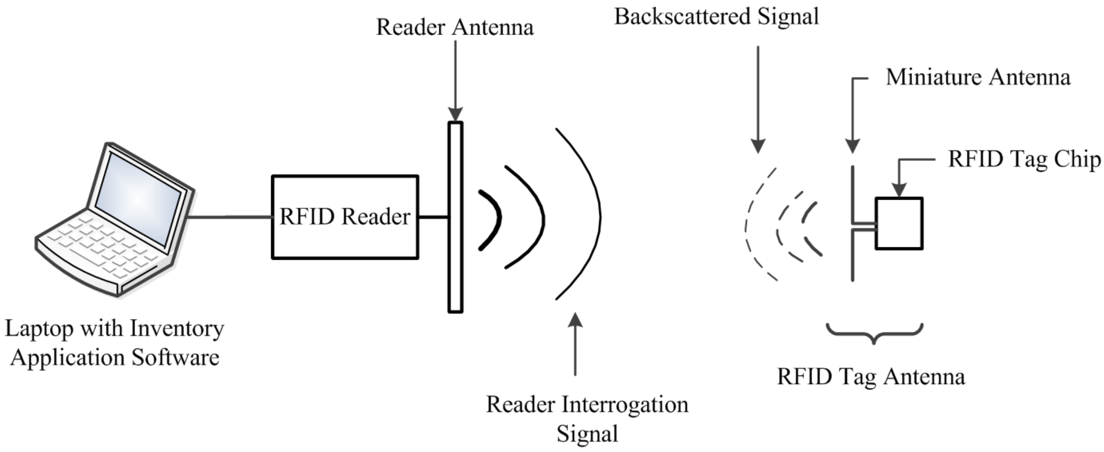

Figure 2.1: General UHF RFID system with tag antenna.

Since modulated backscatter communication of RFID is passive, it does not consume power at the tag antenna. This passive communication technique has encouraged the development of tag antenna integrated sensors. There are several tag antenna types available in RFID technology for integrated sensor development [115]. One is called the "*Passive*" which has no power source available to power up the chip where chip power is supplied by reader interrogation signal itself as mentioned above. Another tag antenna sensor type is called "*Semi-passive*" in which it contains a small power source to power up the tag chip circuitry. However, these semi-passive tag antennas communicate in the same modulated passive backscattering principle as passive tag antennas for which they do not consume battery power [116, 117]. "*Active*" tag antenna integrated sensors consume power from the battery for both communication and powering tag chip circuitry where very high read ranges can be achieved. They also can transmit signals to readers where interrogation by the reader is not essential in the initiation of communication [115].

2.4.1 Passive Sensing

The tag antenna-based sensing methods were investigated for wireless IHM predominantly to acquire the battery-less advantage at the sensor. The investigated methods can be found in most of the RFID system categories which are previously mentioned. A meander line dipole tag antenna was proposed and studied as a passive RFID-based strain sensor in [118]. The backscatter signal power perturbations influenced by compression or expansion of the meander line dipole tag antenna was measured as the indication of strain. The measurements were done at a 60-cm distance between the reader and proposed sensor. A mountable folded patch RFID tag antenna was studied extensively for strain measurements in [41]. The resonant frequency shift due to deformation of the antenna has been exploited as the indicator of strain. Strain transferability from aluminum structure to antenna has been studied while the measurement results from read ranges of 30 cm and 60 cm were compared with conventional strain sensors. However, strain to the resonant frequency linearity has dropped at 60-cm read range. Passive RFID displacement sensor based on the reduction of tag antenna performance near metal was studied in [40]. The backscattered signal power and transmit power was taken as indirect indicators of displacement of the structure. The amount of backscattered signal power received at the reader has been found to be inadequate to measure when the tag antenna was closer to the metal structure. The crack widening detection sensor presented in [119] was consisted of two closely coupled dipole tag antennas. The phase change of the backscattered signal from the both RFID tag antennas due to increasing inter-tag antenna distance is correlated with crack widening.

A method of detecting water infiltration in concrete with embedded dipole tag antenna was presented in [120]. The antenna impedance change influenced by the dielectric permittivity of the surrounding material was presented as the sensing method of water infiltration. A method of detecting water on concrete was also presented by using a RFID tag antenna grid [120]. The amount of backscattered signal power was measured to detect the presence of water. However, the tests were carried out in small read ranges. Low-cost passive RFID tag antenna suitability to monitor concrete degradation in bridge decks has been investigated by exploiting the tag detuning effects due to corrosion in [121]. Tag detuning effect due to reinforcement and concrete found to be problematic and encasements have been introduced to negate the effect. Field experiments have been done using a near-field RFID reader system where tag readability was taken as the measure of degradation of concrete. Another inductively coupled RFID-based wireless sensing system with integrated nanotechnology was presented in [122] for strain and pH measurements of infrastructure. The resonant frequency shift and impedance bandwidth change of the sensor were correlated to strain and pH changes of the structure, respectively.

Chipless RFID tag antennas have been investigated predominantly to achieve the cost reduction without using the RFID tag chip. These tag antennas are categorized into three main categories based on the challenging data encoding methods implemented without the RFID tag chip involvement [123]. They are time domain reflectometry (TDR)-based chipless tag antennas, spectral signature-based chipless tag antennas and amplitude/phase backscatter modulation-based chipless tag antennas. These chipless RFID tag antennas have also been investigated in passive sensing applications in [124-127]. In the context of wireless IHM, a chipless RFID-based strain sensing method was proposed for wireless IHM in [128] with micro resonator-based backscatter target sensors. The resonant frequency shift was taken as the indirect measurement of strain change of the structure. The chipless RFID approach was also investigated in [129, 130] for surface crack detection of infrastructure. The time domain reflectometry signatures from developed surface crack antenna reflectometric sensors (co-planar monopole antenna integrated transmission lines) were used to detect formation of surface cracks and their formation directions.

All of the above passive RFID-based sensing techniques did not have additional electronics attached to the sensor. The passive RFID-based temperature sensor presented in [131] for concrete monitoring had inbuilt temperature sensing ability within the RFID tag chip. The sensor was developed with a dipole tag antenna with the possibility of keeping antenna outside the concrete. A smart RFID-based corrosion sensor with additional electronics for wireless IHM is studied in [42]. The sensor was equipped with a coil antenna for inductive coupling and had the capability of powering the electronics from the same antenna. An architecture of self-powered near-field RFID-based threshold sensor integrated with electronics was presented in [132] for chlorine ingress monitoring in concrete bridge decks. The design of the sensor was carried out in [43] with comprehensive experiments to detect chlorine ion concentration threshold of a concrete bridge deck. Two RFID-based sensors (operating with HF and UHF) to measure temperature and moisture of concrete were studied in [44] for wireless IHM. The sensors were integrated with additional electronics which are powered by harvested power output of the RFID tag chips. The maximum interrogation distance achieved by UHF sensor was 40 cm. HF RFID-based temperature sensors with thermally sensitive resistors for concrete monitoring and strain monitoring of metal structures were presented in [133]. The temperature sensor has shown good agreement with reference measurements and the strain sensor has shown linearity in static strain measurements. Temperature and strain sensing in concrete structures with passive RFID-based tag antennas integrated with extra electronics were performed in [133]. These sensors were HF sensors which were interrogated with coil antennas in short read range. Another strain sensing effort for wireless IHM was presented in [134] with passive tag antenna integrated electronics. Even though the presented sensor had dedicated tag antennas for powering electronics and communication, the tested read range was 20 mm.

However, these RFID-based passive sensors also have issues when considered in field IHM applications. The indirect raw measurements of backscatter signal power, reader transmit power and the resonant frequency can be highly peculiar in real infrastructure environments with multiple concrete and metal structural members with different orientations. In particular, some of them may not function with metal structures. The chipless RFID-based sensing methods also have disadvantages with the number of bits that can be encoded and special reader hardware requirements as discussed in [123]. The ability to measure dynamic responses using passive RFID-based sensing has also not been proven. For some of the above applications, there may have been several interrogation cycles to receive one reading which is not acceptable in measurements of dynamic responses. Furthermore, the low interrogation ranges make it hard to incorporate these RFID-based passive sensing in wireless IHM which require measurements from multiple sensors at different locations. In particular, the above-mentioned systems with coil antennas may require tight antenna alignment which provides the possibility of interrogating only a single sensor at a given time.

2.4.2 Semi-Passive Sensing

As stated earlier, the semi-passive RFID tag antennas communicate using the same modulated passive backscatter technique of passive RFID tag antennas. This is a major advantage that can be acquired to a wireless IHM system over the active sensor nodes which have transceivers that consume power in transferring data. With the advent of new generation RFID tag chips [135], the battery power of semi-passive RFID tag antenna integrated sensors can be utilized only to power the integrated sensors and supporting electronics. Furthermore, there is a great potential of developing semi-passive RFID-based sensors with high read ranges to measure dynamic responses. However, the instances of them being developed to be used in wireless IHM are limited.

Efforts to emulate semi-passive RFID-based sensing using a commercial wireless system [77] was presented by highlighting the unavailability of suitable semi-passive RFID tag antenna integrated sensors [81, 82]. Both dynamic acceleration and strain of a model structure were measured in these research efforts. A semi-passive RFID-based strain sensor was presented in [136] for wireless IHM. The strain gauge sensor consisted of resistance to frequency conversion electronics and two dipole antennas. One antenna is used for modulated backscattering of identification information and for the purpose of waking up the sensor. The other antenna is for backscattering of the output from resistance to frequency conversion electronics. The sensor has shown good read range. The dynamic strain sensing ability of the sensor was demonstrated by measuring the strain of a vibrating cantilever beam. A semi-passive RFID-based sensor included wireless measurement system architecture was detailed in [137] for aircraft health monitoring application. A detailed wireless sensor system architecture including semi-passive RFID-based sensors has also been introduced in [138].

However, the issues with small read ranges still exist even with the semi-passive RFID-based sensors when they are considered for wireless IHM applications. This is predominantly due to tag antenna de-tuning with respect to materials in the vicinity. Mostly, dipole RFID tag antenna performance degradation in close vicinity to material elements has been reported with experiments of tag antenna mounted on several materials [139]. The phenomenon has also been investigated for commercially available and custom made dipole like tag antennas [140-142]. Especially, considerable read range reduction of dipole RFID tag antennas near metal has been reported with simulation based explanations in [46, 143, 144]. However, the presence of concrete and metal structural members in close vicinity is unavoidable in IHM environments. Therefore, optimized tag antennas are necessary for the development of semi-passive RFID-based sensors for wireless IHM. In this context, the research of RFID tag antennas with conductive materials [145-154] and concrete [155-157] is a motivation for further investigation with large scale concrete and metal structural members.

The next issue is the influence of structural member orientation and shapes upon the incident interrogation signal power on the tag antenna integrated semi-passive RFID sensors. This is an important consideration since semi-passive RFID tag antenna based sensors still follow the passive backscatter communication principle where an incident interrogation signal power greater than RFID tag chip sensitivity is necessary to initiate proper wireless communication. Depending on the complexity of the infrastructure environment (e.g., orientation, shape, multiple members, etc.), the incident interrogation signal power upon it can be different in various locations. Previous studies investigating this are limited. RF energy transmission in the metallic environment has been studied in [158] with simulated energy flow streamlines. The study proved that the multi-layer antennas are better in wireless energy reception than dipole antennas in metallic environments. The extended investigation has shown the possibility of blind area occurrence due to metallic obstacles within transmitted signal path. However, this has provided only a macro view of wireless signal power delivery where further studies are necessary for evaluating the wireless power flow for the vicinity of structural members upon which semi-passive RFID tag antenna integrated sensors are intended to be mounted.

The unavailability of suitable semi-passive RFID-based sensors which can provide dynamic response measurement of infrastructure with substantial information is another issue. According to review in Section 2.2.2, the natural frequency information is a vital indicator extracted from measurements of dynamic responses. The natural frequencies of most large-scale civil structures are spread within the band of 0 Hz to 10 Hz [28, 58, 60, 91-93]. Depending upon the structure, possibilities are there that the natural frequencies lie beyond this band [70, 71, 88]. In particular, the natural frequencies of different modes of structural members are well beyond the aforementioned band [13, 94, 96, 97]. Therefore the RFID-based measurement system with semi-passive tag antenna integrated sensors should be capable of measuring dynamic responses with substantial spectral bandwidth.

Furthermore when considering the popular architectures with active sensor nodes for wireless IHM reviewed in Section 2.2.1 and other proposed RFID-based wireless sensor system architectures [137, 159], possibility is there to substitute single hop active wireless nodes (*Leaf nodes*) in lowest tier with semi-passive RFID tag antenna integrated sensors with acceptable read range and cluster heads with RFID reader integrated wireless nodes. Since semi-passive tag antenna integrated sensors are used as *Leaf nodes* (which are normally in multiple deployments, see Section 2.2.1) instead of active nodes, the instances of battery replacement of the sensor system in bulk scale will be reduced.

2.5 Research Methodology

In this thesis, a wireless system with semi-passive RFID tag antenna integrated sensors for dynamic response measurement of infrastructure is presented. The development of the proposed RFID-based wireless IHM system has three major stages of simulation, design, and measurement. These stages are predominantly to fill the research gaps which are identified in previous sections of the chapter.

The simulation stage mainly covers the theoretical part of the development. In this stage, the design and simulation studies will be done to create a relatively small tuneable RFID tag antenna which can be electronically integrated with sensors and has acceptable performance when mounted on members made out of concrete and metal. The modeling, impedance matching and parametric optimization of the tag antenna will be performed using computer simulation technology (CST) Studio Suite [160]. Furthermore, comprehensive simulation-based performance analysis of the tag antenna in free space and when mounted on structural members of different scale will also be performed. An antenna system model consists of a reader antenna and tag antennas mounted on a full-scale structural member will be created in CST Microwave Studio to investigate the wireless signal power flow. The influences of the orientation and shape of the structural member upon wireless signal power flow towards and in the vicinity will be studied with comprehensive simulations.

A prototype RFID-based wireless dynamic acceleration measurement system design with semi-passive tag antenna integrated acceleration sensor will be performed at the initial stage of the development stage. A dynamic measurement oriented comprehensive hardware supported firmware development for semi-passive tag antenna integrated acceleration sensor will be done. The C language will be predominantly used in this task in MPLAB X integrated development environment (IDE) [161]. The fabrication of the designed tag antenna will be performed using printed circuit board (PCB) technology. Novel semi-passive tag antenna integrated acceleration and strain sensors will be created with integrating the fabricated tag antenna and custom designed miniature sensor circuit boards. Furthermore, the enhancement of hardware and firmware will be done along with custom data acquisition application to improve the spectral bandwidth of the dynamic measurements of the system. The data acquisition application will be written in C# language using Microsoft Visual Studio 2012 development environment [162] incorporating Octane software development kit (SDK) [163].

In the measurement stage, the possible design enhancement limits related to hardware and firmware will be investigated. The laboratory measurement equipment such as multimeter and digital oscilloscope will be extensively used in this task. The prototype RFID-based wireless dynamic acceleration measurement system will be tested for acceleration measurement of a simply supported steel structural member (a part used to create a bridge model). The performance of the fabricated tag antenna including the resonant frequency, antenna gain, read range and readability according to mounting orientation will be tested in the laboratory. The laboratory measurement equipment such as a performance network analyzer (PNA) and a signal analyzer (SA) will be used in the testing along with Impinj

Speedway Revolution commercial UHF RFID reader [164]. Then the enhanced system with multiple tag antenna integrated acceleration sensors will be tested by measuring the dynamic acceleration of a simply supported full-scale steel structural member. Finally, the system with tag antenna integrated multiple sensors (i.e., accelerometer and strain gauge) will be tested in measuring simultaneous dynamic acceleration and strain of a cantilever structural member. A standard impact hammer system will be used to induce vibrations of the beams [165]. The natural frequency determination ability of the structural members by the RFID-based wireless system will be comprehensively compared with the same of standard commercial wired and active wireless systems used for IHM [77, 78, 166, 167].

2.6 Conclusion

Even though passive sensing approaches are providing solutions in developing battery-less wireless sensors for IHM, these have certain issues such as adapting the measurement methods to complex infrastructure environments, small communication ranges and inability to measure important dynamic responses. Therefore, their usage in field applications of wireless IHM involving multiple sensing points is limited. On the contrary, active nodes are pervasive in recent wireless IHM field applications due to their capability of measuring dynamic responses and possible implementation in multiple numbers in system level (but as usual these devices consume battery power during data transmission).

Semi-passive RFID-based sensing has the potential to be developed to provide substantial communication ranges and measurement of dynamic responses which makes it a suitable solution for implementing low power wireless sensor systems for IHM. However, there is a lack of information available in the literature about the development of semi-passive RFID-based wireless sensor systems which can measure dynamic responses securing substantial information of infrastructure. This has motivated the work presented in this thesis.

Chapter 3 RFID-Based Wireless System Design for Measurement of Dynamic Acceleration of Infrastructure

3.1 Introduction

This chapter presents a novel RFID-based wireless dynamic acceleration measurement system designed for vibration-based IHM. Even though dynamic acceleration measurements for vibration-based IHM are ubiquitous with active wireless sensor systems, RFID-based dynamic acceleration measurement systems are limited. The concept is realized with a UHF RFID system using passive backscatter wireless communication of a newly designed semi-passive RFID tag antenna integrated acceleration sensor. The inadequacy of previous attempts of RFID-based acceleration sensors; both research and commercial is highlighted in the background considering the necessities of vibration-based IHM. Consequently, the design of the proposed RFID-based dynamic acceleration measurement system is considered. The results of laboratory measurements of the natural frequency of a rectangular steel beam with this system and their comparison with independent commercial systems are presented.

3.2 Background

According to the description in Chapter 2, the measurement of dynamic responses of infrastructure is extremely important for the well-established vibration-based method of IHM. Consequently, dynamic acceleration measurements are commonly performed to acquire the natural frequency information of infrastructure. Although acceleration measurement systems with active wireless sensor nodes are customary in this process, RFID-based systems are limited. This is majorly due to the unavailability of RFID tag antenna integrated sensors which can measure dynamic acceleration in electromagnetically harsh infrastructure environments.

The tip-loaded RFID tag antenna integrated sensor presented in [48] can be highlighted as one of the limited research attempts to measure acceleration. The tag antenna integrated sensor intended for environmental monitoring had integrated sensors of temperature, light, and acceleration. Both light sensor and accelerometer were digital sensors while the used temperature sensor was analog. All the sensors were integrated to the RFID chip via a microcontroller through I^2C (inter-integrated circuit) interface. This tag antenna integrated sensor had two communication modes of passive (P) and battery assisted passive (BAP) and operated with EPC Class 1 Generation 2 protocol [168]. The acceleration measurements were demonstrated only in the BAP mode in 5-s intervals (i.e. 0.1-Hz spectral bandwidth) as static acceleration for an orientation detection application. Passive UHF RFID dipole tag antenna platform presented in [169] is another development which attempted acceleration measurements. This platform was initially integrated with a temperature sensor and subsequently upgraded to sense acceleration in [170]. However, dynamic acceleration monitoring was not possible due to power constraints and the RFID tag antenna platform integrated acceleration sensor is used only to detect orientation.

When considering the available commercial acceleration sensing RFID tag antennas, the active vibration sensor tag antenna which operates in 2.5-GHz ISM band is capable of continuous acceleration measurements [171, 172]. Some other active tag antenna integrated sensors which are capable of monitoring event triggered shock events and 3-axis acceleration can be found in [173, 174]. However, being an active tag antenna integrated sensors these utilize battery power to data transfer. The passive acceleration sensor tag consisting of a dipole antenna is also capable of measuring acceleration at a maximum 5-Hz data rate (i.e. 2.5-Hz spectral bandwidth) on non-metallic backgrounds [175].

The natural frequencies of most large-scale civil structures are spread within the band of 0 Hz to 10 Hz [28, 58, 60, 91-93]. However, depending upon the structure, the natural frequencies can be beyond this band [70, 71, 88]. In particular, the natural frequencies of different modes of structural members are well beyond the aforementioned band [13, 94, 96, 97]. Therefore the RFID-based dynamic acceleration measurement system's spectral bandwidth should be broader than previously discussed research and commercial efforts (excluding active tag antenna sensors).

3.3 Proposed RFID-Based Wireless IHM System

The proposed RFID-based wireless IHM system is shown in Figure 3.1. The RFID tag antenna integrated sensors are mounted on structural members to acquire measurements such as strain, acceleration, and displacement. The long range wireless node is integrated with the RFID reader to provide the system with the capability of wireless networking. The RFID readers of the same type in different sections of large-scale infrastructure can operate in a wireless network where web server in the same wireless network collects the sensor data which can be accessed via the internet. Therefore, tag antenna integrated sensors and reader integrated wireless nodes in combination fulfill the task of single hop active nodes in the lowest tier of wireless IHM system architectures reviewed in Chapter 2. Furthermore, the upper tier task of inter-cluster communication is fulfilled by reader integrated wireless nodes. Overall, this provides the advantage of low cost, low power RFID technology to support the need of dense population of sensors in large scale IHM. Figure 3.2 shows the block diagram of the RFID section of the system which includes a reader integrated wireless node and a tag antenna integrated sensor. Generally, the sensor can be any analog or digital transducer of a physical quantity which is useful in determining the status of the infrastructure.

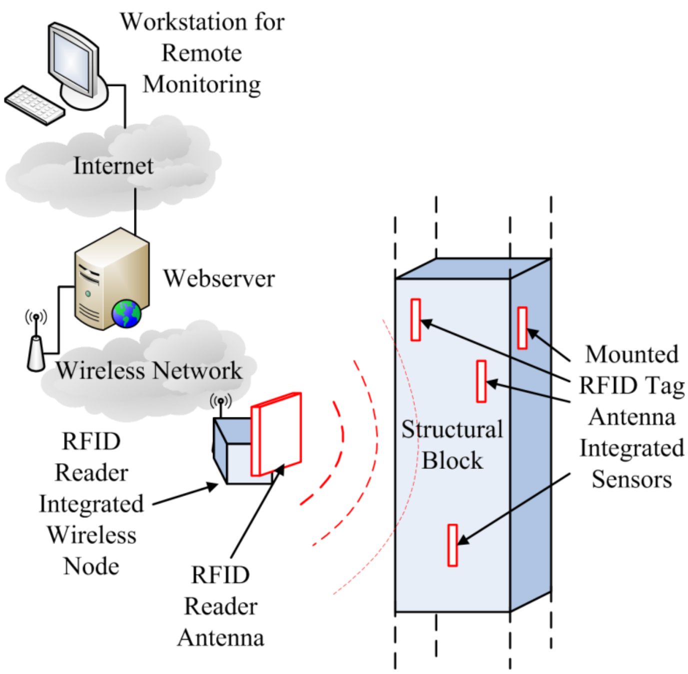

Figure 3.1: Proposed RFID-based wireless infrastructure health monitoring system.

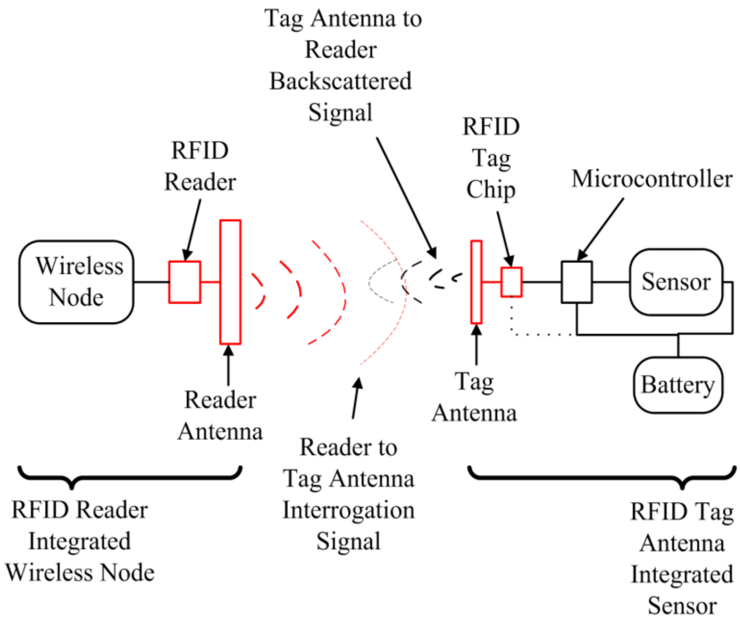

Figure 3.2: RFID section of the wireless infrastructure health monitoring system (dotted line is connected in battery-assisted passive (BAP) operation).

3.4 RFID-Based Dynamic Acceleration Measurement System Design

The designed measurement system is shown in Figure 3.3(a). It consists of a custom designed tag antenna integrated acceleration sensor (TAIAS), Laird Technologies® S9025PR antenna which has maximum far-field gain of 5.5 dBic as the reader antenna (see Figure 3.3(b)) [176] and Indy® RS500 development board which contains Indy® RS500 system-in-package (SiP) as the RFID reader (see Figure 3.3(c)) [177]. A 3-axis accelerometer was used as the sensor according to Figure 3.2. The reader supports EPC Class 1 Generation 2 air interface protocol in the UHF RFID frequency band [168]. In terms of performance, it has a 23-dBm maximum transmit power and –65-dBm receive sensitivity. In the current system development, the RFID reader is directly connected to a laptop for the purpose of acceleration data acquisition.

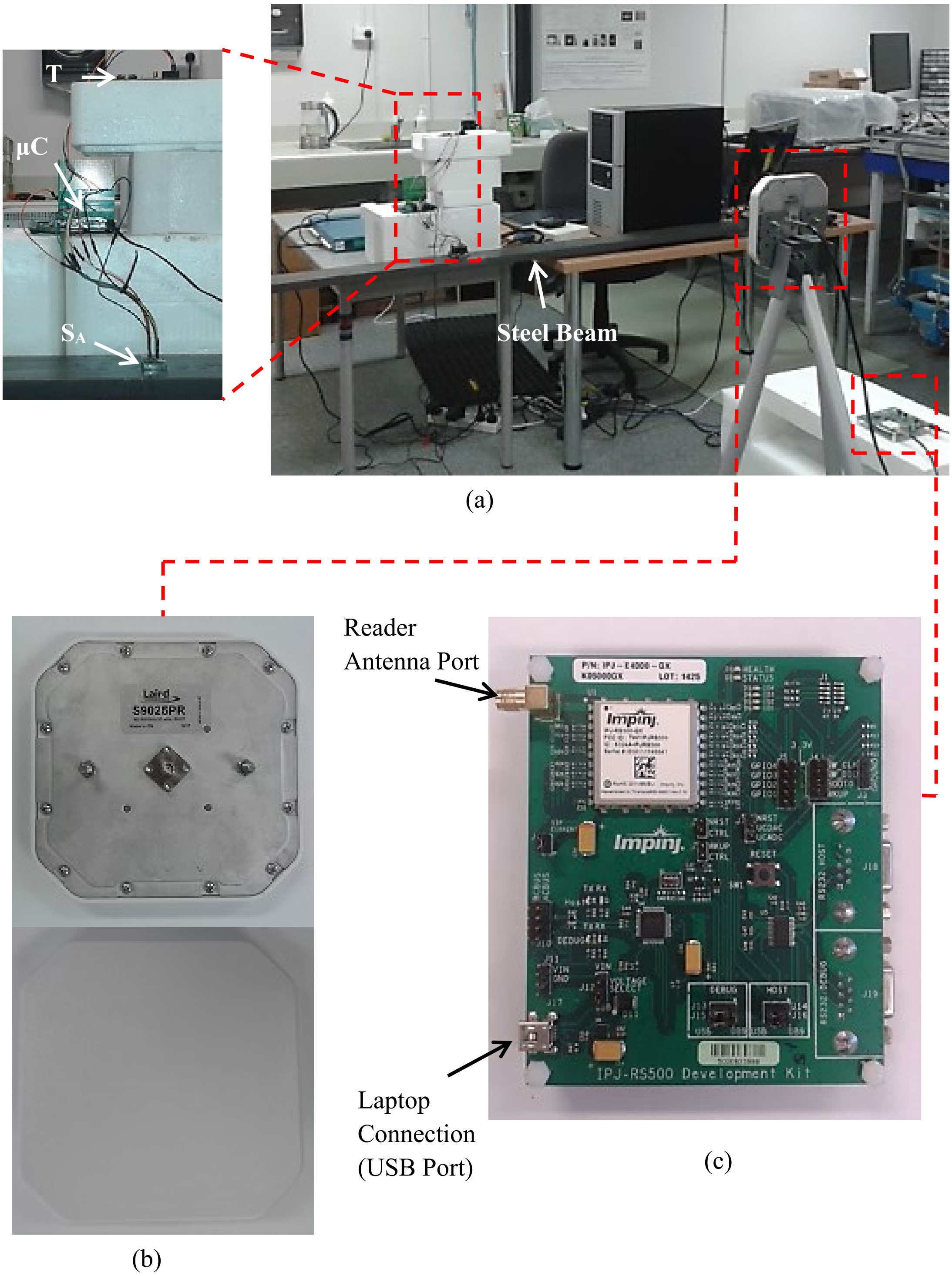

Figure 3.3: (a) RFID-based dynamic acceleration measurement system measuring the vibration of a rectangular steel beam (T - RFID tag antenna, µC - microcontroller and S_A - accelerometer), (b) reader antenna and (c) RFID reader (USB-universal serial bus).

3.5 Tag Antenna Integrated Acceleration Sensor Design

The TAIAS is an important component of the proposed measurement system. It carries out the major tasks of sensing dynamic acceleration of structures and modulation of the sensed data on to backscattered signals of the RFID tag antenna. Additionally, this component has to be compatible with the aforementioned UHF RFID measurement system. Therefore, hardware selection and the functionality setup of the component are important. The design schematic of the TAIAS is shown in Figure 3.4.

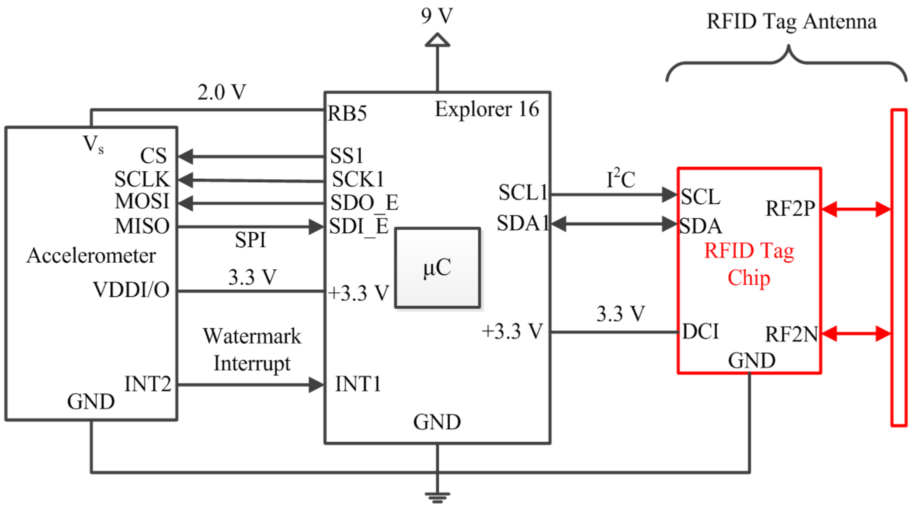

Figure 3.4: Schematic of RFID tag antenna integrated acceleration sensor (*SPI* - serial peripheral interface, *I^2C* – inter-integrated circuit and other notations are in accordance with datasheets [178-181]).

3.5.1 Hardware Design

The hardware implementation of the TAIAS is shown in Figure 3.5. The components used in the design are listed in Table 3.1 in reference to Figure 3.2. The ADXL362 ultra low power 3-axis microelectromechanical systems (MEMS) accelerometer has been used in the design to achieve low power implementation. The operational current required by this accelerometer is in the μA range (1.8 μA at 100 Hz output data rate (ODR) with 2.0 V DC supply) [179]. This is an attractive feature for the IHM application where the acceleration has to be monitored continuously to retain dynamic features. It provides 12-bit acceleration measurement resolution via *SPI* with selectable output data rates, noise modes and different acceleration levels as summarized in Table 3.1. The flexibility of these selections is useful for the application of IHM in different scenarios. Furthermore, it is capable of generating interrupts for certain firmware selectable states and contains a first-in-first-out (FIFO) buffer which can hold up to 512 samples (12-bit acceleration samples).

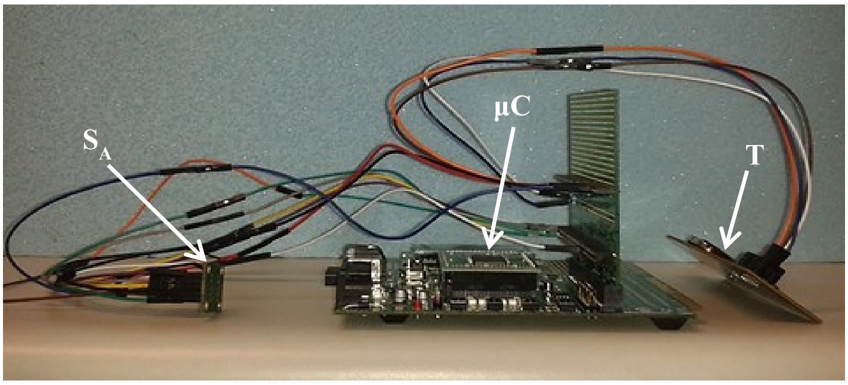

Figure 3.5: Tag antenna integrated acceleration sensor (T - RFID tag antenna, μC - microcontroller and S_A - accelerometer).

Table 3.1: Components and features used in the design.

Component: *Schematic*	Component: *Design*	Features	
Accelerometer	Analog Devices ADXL362 [179, 181]	Acceleration	• 3-axis • +/- 2 g, +/- 4 g and +/- 8 g (configurable)
		Resolution	• 12 bits
		Data rate	• 12.5 Hz to 400 Hz (configurable)
		Antialiasing filter	• Data rate/2 and Data rate/4 (configurable)
		Noise Modes	• Normal, Low noise and Ultra low noise (configurable)
		Interface	• SPI digital (2 MHz to 5 MHz)
		Interrupts	• 2 (configurable)
		Clock	• Internal (51.2 kHz) • External (25.6 kHz to 51.2 kHz configurable)
Microcontroller	PIC24FJ128GA010 [182]	Operation	• 16-bit
		Clock	• 32 MHz maximum with PLL (configurable)
		Interface	• Analog • I^2C and SPI digital
	Explorer 16 development board [180]	Compatibility	• PIC24 range microcontrollers
		Voltage output	• 5.0 V, 3.3 V and 0 V to 3.3 V (adjustable)
RFID tag chip	Impinj® Monza® X-8K Dura development board (RFID tag antenna) [135, 178]	Interface	• EPC Class 1 Generation 2 air interface standards for UHF RFID • I^2C digital (400 kHz maximum)
antenna		On board antenna	• Tip-loaded dipole UHF RFID tag antenna

Impinj® Monza® X-8K Dura development board has been used as the RFID tag which has an on board tip-loaded dipole antenna, Impinj® Monza® X-8K Dura RFID chip and I^2C interface. The RFID chip consists of two firmware configurable RF ports which form the RF air interface that supports EPC Class 1 Generation 2 protocol. This uncommon feature of the chip provides the flexibility of enhancing the readability of the TAIAS using two suitable antennas whenever necessary. Furthermore, it has P and BAP communication modes where the latter has higher sensitivity [135, 178].

The 16-bit PIC24FJ128GA010 microcontroller has been used in the design to avoid unnecessary delays in firmware when handling acceleration data with 12-bit resolution (14 bits in total with 2 sign bits). The microcontroller is equipped with both *SPI* and I^2C interfaces which are necessary for the integration of the accelerometer and the RFID tag antenna. The operational speed of the microcontroller can also be varied using the firmware selectable clocking scheme [182]. Explorer 16 is a recommended development board for 16-bit PIC microcontrollers and it has been used as the interfacing platform in this development [180]. The 3.3-V DC power distribution in the design was done through the Explorer 16 development board where 2.0-V supply is provided to the accelerometer to have a minimum offset in acceleration readings [179].

3.5.2 Firmware Design

Firmware design is an integral part of the accelerometer integrated RFID tag antenna for real-time monitoring of dynamic acceleration. The firmware for the microcontroller of the TAIAS has been written in the C language using MPLAB X IDE [161] giving consideration to the physical quantity of measurement (dynamic acceleration), system in macro level (real-time data acquisition from multiple tag antenna integrated acceleration sensors) and the limitations of the selected RFID hardware.

3.5.2.1 Memory Organization of the RFID Tag Chip

Since the Impinj Monza-X Dura 8K RFID tag chip complies with EPC Class 1 Generation 2 protocol, it has the standard memory organization defined in [168]. The minimum requirements for each memory bank are described in the standards while a given RFID tag chip can have variations upon that. The selected tag chip memory consists of four logical banks identified as "*Reserved*", "*EPC*", "*TID*" and "*USER*" which each has 22 bytes, 18 bytes, 24 bytes and 1024 bytes, respectively [135]. The RF air interface of the tag chip has a word-wise (16-bit) read and write access to these memory banks except some locations in *Reserved*, *EPC,* and *TID* which only has read access. In I^2C transactions, the chip allows word-wise (16-bit) write and byte-wise (8-bit) memory read. In this case, also the tag chip has specific locations in *Reserved* and *TID* banks which are read-only.

Since RFID systems are commercially meant for inventory database handling, the available UHF Generation 2 RFID readers (including the selected reader in Section 3.4) are readily capable of continuous acquisition of the electronic product code (EPC) data located in the *EPC* memory bank. The EPC is normally formatted in words. The selected RFID tag chip has a maximum of 8 words which can be allocated to EPC by configuring the *EPC LENGTH[4:0]* bits found in the *EPC* memory bank. The I^2C address of the RFID tag chip has four selectable combinations providing the opportunity of having a maximum of 4 numbers of them in single I^2C bus. This selection can be achieved by bit configurations of *I2C_ADDR[1:0]* and *LOCK_DA* in the *Reserved* memory bank. Furthermore, the *DCI_RF_EN* bit in *Reserved* memory bank can be configured to control the access of the tag chip from RF air interface. When this bit is configured to be set, the tag chip can be accessed from RF air interface only if the DC input (DCI) is present (i.e. in BAP mode).

3.5.2.2 Operating States of RFID Tag Chip

Selected Impinj Monza-X Dura RFID tag chip has three operating states to be considered. According to the datasheet, they are named as *Internal Control*, *I2C Control* and *Idle or RF Receive* [135]. Table 3.2 provides the summary of conditions which invoke these operating states and constraints generated by them. It shows that the *Internal Control* state has precedence over the other two states and the *I2C control* has precedence over the *Idle or RF Receive* state. When the *DCI_RF_EN* bit is set, the *Idle or RF Receive* state becomes only an idle state if DCI is not present. The state transition diagram of the tag chip is shown in Figure 3.4 [135].

Table 3.2: Operating states of the RFID tag chip [135].

Operating State	Conditions	Constraints
Internal Control	1. Executing an initialization sequence. 2. Writing to non-volatile memory (NVM) 3. Backscattering a response to an interrogation from the reader through RF air interface.	1. I^2C transactions with the RFID chip not possible. 2. Interrogations via RF air interface are not possible.
I2C Control	1. Not in Internal Control 2. Master issuing commands via I^2C interface (state starts when the RFID chip detects its device id in the I^2C commands from the master).	3. Interrogations via RF air interface are not possible.
Idle or RF Receive	1. Receiving reader interrogation from RF air interface or not in Internal Control and I2C Control.	None.

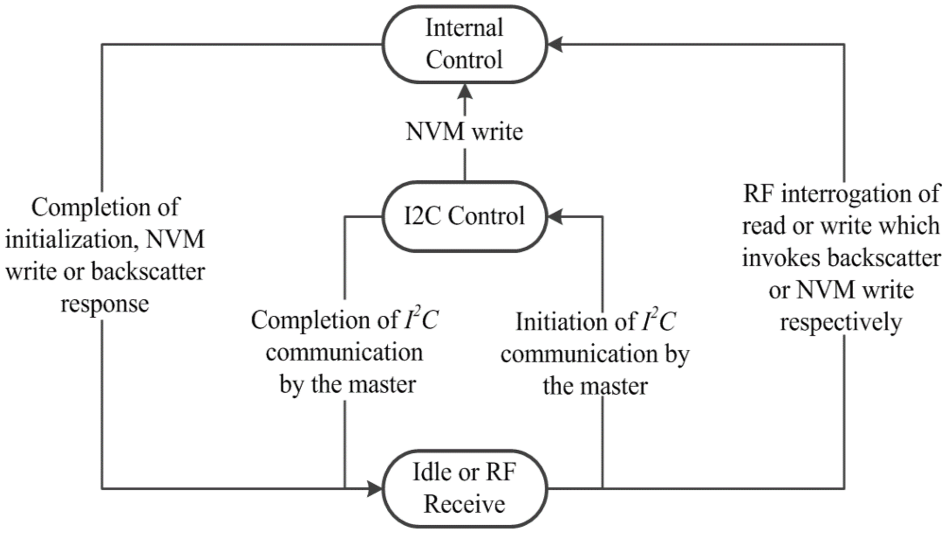

Figure 3.6: State transition diagram of the RFID tag chip [135].

3.5.2.3 Operation of Tag Antenna Integrated Acceleration Sensor

When measuring dynamic acceleration, samples have to be acquired continuously to retain detailed information. However, the previously mentioned operating states of the RFID tag chip add a constraint to continuous data acquisition. RFID tag chip transitioning into *Internal Control* state is the least controllable as it has precedence over the other two states. However, this state transfers back and forth with *Idle or RF Receive* state which provides a slight window in controlling it with firmware that is fast enough. The *I2C Control* state precedence over *Idle or RF Control* state limits the RF access of the RFID tag chip if it is frequently accessed via I^2C interface. However, when transferring acceleration samples continuously via the I^2C bus to the RFID tag chip, those samples cannot be acquired via the RF air interface. This constraint had to be overcome.

In this case, the features of the selected accelerometer were used to work out a solution. The ODR setting of the accelerometer with the internal operating clock of 51.2 kHz determines the time it takes to generate a single 14-bit (2 sign bits + 12 data bits) acceleration sample. If t_s is the time needed to generate a single acceleration sample by the accelerometer and satisfies Equation 3.1, the continuous data acquisition from RF air interface becomes possible.

$$t_{AQ} \leq i \times \left[t_s - \left(t_{SPI} + t_f\right)\right] - (i+1) \times (t_{I2C} + t_{NVM}), \qquad 3.1$$

where t_{AQ} is the maximum time needed to complete a full RF air interface interrogation of EPC having length of (i + 1) number of words, t_{SPI} is the time taken to complete a *SPI* transaction of a single acceleration sample between accelerometer and microcontroller with a specified clock, t_f is the time consumed by microcontroller to handle a single acceleration sample (other than *SPI* and I^2C transactions) in the firmware with a specified instruction cycle clock, t_{I2C} is the time consumed to transfer a single acceleration sample between microcontroller and RFID tag chip via I^2C bus with a specified clock, t_{NVM} is the time consumed by the RFID tag chip to complete a non-volatile memory (NVM) write of a single acceleration sample and *i* is the number of samples (here 1 acceleration sample is taken as 1 word and the reason for *i* + 1 is discussed below).

The maximum time needed to complete a full RF air interface interrogation of EPC having length of (i + 1) number of words (t_{AQ}) is dependent upon the read rate (tags/s in general inventorying) of the RFID reader. This read rate depends upon the setting of *tag population estimate* and the number of RFID tag antennas in range. The maximum read rate for the selected reader is 130 tags/s given that the *tag population estimate* setting is 1 and single tag antenna in range while the tag chip is in *Idle or RF Receive* state [177]. Since the RFID tag chip has to be accessed via I^2C bus when transferring acceleration samples, the tag chip will not always be in *Idle or RF Receive* state which will lower the read rate. However, an approximate value for t_{AQ} ($i = 7$, $i + 1 =$ maximum available EPC length of 8 words) would be 5.0 ms to 5.7 ms considering maximum data rates of forward the link (reader to tag antenna) 40 kbits/s and backward link (tag antenna to reader) 62.5 kbits/s [177] for an interrogation cycle with query repeat (*QueryREP*). The possible variation is due to automatic selection of preamble (PR) and frame synchronization (FS) by the reader (not user selectable), and tolerance of T_1 and T_2 time intervals EPC Class 1 Generation 2 protocol. The general interrogation cycle of EPC of the tag antenna can be given as in Figure 3.7 as defined in [168]. A reduction of EPC length by 1 sample would theoretically reduce aforementioned t_{AQ} by 256 μs. If the ODR of the accelerometer is 100 Hz, it generates 3 acceleration samples (3-axis) within a 10-ms period. Even though the accelerometer does parallel sampling for the 3 axes, the acquisition by the microcontroller and from the RF air interface is serial. Table 3.3 provides approximate values for t_{AQ} and for $i \times t_s$ up to maximum EPC length with additional tracking word T_W to filter the possible interrogation repetitions due to query repeat.

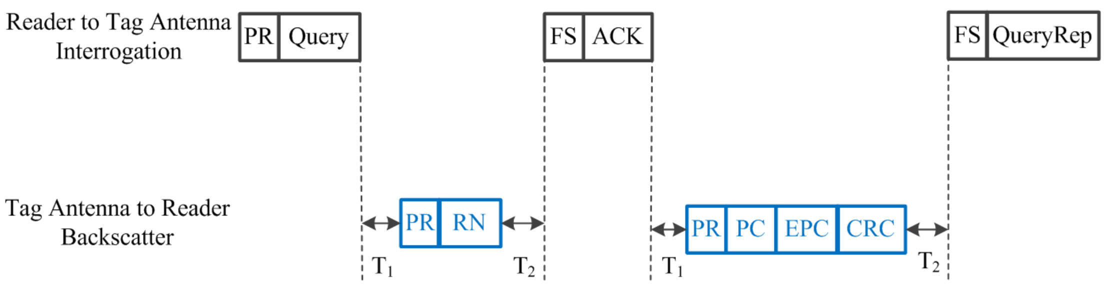

Figure 3.7: Interrogation cycle of EPC (PR - preamble, Query - query command, RN - random number, FS - frame synchronization, ACK - acknowledgment, PC - protocol control, CRC - cyclic redundancy check and QueryRep - query repeat command) [168].

Table 3.3: Approximate time values for the acquisition of EPCs with different lengths via RF air interface.

i	EPC length* (words)	t_{AQ} (ms)	$i \times t_s$ (ms)	$i \times t_s - t_{AQ}$ (ms)
1	2	4.14	3.33	−
2	3	4.40	6.66	2.26
3	4	4.66	9.99	5.33
4	5	4.92	13.32	8.40
5	6	5.18	16.65	11.47
6	7	5.44	19.98	14.54
7	8	5.70	23.31	17.61

* including tracking word (T_W).

According to Equation 3.1 and Table 3.3, acquisition of accumulated samples provide more time duration for $i \times (t_{SPI} + t_f) + (i + 1) \times (t_{I2C} + t_{NVM})$. In order to achieve sample accumulation, the FIFO buffer of the accelerometer was used. In this stage of the design, a maximum of 21 acceleration samples (7 sets of 3-axis acceleration) were set to accumulate in the FIFO buffer, and only the Z-axis samples were subsequently transferred to the extended 8-word *EPC* memory of the RFID tag chip (i = 7). This was done deliberately to provide an elongated time interval of ($t_{RFz} = 3i \times [t_s - (t_{SPI} + t_f)] - (i + 1) \times (t_{I2C} + t_{NVM})$) to acquire samples from RF air interface with the time saved by neglecting X and Y axes samples. The EPC arrangement with Z-axis acceleration samples is shown in Figure 3.8 (this fits in to EPC section of tag antenna to reader backscatter shown in Figure 3.7). T_W is toggled in the firmware at the time of generation of the *Watermark interrupt* of the accelerometer [179] for accumulation of aforementioned acceleration samples in the FIFO buffer. The firmware configuration of the TAIAS is given in Table 3.4. The flow diagram of the firmware operation is shown in Figure 3.9 with RFID tag chip state transitions at relevant stages.

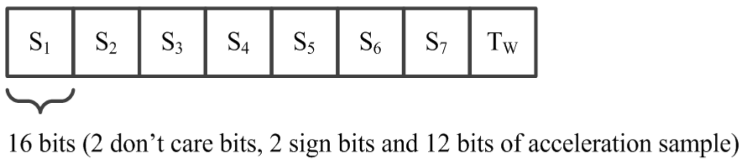

Figure 3.8: EPC arrangement with acceleration samples (i = 7).

Table 3.4: Configuration settings in the firmware.

Component	Configuration
Accelerometer	Acceleration level: ± 2 g Clock: Internal (51.2 kHz) Output data rate (ODR): 100 Hz Noise mode: ultra-low noise Interface: SPI (slave) Anti-aliasing filter: ODR/2 Interrupt: Watermark configured at 21 acceleration samples
RFID tag antenna	RF ports: 1 blocked, 2 in use Interface: I^2C (slave)
Microcontroller	Interface: I^2C (master) 400 kbps, SPI (master) 4 MHz Oscillator: Internal 8 MHz RC oscillator with 4×PLL*

* phase-locked loop.

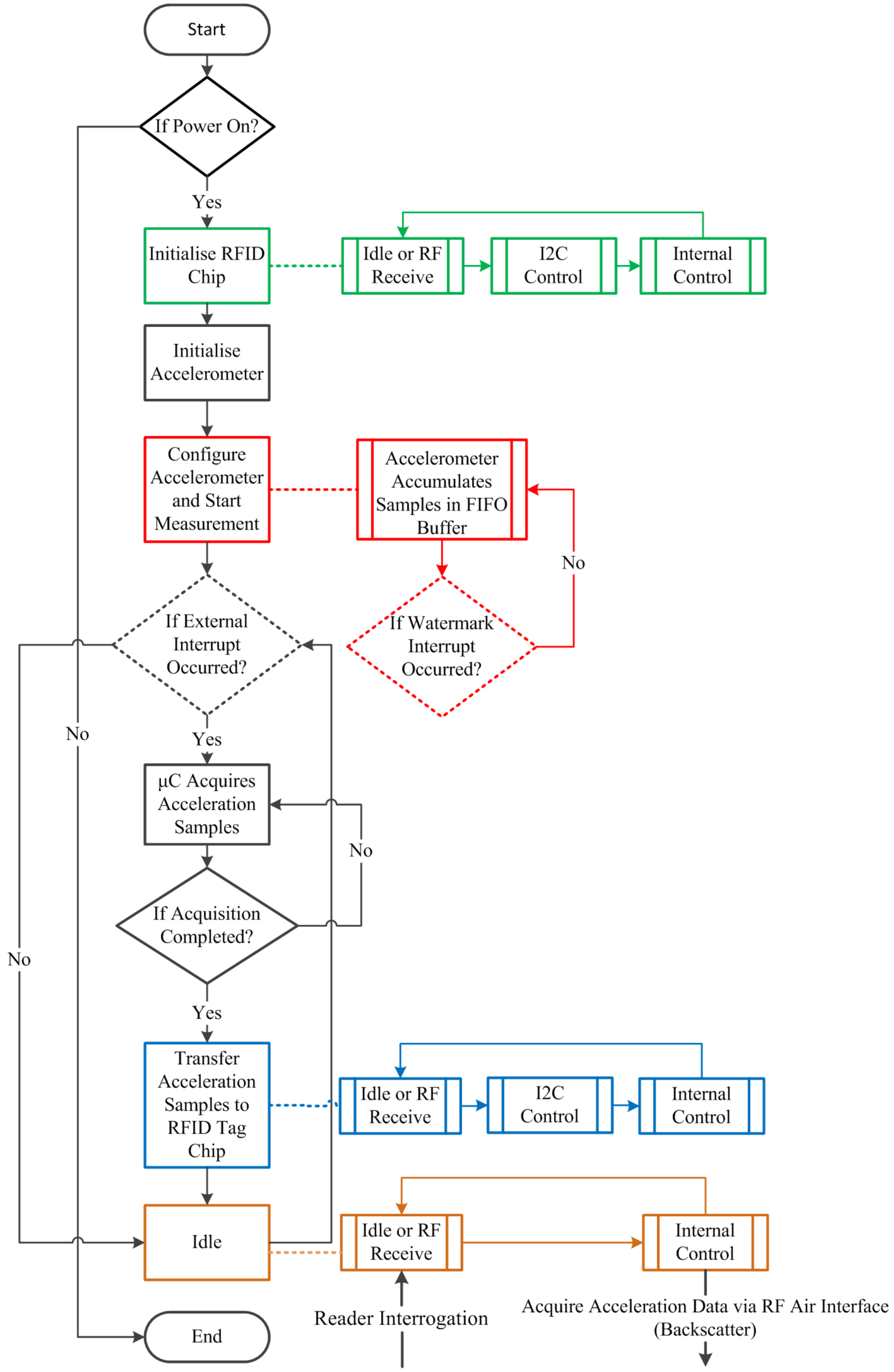

Figure 3.9: Flow diagram of the firmware of RFID tag antenna integrated acceleration sensor.

At initialise stage of the RFID tag chip the microcontroller starts I^2C communication and tries to identify the tag chip on the I^2C bus. Therefore the microcontroller reads the part id of the tag chip via the I^2C bus to establish a communication. Due to this reason the tag chip moves to *I2C Control* operating state from *Idle or RF Receive*. Subsequently, it moves to *Internal Control* in the initialization process and moves back to *Idle or RF Receive* state after the initialization of the tag chip. In the accelerometer initialization phase, the microcontroller starts *SPI* communication with the accelerometer and identifies it using the part id. Then at the configuration stage, it configures the accelerometer settings as given in Table 3.4. When the microcontroller sets the number of samples that should be accumulated in FIFO buffer, accelerometer starts measurement process and accumulates acceleration samples. At the time in which accelerometer generates the *Watermark interrupt* (mapped to external interrupt of the microcontroller), the microcontroller acquires the accumulated acceleration samples. Since microcontroller acquires the samples immediately after the occurrence of *Watermark interrupt*, the accelerometer keeps accumulating acceleration samples since it can fill already freed FIFO buffer locations [179]. After completing the sample acquisition process, the microcontroller transfers the samples to *EPC* memory of the RFID tag chip via I^2C bus. Due cause, the chip moves to *I2C Control* state from *Idle or RF Receive* state. Subsequently, it moves to *Internal Control* since there are NVM writes. Then the chip moves back to *Idle or RF Receive* state. At this stage, the microcontroller is idling providing a time window (t_{RF}) for the RFID reader to access the tag chip and acquire acceleration data (until the next occurrence of *Watermark interrupt*). The t_{RF} is actually the right hand side of the Equation 3.1. In this process the chip moves to *Internal Control* state since backscattering is necessary for the data acquisition via RF air interface.

3.6 Measurement Results

The laboratory measurements conducted using the designed system can be categorized into three major sections. First, the read range measurement of the system is conducted to identify the boundaries of the backscatter wireless range in which the system can acquire acceleration data. Then the lateral vibration of a rectangular steel beam is measured by the system setup shown in Figure 3.3(a). Finally, the measurements results are compared with those from independent wired and wireless commercial acceleration measurement systems.

3.6.1 Read Range Measurement

The system arrangement for read range measurement in the laboratory is shown in Figure 3.10(a). Both the reader antenna and the RFID tag antenna were kept 1.1 m above ground in line-of-sight orientation. A polystyrene mount was used to support the RFID tag antenna. The measurements were conducted for both options of P and BAP modes of the RFID tag chip with maximum 23-dBm reader transmit power in 923-MHz transmit frequency (center frequency of Australian UHF RFID band of 920-926 MHz) [113]. Figure 3.10(b) shows the average number of reads/s which can be achieved with increasing distance between RFID tag antenna and the reader antenna. The reader achieves its maximum read rate ~125 reads/s (close to the value mentioned in [177]) when the tag antenna is in range and always in *Idle and RF Receive* state. The maximum read range that can be achieved in open space for P and BAP modes were 1.1 m and 1.8 m respectively. Measurement of the read range on metal was done by mounting the RFID tag antenna on the steel beam. However, the achievable read range is reduced to ~0.1 m for BAP mode which clearly shows the RFID tag antenna de-tuning effect. A noticeable read range was not achieved when RFID tag was mounted on the steel beam in P mode.

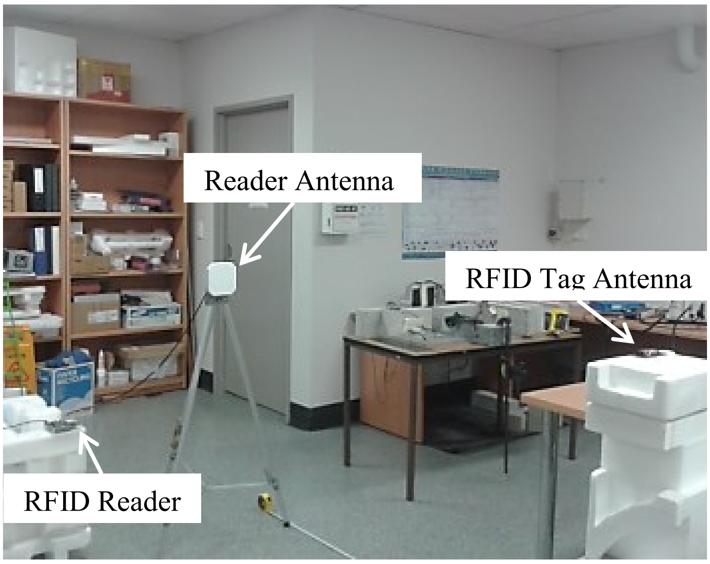

(a)

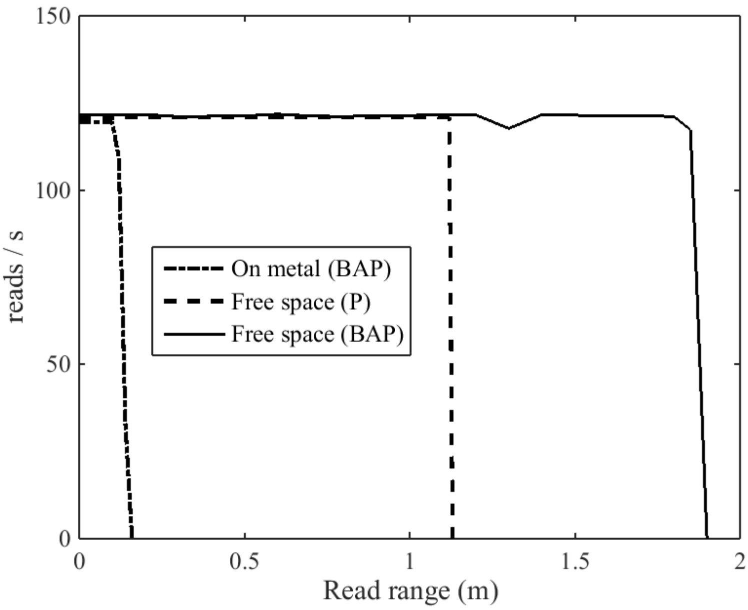

(b)

Figure 3.10: System read range measurement: (a) setup and (b) results.

3.6.2 Dynamic Acceleration Measurement

The simply supported rectangular steel beam with length (l) of 3 m, width (b) of 0.1 m and height (h) of 0.025 m shown in Figure 3.11(a) was used in dynamic acceleration measurement. The polystyrene mounting arrangement shown in Figure 3.3 was used to avoid the drastic read range reduction observed when the tag antenna was mounted on the steel beam. The accelerometer was mounted at the mid-span of the steel beam. The beam was excited by applying impacts using PCB PIEZOTRINICS 086C04 ICP impact hammer setup shown in Figure 3.11(b) [165]. Impact points A, B and C had 123.5-cm, 75-cm and 40-cm distances from O.

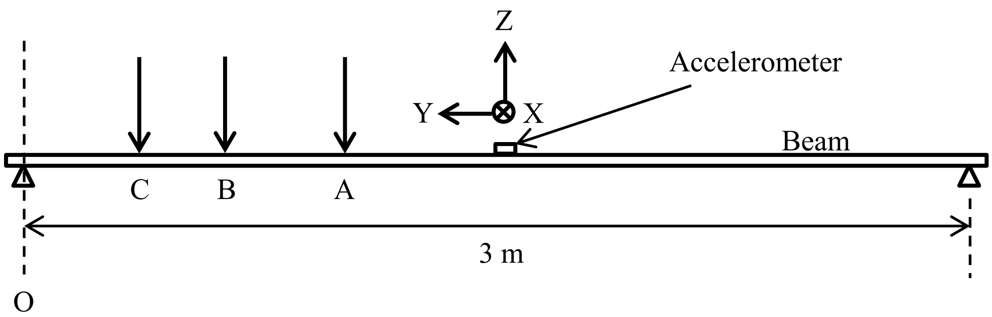

(a)

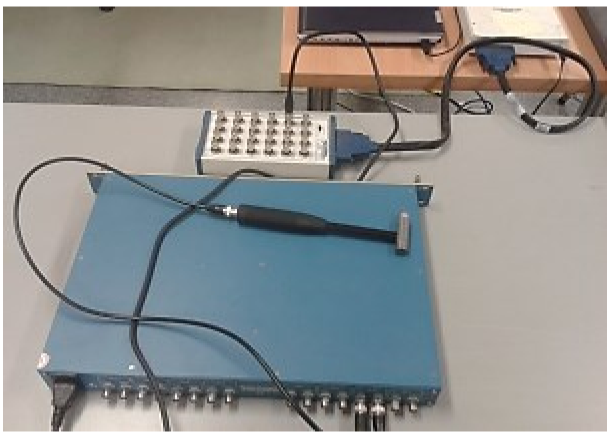

(b)

Figure 3.11: (a) Rectangular beam arrangement and (b) impact hammer setup.

Several dynamic acceleration measurements were conducted by applying random impacts at point A. In this process, the number of Z-axis acceleration samples carried by EPC was increased. All possibilities under the available EPC length have been analyzed by increasing the number of samples from 1 to 7, and these are denoted by scenarios S1 to S7, respectively (S1 - i = 1 and S7 - i = 7) in Figure 3.12 where the scattered plot of acquired sample rates via RF air interface is shown for 10 numbers of random impacts for each scenario. A 1.5-m read range was chosen and the measurements were conducted in BAP mode of the RFID chip. The firmware of the accelerometer integrated RFID tag was adjusted accordingly to form the EPC length of each case with T_W. The transmit power and the frequency were kept unchanged as in Section 3.6.1. Figure 3.13 shows one of the results of the Z-axis acceleration measurement. Time history results of both acceleration and impact hammer data show a negligible delay in measurements (FoI – force of impact). However, due to aforementioned data acquisition method, a delay of 1 microcontroller acquisition cycle exists. According to Figure 3.12 the average value of sample rate increases from S1 to S3 and holds the same level ~100 Hz up to S7 which is, in fact, the ODR setting of the accelerometer by the firmware. From S4 to S7 sample rate shows negligible variations between trials (i.e. between 10 random impacts). This shows that S1 and S2 do not provide enough t_{RFz} ($> t_{RF}$) for the reader to access the tag chip via RF air interface (i.e. $t_{RFz} < t_{AQ}$ for i = 1, 2 and does not satisfy Equation 3.1).

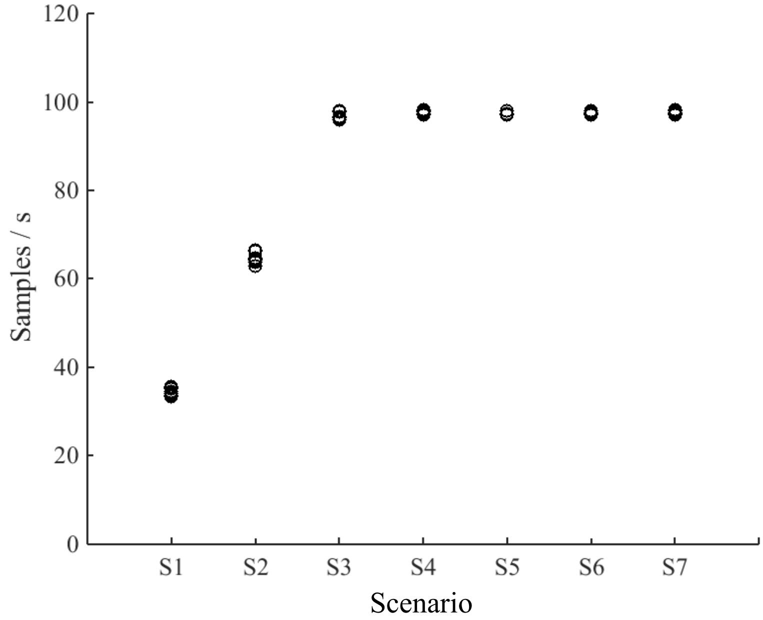

Figure 3.12: Sample rates achieved via RFID link for 10 impacts at point A for each scenario S1 to S7.

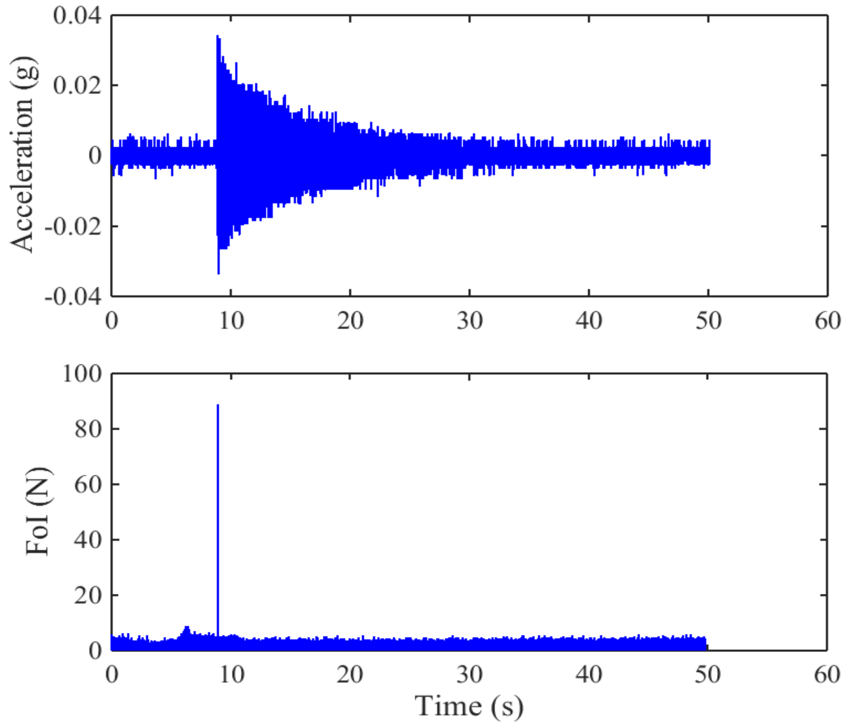

Figure 3.13: Z-axis acceleration measurement for the force of impact at point A.

Figure 3.14 shows the timing diagram (acquired by Agilent DSO-X 2024A oscilloscope) of the TAIAS for i = 7 and single word transfer within an I^2C transaction with *EPC* memory of the tag chip (8 number of I^2C transactions were necessary to cater i + 1 number of words). The *Watermark interrupt* has occurred in ~70 ms ($3i \times t_s$) intervals which tallies with the time required to accumulate 7 samples sets from each of the 3-axis in 100-Hz ODR. Therefore $t_s \approx 3.33$ ms for i = 1 as expected. The $(i+1) \times (t_{I2C} + t_{NVM})$ is about 35 ms which provides $(t_{I2C} + t_{NVM}) \approx 4.37$ ms for i = 1. Since these values do not satisfy Equation 3.1, it is evident that acquiring the total number of samples generated by the accelerometer via RF air interface is not possible with the current form of firmware settings (e.g., 100 Hz ODR) using maximum EPC length.

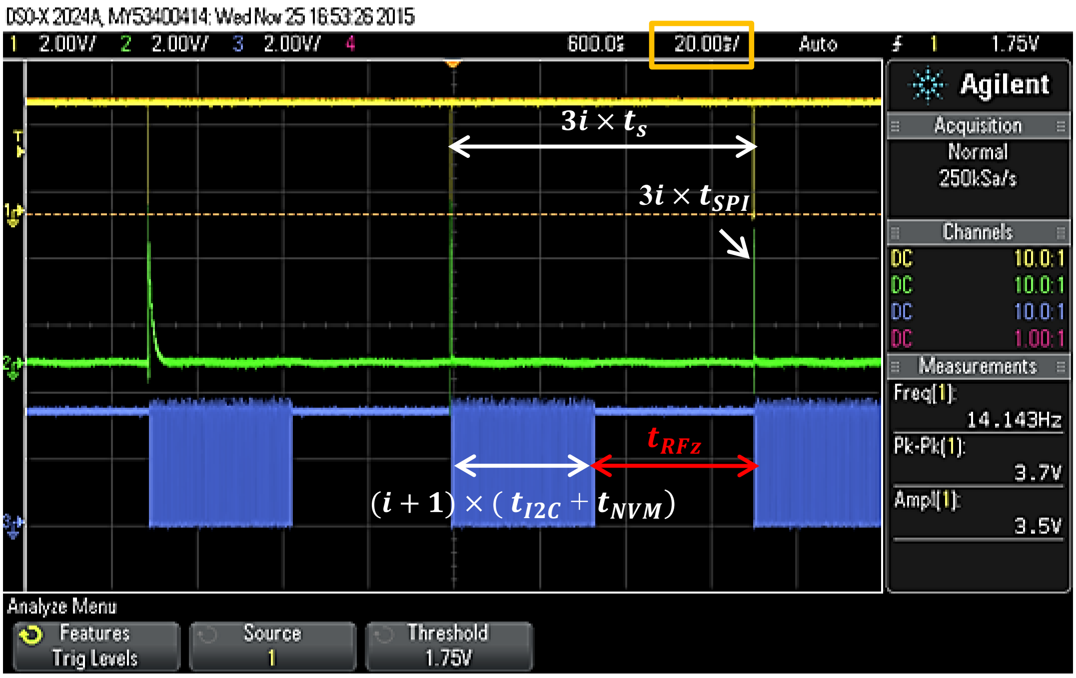

Figure 3.14: Timing diagram of *Watermark interrupt* (yellow), *SPI* receive (green) and I^2C write (blue) of the tag antenna integrated acceleration sensor with settings provided in Table 3.3 for i = 7 (t_f is not visible).

However, the above evidence suggests that the scenarios of S4 to S7 can be effectively used to acquire single axis dynamic acceleration measurement for 100-Hz ODR with available EPC length of the RFID tag chip. The calculated amplitude spectra of the dynamic acceleration measurements with random impacts at point A for these four scenarios are shown in Figure 3.15. All of those show a prominent peak approximately at 6.24 Hz. This value is almost close to the calculated value of 6.4 Hz which is the frequency of the 1st mode (i.e., the natural frequency) of the rectangular steel beam (see Figure 3.11(a)) using Equation 2.1. Apart from random noise, some other peaks (smaller than the prominent peak) are visible in the amplitude spectra. Theoretically, the next frequency with the highest amplitude detectable at mid-span of the beam is the frequency of 3rd mode [90] which is ~57.3 Hz. Therefore, this frequency is not detectable since achieved spectral bandwidth of the measurement system for the single axis is ~50 Hz. Detecting an alias of a higher frequency signal is also not possible within this spectral band according to anti-alias filter setting of the accelerometer given in Table 3.3. According to Figure 3.15, the position and the number of the subtle peaks vary between scenarios. Additional investigation into these peaks will be conducted in Chapter 5. The measurement results which are discussed in the following sections of the current chapter had the EPC length according to scenario S6 (i = 6).

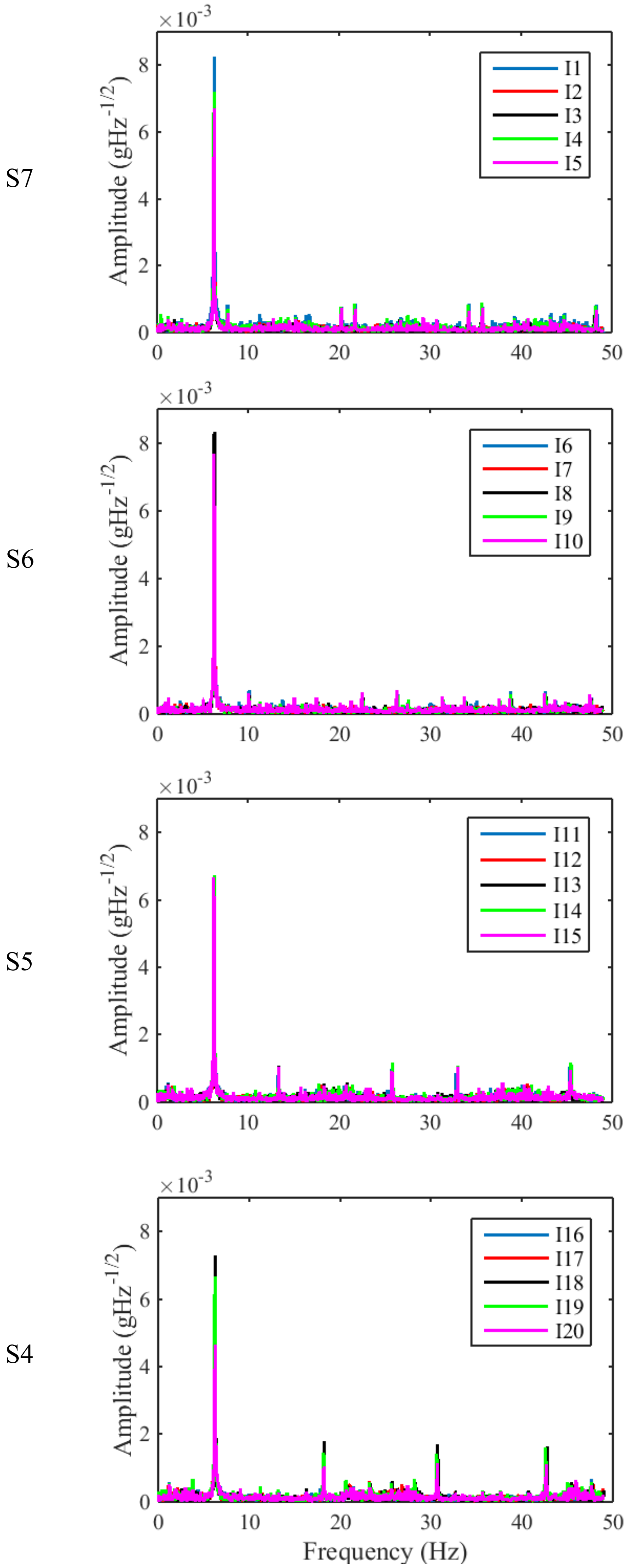

Figure 3.15: Single-sided amplitude spectra of acceleration measurements for scenarios S4-S7 with random impacts of I1-I20.

The measurement of 3-axis acceleration has been performed in the same testing setup by applying impacts at point A and the results are shown in Figure 3.16(a). In this measurement, EPC have been used to hold two of every third set of 3-axis acceleration samples with T_W (i.e. the effective ODR became 33.33 Hz). The information of the natural frequency can only be noticed in the Z-axis measurement as shown in Figure 3.16(b) mostly due to the orientation of the beam setup and the direction of impact. This 3-axis measurement is useful in monitoring particular structures with random orientations and random vibration directions.

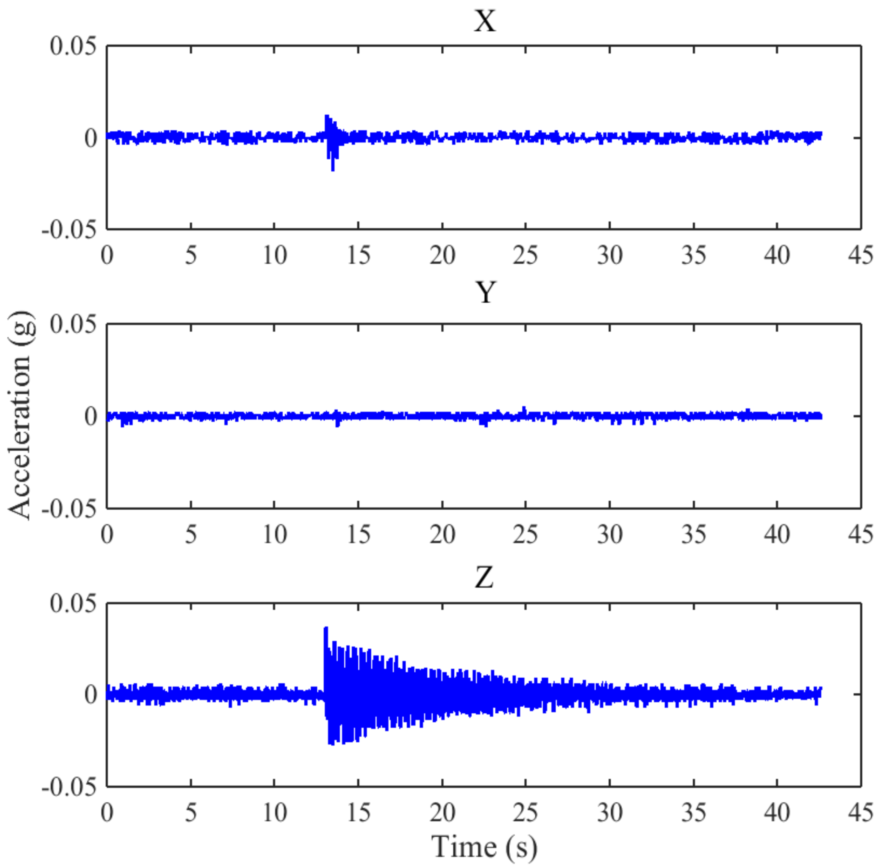

(a)

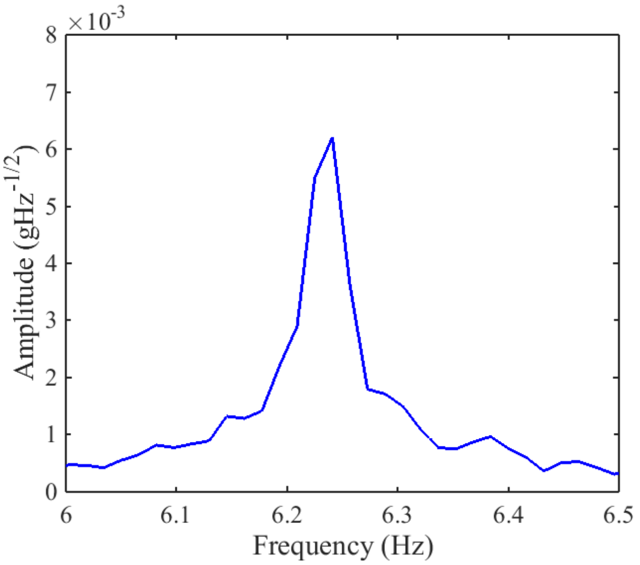

(b)

Figure 3.16: Three-axis acceleration measurement: (a) time history and (b) single-sided amplitude spectrum of Z-axis data.

3.6.3 Spatial Sensitivity Test

Several dynamic acceleration measurements were conducted applying impacts at points B and C additional to point A. One of those results is shown in Figure 3.17(a). The time history of the acceleration is different as applied impacts were random. However, the amplitude spectra shown in Figure 3.17(b) indicate that the prominent peak is approximately the same at 6.24 Hz for all impacts. Therefore, the information that can be acquired from the measurement is retained even though the height of the peaks reduces from point A to C due to energy dissipation of the vibration along the beam. This can also be seen when comparing the decay of acceleration levels depicted in Figure 3.17(a).

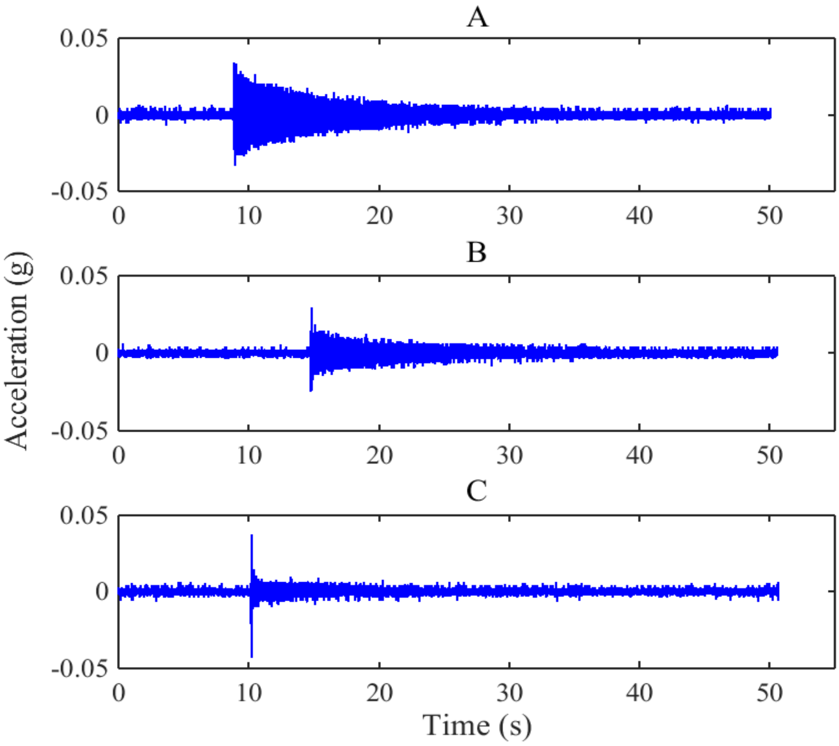

(a)

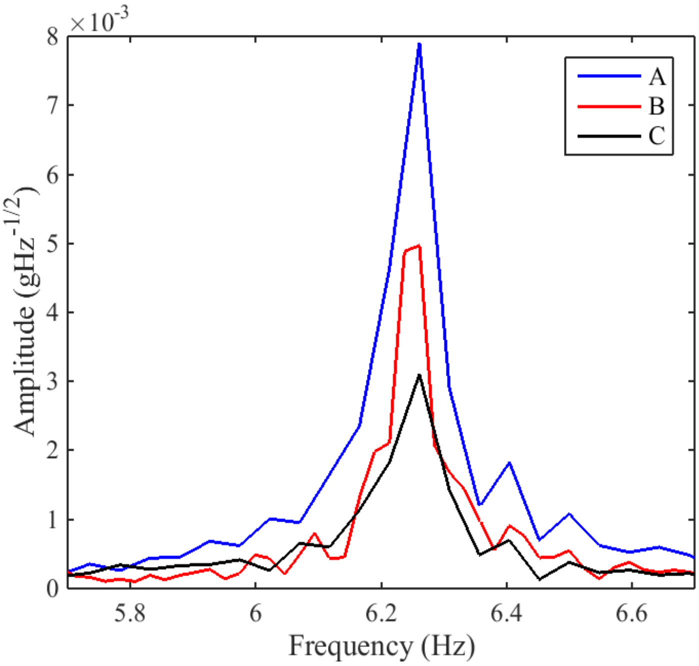

(b)

Figure 3.17: Z-axis dynamic acceleration measurements for random impacts at points A, B, and C: (a) time history and (b) single-sided amplitude spectra.

3.6.4 Test with Imposed Load on Steel Beam

The dynamic acceleration was measured with an extra load imposed on the rectangular steel beam. The beam that had a mass (m) of 59 kg was loaded with a mass (M) of 11 kg at a distance (d) of 180 cm from the point O in –Y direction (see Figure 3.11(a)), and the impacts were applied at point A. The amplitude spectra of the acquired acceleration measurements are shown in Figure 3.18 in comparison with results from the unloaded specimen. It shows change of the natural frequency of the specimen where it has shifted approximately to 5.48 Hz. This value is almost to the calculated analytical natural frequency value of 5.58 Hz (1st mode) which is acquired for off-center loaded simply supported rectangular steel beam using [183]:

$$f = \frac{1}{2\pi}\sqrt{\frac{KEI}{Ml^3}\frac{(A_\alpha + A)}{(B_\alpha + B)}}, \tag{3.2}$$

where, f is the natural frequency (1st mode) of loaded specimen (Hz). A_α and B_α are functions of both mass ratio (m/M) and load's position (d/l) where A and B are functions of only (d/l) [183]. Under the consideration of deflection curves of the specimen by combined contribution of both m and M, the values K, A_α, B_α, A and B are found to be 48, 1.1183, 4.1078, 0.0576 and 0.0531, respectively. Therefore system has demonstrated its ability of distinctively acquiring the state change of the steel beam (triggered by loading) using frequency shift of the 1st mode.

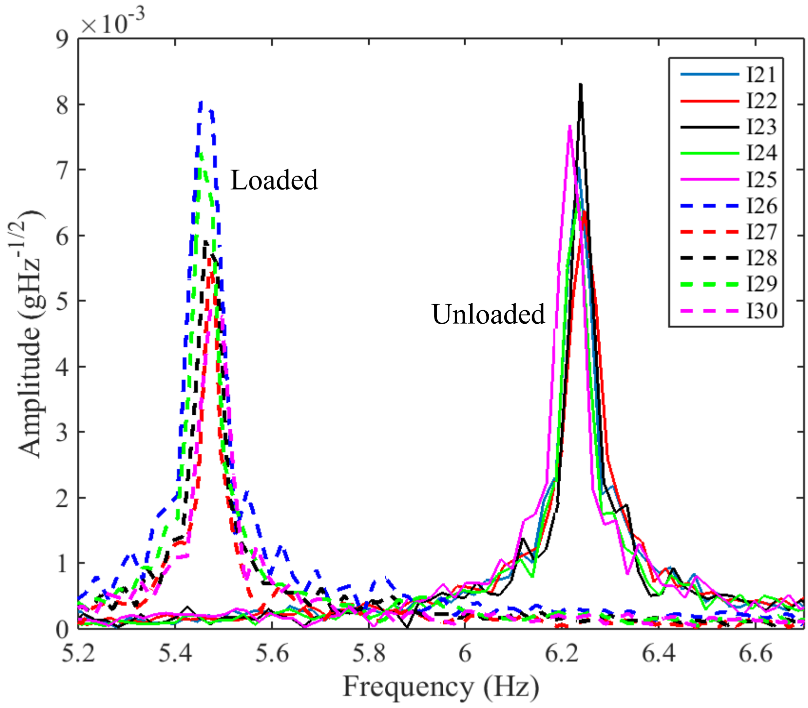

Figure 3.18: Single-sided amplitude spectra for acceleration measurements of the unloaded and loaded specimen with random impacts of I21 to I30 at point A.

3.7 Comparison with Commercial Systems In Order to Benchmark the Designed System

The results of the designed RFID-based dynamic acceleration measurement system have been compared with the results from commercially available independent wired and wireless acceleration measurement systems. PCB PIEZOTRONICS 352C34 single axis commercial wired accelerometer [166] and LORD Microstrain G-Link® -LXRS® commercial wireless accelerometer [77] have been used to acquire these independent measurement results. Commercial wired and wireless accelerometers have been collocated accordingly on the steel beam with the mounting arrangement of the TAIAS. National Instruments' NI USB-6251 multifunction DAQ module [167] and LORD Microstrain WSDA® -Base-104 -LXRS® base station [78] have been used for the acceleration data acquisition from the commercial wired and wireless accelerometers, respectively. Each system has been used for simultaneous dynamic acceleration measurements with the proposed RFID-based system and acquired Z-axis acceleration measurements have been analyzed. Figure 3.19 shows the comparison of the amplitude spectra of the acceleration measurements obtained using proposed system and those obtained with commercial wired accelerometer (c.f. Figure 3.19(a)) and wireless accelerometer (c.f. Figure 3.19(b)) in different instances. Figure 3.19(a) demonstrates that both systems have shown prominent peaks (i.e., the natural frequency) near 6.1 Hz and 5.4 Hz for the unloaded and loaded states of the beam, respectively. According to Figure 3.19(b), both the proposed and commercial wireless systems have also shown prominent peaks near 6.1 Hz for the unloaded state and at 5.4 Hz for the loaded state. The reason for the shift in the spectra in this set of experiments can be due to slight changes in the boundary conditions (e.g., placement of supports) that might have occurred in the testing arrangement. Overall, the comparison with the commercial systems confirms that the proposed system provides approximately the same 1st mode frequency information of the beam.

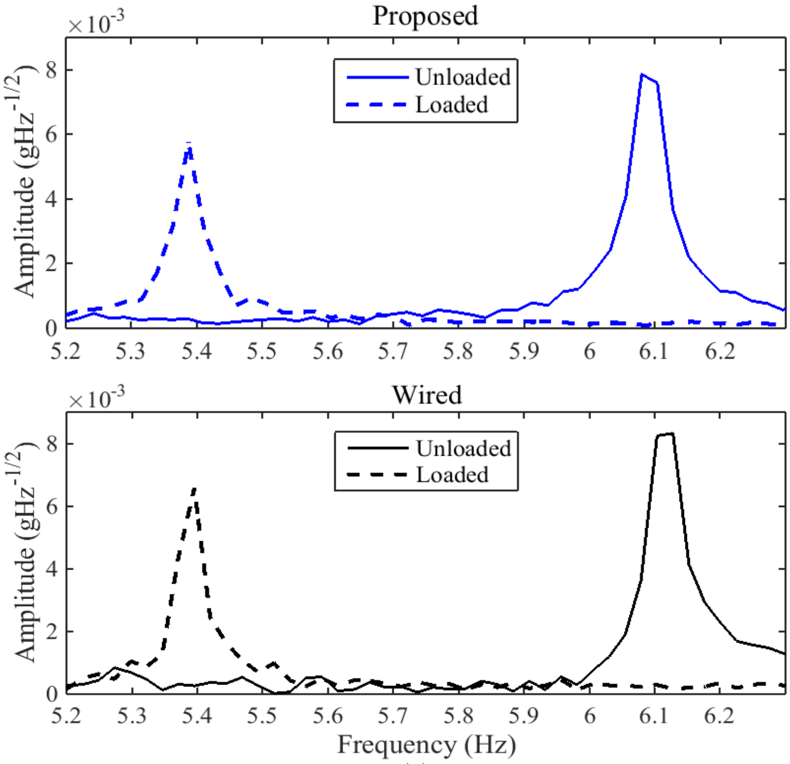

(a)

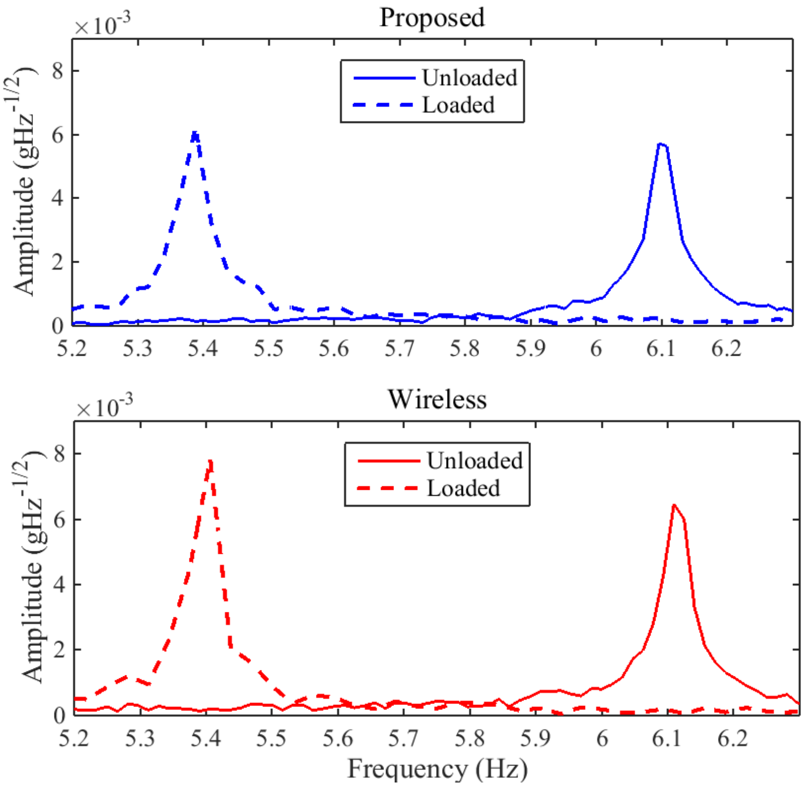

(b)

Figure 3.19: Comparison of single-sided amplitude spectra of the acceleration measurements at point A, between: (a) proposed system and commercial wired accelerometer system and (b) proposed system and commercial wireless accelerometer system.

3.8 Conclusion

This chapter presented the proposed RFID-based wireless system design for dynamic acceleration measurement of infrastructure. The considerations of the initial system development have been presented with a novel design of a semi-passive UHF RFID tag antenna integrated acceleration sensor. The firmware of the RFID tag antenna integrated acceleration sensor was designed for continuous acceleration monitoring for the purpose of retaining important information related to infrastructure (e.g., natural frequencies). Furthermore, it was developed providing opportunities for the future development of the system which will be discussed in Chapter 5.

The current system which operated in the battery assisted passive communication mode of the tag chip has shown the capability of acquiring single axis dynamic acceleration data with ~50 Hz spectral bandwidth using maximum EPC length. However, this bandwidth had to be equally allocated among the axes when measuring 3-axes acceleration. The constraint was caused by the time required for single word non-volatile memory writes which did not allow sufficient time to transfer more acceleration samples while keeping a window with enough time duration to acquire them via RF air interface.

The measurements conducted with a simply supported rectangular steel beam have shown that the system is capable of acquiring the natural frequency (frequency of the1st mode) of the structure. Furthermore, it has shown the capability of identifying state changes of the beam with the natural frequency shift. The determined natural frequency values of loaded and unloaded states of the beam were in good agreement with the calculated theoretical values. The natural frequency values determined from the simultaneous measurements from two other commercially available independent acceleration measurement systems were also in good agreement with those acquired by the proposed system. Therefore, the proposed RFID-based wireless system has the potential to be used in infrastructure health monitoring applications.

However, it has been observed that the designed RFID tag antenna integrated acceleration sensor has a reduced performance in read range when mounted on the steel beam. This is unacceptable when considering the system in macro level. First, the RFID tag antenna integrated acceleration sensors should be conveniently mounted on the structures which are made out of different types of construction materials (e.g., concrete, metal) to monitor their health in field measurements. Secondly, the reduction of read range increases the possibility of the influence of the structure upon reader antenna properties (e.g., reflection characteristics, antenna gain). Furthermore, it reduces the possibility of simultaneous data acquisition from multiple RFID tag antenna integrated acceleration sensors positioned at different locations of the structure. Therefore, the proposed system can be further enhanced to be more suited to electromagnetically harsh infrastructure environments.

Chapter 4 Construction Material Mountable UHF RFID Tag Antenna: Design and Performance Analysis

4.1 Introduction

This chapter presents a design and performance evaluation of a RFID tag antenna which can be used as an I^2C slave component for the development of semi-passive RFID tag antenna integrated sensors mountable on construction materials. The proposed tag antenna which can easily be fabricated using printed circuit board (PCB) technology has been designed using a new generation RFID tag chip. It is relatively small and tuneable. The background leading to this design, the design considerations, performance simulations and experimental proof have been presented in subsequent sections of the chapter.

4.2 Background

The RFID tag antenna is a very important component of an entire RFID system, especially when the system is used in demanding applications. Performance degradation of the system can be caused by the reduction of read range due to RFID tag antenna detuning in the vicinity of surfaces made out of different types of materials. In an RFID-based wireless sensor system, drastic read range reduction of the system is not acceptable as it limits the number of RFID tag antenna integrated sensors which can be monitored by a single reader antenna. However, this phenomenon was observed in the experimental phase of the wireless

IHM system design with accelerometer integrated RFID tag in Chapter 3. In the improvement of the aforementioned system, it is important to design a UHF RFID tag antenna which can perform properly when mounted on concrete or metal members. Furthermore, the tag antenna should be compatible with electronic integration with different types of sensors used in IHM (e.g., accelerometers, strain gauges, etc.).

It is well known that the performance of any antenna deviates from free space performance according to the environment in which it is being used unless specifically designed for the application environment. If the antenna is mounted on a surface, its performance is different from that of the antenna in free space. These performance differences are considerably negative when considering typical dipole UHF RFID tag antennas since most of them are miniature antennas with compromised antenna gain and they are carefully matched to RFID tag chip impedances [46, 184]. The influence from the objects in the vicinity on read range, impedance pattern and radiative efficiency of antennas have been investigated in [140] for constructed "*I-type*" and "*M-type*" folded dipole tag antennas. The study has shown that the read range of these tag antennas reduces considerably in the vicinity of metal and liquid material. RFID tag antenna performance in the vicinity of various materials has been experimentally evaluated in [139] using radio link budgets with a planar folded dipole tag antenna. This study has shown that the tag antenna performance (e.g., the antenna gain and the read range) reduces considerably in the vicinity of highly conductive materials. The performance of a planar dipole tag antenna with an inductive coil has been studied in [142] mounted on different types of material. The inductive coil was used to minimize the antenna impedance change when mounted on those materials. However, the tag antenna had shown low performance when mounted on thick paper and glass. Simulation studies reported in [46] for a folded dipole tag antenna mounted on metal have shown that generated surface currents on the metal mount, in the opposite direction to those of the dipole tag antenna neutralize its effective electric field and therefore reduce the antenna gain. Clearly, the performance of commercially available dipole tag antennas deteriorates when mounted on different types of material, especially near conductive surfaces. However, the necessity of mounting sensors on structural members made out of metal or concrete is unavoidable in IHM applications. Furthermore, the acceptable read range is also critical as sensors are most likely to be installed in places which are difficult in frequent accessing.

The complex input impedance of a RFID tag chip is frequency dependent. This makes the RFID tag antenna design entirely different from conventional antenna design which is normally matched to 50 Ω impedance [46]. The input impedance has to be conjugately matched to that of the tag antenna using creative techniques [112] while achieving the performance parameters such as operating frequency and antenna gain. Various forms of dipole tag antenna designs were presented in [46, 112, 184, 185] with different types of matching techniques such as T-match, inductively coupled loops and series tuning inductors. The use of slots and inductive loops were effective for impedance matching in multi-layer tag antenna designs [112, 186, 187].

It has been observed that multilayer antennas generally perform better in metallic environments than dipole antennas [158]. The ground plane of multilayer antennas such as microstrip patch antennas appears to help electromagnetically isolate the material on which they are mounted [46]. This feature has led the development of metal mountable RFID tag antennas which are different to dipole-like tag antennas. Various designs of microstrip patch type tag antennas have been studied mostly for logistic purposes and tagging metallic items using different approaches. A tag antenna design with two rectangular patches grounded at opposite ends to the feeding location is proposed for metal object tagging applications in [147]. A compact version of this antenna has been studied using a multi-layer model with an inner conductive layer in [148]. The length of the inner layer was used as the impedance tuning parameter. An inset-fed patch was employed to develop a metal mountable RFID tag antenna where impedance matching was achieved changing the length of inset-feed and open stubs in the grounding microstrip [146]. Another metal mountable RFID tag antenna with rectangular patch and tuning stubs was studied to achieve impedance matching with the

RFID chip in [145]. A new compact RFID tag antenna which can be effectively mounted on metal was designed with slits and inset feed in [150]. The inset feed length was used to change the antenna impedance for matching purposes. A RFID tag antenna which has a trapezoidal patch was studied in [149] to mount on metal where impedance matching was achieved by changing the upper side width and the height of the trapezoidal patch. An inset-fed patch antenna with an open stub was studied for metallic object tagging in [151]. Both inset length and open stub length were varied to achieve required impedance matching. Four rectangular patches designed to resonate at different frequencies were used in [186] to develop a broadband RFID tag antenna for metal mount applications. A square microstrip loop was used in the middle of the tag to feed the rectangular patches and to achieve required impedance matching with the RFID tag chip. Another complex design of a wideband multilayer tag antenna was studied in [152] using proximity coupled approach where impedance tuning was achieved with the parametric study of feed line length and its position related to patch edge. Furthermore, a complex design of multi-slotted dual patch type RFID tag antenna was presented for metallic tagging applications with incorporated microstrip loop as the feeding arrangement in [187]. Antenna had several tunable parameters to achieve required impedance match owing to the complex design.

Even though there is considerable research work on metal mountable RFID tag antennas, research, and development of mounted on concrete are limited. An inkjet-printed square loop antenna on paper was studied with a concrete tile for an indoor localization application in [155]. The tag antenna had large dimensions close to the size of the tile. Additionally, an attempt to adjust a commercially available dipole tag antenna to have improved performance with concrete was presented in [156] for a way-point positioning application. An instant where a multilayer tag antenna model has been studied with concrete is presented in [157] to be used in location tracking application. In this research, a ceramic patch was studied for merge in concrete up to surface level with a complex assembly of a parasitic patch and a metal cavity.

However, almost all the tag antenna designs were carried out using conventional strap type RFID tag chips which cannot be used to develop tag antenna integrated sensors. Furthermore, they have been optimised in different UHF RFID frequency ranges to use with only one material (e.g., metal) in which case they may not perform well when mounted on concrete or other construction material. Therefore, for the read range enhancement of the proposed RFID-based wireless IHM system in Chapter 3, a further study is needed to develop a UHF RFID tag antenna which has the capability of electronic sensor integration and desired performance mounted on both concrete and metal.

4.3 RFID Tag Antenna Design

The microstrip patch antenna shown in Figure 4.1 is designed for a new generation RFID tag chip Impinj Monza X-8K Dura which has an I^2C digital interface [135] to be compatible with the semi-passive RFID tag antenna integrated sensor development proposed in Chapter 3. This design is based on the rectangular tag antenna presented in [145] which used tuning stubs with three grounding points to achieve impedance matching for a conventional strap type RFID chip. In this design, two microstrip lines were employed to connect RF terminals of the RFID chip pad for both the radiating patch and the ground plane of the tag antenna as shown in the magnified view of Figure 4.1. The tiny sections of the microstrip lines are governed by the RFID chip pad dimensions [135]. The connection to the ground plane was provided by a 0.9-mm diameter grounding pin using the lower microstrip line. The substrate material is Rogers 5880 with relative dielectric constant (ε_r) of 2.2, loss tangent (tan δ) of 0.0009 and thickness of 3.175 mm. The Copper patch and ground plane have a thickness of 0.035 mm. Slits (1-mm) which are symmetrical around *XZ* and *YZ* planes were employed along the two radiating edges of the copper patch to achieve the miniaturized effect and the required impedance matching at 923 MHz. The modeling of the tag antenna is done in CST Microwave Studio [160].

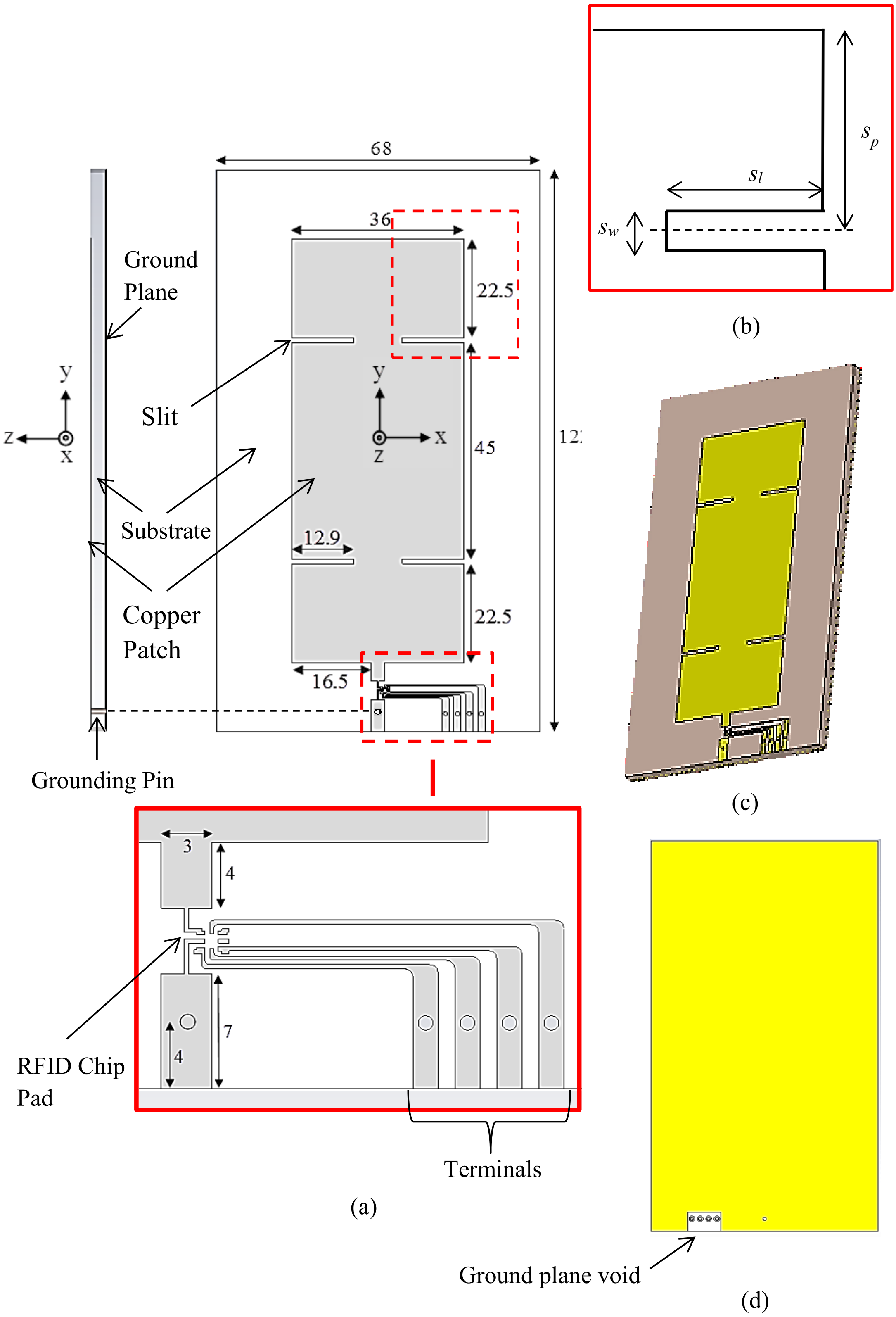

Figure 4.1: RFID tag antenna (a) geometry of the side view, top view, and magnified view of feeding arrangement (Terminals: *serial clock*, *power*, *serial data* and *ground* from left to right), (b) schematic of slit (not to scale), (c) perspective and (d) bottom view of the antenna model in CST (dimensions are in millimeters).

4.4 Simulation Results

The simulations were conducted using CST Microwave Studio. The hexahedral meshing technique was used in transmitting mode electromagnetic simulation of the tag antenna model using time domain solver. The local mesh properties at tiny features such as slits, RFID chip pad, and terminals were taken into consideration in the simulations.

4.4.1 Impedance Matching of the RFID Tag Antenna

The length and the placement of the slits were optimized by comparing the simulated tag antenna impedance (Z_a) and the input impedance of the RFID chip ($Z_c = 18.37 - j170.45\ \Omega$ at 923 MHz) from the RF front-end model provided in [188]. Since the RFID chip-input impedance is capacitive, the tag antenna should have an inductive impedance to achieve a conjugate match. Both the slit length (s_l) and their position (s_p) (see Figure 4.1) were simultaneously varied from 10 mm to 15 mm (in 0.5-mm intervals) and 11 mm to 35 mm (in 4-mm intervals) in the simulation in order to obtain the best tag antenna impedance which conjugate match with tag chip impedance.

The reactance values of the tag antenna impedance at the desired frequency were observed since it is important in achieving conjugate impedance match. Figure 4.2 shows simulated tag antenna reactance with different slit lengths at two slit positions. According to Figure 4.2(a), the tag antenna reactance can be increased by increasing the slit length. The increase of reactance becomes larger when with a gradual increase of slit length. However, when the slit position is moved more towards the middle of the patch (see Figure 4.2(b)), the variation of reactance is relatively high. Furthermore, tag antenna starts to demonstrate capacitive impedance for increasing slit length making conjugate match not possible.

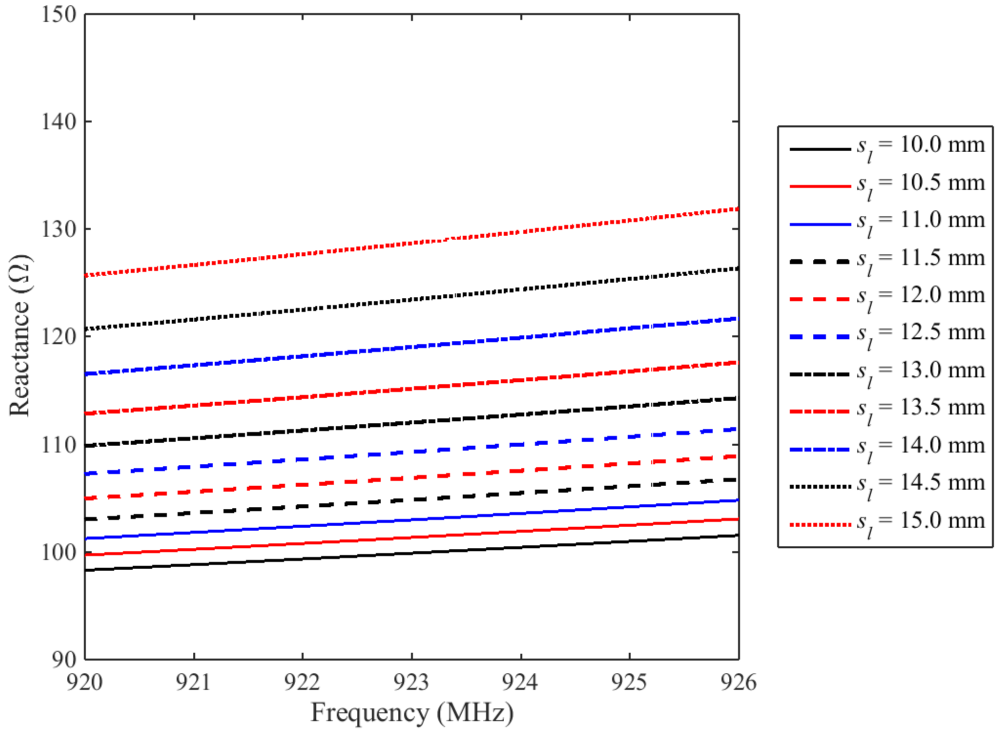

(a)

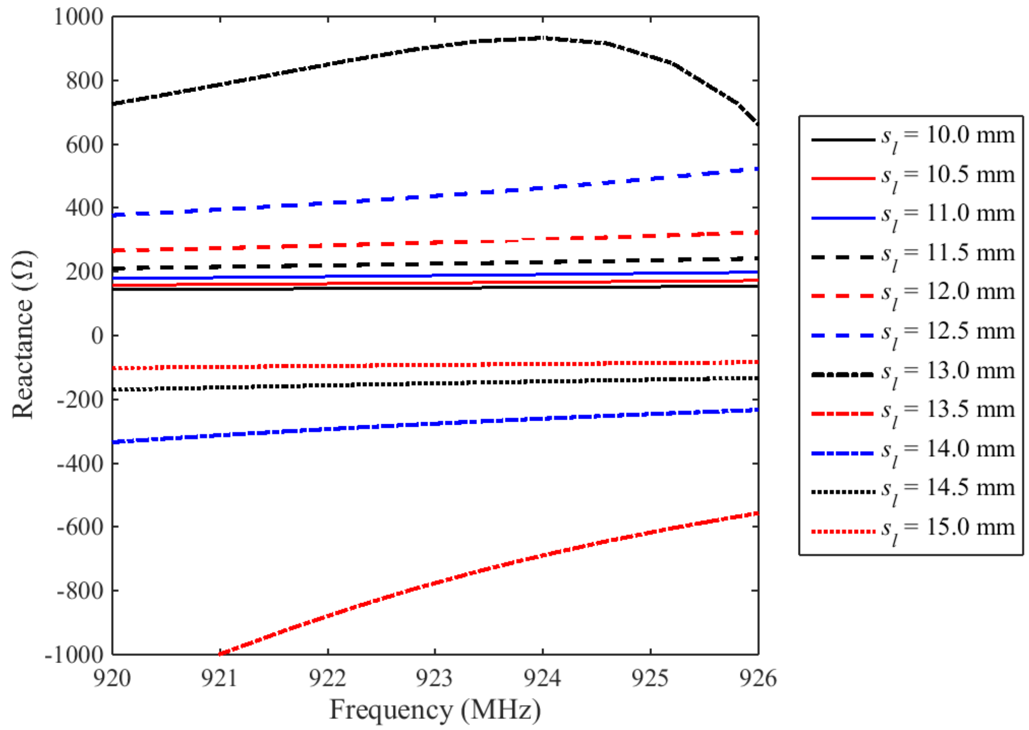

(b)

Figure 4.2: Simulated tag antenna reactance of two slit positions: (a) s_p = 11 mm and (b) s_p = 35 mm.

Figure 4.3 shows the selected parameter study results on impedance near to the conjugate match with the RFID tag chip. All of them converge on nearly the same Z_a as shown in Table 4.1 with slight variations of slit length from the results presented in Figure 4.3. It can be seen that when the value of slit position increases the required slit length value to achieve the impedance matching decreases. The simulated magnitude of the reflection coefficient ($|S_{11}|$ in dB) versus frequency shown in Figure 4.4 for these selected matching cases. It shows that the tag antenna is having nearly identical reflection characteristics in all the matching cases at 923 MHz. Therefore, this impedance matching method provides multiple options to achieve conjugate impedance match in the design of the tag antenna.

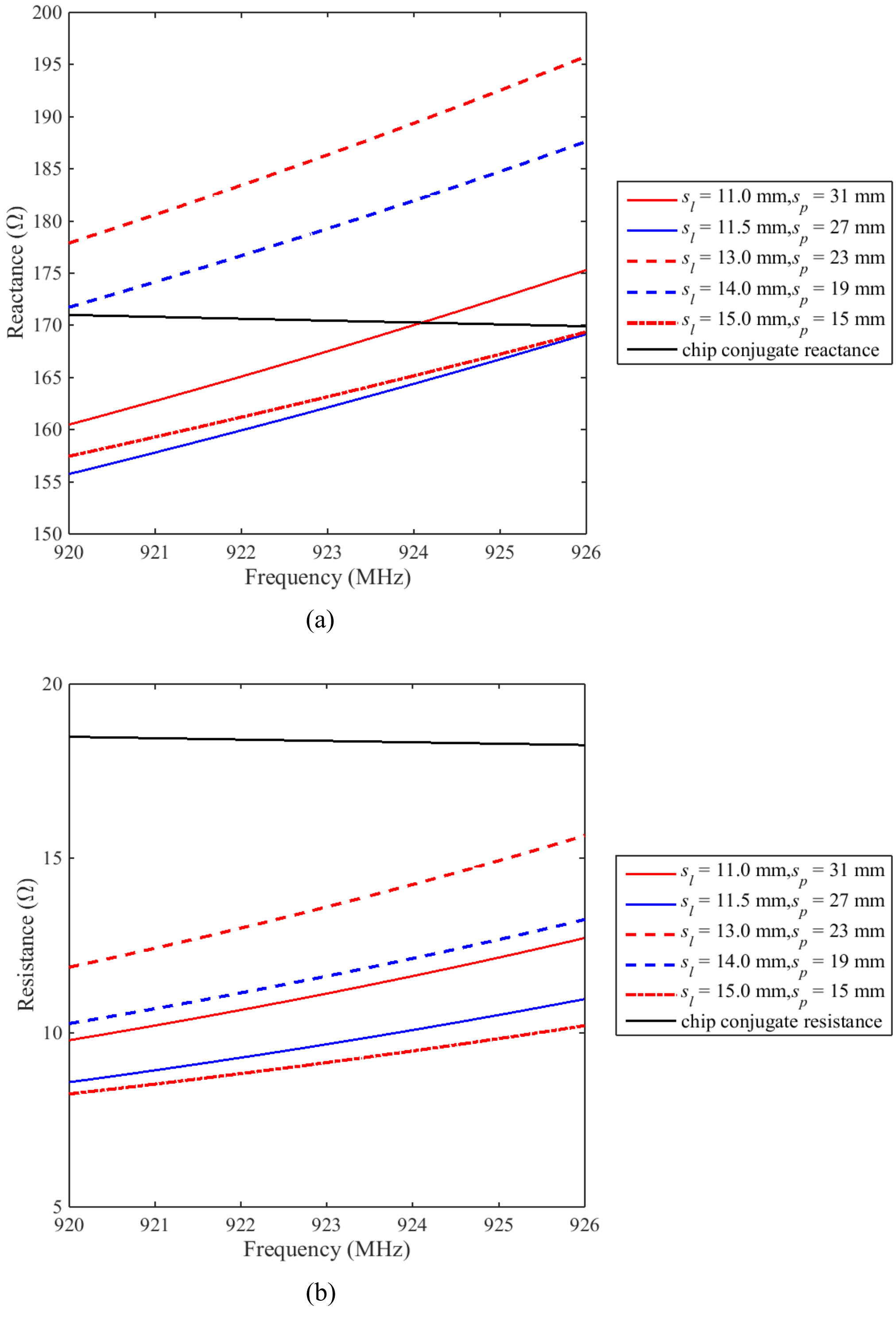

Figure 4.3: Tag antenna impedance matching at different slit positions: (a) reactance and (b) resistance.

Table 4.1: Matched impedances for different slit positions.

s_p (mm)	s_l (mm)	Adjusted s_l (mm)	Z_a (Ω)
15.0	15.0	15.2	$10.03 + j169.25$
19.0	14.0	13.8	$10.40 + j172.79$
23.0	13.0	12.9	$11.90 + j171.18$
27.0	11.5	11.8	$11.34 + j173.08$
31.0	11.0	11.1	$11.74 + j171.50$

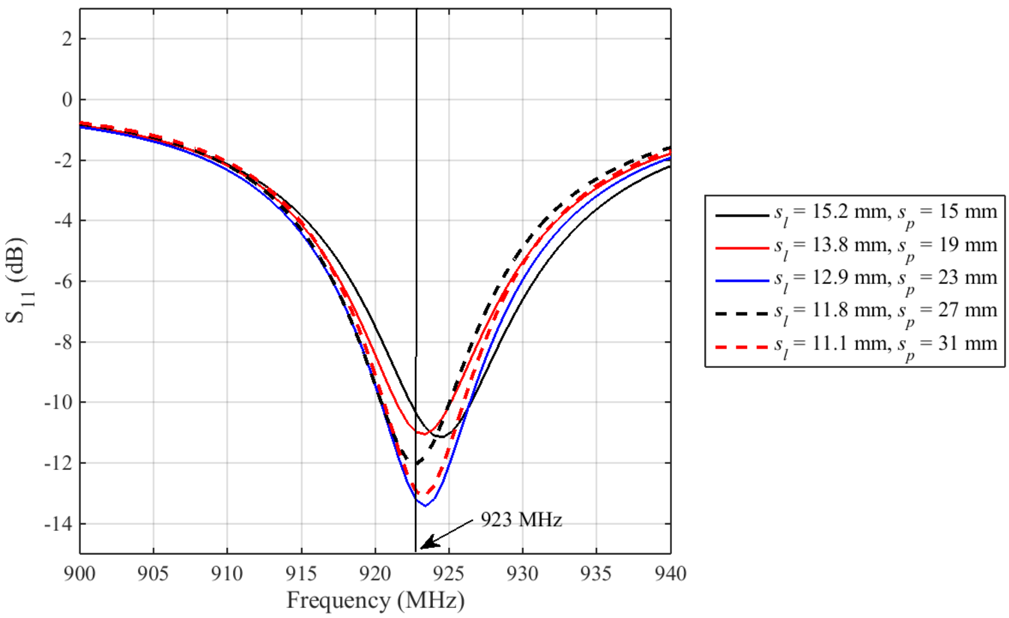

Figure 4.4: S_{11} (dB) versus frequency for impedance matching at different slit positions.

Finally, the given dimensions in Figure 4.1 were selected for the slit parameters which gave simulated tag antenna impedance of $Z_a = 11.90 + j171.18$ Ω. The resonant frequency at this matching impedance was 923.4 MHz. The simulated far field tag antenna gain pattern in free space for the impedance matched tag antenna in CST Design Studio is shown in Figure 4.5. It can be seen that the tag antenna radiates along Z axis with a maximum gain of ~4.58 dBi. The surface current density distribution of the tag antenna is shown in Figure 4.6. It can be clearly seen that the electrical path of the surface currents is exaggerated by the slits along the radiating edge. This helps to minimize the size of tag antenna [189]. The ground plane void for the terminal soldering shown in Figure 4.1 has been placed after observing the surface current distribution pattern on the ground plane. According to Figure 4.6, the area where the void is placed has low surface current density distribution.

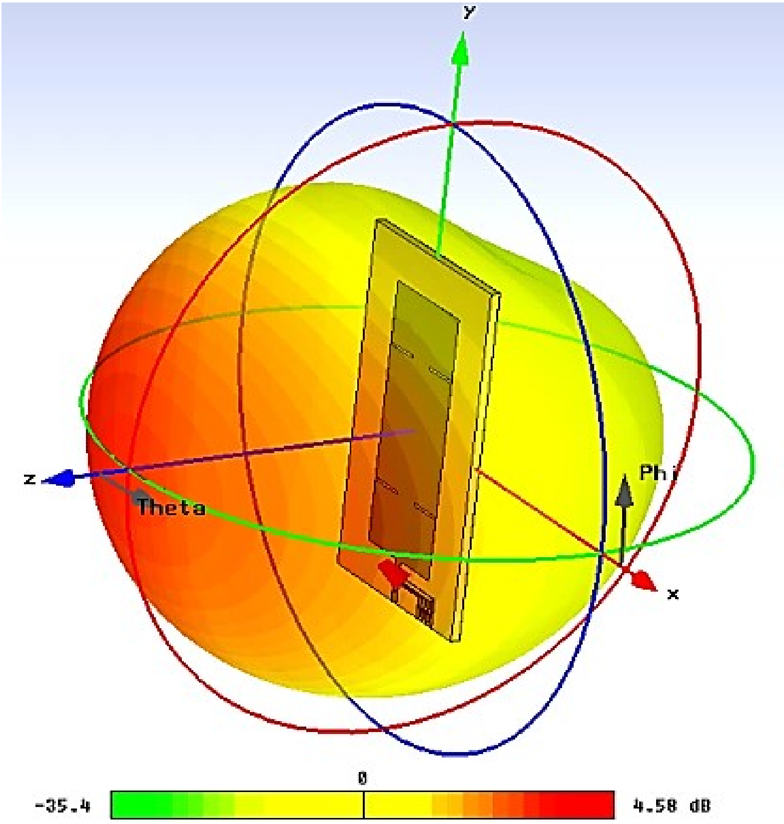

Figure 4.5: Simulated far-field gain pattern of the tag antenna at 923 MHz.

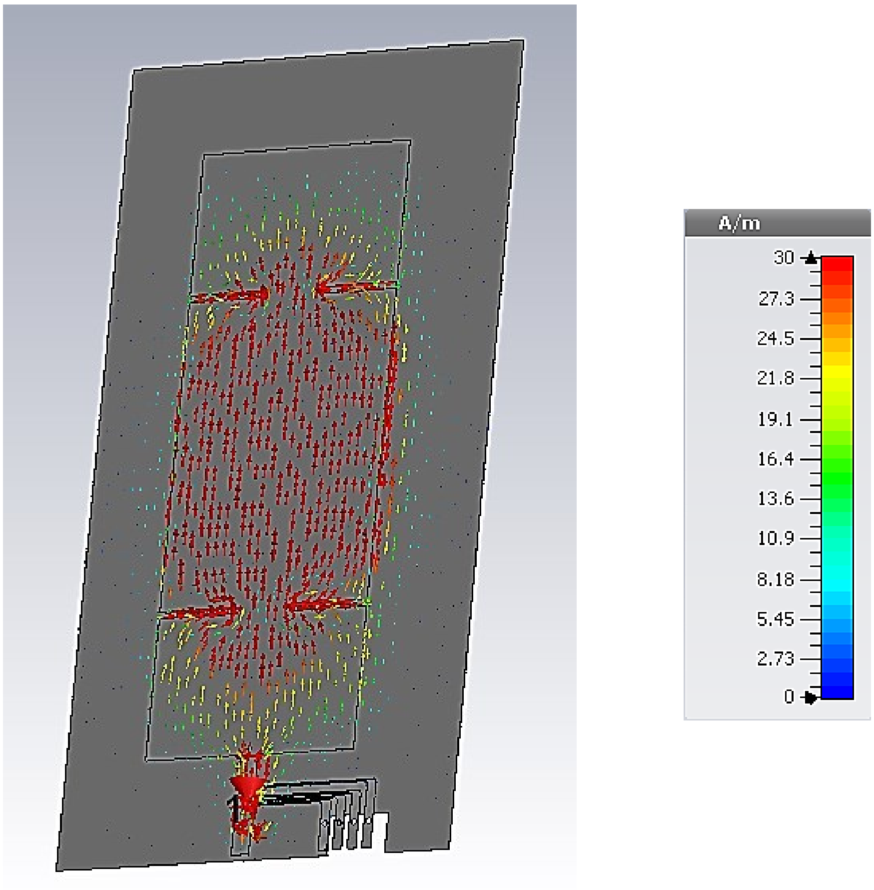

Figure 4.6: Surface current density distribution of the tag antenna at 923 MHz (phase of 11.25˚).

4.4.2 Performance of RFID Tag Antenna Mounted on Construction Material

The performance of the proposed RFID tag antenna mounted on a metal plate, a large metal block, and a large concrete block (referred to as mounts) was studied. Table 4.2 summarizes the details of the mounts used in the investigation and the simulation results. The lengths and widths of metal and concrete blocks were selected as ~10λ (λ = 0.325 m at 923 MHz) to simulate the effect of large scale structures. The RFID tag antenna was mounted in the middle of these mounts in the simulations (see Figure 4.7) and the same local mesh properties used in free space simulation were retained to achieve the same simulation accuracy of the RFID tag antenna in higher volume simulations. The dielectric properties of dry concrete was chosen as $\varepsilon_r = 4.75$ and $\tan\delta = 0.081$ [190, 191].

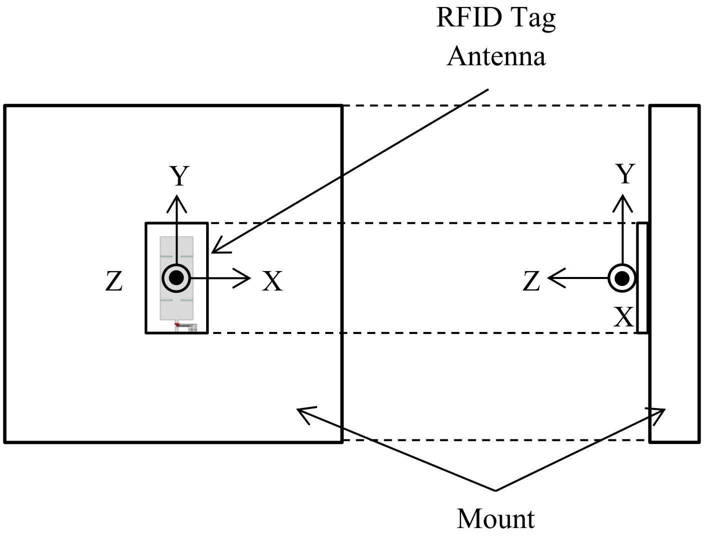

Figure 4.7: Schematic of the RFID tag antenna mounting arrangement (not to scale, mounts have the dimensions given in Table 4.2).

Figure 4.8 shows the simulated S_{11} in dB, for the mounted and free space scenarios. The changes of the resonant frequency in mounted scenarios of the tag antenna are acceptable as the intended frequency band is inside the −3-dB impedance bandwidth. The RFID tag chip uses Miller encoding at a data rate of 62.5 kbps and Miller (M = 4) backscatter subcarrier modulation technique. In this case, the maximum bandwidth needed around a carrier is ~750 kHz [168, 177]. Therefore, the RFID tag antenna has ample 3-dB bandwidth for not to attenuate the subcarrier amplitudes generated for the edge carrier frequencies of the intended band (920. 25 and 925.75 MHz) by the backscatter modulation of the RFID tag chip. Furthermore, it can be seen that the increasing size of the metal mount has negligible influence on the S_{11} characteristics of the RFID tag antenna.

Table 4.2: Mounting types and materials used and simulation results.

Mount	Material	Dimensions (m^3)	Gain (dBi)	Directivity (dBi)	XZ Plane Angular Width (degrees)
Free space*	NA	NA	4.6	5.76	121.8
Metal plate	Copper	0.43 × 0.43 × 0.001	4.9	7.61	86.5
Metal block	Copper	3.25 × 3.25 × 0.25	4.4	7.06	90.5
Concrete block	Dry concrete	3.25 × 3.25 × 0.25	3.4	7.66	93.6

* Free space parameters are given only for the comparison.

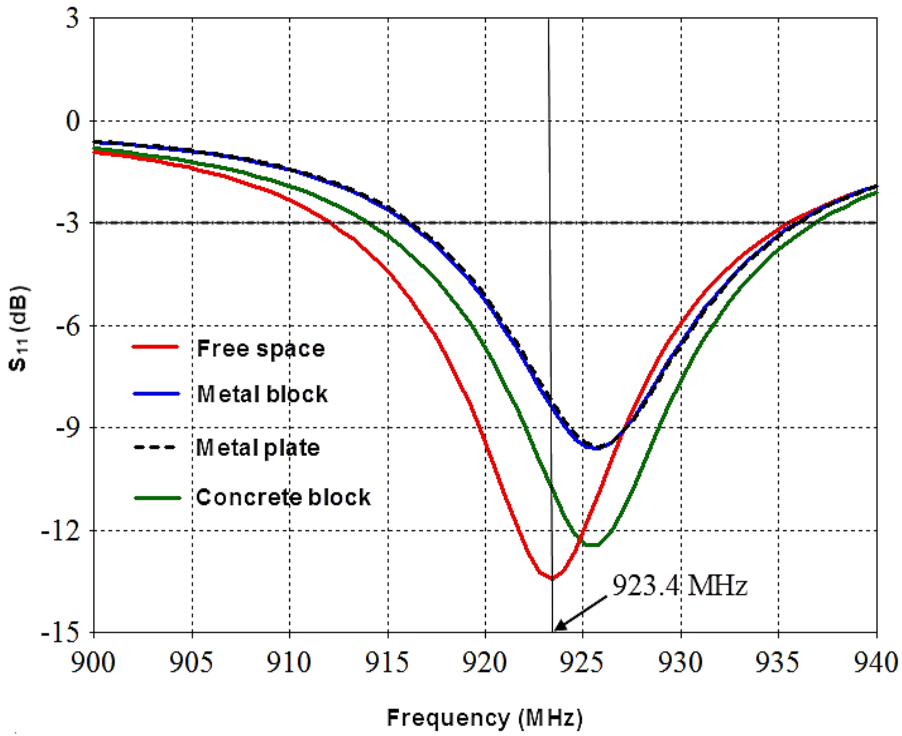

Figure 4.8: Simulated S_{11} (dB) versus frequency for the RFID tag antenna in free space and on different mounts.

However, the size of the mount affected the simulated far-field gain patterns of the RFID tag antenna as shown in Figure 4.9. From Table 4.2 and Figure 4.9(a) it can be seen that the RFID tag antenna becomes more directive when mounted on a surface. Furthermore, the angular width on *XZ* plane has no major variations depending on the mounting material and the dimensions. This radiation characteristic of the tag antenna is useful for wireless connection with RFID tag antenna integrated sensors mounted on concrete or metal structures in a higher read range. The back lobe present, when mounted on the concrete block, is due to electromagnetic signal propagation through concrete as shown in Figure 4.10. The reflections of the signals caused by the back surface of the concrete create the varying pattern of the back lobe.

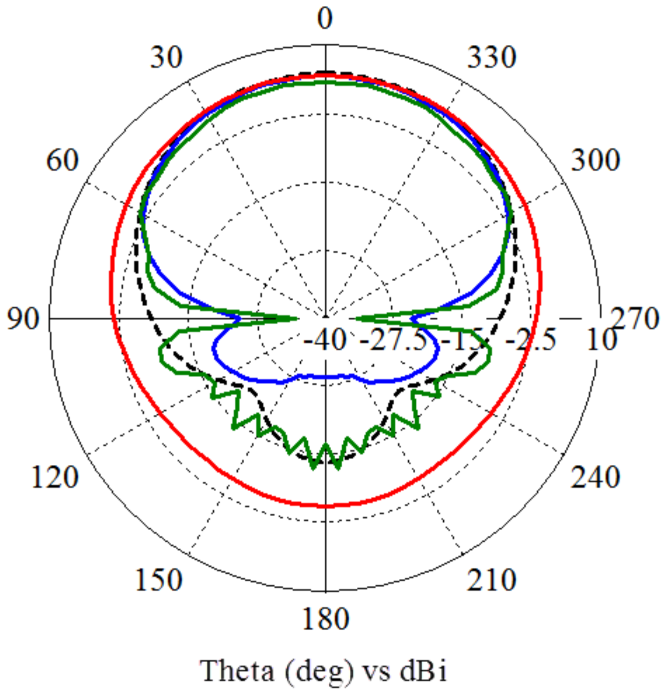

(a)

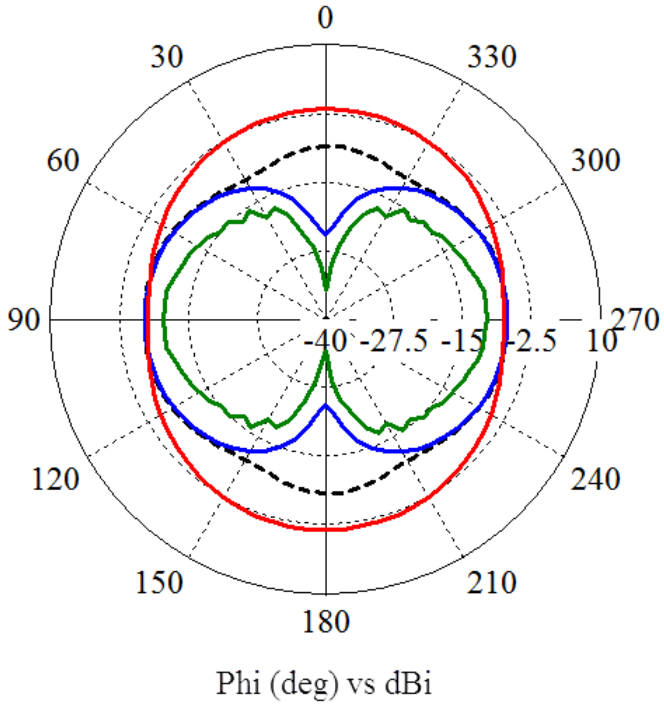

(b)

Figure 4.9: Simulated far-field gain patterns of the RFID tag antenna at 923 MHz: (a) *XZ* plane and (b) *XY* plane (red - free space, blue - metal block, dashed black - metal plate and green - concrete block).

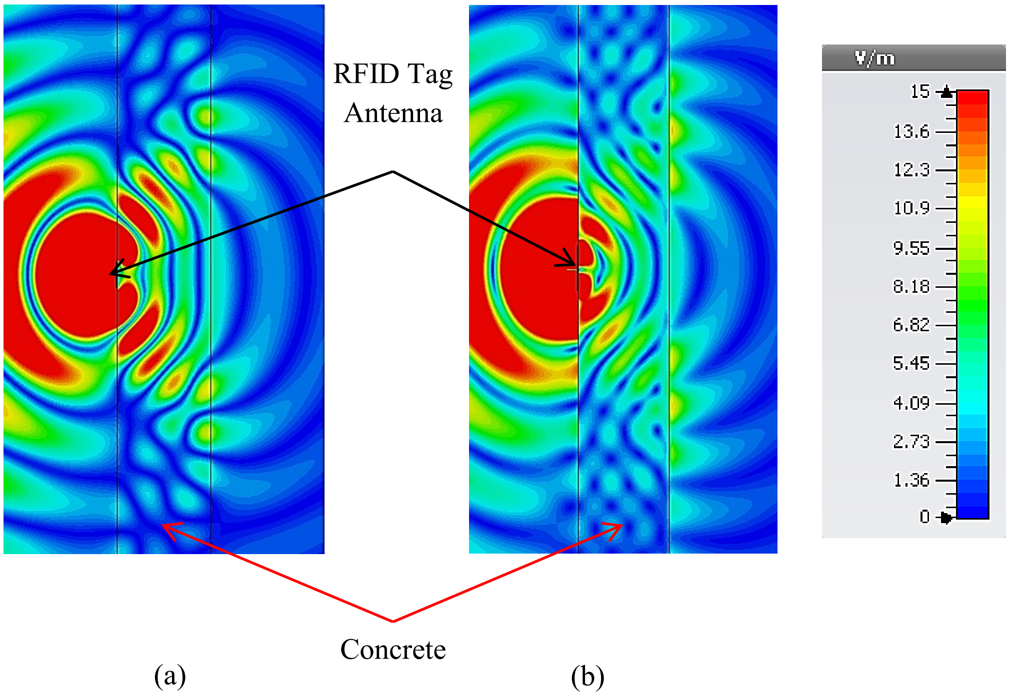

Figure 4.10: Electric field intensity distribution around tag antenna mounted on the concrete block at 923 MHz (phase of 11.25˚): (a) *XZ* plane and (b) *YZ* plane.

Larger and smaller back lobe levels can be seen in Figure 4.9(a) when the tag antenna is mounted on the metal plate and the metal block, respectively. These are due to the radiations from the edges of the mounts since the surface currents spread throughout both mounts as shown in Figure 4.11 and Figure 4.12. Figure 4.11(a) and Figure 4.11(b) show the surface current density spread near the edges of the metal mount. In the case of the metal plate, the surface current density distribution at the edges is higher than that of the metal block. Furthermore, the surface current density distribution patterns on *XY* plane of both mounts as shown in Figure 4.11(c) and 4.12 have a clear relationship with the gain pattern shown in Figure 4.9(b). In fact, the changes in the tag antenna gain pattern on *XY* plane is influenced by the surface current density distribution on the surface of the mounts.

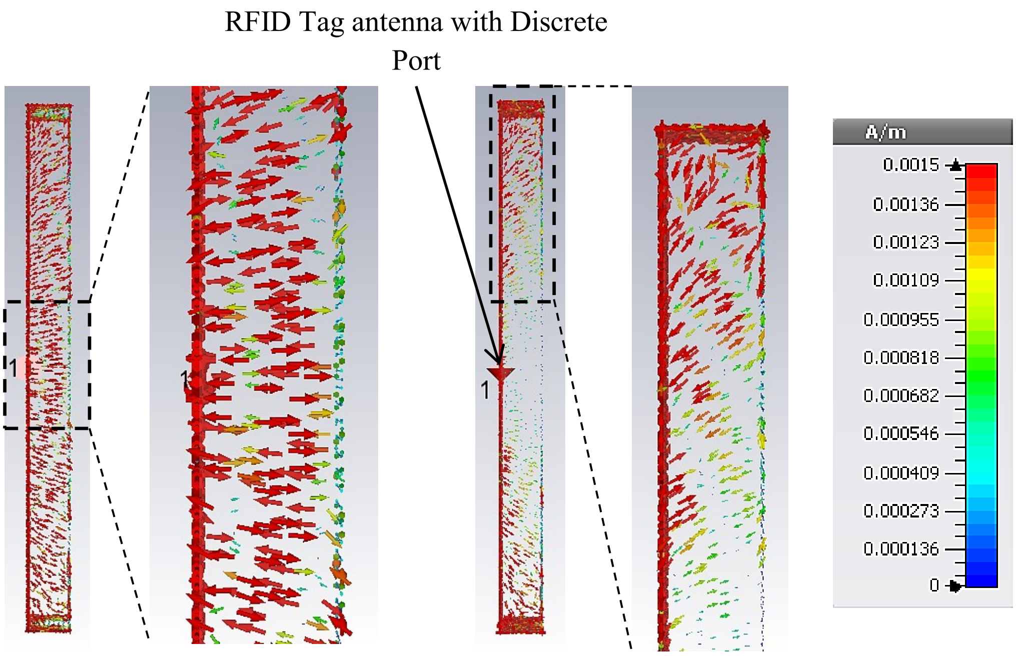

(a) (b)

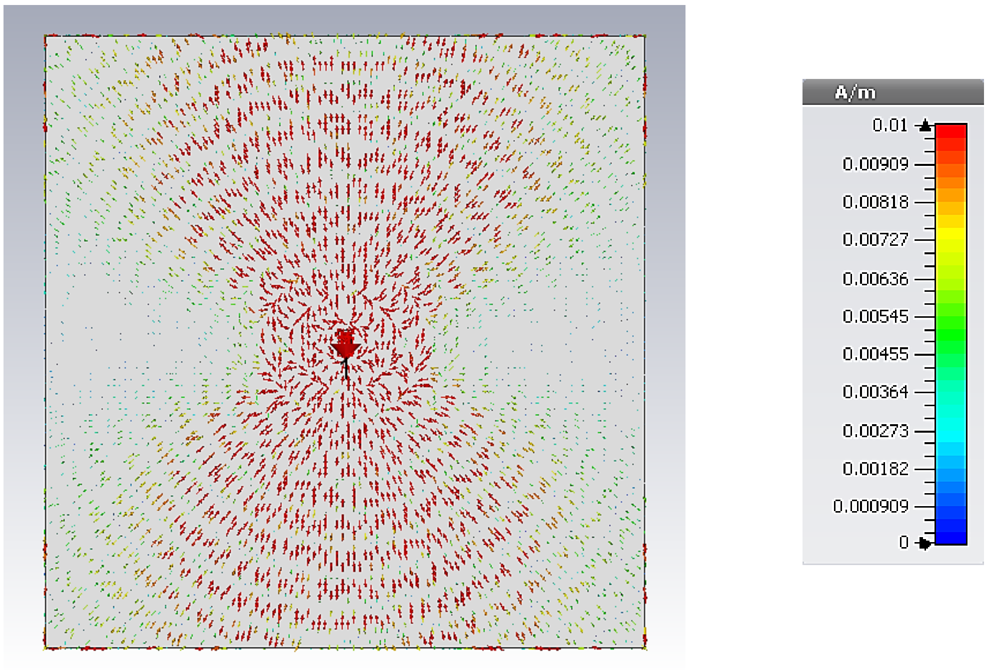

(c)

Figure 4.11: Surface current density distribution over the tag antenna mounted metal block at 923 MHz (phase of 11.25˚): (a) *XZ* plane (enlarged view), (b) *YZ* plane and (c) *XY* plane (different scales are for clear presentation).

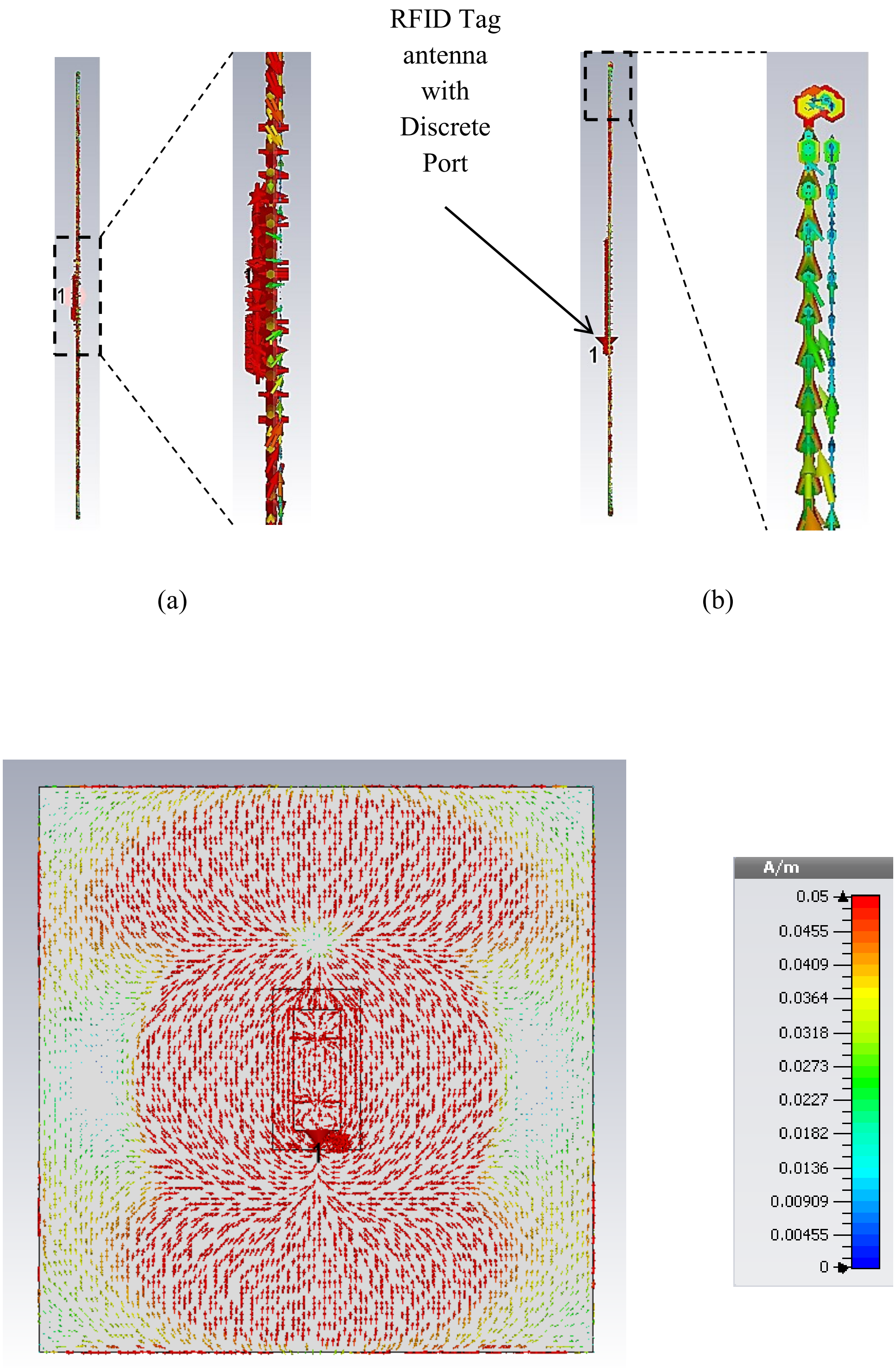

(c)

Figure 4.12: Surface current density distribution on tag antenna mounted metal plate at 923 MHz (phase of 11.25˚): (a) *XZ* plane, (b) *YZ* plane and (c) *XY* plane.

4.5 Tag Antenna Fabrication and Measurement Results

After the completion of simulation studies, the tag antenna was fabricated using PCB technology. Gerber format files extracted from the CST Microwave Studio model were used for this purpose. Then the RFID chip with XQFN package [135] was soldered on to the tag antenna using a hot air gun. Figure 4.13 shows the fabricated RFID tag antenna along with the RFID chip, soldered grounding pin, and terminals for the I^2C interface.

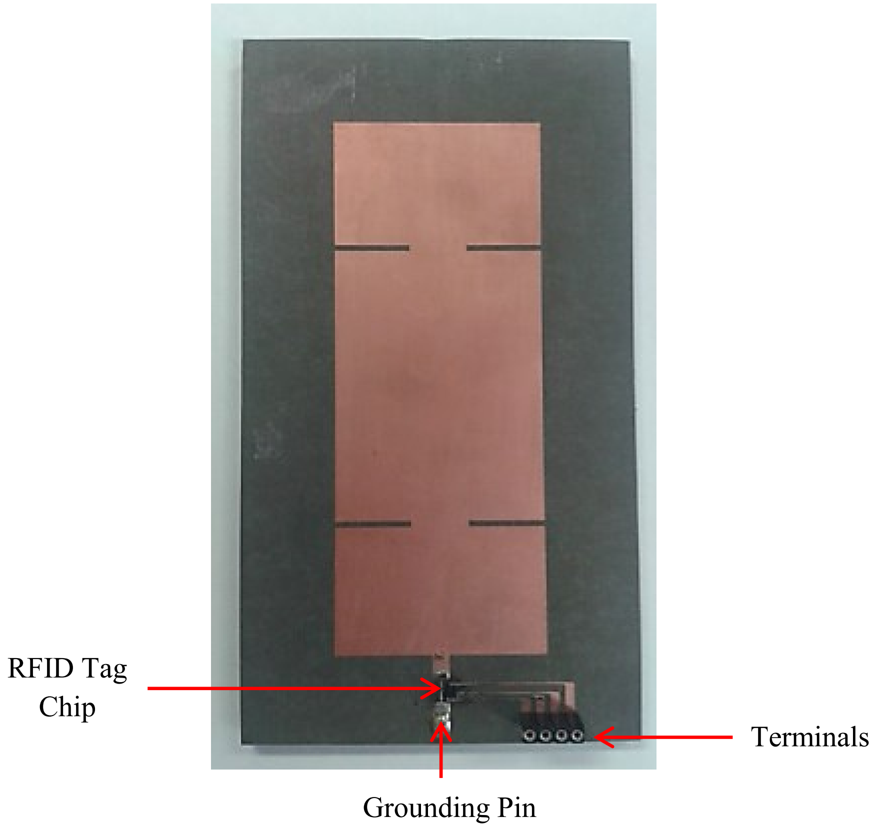

Figure 4.13: Photo of fabricated RFID tag antenna.

4.5.1 Measurement of the Resonant Frequency

Verification of the resonant frequency of the fabricated RFID tag antenna is important and challenging since this antenna does not have a port for connection with an external measurement device. Therefore, a non-contact measurement setup has been used as shown in

Figure 4.14. The measurement setup includes A-INFOMW broadband horn antenna (0.8–8.0 GHz) [192] kept at a height of 1.25 m above floor and Agilent N5225A performance network analyzer (PNA). The fabricated tag antenna upon a polystyrene mount was kept in the vicinity of the horn antenna in the line-of-sight. The measured resonant frequency was 922.8 MHz which was in good agreement with the simulated resonant frequency (923.4 MHz) in free space (see Figure 4.8).

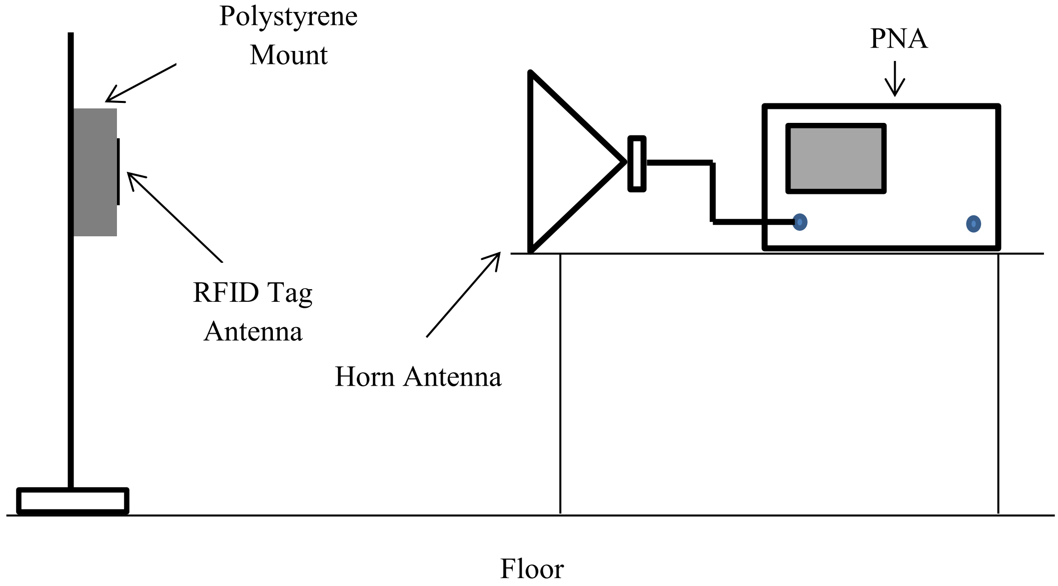

Figure 4.14: Schematic of the non-contact measurement setup for measuring the resonant frequency of the RFID tag antenna.

4.5.2 Determination of Maximum Gain

In addition to the resonant frequency, the maximum gain of the tag antenna is an important parameter which determines the read range of the RFID-based system. To determine the maximum gain of the fabricated tag antenna, the minimum transmitted power required to receive a response from the tag antenna was measured. The measurement setup is shown in Figure 4.15(a). A right hand circular polarized Laird Technologies® S9025PR antenna which has a gain of 5.5 dBic was used with Impinj Speedway Revolution Gen2 RFID reader

[176] to transmit the interrogation signal. Both the fabricated tag antenna and the reader antenna have been kept 1.25 m above the floor and in the direction of their maximum gain. The transmit power was incrementally increased by 0.25 dBm using Impinj Multireader software [193] installed in a laptop computer and the minimum power required to receive a response from the RFID tag in five different distances were recorded as shown in Table 4.3. The test has been carried out for both P and BAP modes of the RFID tag antenna. A 3-V coin cell has been connected between the *power* and *ground* terminals (see Figure 4.1) when conducting measurements for the BAP mode. Measurement of the minimum transmitted power for BAP mode at distance of 1.0 m and 1.5 m was not possible due to transmit power limitation of the reader (minimum setting is 10 dBm). Sensitivities (minimum threshold power necessary for tag chip to operate) of the P and BAP modes of the RFID chip are −17 dBm and −24 dBm, respectively, (i.e., the difference is 7 dBm) [135] where the differences of recorded values in Table 4.3 show a close resemblance to the sensitivity difference. Then the gain of the RFID tag antenna was calculated using the link budget given by [194, 195],

$$G_t = P_{th} - P_r - G_r - L_f - 10\log(\tau) - 10\log(p), \qquad 4.1$$

$$L_f = 20\log\left(\frac{\lambda}{4\pi d}\right), \qquad 4.2$$

$$\tau = \frac{4R_c R_a}{|Z_c + Z_a|^2}, \qquad 4.3$$

where, G_t is the maximum gain of tag antenna (dBi), P_{th} is the sensitivity of the RFID tag chip (dBm), P_r is the measured minimum transmitted power of the reader needed to receive tag response (dBm), G_r is the reader antenna gain (dBic), L_f is free space path loss (dB), λ is the wavelength (m), d is the distance between reader antenna and tag antenna (m), τ is power transmission coefficient, p is polarization efficiency, R_c is RF input resistance of RFID chip (Ω), R_a is the input resistance of the tag antenna (Ω), Z_c is the RF input impedance of RFID tag chip (Ω) and Z_a is the input impedance of tag antenna (Ω).

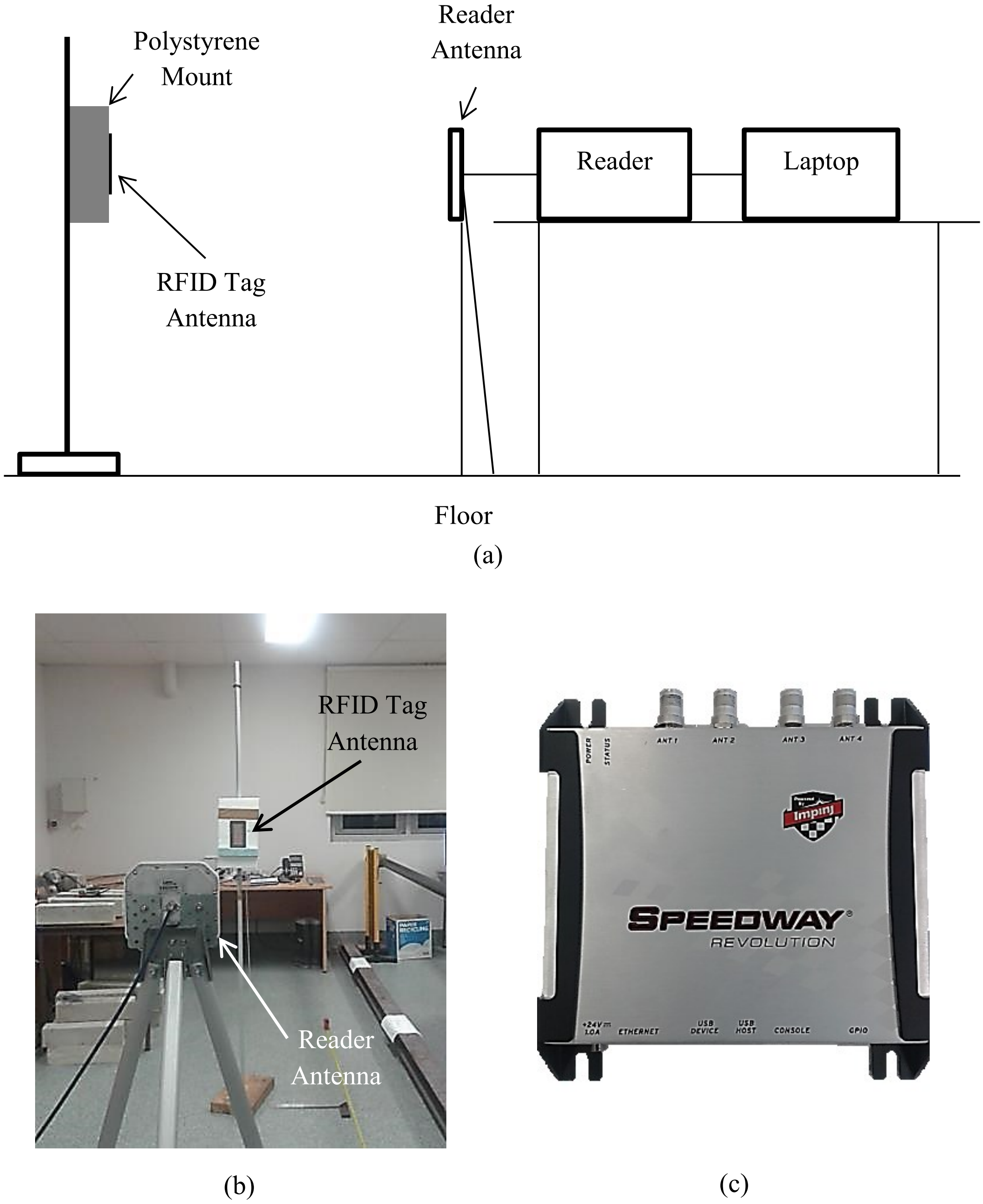

Figure 4.15: Measurement setup for measuring minimum transmitted power and read range: (a) schematic and (b) picture, and (c) RFID reader.

The measured minimum transmitted power values in P mode have been used in this calculation with free space path loss. A polarization efficiency of 0.5 was used in the calculation for the right hand polarized reader antenna [194]. Furthermore, simulated free space impedance value of the tag antenna was used for the calculation of power transmission coefficient. The RFID tag antenna gain was calculated for five different distances in which the minimum power has been measured. The calculated values are given as Gain 1 in Table 4.3. It can be seen from Table 4.3 that the calculated values are entirely different from the simulated free space maximum gain value (4.58 dBi) of the tag antenna and have large variations.

Table 4.3: Measured minimum transmitted power and calculated gain of the proposed tag antenna.

Distance (m)	**Minimum transmitted power (dBm)**		**Gain 1* (dBi)**	**Gain 2** (dBi)**
	P	***BAP***		
1.0	13.25	NA	−0.79	3.21
1.5	16.25	NA	−0.27	2.81
2.0	19.50	12.25	−1.02	3.08
2.5	19.75	12.50	0.67	3.35
3.0	23.75	16.75	−1.75	3.30

*obtained from Equations (4.1) and (4.2).
**obtained from Equations (4.1) and (4.4).

Owing to the fact that a conclusion is not possible upon the maximum gain of the fabricated tag antenna with only the measurement of minimum transmitted power, further experiments have been carried out by measuring received power at different distances. The setup shown in Figure 4.16(a) has been used for this measurement. The horn antenna which was used in the non-contact measurement (see Figure 4.14) has been used as the receiving antenna and the received power has been measured by Agilent EXA N9010A signal analyzer as shown in Figure 4.16(b). This antenna has a gain of 7.5 dBi at 923 MHz. Other equipment used in the measurement setup is the same as those used in the setup shown in Figure 4.15(a). Both antennas have been kept at a height of 1.25 m above the floor in the line-of-sight. The received power has been measured for 11 different transmit power values (10 dBm to 30 dBm) for each distance. Then the path loss for each distance has been calculated using Friis link budget given by,

$$L_a = P_{rx} - G_{rx} - P_{tx} - G_r - 10\log(p), \quad 4.4$$

where, L_a is the path loss from received power measurement (dB), P_{rx} is the measured received power, G_{rx} is the gain of the receive antenna (dBi), and P_{tx} is the transmitted power of the reader. Figure 4.17 shows the calculated path loss for each distance with a 95% confidence interval. It can be seen from Figure 4.17 that the calculated path loss values from the received power measurement for different distances are always higher than free space path loss (L_f) as expected since the laboratory environment where the measurements have been carried out is not perfect free space. Substituting L_f by the average L_a values at each distance, the RFID tag antenna gain was calculated for the second time using Equation 4.1 and the values are shown in Table 4.3 as Gain 2. The values are in good agreement with simulated maximum far-field gain in free space (4.58 dBi) and they also have less variation compared to Gain 1. Overall, the results demonstrate that the fabricated RFID tag antenna has a maximum gain $\geq$ 3.0 dBi in *XZ* plane at 0° in actual environment. However, the remaining difference between experimental and simulated maximum gain of the RFID tag antenna could be due to fabrication errors (variations of the dielectric properties of substrate, quality of soldering of the grounding pin, mismatching between the tag antenna and the RFID chip in soldering) and the influence of environment.

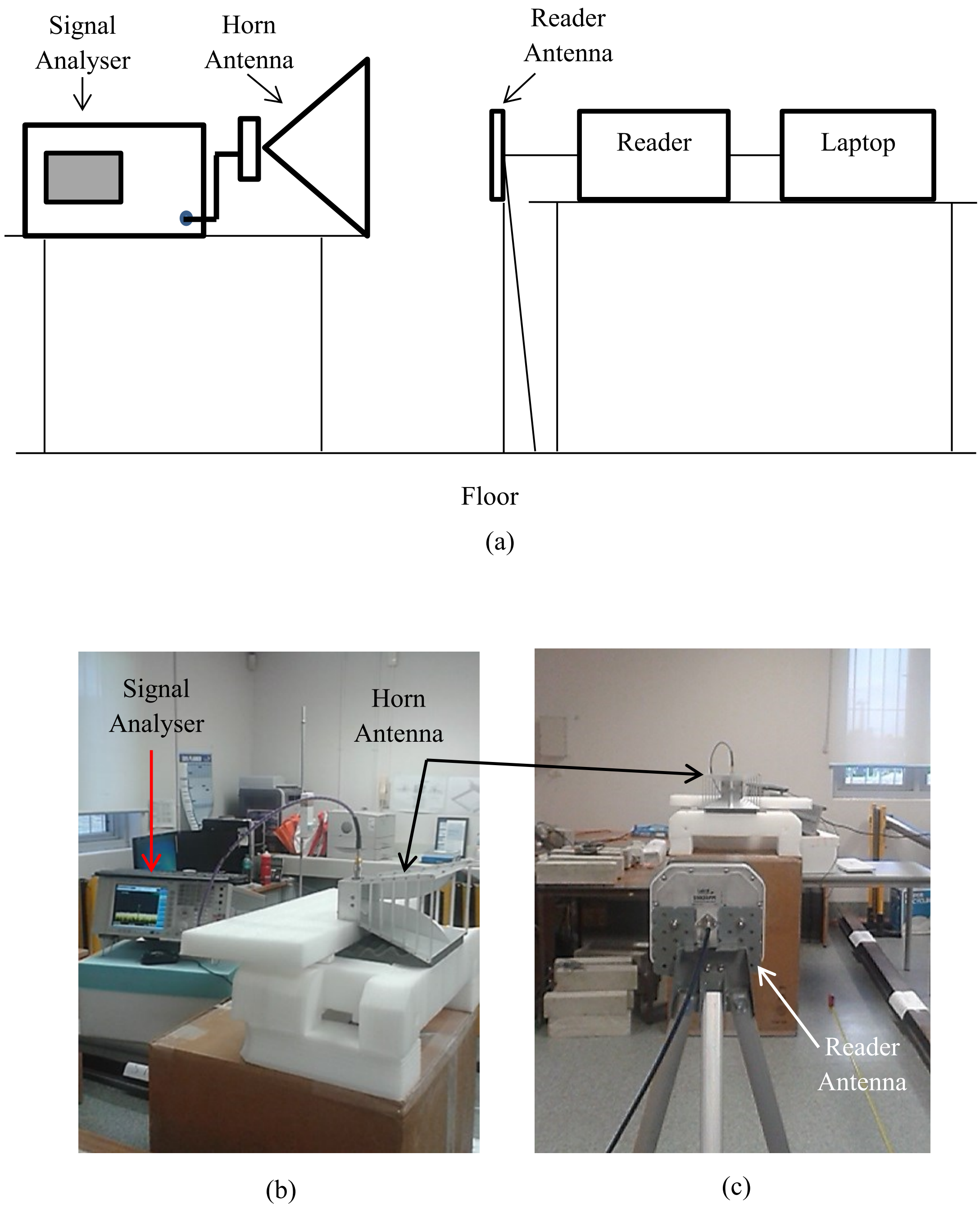

Figure 4.16: Measurement setup for measuring received power at different distances: (a) schematic, (b) picture of the horn antenna and signal analyzer, and (c) picture of the reader antenna and the horn antenna.

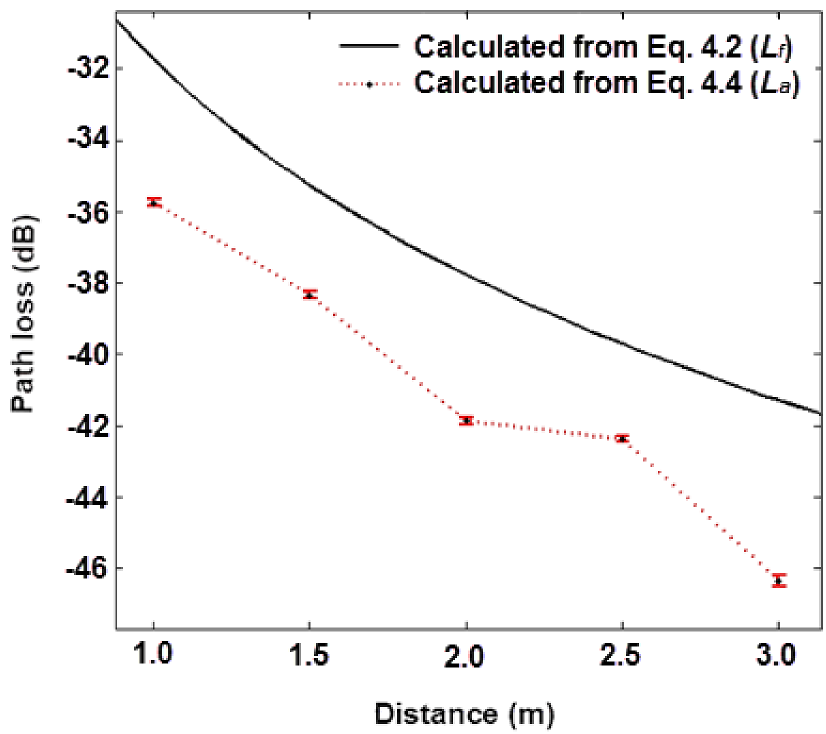

Figure 4.17: Calculated free space path loss (L_f) and calculated path loss with received power measurement (L_a is shown with the confidence interval and the points are connected only for illustrative purpose).

4.5.3 Performance Comparison and Read Range Measurement

Figure 4.18 shows simulated gain vs power transmission coefficient of the designed RFID tag antenna along with two commercially available tag antennas (including tip loaded dipole tag antenna used in Chapter 3) at 923 MHz when mounted on the mounts presented in Section 4.4.2. The 3-dBi line represents the gain value obtained for the fabricated RFID tag antenna from measurements in Section 4.5.2. The 1-m, 2-m and 3-m curves represent the antenna gain needed to achieve those read ranges with 23-dBm transmitted power for the P mode under related average L_a values in Section 4.5.2. This was done to acquire clear comparison of read range between the designed tag antenna and the tag antenna used in Chapter 3. The measured free space read range value for tip loaded tag antenna in Chapter 3 was ~1.2 m in P mode. According to Figure 4.18 the simulated performance of it lies under and near 2-m curve which tallies with the measured value given the fact that the simulated free space performance of the tag antenna is always better than that measured in actual environment.

Furthermore, Figure 4.18 shows that the performance variation of the designed tag is less as the points are clustered nearby when compared to the performance variations of the other reference tag antennas. It shows that there is a considerable performance variation of the other tag antennas when mounted on concrete other than the drastic variation they show when mounted on metal. Even though the bow-tie tag antenna has higher performance than the tip-loaded tag antenna in free space, they have inverse performance on the concrete block which shows the unpredictability of performance variation.

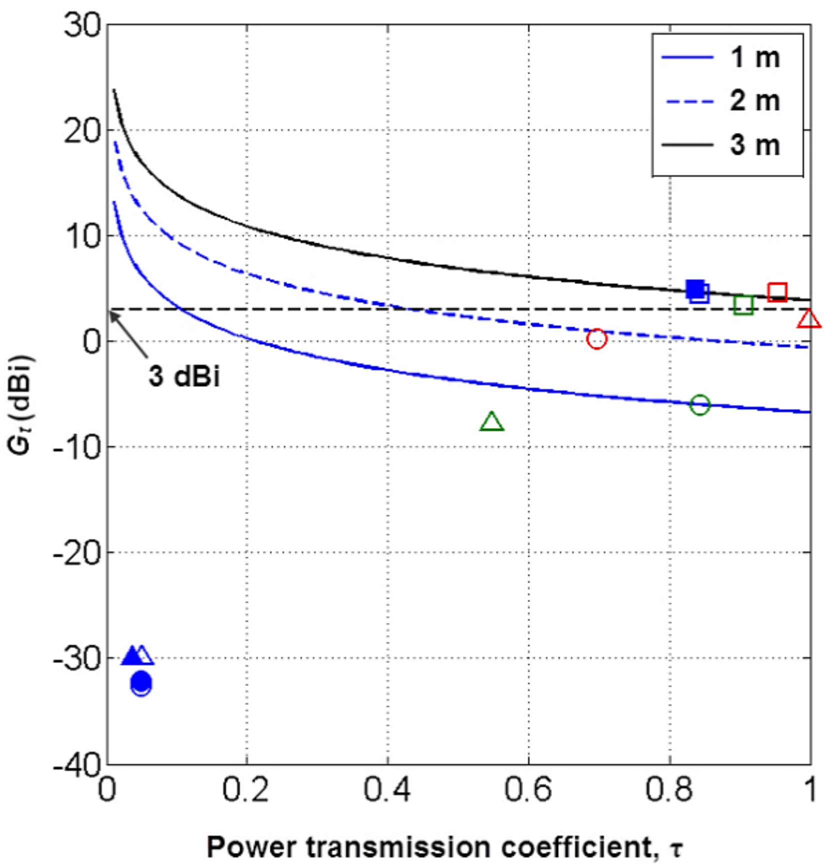

Figure 4.18: Gain (dBi) versus power transmission coefficient (□ - proposed RFID tag antenna, ○ - tip loaded RFID tag antenna, Δ - bow tie RFID tag antenna, red - free space, blue - metal block, blue filled - metal plate and green - concrete block).

Read range measurements of the fabricated RFID tag antenna has been conducted using the setup shown in Figure 4.15(a). The transmit power of the reader has been set to 23 dBm and the tag antenna has been moved away from the reader antenna. The measured read range under this condition is 2.9 m for P mode. Therefore, the fabricated tag antenna performance should be under and near the 3-m curve of the Figure 4.18, where it tallies with the obtained tag antenna gain in Section 4.5.2. The read range under the same transmit power conditions has been measured for the fabricated tag antenna mounted on a metal plate with the same dimensions used in the simulation as shown in Figure 4.19. The mounting arrangement is shown in the enlarged view of Figure 4.19(a) and the measured read range was 2.85 m and 3.35 m for P and BAP modes, respectively. Even though the read range measurement for P mode shows a slight reduction compared to previous, it shows that the tag antenna has acceptable performance even when placed on metal mounts. Finally, the read range of the RFID tag mounted on the metal plate was measured with increased reader transmit power of 30 dBm (added reader antenna gain of 5.5 dBic ≈ EIRP of 36 dBm) and it has been seen that the tag antenna can be read at a 6.7-m distance in the P mode.

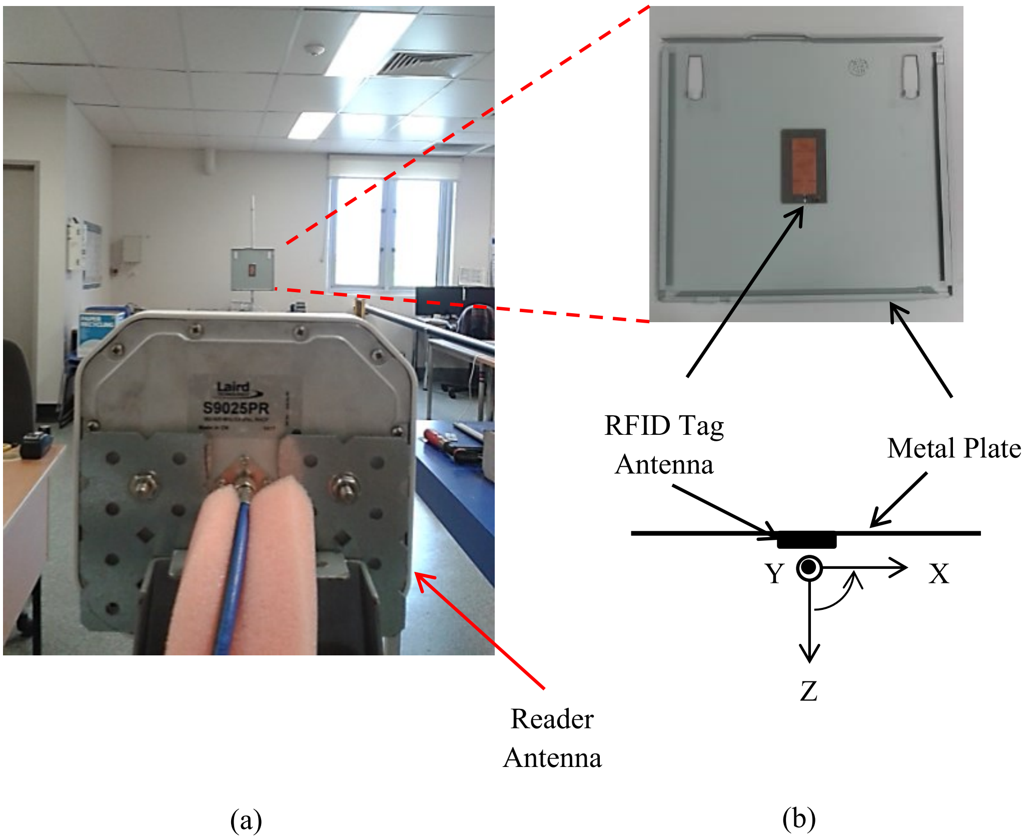

Figure 4.19: Measurement setup for measuring read range of fabricated tag antenna mounted on metal: (a) picture and (b) top view and rotation direction.

4.5.4 Tag Antenna Readability Test in Different Orientations

This test was carried out to investigate the readability of the tag antenna in different orientations. The same setup in read range measurement was used where the tag antenna was mounted on the metal plate at the distance of 6.7 m from the reader antenna as shown in Figure 4.19(a). The orientation of the metal plate was rotated from the line-of-sight to 90˚ anti-clockwise (turning 90˚ anti-clockwise around *Y* axis as shown in Figure 4.19 (b)) during the test. Figure 4.20(a) shows how the average received signal strength indicator (RSSI) for 7 discrete orientations of the metal plate. All instances where RSSI is present, the readings were achieved at the maximum tag antenna read rate by the reader. The experiment shows that the RFID tag mounted on the metal plate can be read at 75˚ when the tag antenna is mounted horizontally even though the RSSI drops with increased angle. The maximum orientation value that the tag antenna could be read was 30˚ when mounted vertically. For the both vertical and horizontal mounting of the tag antenna, reading the tag antenna after plate rotation of 90˚ anti-clockwise around *Y* implies reading it in 180˚ and 90˚ directions on the *XY* plane, respectively. Therefore aforementioned RSSI measurements can be justified as the tag antenna has a low gain at 180˚ than 90˚ on *XY* plane when mounted on the metal plate (see the normalized gain pattern in Figure 4.20(b)) due to the surface current distribution pattern shown in Figure 4.12(c). Therefore, the fabricated tag antenna mounted on the metal plate has a higher angle of readability on *XZ* plane when mounted horizontally at a 6.7-m distance.

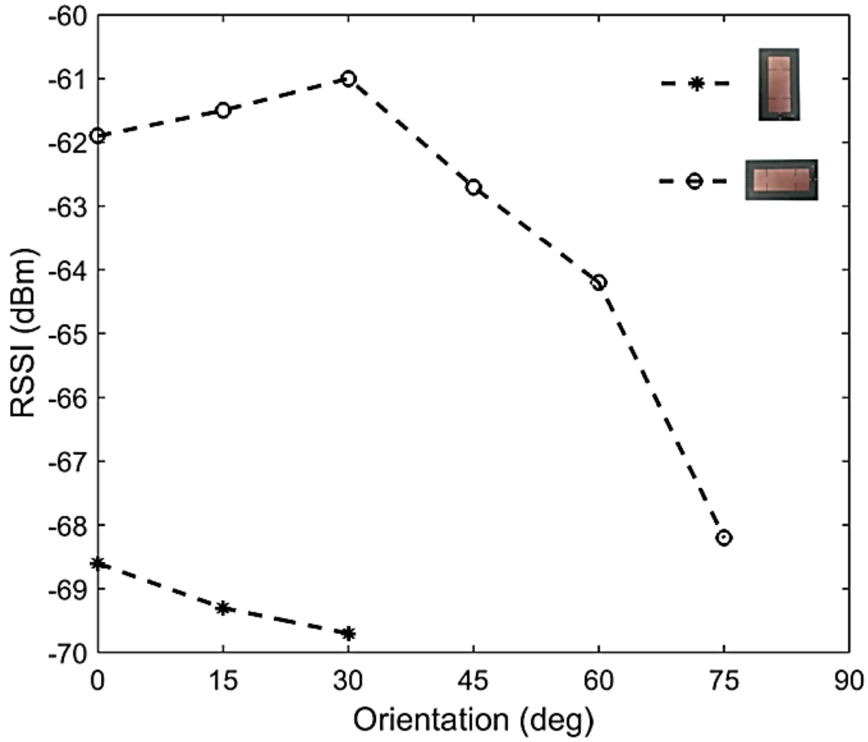

(a)

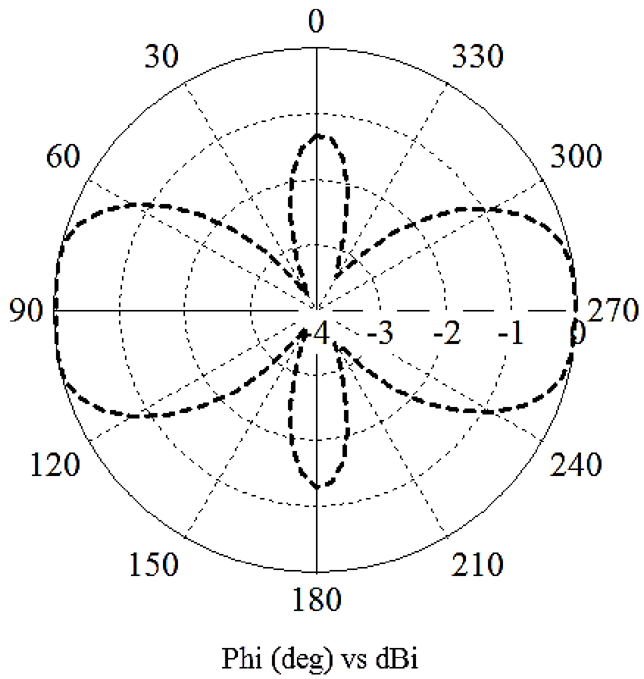

(b)

Figure 4.20: RFID tag antenna mounted on metal plate: (a) received signal strength indicator (RSSI) versus orientation at 6.7-m read range (points are connected only for illustrative purpose) and (b) normalized gain pattern on *XY* plane.

4.6 Modification of the Tag Antenna for Other Frequency Bands

Although the RFID tag antenna has been optimized for the Australian UHF RFID frequency band, it can be easily modified to operate in other UHF RFID frequency bands using slit parameters. Table 4.4 provides the slit parameter values required to achieve this at the selected slit position in Section 4.3. Figure 4.21 shows simulated S_{11} (in dB) along with maximum gains attained in free space for near conjugate impedance matched state between the tag antenna and the RFID tag chip at 866.5, 915, and 953 MHz for frequency bands of Europe, USA, and Japan, respectively. The achievable gain in the European band is slightly less than that achieved in the other two bands due to a reduction of the antenna input resistance. This can also be seen in the reduced power transmission coefficient in Table 4.4. However, the tag antenna maintains a simulated gain greater than 3 dBi over the entire frequency band. In the case of USA frequency band, the tag antenna has a gain exceeding 2 dBi for a major portion of the frequency band. The highest gain is obtained in the frequency band of Japan with the value of approximately 5 dBi.

Table 4.4: Frequency bands, slit parameters, and power transmission coefficients.

Frequency band (MHz)	s_l (mm)	s_w (mm)	τ
865 – 868 (Europe)	13.4	4.1	0.82
902 – 928 (USA)	13.4	1	0.97
950 – 956 (Japan)	10.4	1	0.97

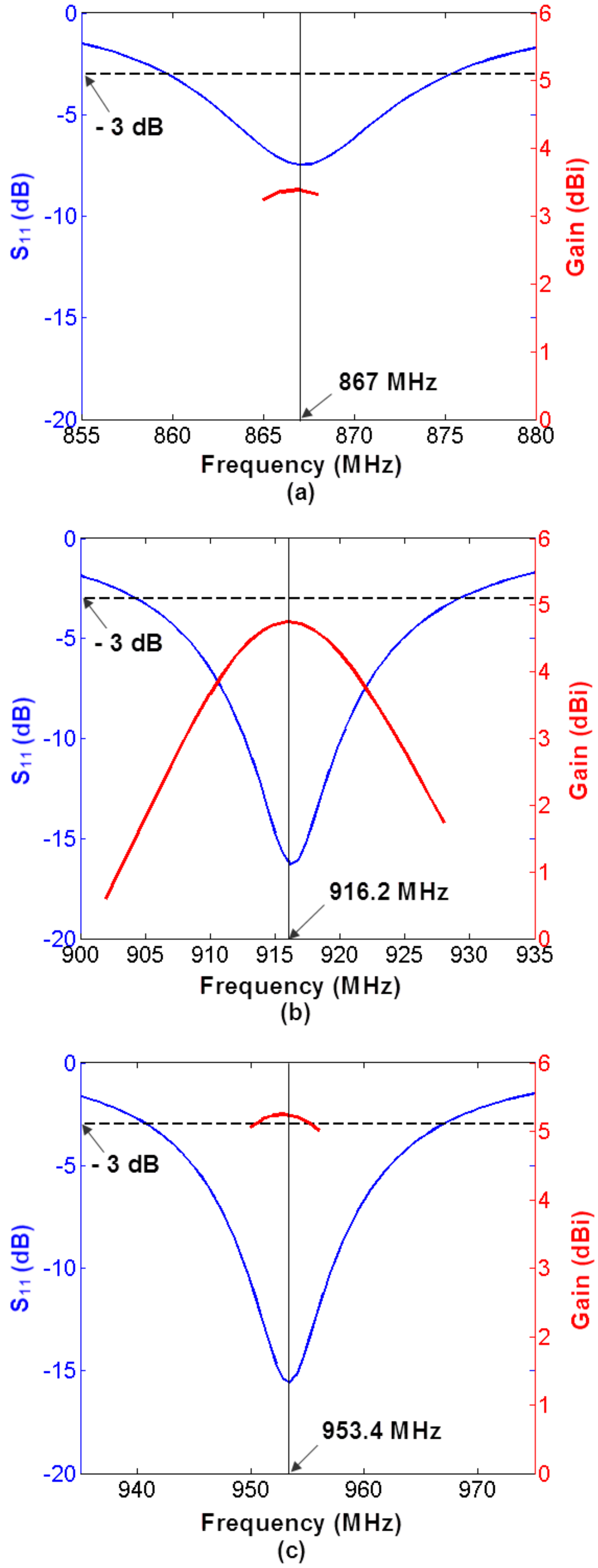

Figure 4.21: S_{11} (dB) and gain versus frequency at three frequency bands: (a) 865-868 MHz, (b) 902-928 MHz, and 950-956 MHz.

4.7 Conclusion

In this chapter, design considerations and performance analysis of a construction material mountable RFID tag antenna was presented. The tag antenna was designed to operate in the Australian UHF RFID frequency band incorporating the new generation RFID chip used in Chapter 3. A relatively small tuneable tag antenna was modeled in CST. Symmetrical slits along the radiating edge were used for tuning, conjugate impedance matching and miniaturizing.

The simulated magnitude of reflection coefficient ($|S_{11}|$ in dB) of the tag antenna on the concrete and metal mounts showed that the tag antenna has more than enough impedance bandwidth for the intended frequency band even though the resonant frequency changes slightly. The simulated resonant frequency of the proposed antenna in free space was proved to be correct by the conducted non-contact laboratory testing which gave the measured resonant frequency of 922.8 MHz.

The results showed that simulated gain of the tag antenna mounted on concrete and metal mounts have retained the direction of maximum gain with slight variations of the maximum gain values. It became more directive when mounted on larger mounts. The wireless link budget calculations from measurements of the minimum transmit power and received power showed that the fabricated tag antenna has a maximum gain $\geq$ 3 dBi. The read range measurements were conducted to compare the performance of designed tag antenna with the tag antenna used in Chapter 3 and another commercially available tag antenna. The comparison showed that the performance of proposed tag antenna mounted on concrete and metal is close to that of it in free space. Furthermore, it shows that the performance variation of commercially available tag antennas can be unpredictable when mounted on concrete and they have poor performance when mounted on metal. Nearly the same read ranges achieved with transmit power of 23 dBm in the laboratory (2.9 m in P mode) and when mounted on a metal plate (2.85 m in P mode) justifies this. Furthermore, the performance variation is lower than the reference tag antennas. Consequently, the read range measurement with transmit power of 30 dBm and the readability test showed that the fabricated tag antenna has higher readability within a range of 6.7 m when mounted horizontally under the EIRP regulations.

In conclusion, the proposed tag antenna can be used to improve the read range of the wireless infrastructure health monitoring system with RFID tag antenna integrated acceleration sensor proposed in Chapter 3. The capability of the tag antenna to tune into other UHF RFID frequency bands ($\in$ 860 MHz to 960 MHz) was studied and the results showed satisfactory performance. Therefore, the proposed tag antenna can be used electronically as an I^2C slave component to develop UHF RFID tag antenna integrated sensors to the worldwide use. The electronic integration capability of the tag antenna via I^2C bus will be presented in Chapter 5.

Chapter 5 RFID-Based Wireless System with Multiple Tag Antenna Integrated Sensors for Measurement of Dynamic Acceleration of Infrastructure

5.1 Introduction

In this chapter, the performance of the enhanced RFID-based dynamic acceleration measurement system is further investigated upon a full-scale steel I-beam which is one of the critical and ubiquitous structural elements [196, 197]. In this investigation, the system will be upgraded with novel semi-passive tag antenna integrated acceleration sensors which are directly mountable on metal structural elements. The mountable tag antenna integrated acceleration sensors are created out of custom designed tag antennas in Chapter 4 and specifically fabricated acceleration sensor circuits. The enhancement of the system to measure simultaneous 3-axis acceleration with higher spectral bandwidth with lower microcontroller operational clock than the system proposed in Chapter 3 is discussed in detail. The feasibility of expansion of the system to have multiple wireless sensors also shown by implementing the system with two tag antenna integrated acceleration sensors (3-axis acceleration measurement with enhanced spectral bandwidth) in different positions. Additionally, the benchmarking of the RFID-based wireless dynamic acceleration measurement system is provided by comprehensive comparison of the results with measurements from commercial wired and wireless acceleration measurement systems.

Finally, the conclusions summarizing the aforementioned system enhancement efforts and comparisons are made.

5.2 Enhanced RFID-Based Wireless Dynamic Acceleration Measurement System

The enhanced system measuring the dynamic acceleration of the I-beam is shown in Figure 5.1 (a). Two major enhancements compared to what presented in Chapter 3 have been done for the RFID-based wireless dynamic acceleration measurement system. First, the novel semi-passive RFID tag antenna integrated acceleration sensor (TAIAS) was developed (shown in Figure 5.2) and applied as shown in Figure 5.1 (b). The TAIAS includes the construction material mountable RFID tag antenna designed in Chapter 4 and a custom designed acceleration sensor circuit as shown in Figure 5.2 (b). The tag antenna is integrated with the acceleration sensor circuit via I^2C interface. Secondly, the Impinj RS500 Development Board (i.e. RFID reader) used in the developed system prototype in Chapter 3 was substituted with Impinj Speedway Revolution Generation 2 UHF commercial RFID reader. The substitution has the capability of reaching higher signal transmit power (31.5 dBm maximum), higher read rates and handling a higher number of reader antennas simultaneously [164]. Furthermore, Impinj Octane software development kit (SDK) [163] which linked with the reader provides convenience in creating custom user application to acquire acceleration measurements. All other system components used in Chapter 3 were unchanged.

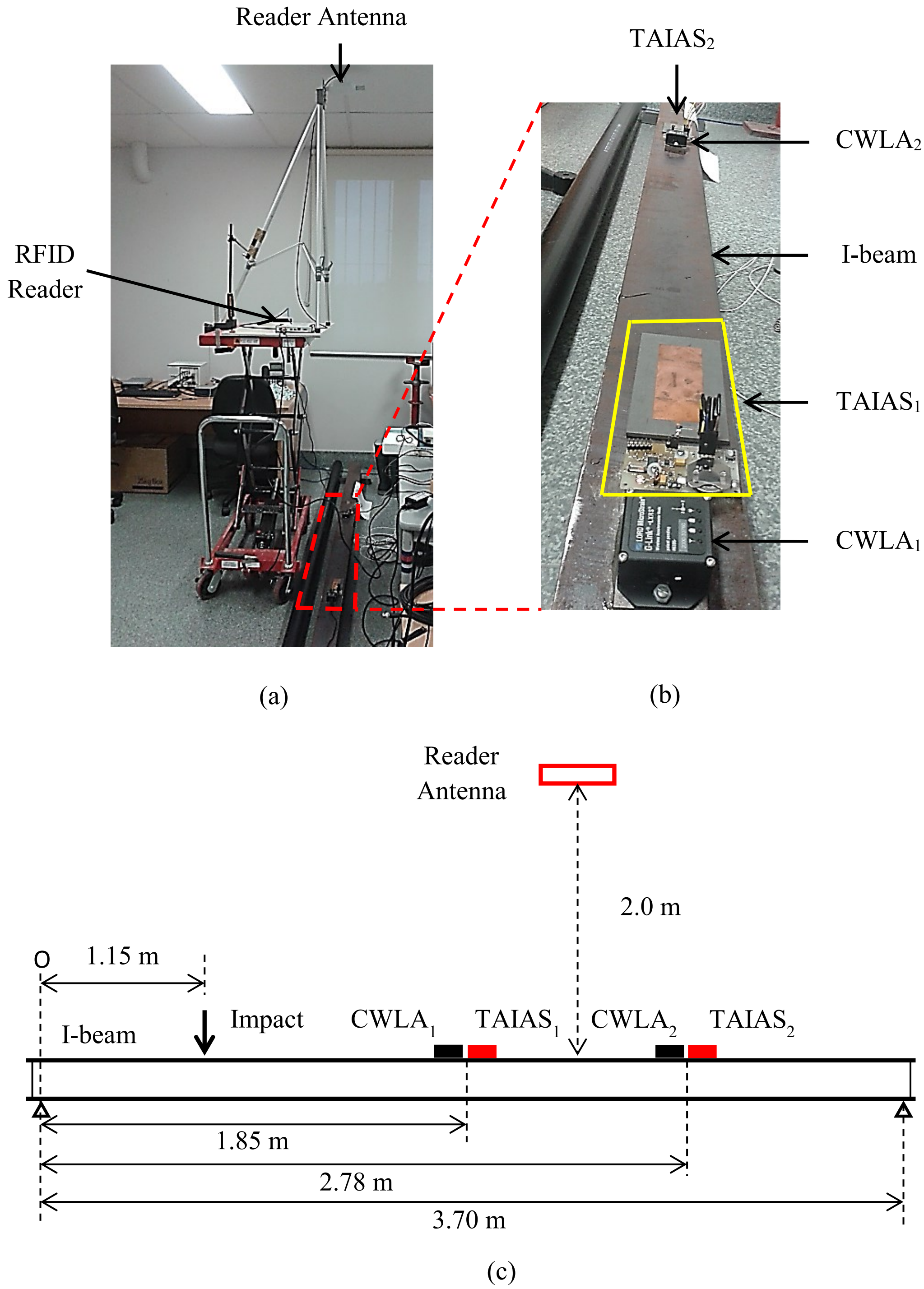

Figure 5.1: System measuring the dynamic acceleration of I-beam: (a) laboratory setup, (b) enlarged view of the positioning of tag antenna integrated acceleration sensors (TAIASs) and (c) schematic (CWLA-commercial wireless accelerometer).

5.2.1 Acceleration Sensor Circuit Design

Figures 5.2 (a) and (c) depict the acceleration sensor circuit in detail. This was a custom designed miniaturized version which substitutes the *Explorer 16* development board and the accelerometer used in Chapter 3. The capabilities and number of pins of *PIC24FJ128GA010* microcontroller used in Chapter 3 were abundant for this purpose and it was substituted with miniature *PIC24F16KA102* microcontroller [198] which has adequate capabilities. Additionally, the newly selected *PIC24F16KA102* microcontroller is an ultra-low power microcontroller which has a configurable "*Deep Sleep*" operational state that can be exploited to save battery (3-V coin cell) power [199, 200] at times when acceleration measurements are not being acquired by the system. This microcontroller has been previously proven for low power applications in [201]. The capability of supplying an external clock to accelerometer from the microcontroller was added using the pulse-width modulation (PWM) output of the microcontroller which provides extra control over ODR [179]. Furthermore, the circuit was designed with the hardware capability of supplying DCI to RFID tag chip by the microcontroller itself which provided the opportunity of switching between BAP and P communication modes in the firmware. Additionally, it has been equipped with the possibility of acquiring a wakeup interrupt to the microcontroller from the RFID tag chip which provides the capability of waking the TAIASs up from aforementioned *Deep Sleep* state upon "*Write*" transactions of the reader via the air interface. The added connection between *external interrupt 0* (INT0) of the microcontroller and the SCL (i.e. serial clock connection of I^2C bus) provides the necessary hardware support to implement the wake-up procedure. The holes for mounting screws were provided in compliance with the mounting specifications described in the accelerometer datasheet [179].

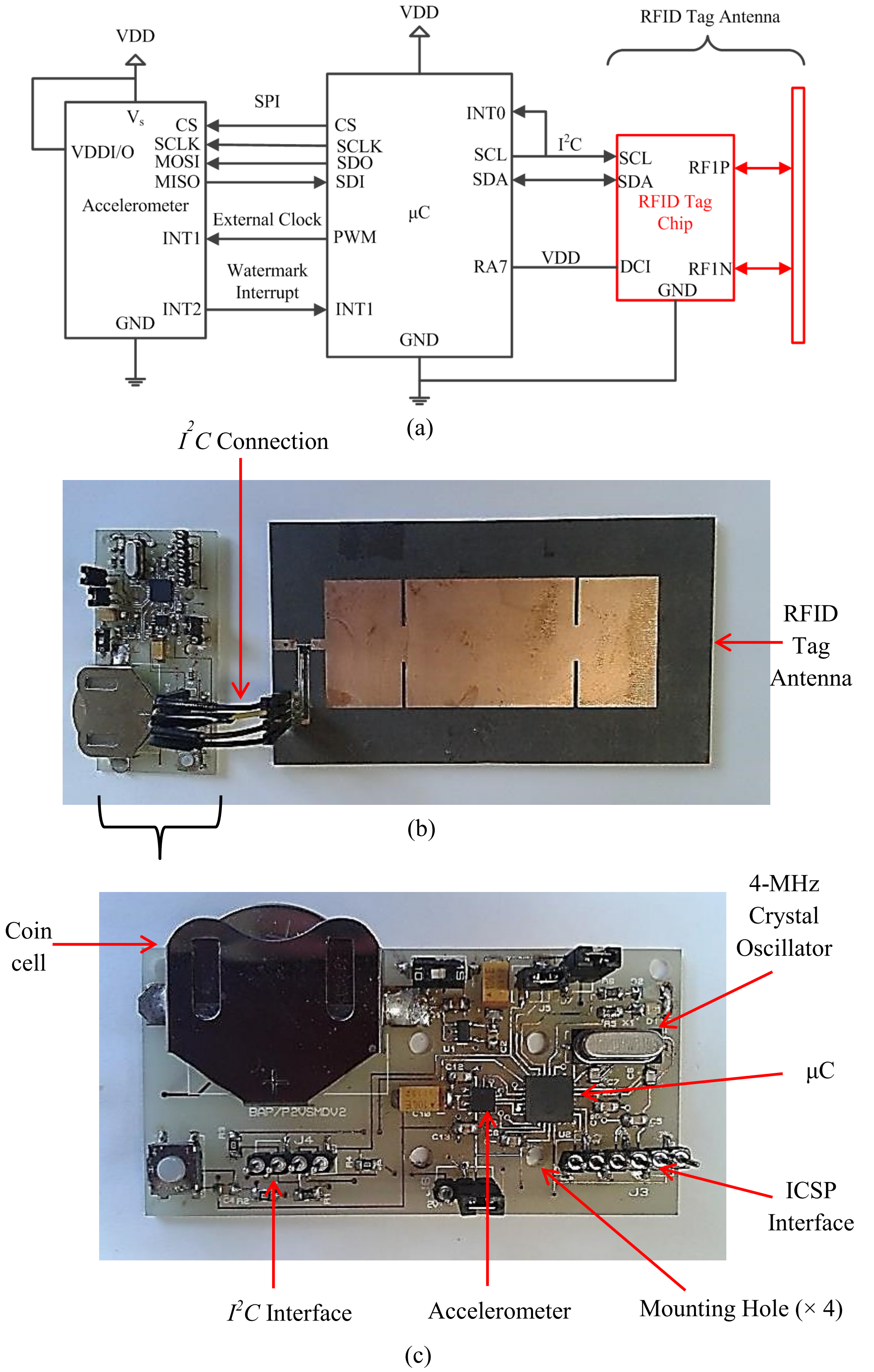

Figure 5.2: Tag antenna integrated acceleration sensor (TAIAS): (a) schematic, (b) picture of implementation and (c) enlarged view of acceleration sensor circuit (VDD = 2.0 V and other notations are in accordance with datasheets [135, 179, 198]).

5.2.2 Firmware Improvement for 3-Axis Dynamic Acceleration Measurement with 50-Hz Spectral Bandwidth

Figure 5.3 (replica of Figure 3.12) provides the timing diagram of the TAIAS proposed in Chapter 3 (*i* is the number of acceleration samples). The main requirement of the firmware proposed in Chapter 3 was to achieve adequate t_{RF} for reader to acquire acceleration samples within one acquisition cycle. One of the major constraints was the use of EPC code of the tag chip which had a maximum length of 8 words. This constraint had limited the number of single axis acceleration samples which can be acquired in single acquisition cycle to 7 and sets of every third 3-axis acceleration samples to 2, including the tracking word T_W. Second constraint was the time consumption of $t_{I2C} + t_{NVM}$ (~4.37 ms) with *single word-NVM writes* between the microcontroller and the tag chip. The combined effect of these two constraints had made 3-axis acceleration measurement only possible with a lower spectral bandwidth of 16.67 Hz.

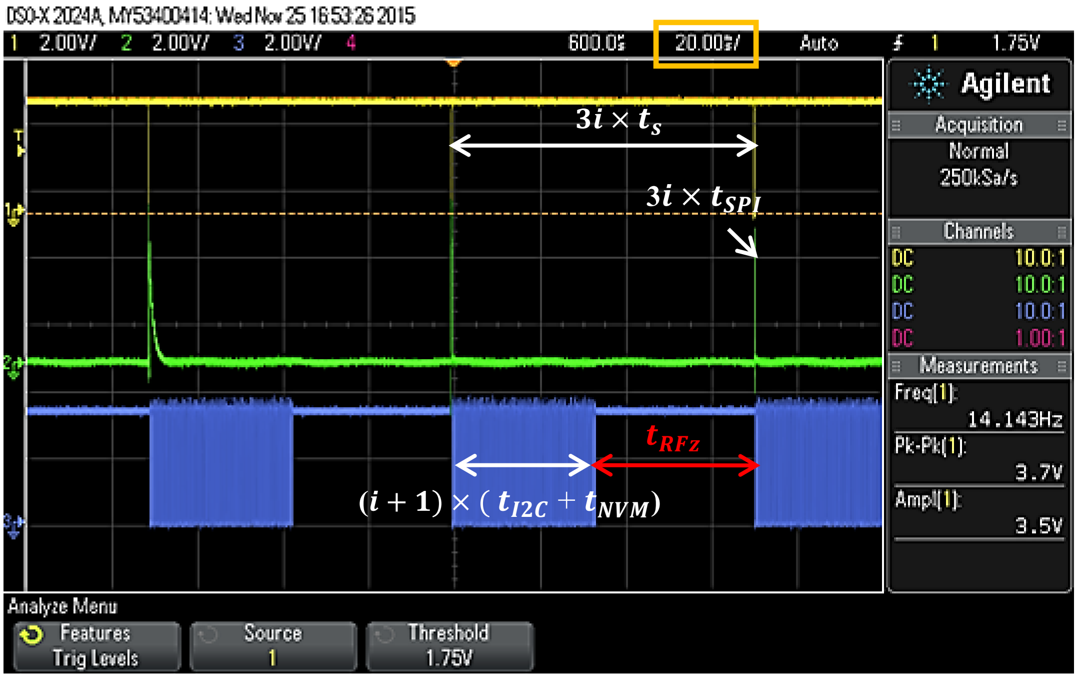

Figure 5.3: Timing diagram of *Watermark interrupt* (yellow), *SPI* receive (green) and *I²C* write (blue) of the RFID tag antenna integrated acceleration sensor with *single word-NVM writes* for *i* = 7 (t_f is not visible).

The current design of firmware is adjusted to use *USER* memory of the RFID tag chip instead of EPC code (in *EPC* memory) to eliminate the limitation of maximum 8 numbers of words. The *USER* memory of the RFID chip has 1024-bytes (512 words) which can be used accordingly. Consequently, the EPC code can be used solely for identification of the TAIASs. The influence of the second constraint could be reduced implementing I^2C transactions with *two word-NVM writes* between the RFID tag chip and the microcontroller. According to [135] the t_{NVM} value for a *single word* and a *two word-NVM write* of the RFID tag chip is the same. Therefore, $t_{I2C} + t_{NVM}$ value could be reduced by ~50 % as seen in Figure 5.4 (all other firmware configurations are same as for Figure 5.3) since t_{NVM} occupies a major portion of it. Consequently it provides the possibility of transferring all 3-axis acceleration samples as shown in white dashed lines in Figure 5.4. This decreases t_{RF} (c.f. Figure 5.3 and Figure 5.4) which can be re-increased according to Equation 3.1 by increasing i as now the $t_s > t_{I2C} + t_{NVM}$ for ODR of 100 Hz ($t_s = 3.33$ ms and $t_{I2C} + t_{NVM} \sim 2.18$ ms).

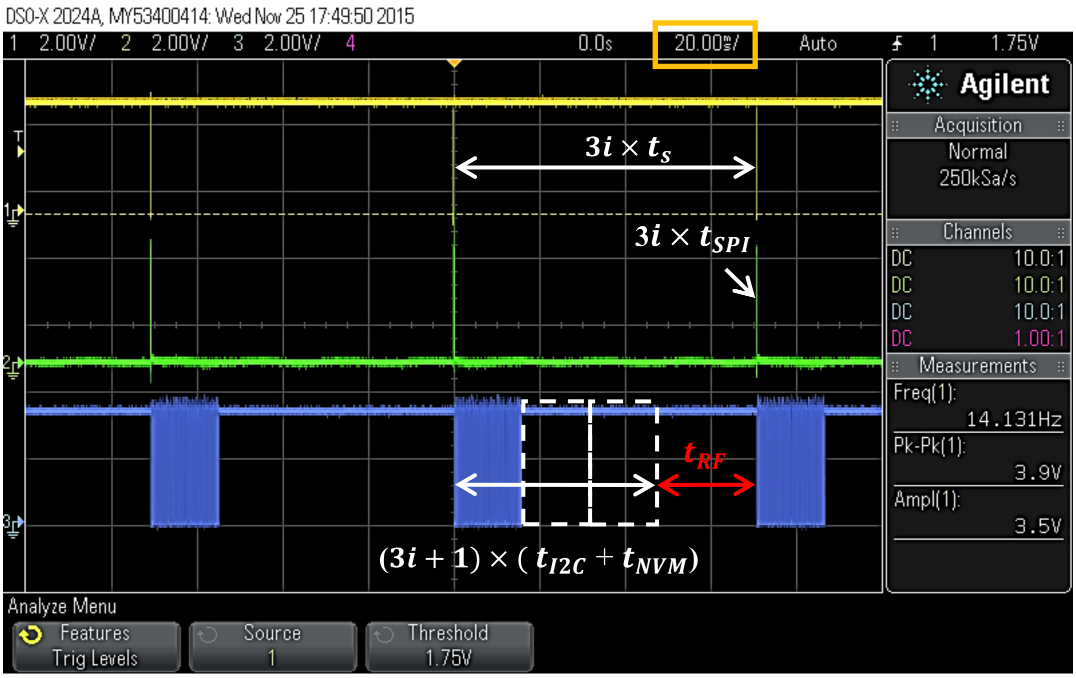

Figure 5.4: Timing diagram of *Watermark interrupt* (yellow), *SPI* receive (green) and I^2C write (blue) of the RFID tag antenna integrated acceleration sensor with *two word-NVM writes* for $i = 7$ (t_f is not visible).

At this stage of the firmware design, the option of lowering the operating clock of the microcontroller was considered since t_{SPI} , t_f and t_{I2C} have minor effects on the timing of the TAIASs. The initial firmware design in Chapter 3 was done for 32-MHz (i.e. internal 8-MHz RC oscillator with 4 × PLL) operating clock of the microcontroller. In the current firmware design, the operating clock was lowered to 4-MHz frequency which will reduce the microcontroller power consumption roughly by 8 times than previous according to [202] (lowering the operating clock than this is not possible due to the requirements of I^2C and *SPI* peripheral clock frequencies demanded by RFID tag chip and accelerometer). Consequently, this helps to save the battery power of the TAIASs. Table 5.1 contains the configuration settings of TAIASs and combined Figures 5.5 and 5.6 provide the flow diagram of the current firmware design. The next additional feature implemented in the firmware is the "*Deep Sleep*" mode as can be seen from Figure 5.5. Since TAIASs are semi-passive devices, conserving power is important to have longer battery life. In this context TAIASs should only be in measurement mode at the time of acceleration samples being acquired by the reader. The *Deep Sleep* mode of the microcontroller [198, 203] was implemented for all other times. This mode is the lowest power consumption mode available in the microcontroller which draws currents as low as 350 nA (watchdog timer in operation) and consumes 40 % less power than normal "*Sleep*" mode [200]. The RFID chip has the capability of pulling-down the SCL connection for the duration of reader write over air interface given that the DCI is already pulled-down [135]. This feature was exploited in the firmware to wake up the TAIASs from *Deep Sleep* mode upon reader *Writes* over air interface using *External Interrupt 0* as the wake up source (during the measurement mode in which I^2C is in operation, this interrupt is disabled). The tag chip changes from *Idle and RF Receive* state to *Internal Control* state as shown Figure 5.5 since *NVM-writes* are involved in this operation.

The addition of wake-up upon *Write* feature to TAIASs makes the overall read range shorter as the RFID chip sensitivity is −12 dBm for reader *Writes* over the air interface (sensitivities for reading over the air interface are −17 dBm and −24 dBm for P and BAP, respectively) [135]. However, the system was tested from a distance of 2 m between reader and TAIASs as shown in Figure 5.1. Therefore, the system has proven read range enhancement from 0.1 m (see Chapter 3) to 2 m in both P and BAP mode and TAIASs directly mounted on metal.

Table 5.1: Configuration settings in the firmware.

Component	Configuration
Accelerometer	Acceleration level: ± 2 g Clock: External (51.2 kHz) Output data rate (ODR): 100 Hz Noise mode: ultra-low noise Interface: SPI (slave) Anti-aliasing filter: ODR/2 Interrupt: Watermark configured at 60 acceleration samples
RFID tag antenna	RF ports: 1 blocked, 2 in use Interface: I^2C (slave)
Microcontroller	Interface: I^2C (master) 400 kbps, SPI (master) 2 MHz Oscillator: Primary (4 MHz crystal oscillator)

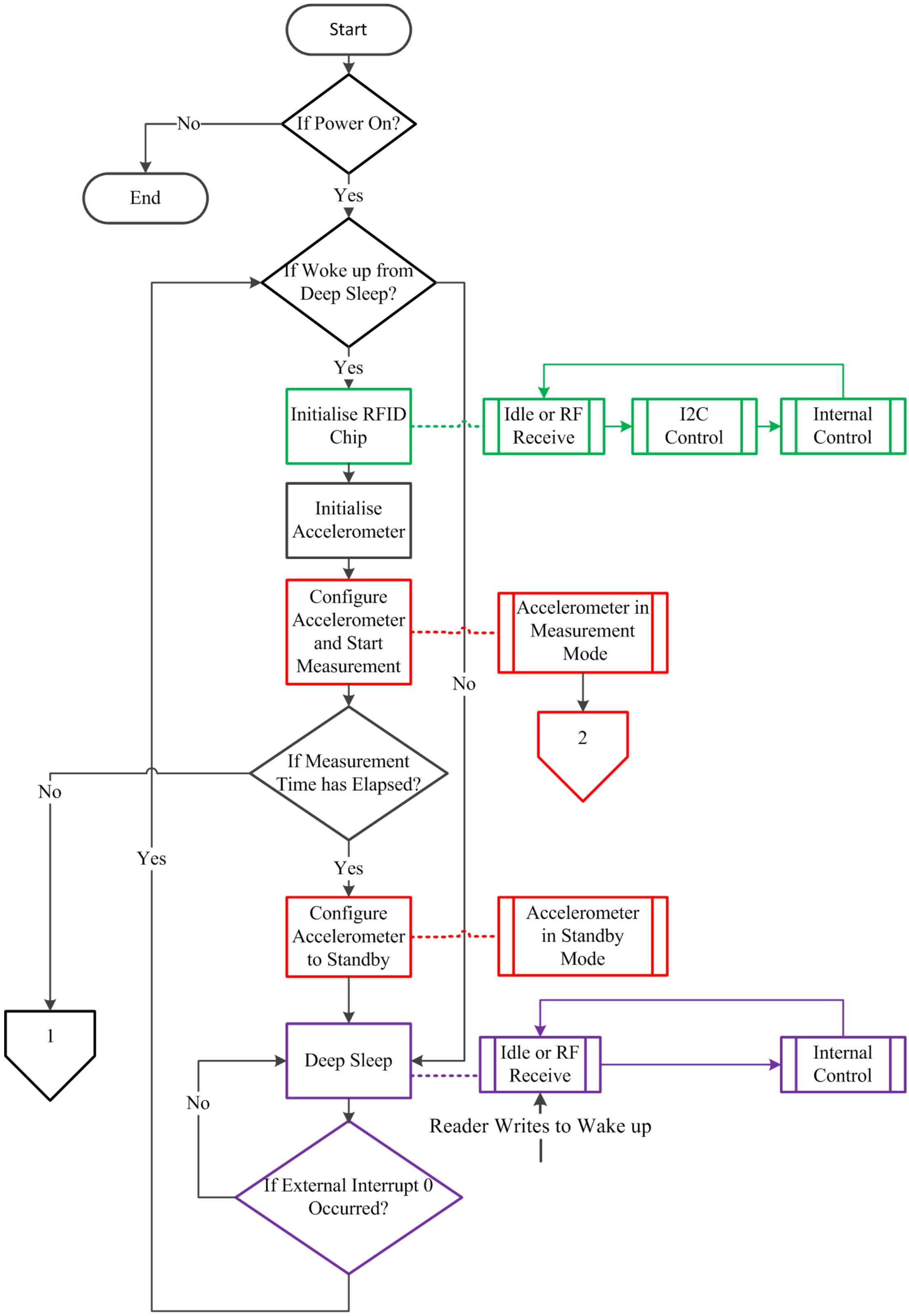

Figure 5.5: Flow diagram of the TAIAS firmware.

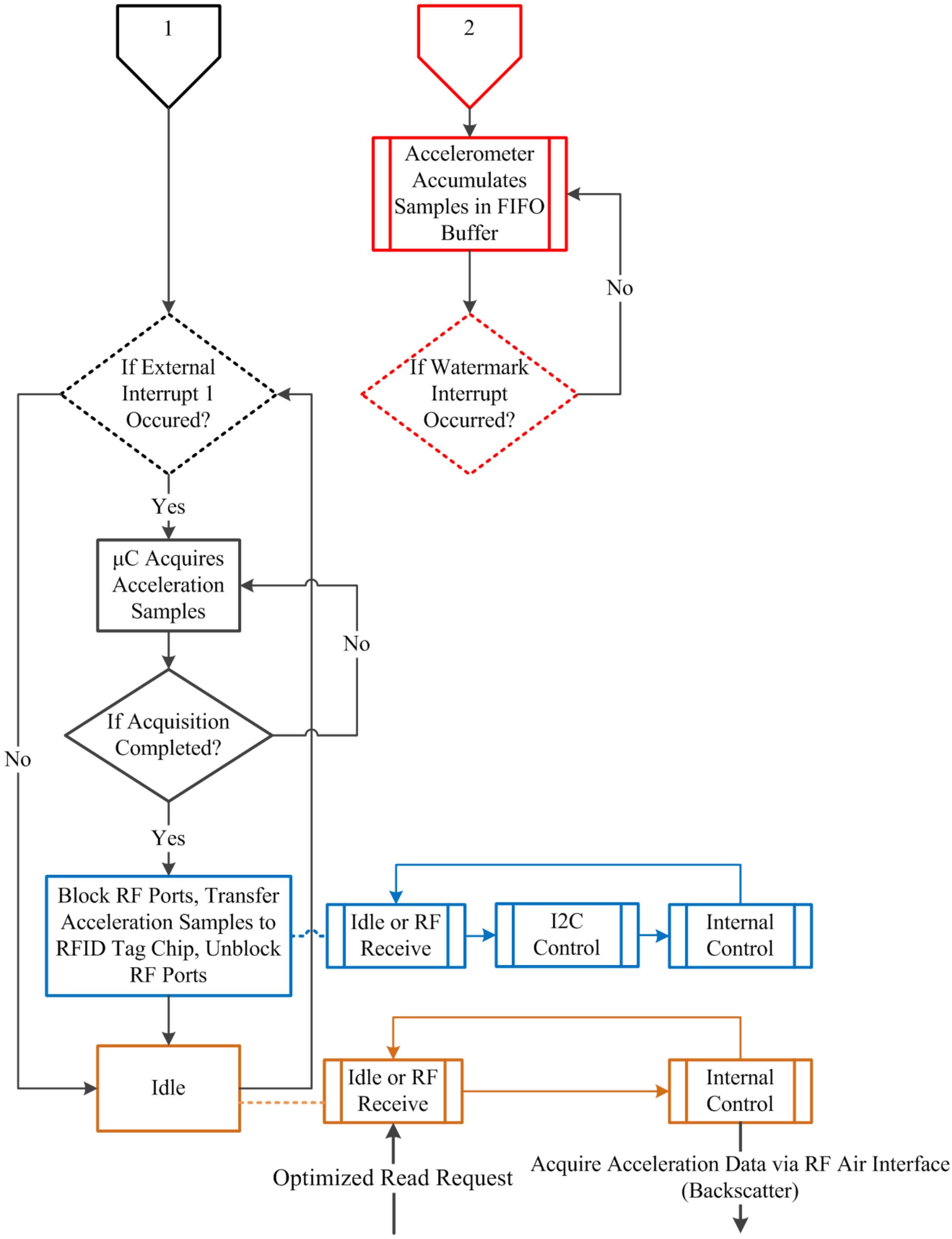

Figure 5.6: Continuation of the flow diagram of TAIAS firmware.

When referring to Figure 5.7 (in particular see the magnified view of Figure 5.7), transferred additional data can be seen within the I^2C transaction both prior to acceleration data and after. This was another enhancement to the firmware of TAIASs carried out to terminate any unwanted reader access via air interface while I^2C transactions happening between the RFID tag chip and the microcontroller. The operation state of *Internal Control* of the RFID tag chip has precedence over all other operating states as stated earlier in Chapter 3. Consequently, there is a possibility of RFID tag chip may ignore the initial portion of the I^2C transaction if backscattering is not finished at the end of t_{RF} window for the immediate previous acquisition cycle (tag chip is in *Internal Control* when backscattering). As a solution, a word which carries the configuration bits to block air interface (RF ports) of the tag chip (*RF1_DIS*) was send twice at the beginning of I^2C transaction prior to acceleration data. The word was sent twice as there is the possibility of ignoring the 1st word unless backscattering has been terminated. If a word is being ignored, the NVM write inside the tag chip will not happen and there will be no time consumption for it. Therefore a minor time gap was provided between the initial RF port configuration words and acceleration data to track any disregard of words in I^2C transaction by the tag chip. This was done only for the testing purpose and the gap can be removed from the final version of the firmware. Finally, at the end of sending acceleration data to tag chip, the air interface unblocked by reconfiguring *RF1_DIS* bits which allows the reader to access TAIASs via air interface. This procedure has introduced 3 more additional I^2C transactions between microcontroller and tag chip which include 3 number of *single word-NVM writes* which consume ~13.11 ms (3 × 4.37 ms) in the timing diagram.

5.2.3 Data Acquisition with Dual Target Search Mode

A client application was created using Octane SDK [163] for acceleration data acquisition of the system shown in Figure 5.1 which included two TAIASs. The "*Optimized tag read*" method was used in this application which provides the capability of acquiring up to 64 numbers of words from *USER* memory of the RFID tag chip in one acquisition cycle. The application is capable of recording acceleration samples to different text files depending on the EPC codes of TAIASs. Figure 5.7 shows the timing diagram for TAIASs acquiring 61 numbers of words from USER memory in which 60 of them were occupied by 3-axis acceleration samples with additional tracking word T_W.

EPC Class 1 Generation 2 protocol has a defined concept known as "*Sessions*" to specify the response frequency of tag antennas to reader interrogations and allow multiple readers to conduct interrogations upon a tag antenna population [168]. The protocol supports up to four *Sessions* in which tag antennas keep separate flag known as "*inventoried flag*" for each session. This flag stores the information of whether the tag antenna has been inventoried or not in a single interrogation cycle. Therefore the flag has two states normally denoted by "*A*" and "*B*". When an interrogation of a tag antenna (out of a given tag antenna population) has finished the reader will issue a command to the tag antenna to change the *inventoried flag* state from $A \rightarrow B$. Then the reader will interrogate another tag antenna in the population which will also change its state from $A \rightarrow B$. This practice will be continued until all of the tag antennas in the population turn their inventoried flag state from $A \rightarrow B$. The time interval of a tag antenna be in *B* state is known as "*persistence*" and it is defined according to the *Session* (e.g., for *Session 1*, *persistence* can be from 0.5 s to 5.0 s and for *Session 2* and *Session 3*, it can be 2.0 s minimum with no maximum limit specified) [168]. When the *persistence* is being elapsed the tag antenna changes the *inventoried flag* from $B \rightarrow A$ which will allow the reader to read it again. This guarantees that all the tag antennas inside the system read range are interrogated within an interrogation cycle. Furthermore, multiple readers operating with different *Session* setting can independently interrogate same tag antenna population. In the context of this chapter, the system comprises a single reader and two numbers of TAIASs.

The reader equipment used in the system offers three "*search*" modes which are user configurable with aforementioned *Sessions* [204]. Although the *sessions* are in effect under "*Single Target*" and "*Single Target with Suppression*" search modes and they are obsolete under "*Dual Target*" search mode [204]. In detail, under *Dual Target* search mode the *inventoried flag* of the tag antennas change from $B \rightarrow A$ immediately after changing $A \rightarrow B$ without any *persistence*. Furthermore, the reader is allowed to read the tag antennas even they are in B state since *Sessions* are ineffective. However, the reader follows the same pattern of reading all A state tag antennas initially and then B state tag antennas. The "*Dual Target*" search mode is implemented in acceleration data acquisition application as shown in Figure 5.7 (magnified view) since it guarantees reads from the two TAIASs within t_{RF}. Multiple acquisitions of same data occur as the acquisition time from single TAIAS $\ll$ t_{RF}. Numbers of multiple acquisitions depend upon the time consumed to complete an "*Optimized tag read*" upon a TAIAS. These multiple acquisitions were filtered out using the tracking word T_W as done in Chapter 3. However, the implementation of "*Single Target*" search mode with "*Session 1*" is a possibility to lower the multiple acquisitions. This could have been implemented by varying i to adjust t_{RF} in a way that t_{RF} < *persistence*, which would provide only one acquisition from a TAIAS given that inventoried flag changes from $B \rightarrow A$ before next acquisition window of t_{RF} arrives. However this implementation is tedious due to unknown *persistence* of RFID tag chip and necessary synchronisation with t_{RF} window to avoid the possibility of data acquisition losses (if $B \rightarrow A$ change does not happen before the immediate next t_{RF} window, possibility of data loss is there at some stage of measurement duration).

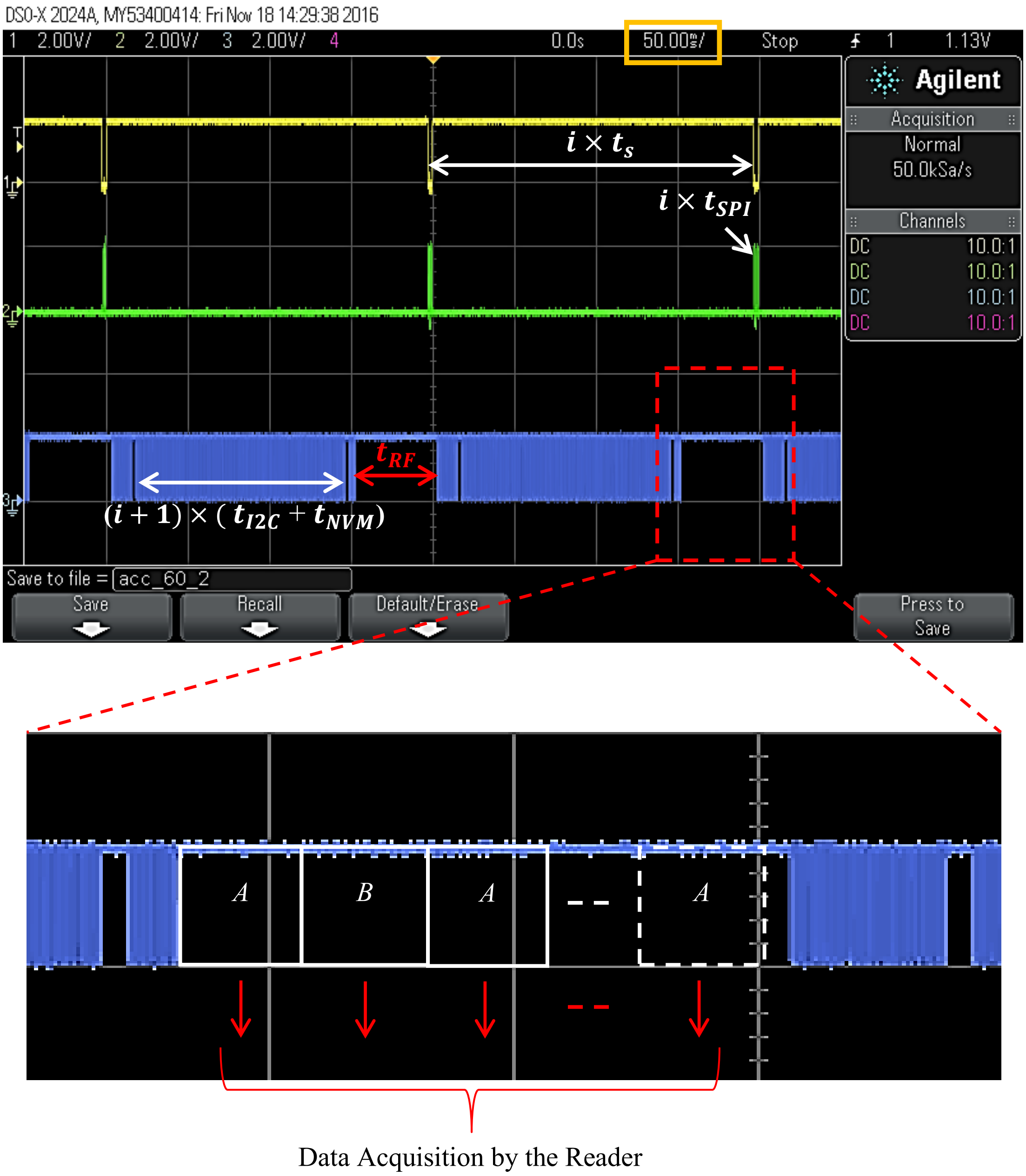

Figure 5.7: Timing diagram of *Watermark interrupt* (yellow), *SPI* receive (green) and I^2C write (blue) of a TAIAS with *two word-NVM writes* for $i = 60$ (t_{I2C} and t_{NVM} for $i + 1$ due to additional T_W and t_f not visible) and illustration of *inventoried flag* state change in *Dual Target* search mode (the 3-axis acceleration data of TAIAS will be acquired at every A and B).

5.3 Dynamic Acceleration Measurement of a Steel I-beam

The RFID-based wireless acceleration measurement system was applied to measure the dynamic acceleration of a full-scale steel I-beam (100UC14.8) as shown in Figure 5.1(a). The 4-m length I-beam was simply supported at the two ends with 15-cm overhang. Two TAIASs were mounted on the I-beam as shown in Figure 5.1(b) and Figure 5.1(c). The I-beam orientation 2 with respect to reader antenna (see Chapter 7) was used in the measurement setup. The reader antenna was kept 2.0 m away from the I-beam at the line-of-sight of the center point between TAIAS placements to have approximately equal interrogation signal power delivery. The same impact hammer system used in Chapter 3 was used to excite the I-beam at chosen random location shown in Figure 5.1(c).

Figure 5.8(a) and Figure 5.8(b) show the time history of 3-axis acceleration measurement and the amplitude spectra, respectively, from $TAIAS_1$. Figure 5.9 shows the same detail from $TAIAS_2$ for the same impact on I-beam. According to Figure 5.8(b) and Figure 5.9(b) both TAIASs show a prominent peak at ~23.56 Hz. This value agrees well with the 1st mode theoretical natural frequency of 23.30 Hz calculated using Equation 2.1. There are no indications of the natural frequency in the amplitude spectra from X and Y axes measurements. This is majorly due to the direction of impact applied which influenced the I-beam to vibrate exclusively on the Z-axis. The time history also proves this fact in which Z-axis acceleration is considerably larger than acceleration on other two axes. Figure 5.10 provides a comparison of the amplitude spectra from the RFID-based wireless system and a commercial LORD Microstrain G-Link® -LXRS® 2g wireless accelerometer system [77] for the same impact as an additional proof (comparison with commercial systems will be discussed in detail in Section 5.3.2). Furthermore, the acceleration signal acquired by $TAIAS_2$ has higher noise than the acceleration signal from $TAIAS_1$ which can be visualized when comparing both time history and the amplitude spectra of TAIASs. Figure 5.10(b) and Figure 5.10(d) also indicate this in which the amplitude spectra of $CWLA_2$ have higher distortion than that of $CWLA_1$ (in particular the spectrum of Z-axis measurements). This demonstrates the decay of vibration along the I-beam (from the position of impact) where acceleration signal to noise ratio (SNR) is intuitively higher at the nearest position (i.e., at the position of $TAIAS_1$ and $CWLA_1$) to the impact location.

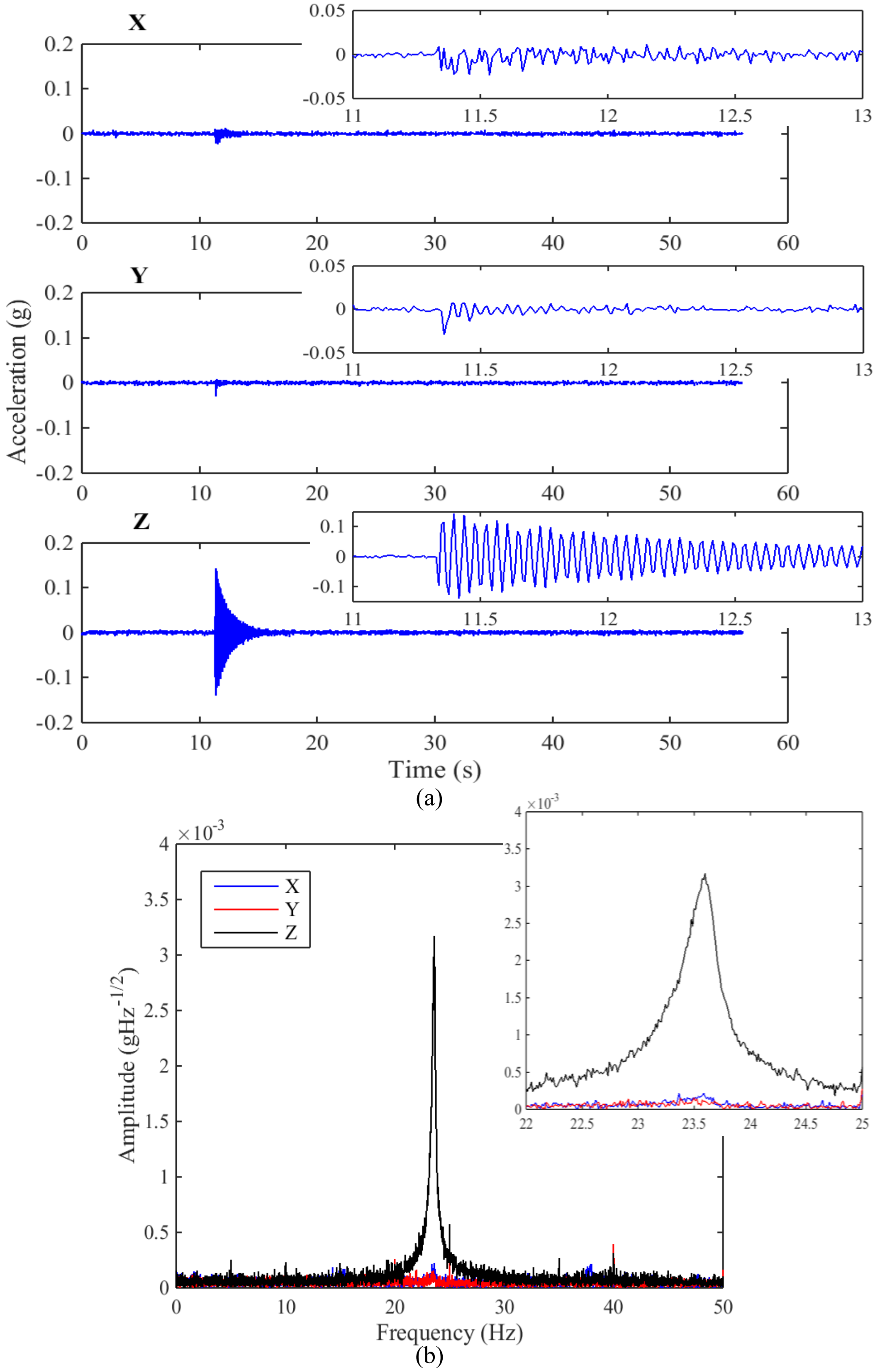

Figure 5.8: 3-axis dynamic acceleration measurement from $TAIAS_1$: (a) time history and (b) the single-sided amplitude spectra.

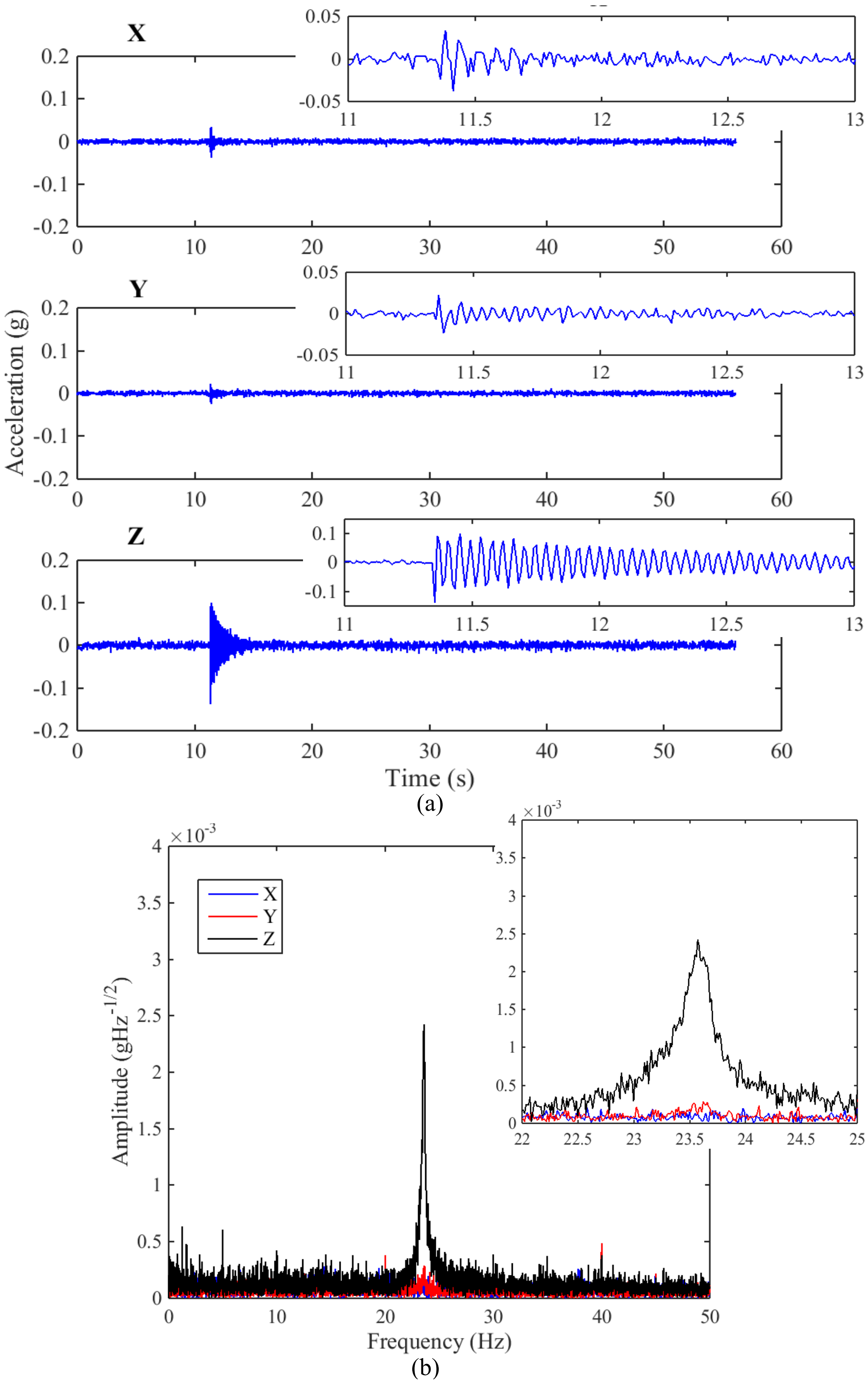

Figure 5.9: 3-axis dynamic acceleration measurement from $TAIAS_2$: (a) time history and (b) the single-sided amplitude spectra.

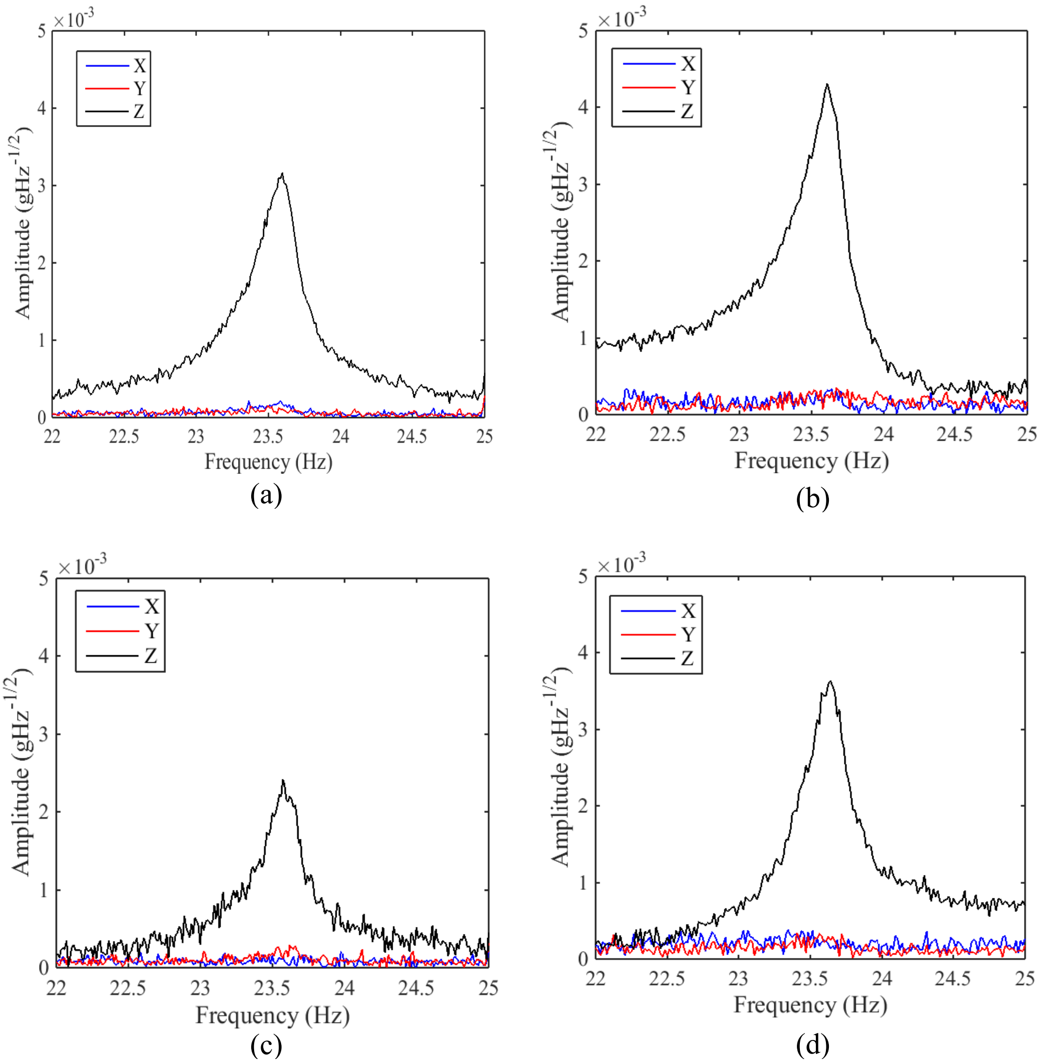

Figure 5.10: Single-sided amplitude spectra for 3-axis acceleration: (a) $TAIAS_1$ collocated with (b) $CWLA_1$ and (c) $TAIAS_2$ collocated with (d) $CWLA_2$.

5.3.1 Distortion Introduced by Acceleration Sensor Circuits and Its Removal in Data Analysis

5.3.1.1 Identification of Distortion

Figure 5.11 shows the amplitude spectra of Z-axis acceleration of the I-beam from $TAIAS_1$ for different measurement durations (Z-axis is considered as it provides the information of the natural frequency of the I-beam for the experimented case and the measurement results from either TAIAS can be used for this description). These are for 60 numbers of acceleration samples acquisitions within a single acquisition cycle (i = 60) which relates to the timing diagram shown in Figure 5.7. When the amplitude spectra of these results are considered, there are noticeable peaks other than the prominent peak (at the natural frequency) appearing with almost equal spacing ~5 Hz. According to Figure 5.11(d) they become more prominent when $\frac{t_a}{t_m}$ becomes low (t_a - time duration of acceleration signal, t_m - time duration of measurement and $(t_m - t_a)$ - time duration of the default output). Therefore, it can be concluded that this distortion in the amplitude spectrum appear mostly due to the composition of the default signal portion (the portion which does not contain the acceleration signal) of the TAIAS measurement. The energy from the default signal portion will be prominent when $\frac{t_a}{t_m}$ is low (i.e. low SNR) and increase the distortion of the amplitude spectrum. In the process of identifying the cause of the distortion, the number of acceleration samples acquired in an acquisition cycle was increased to 120 (i = 120) in the firmware. The related timing diagram is shown in Figure 5.12. Two t_{RF} windows were created inside a single acquisition cycle since "*Optimized tag read*" method used in reader application is only capable of reading maximum of 64 words as stated earlier. The acceleration samples that can be acquired within one acquisition cycle can be increased following the same procedure. However, it will be constrained by the FIFO buffer of the accelerometer or the data memory of the microcontroller; whichever the lesser capacity. The time histories and relevant amplitude spectra of Z-axis acceleration measurement for different durations in this firmware setting is shown in Figure 5.13. Now the distortion appears with an equal spacing of ~2.5 Hz. It has become prominent when $\frac{t_a}{t_m}$ is low when comparing Figure 5.13(b) and Figure 5.13(d) as observed earlier. The spectrum of the distortion is similar to the frequency spectrum of an asymmetrically distorted sine wave (which has both odd and even harmonics) [205]. According to above observations, it has a fundamental frequency of $\frac{1}{i \times t_s}$ Hz. Most of the harmonics of the distortion which falls into 50-Hz spectral bandwidth can be visible in Figures 5.11(d) and Figure 5.13(d).

The data acquisition technique of developed RFID-based wireless dynamic acceleration measurement system was discussed in detail in Section 5.2.2 of this chapter and previously in Section 3.5.2 of Chapter 3. According to it, the microcontroller acquires acceleration data from the accelerometer upon the *Watermark interrupt* which always has the frequency of $\frac{1}{i \times t_s}$ Hz. The *Watermark interrupt* has an asymmetric square wave form (see Figure 5.12) which can also be viewed as an asymmetrically distorted sine wave. Therefore the distortion is an influence of *Watermark interrupt* signal upon the connection of master in slave out (MISO) to slave data in (SDI) (see Figure 5.2(a)) which carries acceleration data. However the peak related to the natural frequency of the I-beam can be easily distinguished since it has larger area under it (see Figure 5.11 and Figure 5.13). This area will be reduced for minor vibrations making the distinguishing a difficult task. Therefore removal of the introduced distortion is important.

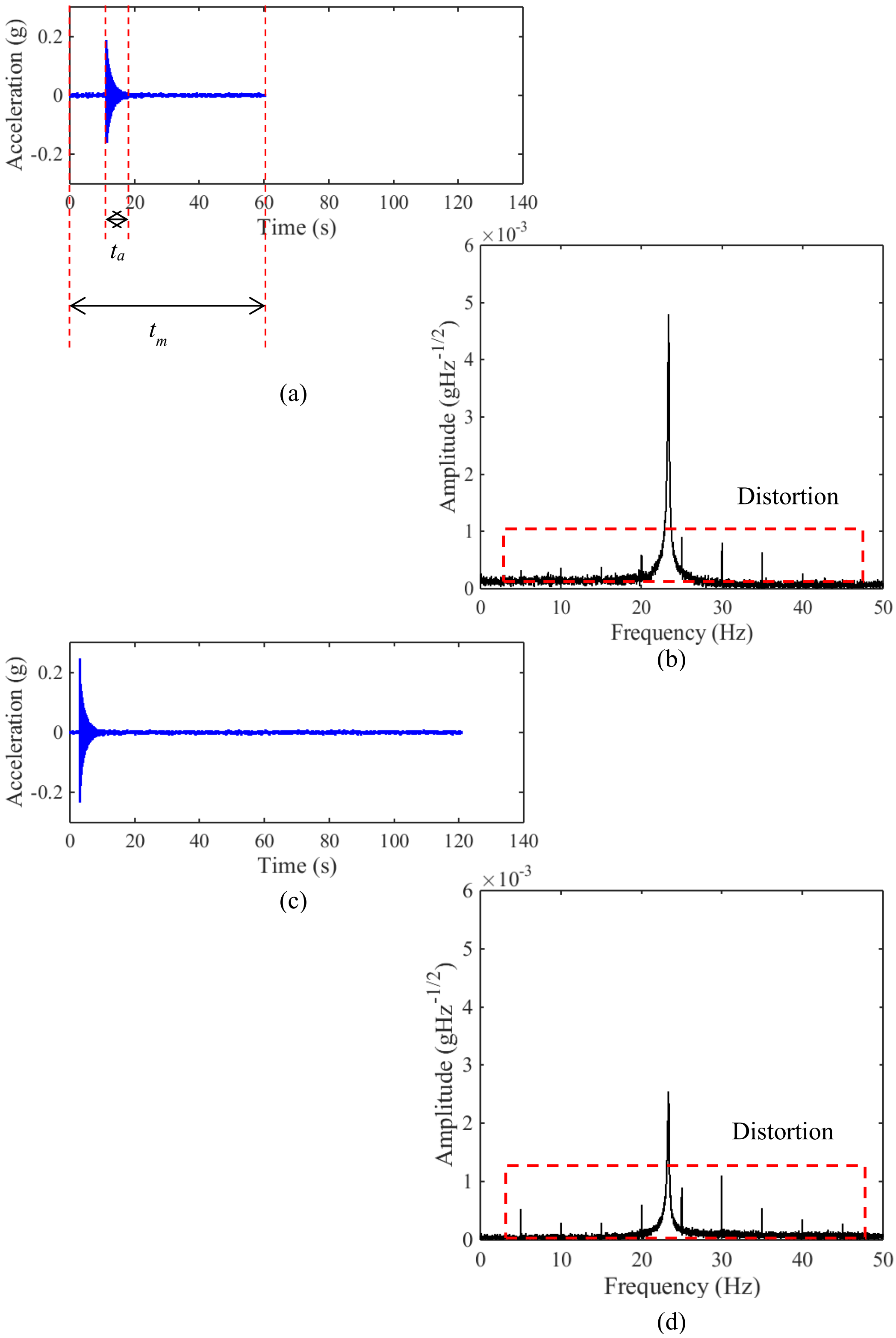

Figure 5.11: Z- axis acceleration for different measurement durations with 60 numbers of acceleration samples acquisition in single acquisition cycle: (a) 60-s measurement time history, (b) relevant single-sided amplitude spectrum, (c) 120-s measurement time history and (d) relevant single-sided amplitude spectrum.

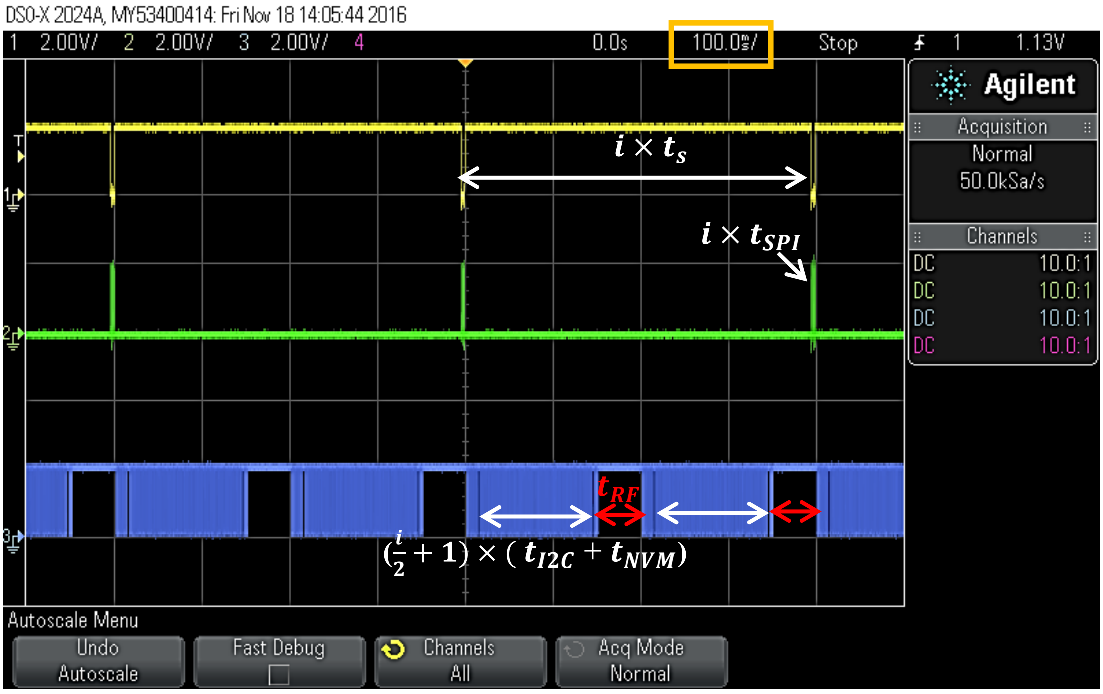

Figure 5.12: Timing diagram of *Watermark interrupt* (yellow), *SPI* receive (green) and I^2C write (blue) of TAIAS$_1$ with *two word-NVM writes* for i = 120 (t_{I2C} and t_{NVM} are for $\frac{i}{2} + 1$ due to additional T_W, and t_f not visible).

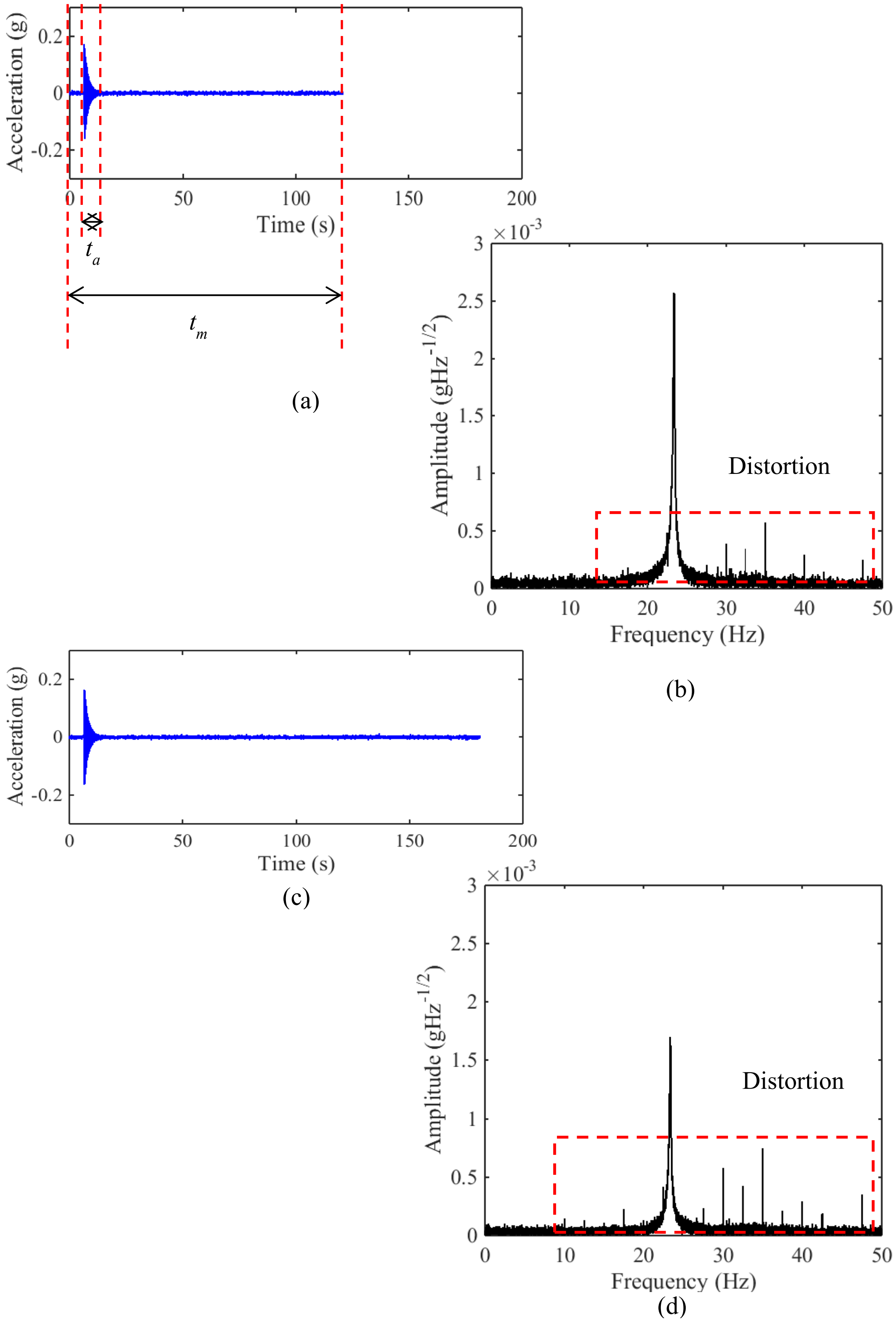

Figure 5.13: Z- axis acceleration for different measurement durations with 120 numbers of acceleration samples acquisition in single acquisition cycle: (a) 120-s measurement time history, (b) relevant single-sided amplitude spectrum, (c) 180-s measurement time history and (d) relevant single-sided amplitude spectrum.

5.3.1.2 Distortion Removal and Peak Smoothing in Data Analysis

In this section, the solutions which can be implemented at acceleration data analysis were considered. First, a data set can be selected by neglecting considerable portion of t_m by observing the time history which provides a higher $\frac{t_a}{t_{sel}}$ (t_{sel} - time duration of selected data set, $t_a \in t_{sel} < t_m$). According to the observations in the above analysis, this would suppress the distortion due to increased SNR as shown in Figure 5.14. It shows the amplitude spectrum for selected data set with $\frac{t_a}{t_{sel}} = 0.71$ for measurement shown in Figure 5.13 (c) (the initial $\frac{t_a}{t_m} = 0.035$ for the total measurement duration). However, this is not a straight forward solution since a data set has to be selected out of original measurement by observing the time history prior calculating the amplitude spectra. Furthermore, it reduces the frequency resolution of the amplitude spectrum due to consideration of low number of data points.

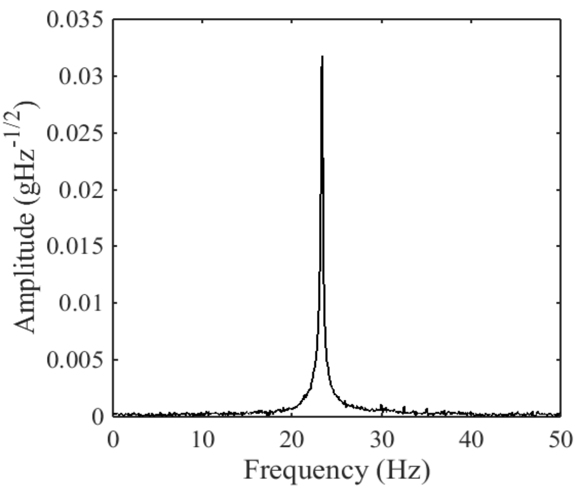

Figure 5.14: Single-sided amplitude spectra with removed unwanted peaks by data selection considering the acceleration signal.

Since the introduced distortion by the data acquisition technique lies within default output of TAIASs (which also consists of default noise), a denoising method can be applied to acquired acceleration data to remove it. This denoising method should be capable of suppressing the distortion consisted of low-frequency components spread throughout the amplitude spectrum of interest. The widespread nature of the distortion and the definite shed of the spectrum of interest make application of filter-based methods not suitable for this purpose. Therefore, wavelet denoising method was examined upon measured acceleration data to remove the distortion in question. The significance of wavelet denoising has been detailed in [206] for extraction of weak original signals out of distorted and noisy measurements. This method has been applied in [57] to remove the low-frequency distortion in a shock signal of a missile launch. Vibration signals acquired from an air compressor sensor were denoised using wavelet decomposition in [207] for monitoring of faults related to various parts of the compressor. It has been implemented for denoising of partial discharge signals of high voltage equipment in [208, 209]. Even though these partial discharge signals are high-frequency signals, their wave pattern with exponential decay is similar to the acceleration signals analyzed here. Therefore, appropriate wavelets to denoise acceleration signals can be chosen as discussed in [210].

Wavelet denoising involving Symlet and Daubechies wavelets has been carried out upon acceleration data acquired from the RFID-based wireless system. The Wavelet toolbox [211] provided in MATLAB computational tool was used in this process of denoising. Figure 5.15 and Figure 5.16 show the time history of denoised acceleration measurements from $TAIAS_1$ (previously shown in Figure 5.13(c)) and $TAIAS_2$, respectively. The amplitude spectra for aforementioned, are shown in Figure 5.17. The same parameters given in Table 5.2 were used for denoising with both Symlet2 (i.e. sym2, 2 denotes the order of the wavelet) and Daubechies2 (i.e. db2) wavelets (this selection is justified in Section 5.3.2). The maximum decomposition level for selected wavelets can go up to 11 depending on the data points of the measurement [211]. However, it has been set to 7 by conducting several trials which would reduce time consumption of the denoising method than using maximum level [208]. When considering enlarged views of Figure 5.15 and Figure 5.16, it can be seen that the denoised measurement has the same waveform of the original acceleration signal in the measurement for both wavelet and thresholding types. However, it can be seen that soft thresholding provides higher smoothing for both wavelet types when considering the denoised default signal output. The amplitude spectra are cleared with introduced distortion (see Figure 5.17). The noise floor has been reduced nearly an equal amount and there are no identifiable differences between using sym2 or db2. However, the difference of smoothing observed in time history can be highlighted in the peak of the amplitude spectra in which soft thresholding has provided higher smoothing than hard thresholding for both wavelets. Consequently, soft thresholding would provide unambiguous natural frequency determination (peak detection). The wavelet denoising method provides an advantage of removing distortion without selecting any dataset from original acceleration measurement.

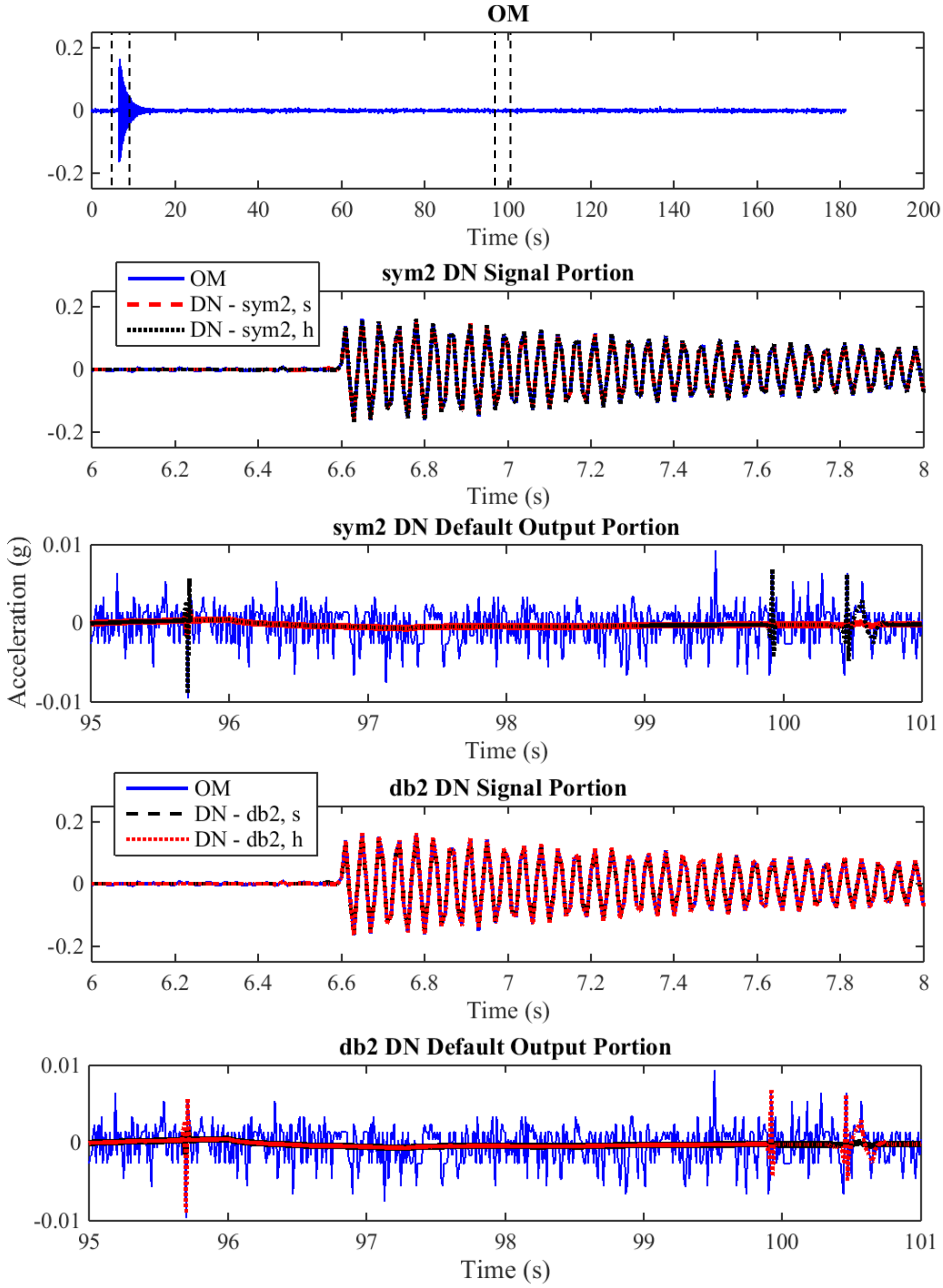

Figure 5.15: Wavelet denoised acceleration measurement time history of $TAIAS_1$ (OM - original measurement, DN - denoised, s – soft thresholding and h – hard thresholding).

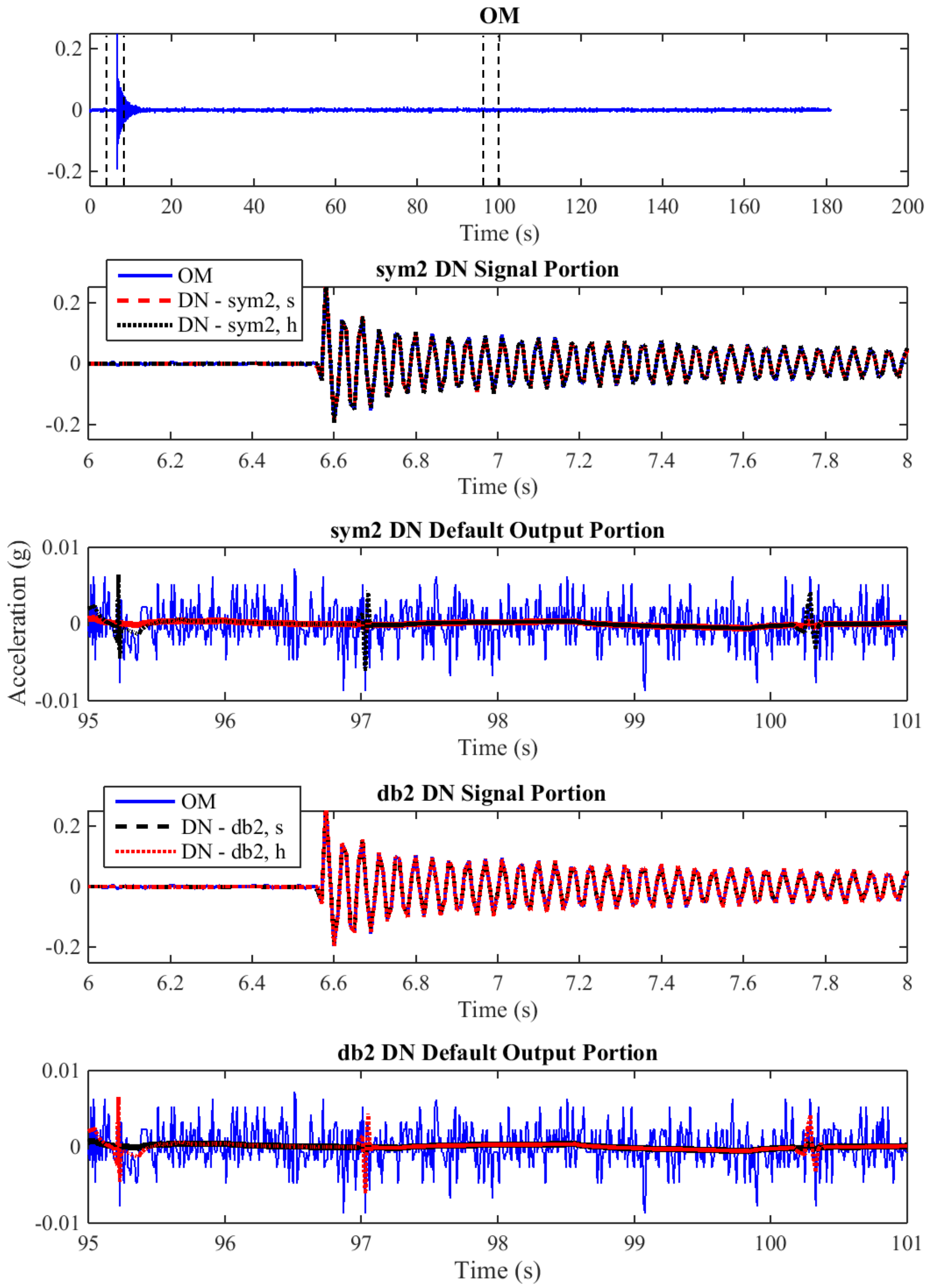

Figure 5.16: Wavelet denoised acceleration measurement time history of $TAIAS_2$ (OM - original measurement, DN - denoised, s – soft thresholding and h – hard thresholding).

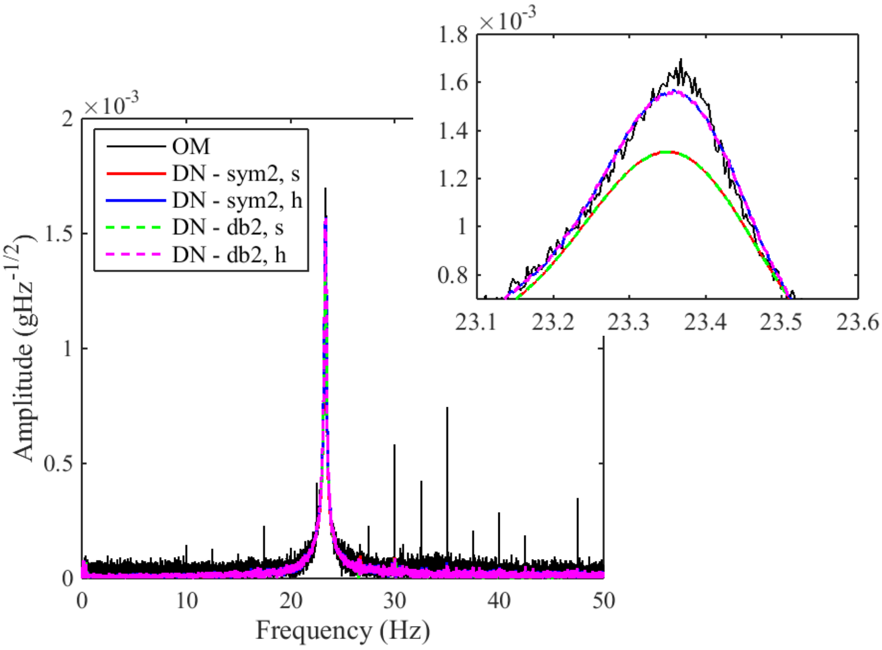

(a)

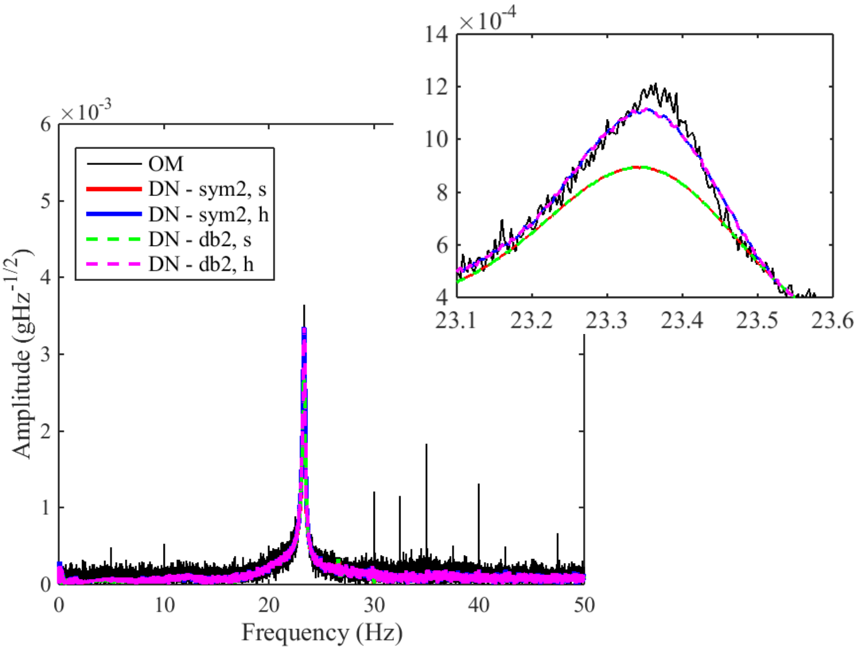

(b)

Figure 5.17: Single-sided amplitude spectra of wavelet denoised acceleration measurements: (a) $TAIAS_1$ and (b) $TAIAS_2$ (OM – original measurement, DN – denoised, s – soft thresholding and h – hard thresholding).

Table 5.2: Parameters used in implemented wavelet denoising.

Parameter	Selection
Threshold selection rule	Minimax*
Thresholding	soft (s)**
Multiplicative threshold rescaling	Level-dependent estimation of noise (mln)**
Level	7**
Wavelet	Symlet2 (sym2) / Daubechies2 (db2)* **

*selected according to [210].
**Examined upon measured acceleration data of I-beam.

5.3.2 Comparison of Measurement Results

The dynamic acceleration measurement results obtained with the RFID-based wireless system were compared with measurement results from both commercial wired and wireless acceleration measurement systems. The commercial sensors were collocated with TAIASs as shown in Figure 5.1. The commercial wireless system comprised of LORD Microstrain G-Link® -LXRS® 2g wireless accelerometers and LORD Microstrain WSDA® -Base-104 -LXRS® base station [78] while PCB PIEZOTRONICS 352C34 single axis wired accelerometers [166] with National Instruments' NI USB-6251 multifunction DAQ module [167] comprised the commercial wired system. In this comparison, the results were analyzed mainly to determine the accuracy of the natural frequency detection and the acceleration sensitivity of the RFID-based wireless system. The measurement results from each system were smoothed by wavelet denoising prior to the comparison; since it provides unambiguous prominent peak detection as seen in Figure 5.17 (the measurement results from other systems also provided distorted peaks in the amplitude spectrum as seen in Figure 5.10(d)).

5.3.2.1 Analysis of the Natural Frequency Determination

In this examination, the calculated amplitude spectra of denoised dynamic acceleration measurements of the steel I-beam from the different systems were primarily compared considering the determination of the natural frequency. According to [179] the ODR which determines the achievable spectral bandwidth from RFID-based wireless system depends upon the frequency of the clock out of which accelerometer operates on. The accelerometer is capable of operating with internal 51.2-kHz clock or an external clock (f_{ec} $\in$ [25.6 kHz, 51.2 kHz]) connected to *INT2* pin which would set the actual output data rate (ODR_{Actual}) according to following equation [179]:

$$ODR_{Actual} = ODR_{Selected} \times \frac{f_{ec}}{51.2\ kHz} \tag{5.1}$$

First, the comparison of the natural frequency determination was done for the simultaneous acceleration measurements acquired from the RFID-based wireless system and commercial wireless system. Two sets of measurements were conducted with TAIASs operating with internal and external 51.2-kHz clocks with selected output data rate ($ODR_{Selected}$) of 100 Hz. The external clock to the accelerometer was provided by PWM (50 %) output of the microcontroller as indicated in Figure 5.2(a). Each measurement set consisted of 20 trials for random impacts applied upon the I-beam. Figure 5.18 shows the natural frequency determination of the measurements from those trials for TAIASs and CWLAs (sampling frequency of CWLA system was set to be 128 Hz which was the closest setting possible to 100-Hz ODR_{Actual} of TAIASs). Both Symlet and Daubechies wavelets provided same amount of smoothing as seen in Figure 5.17. Therefore, the natural frequency determination from denoised acceleration measurements using sym2 wavelet is presented in Figure 5.18. According to Figure 5.18(a) and Figure 5.18(b), the natural frequency detection of both systems shows variations within a range of $2 \times$ frequency resolutions of the spectra (0.0488 Hz for TAIASs and 0.0626 Hz for CWLAs, denoted by dashed lines). The mode value can be given as the natural frequency of the I-beam acquired by each system. Table 5.3 provides this information relevant to Figure 5.18(a) and Figure 5.18(b).

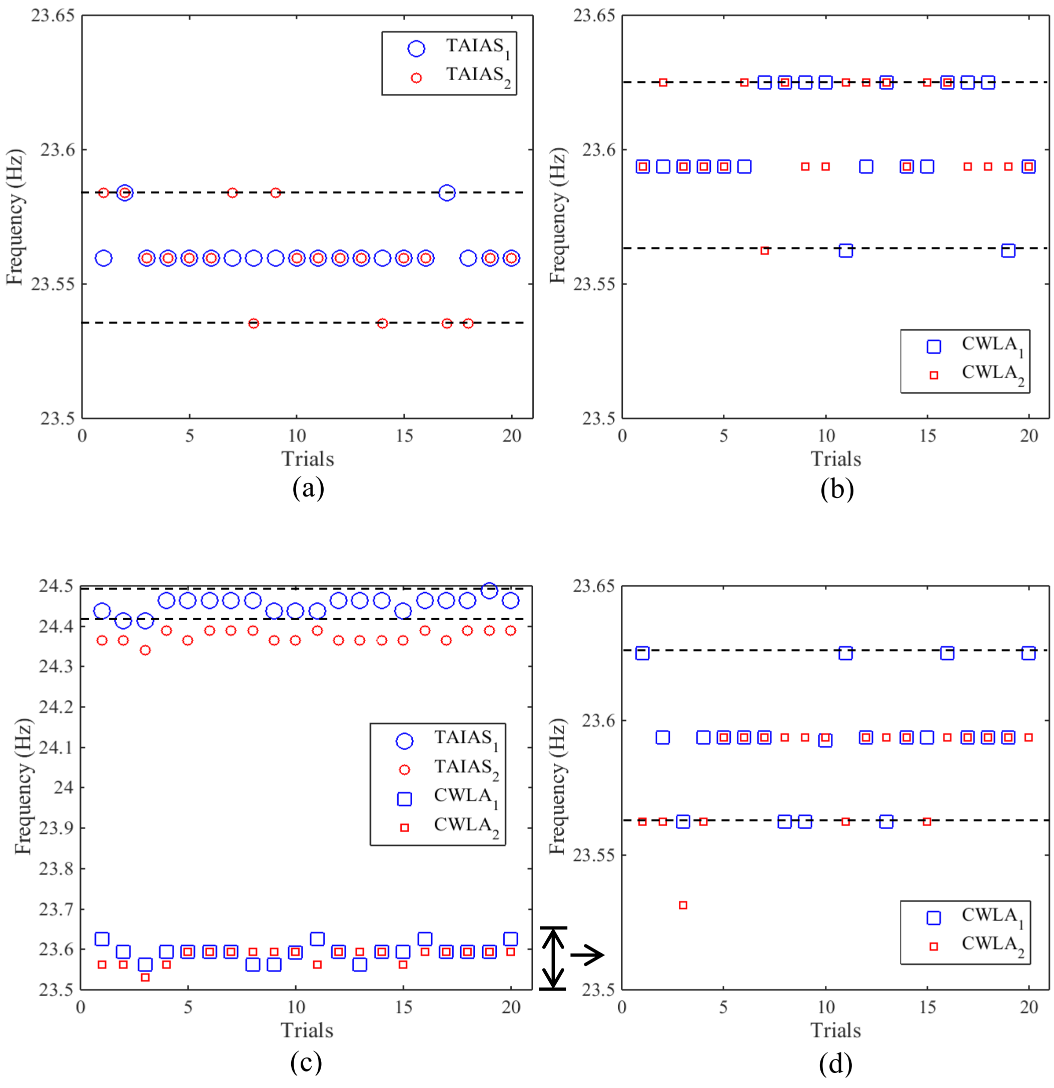

Figure 5.18: Natural frequency determination from amplitude spectra of denoised simultaneous acceleration measurements by: (a) TAIASs with an external accelerometer clock, (b) CWLAs (relevant to (a)), (c) TAIASs with an internal accelerometer clock and CWLAs and (d) CWLAs (relevant to (c)).

Table 5.3: Natural frequency determination from the RFID and commercial wireless systems.

Frequency Determination	$TAIAS_1$*		$CWLA_1$**	$TAIAS_2$*		$CWLA_2$**
	External	Internal		External	Internal	
Mode (Hz)	23.56	24.46	23.59	23.56	24.37	23.59
Difference (Hz)***	−0.03	+0.87		−0.03	+0.78	

*at a frequency resolution of 0.0244 Hz.
**at a frequency resolution of 0.0313 Hz (different from above due to 128-Hz sampling rate).
***benchmarking against the natural frequency determination from CWLA system.

According to Table 5.3, both TAIASs and CWLAs have determined similar natural frequency values (considering the mode values). However, the determined natural frequency values for TAIASs operated with the internal accelerometer clock are different from each other (see Figure 5.18 (c)). In fact, there was 0.0976 Hz difference between the natural frequency values (considering the mode values) determined from each TAIAS. This is due to internal clock frequency differences between the accelerometers used in each TAIASs even though they are identical components from the same manufacturer. According to Figure 5.18(a) and Figure 5.18(b), providing an external operating clock to accelerometers of TAIASs has improved the accuracy of the natural frequency determination. The difference between the natural frequency determination of CWLAs and TAIASs (with the external clock) −0.03 Hz can be given as the RFID-based wireless measurement system error of the natural frequency determination (benchmarking against CWLA system, this value has an influence of the higher sample rate of CWLA than TAIAS). However, this error is higher when the TAIASs operated with internal accelerometer clock as given in Table 5.3. This happens due to different offsets of the accelerometer internal clock frequency from 51.2 kHz of TAIASs at a given instance.

Figure 5.19 shows the natural frequency determination of denoised simultaneous measurements from TAIASs (with the external clock) and CWAs (100-Hz sampling rate). In the process of denoising, three scenarios given in Table 5.4 were performed on the measurements of both systems predominantly to achieve adequate peak smoothing of the amplitude spectra from CWAs. They had low SNR due to higher noise content than the original acceleration measurement of TAIASs as shown in Figure 5.20. The natural frequency determination with 0.0244-Hz frequency resolution and wavelet decomposition level 7 of TAIASs in Figure 5.19(a) and Figure 5.19(b), is given as extension for the previous analysis with CWLAs with same conditions. According to Table 5.4, the maximum variation of the natural frequency determination is within almost the same range for TAIASs for different scenarios (denoted by dashed lines for Scenario 1). This shows that increase of wavelet decomposition level has no additional advantage in smoothing the acceleration signal. The maximum variation range of the natural frequency values for TAIASs is lower than that for the CWAs. This is majorly due to the low SNR of acquired acceleration signals from CWAs at 100-Hz sampling rate upon I-beam. When considering Figure 5.19(a) and Figure 5.19(b), the majority of the determined natural frequency values for any scenario are concentrated around ~23.35 Hz. However the mode value of 23.34 Hz for scenario 1 is considered as the natural frequency of the I-beam for the comparison purpose in Table 5.5 as it provides low variation in consecutive trials for CWAs than other scenarios (this is a result of low frequency resolution of the amplitude spectrum and increased SNR due to consideration of less number of data points, see Figure 5.19(c) and Figure 5.19(d)). The determined natural frequency value is different from what was acquired for the previous comparison with CWLA system (i.e. 23.56 Hz). This change is predominantly a shift in the amplitude spectrum due to slight variations of boundary conditions of I-beam arrangement caused by removing of hard bonded mounts for CWLAs prior installing mounts for CWAs.

Table 5.4: Scenarios of denoising and maximum range of variation of the determined natural frequency values.

	Level*	Data points	Resolution** (Hz)	Max. Range of Variation (Hz)	
				TAIASs***	CWAs
Scenario 1	7	4096	0.0244	0.0976	0.1465
Scenario 2	7	16384	0.0061	0.0916	0.2014
Scenario 3	11	16384	0.0061	0.0916	0.2014

* wavelet decomposition level in denoising (11 is maximum when considering the number of data points and sym2 wavelet [211]).
** frequency resolution of the single-sided amplitude spectrum.
*** even though maximum range variation is provided, the majority of trials (18/20) determined the natural frequency values within 0.0488-Hz range for TAIASs (2 × resolution of scenario 1 and 8 × resolution of scenario 2 and 3).

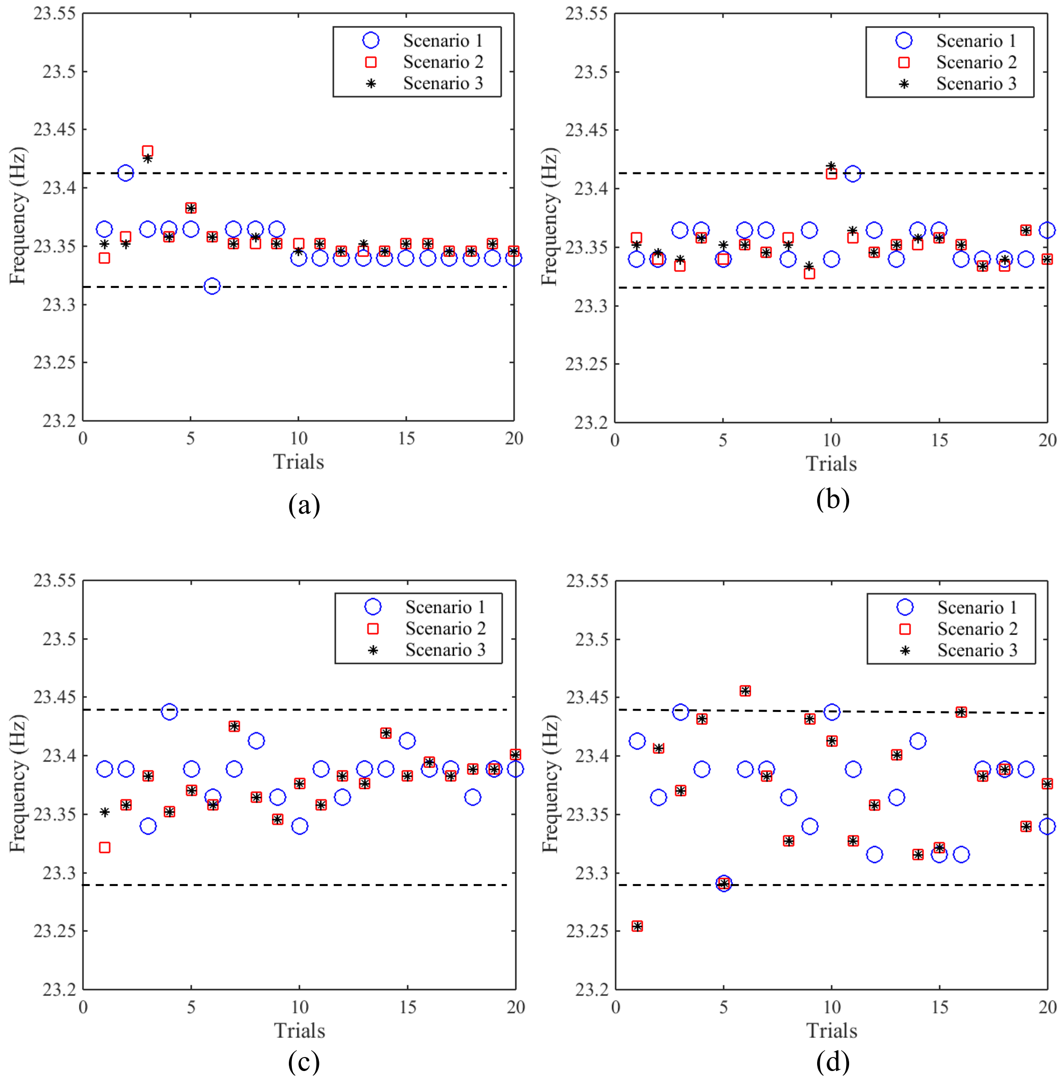

Figure 5.19: Natural frequency determination from amplitude spectra of denoised acceleration measurements by Sym2 wavelet: (a) $TAIAS_1$, (b) $TAIAS_2$ (accelerometers of TAIASs operated with the external clock), (c) CWA_1 and (d) CWA_2

Table 5.5: Natural frequency determination from the RFID and commercial wired systems.

Frequency Determination	**$TAIAS_1$**	**CWA_1**	**$TAIAS_2$**	**CWA_2**
Mode (Hz)	23.34	23.39	23.34	23.39
Difference (Hz)	−0.05		−0.05	

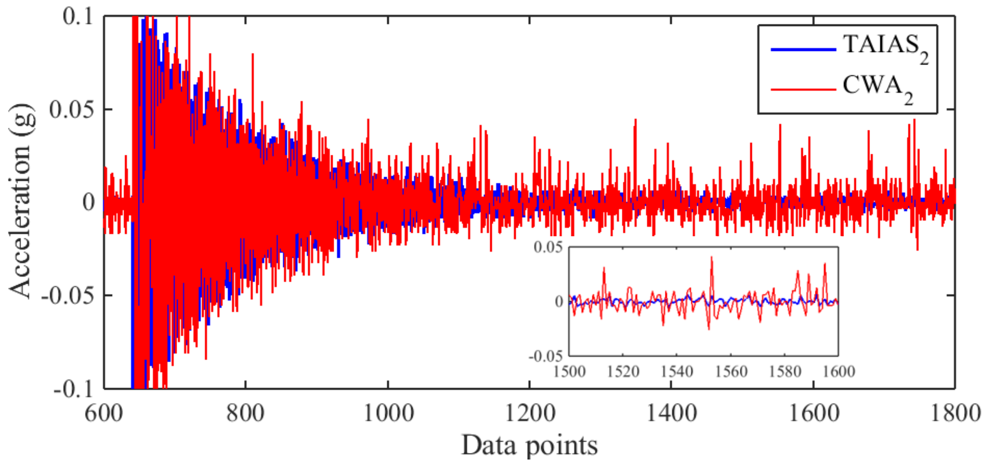

Figure 5.20: Example of simultaneous Z-axis acceleration measurement of I-beam from $TAIAS_2$ and CWA_2 corresponds to trial 1 (presented against data points for the overlapping purpose as there is a timing difference between the two systems).

The maximum range of variation of the natural frequency determination shown by TAIASs previously with internal acceleration clock was within a 0.0732-Hz range (3 × frequency resolutions, see Figure 5.18(c)). Therefore, when considering Table 5.3 and Table 5.4, the provision of the external clock had only increased the natural frequency determination accuracy but not the precision of TAIASs. The PWM signal (i.e. the external clock) provided by the microcontroller was derived from the operating clock of the microcontroller. This operating clock was given by the 4-MHz crystal oscillator (see Figure 5.2(c)) which had ±20 parts per million (ppm) precision. An introduction of a crystal oscillator with higher precision than this would have increased the precision of the natural frequency determination and lowered the range of the determined natural frequency variation.

5.3.2.2 Analysis of Acceleration Sensitivity

The acceleration sensitivity of the RFID-based wireless measurement system can be benchmarked with CWLA and CWA systems by comparing the amplitude of the amplitude spectra for simultaneous measurements with each system. Theoretically, the amplitude of single-sided amplitude spectrum of a signal should provide the magnitudes of all the components comprised by the signal. However, low SNR has a negative influence upon the amplitude of a spectrum. Therefore, the amplitude spectra of denoised acceleration signals would provide a proportionally accurate amplitude of signal components (denoised signals has good correlation with the acceleration signal with reduced noise in the default output portion, see Figure 5.15 and Figure 5.16). Even though, the three considered systems had different values of SNR in their measurements (c.f. Figure 5.20 and Figure 5.21), the amplitude of the spectra under the same amount of denoising can be compared.

Figure 5.22 provides the comparison of the amplitude of the determined natural frequency in the amplitude spectra in simultaneous measurements of acceleration of the I-beam by each commercial system and the RFID-based wireless system. The measurements from $TAIAS_2$ with relevant collocated commercial accelerometers were considered as they provide critical comparison being mounted on the position of lowest acceleration SNR of the I-beam (due to higher distance from impact position). The amplitudes of the single-sided spectra of acceleration signals by $TAIAS_2$ for each trial are always lower than that of $CWLA_2$ and higher than that of CWA_2 as seen in Figure 5.22. According to Figure 5.22(a) the acceleration sensitivity of the RFID-based wireless system is 61.3 % (considering average amplitude values of all trials) of that of CWLA system. This can be visualized also in Figure 5.21 in which CWLA system shows higher acceleration signal and slightly lower default noise (i.e. CWLA has higher SNR than TAIAS). The acceleration signal sensitivity of the RFID-based wireless system is 140.0 % of that of CWA system according to Figure 5.22(b). The lower sensitivity of CWA system is predominantly due to higher default noise content (i.e. CWA has lower SNR than TAIAS) in acquired acceleration signals (see Figure 5.20) which suppresses the amplitude of the natural frequency in the spectrum.

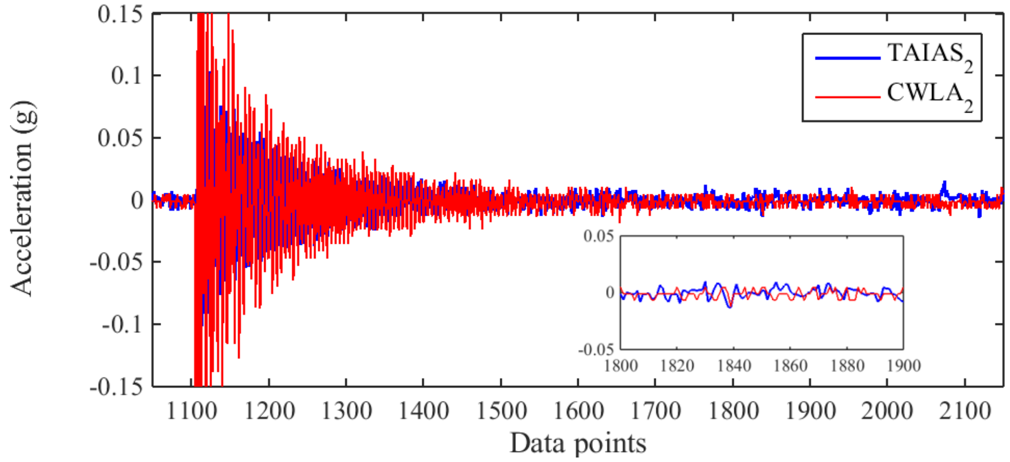

Figure 5.21: Example of simultaneous Z-axis acceleration measurement of I-beam from $TAIAS_2$ and $CWLA_2$ correspond to trial 1 (presented against data points for the overlapping purpose as there is a timing difference between both systems).

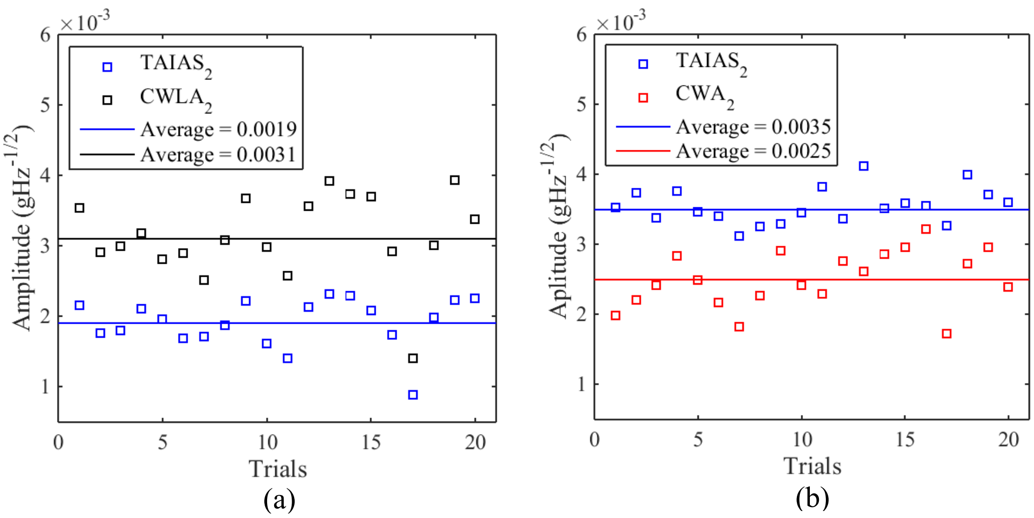

Figure 5.22: Comparison of amplitudes of single-sided amplitude spectra: (a) between $TAIAS_2$ and $CWLA_2$ (relates to Figure 5.18(a) and 5.18(b)) and (b) between $TAIAS_2$ and CWA_2 (relates to scenario 1 of Figure 5.19(b) and Figure 5.19(d)).

5.4 Conclusion

The enhanced RFID-based wireless dynamic acceleration measurement system was developed and tested. A novel semi-passive tag antenna integrated acceleration sensor consisting the construction material mountable UHF RFID tag antenna designed in Chapter 4 and a custom designed miniature accelerometer circuit was introduced to the system. It provided direct mounting capability on structural members. Furthermore, new UHF RFID reader with higher performance than that used in Chapter 3 was added to the system. Essentially, the performance of the enhanced system with two tag antenna integrated acceleration sensors was investigated by applying it to monitor the vibration of a full-scale steel I-beam which is one of the critical and ubiquitous structural members.

The firmware of the tag antenna integrated acceleration sensors was updated to use *USER* memory of the RFID tag chip with I^2C transactions consisting *two word-NVM writes*. This combined with enhanced data acquisition using implementation of *Optimized tag read* method in the reader provided the system with 50-Hz spectral bandwidth for all three acceleration axes (2 number of tag antenna integrated acceleration sensors). The possibility of determining the natural frequency of 23.30 Hz (1st mode) of the I-beam was gained due to the aforementioned enhancement for 3-axis measurements (which would not be possible with the initial system which had 16.67-Hz spectral bandwidth for 3-axis described in Chapter 3). Additionally, the microcontrollers of TAIASs now operate 8 times less clock frequency than the system in Chapter 3 which reduced the power consumption of tag antenna integrated acceleration sensors. Furthermore, the *Deep Sleep* mode was introduced to tag antenna integrated acceleration sensors with wake upon reader *Write* functionality to achieve highest possible power conservation in microcontroller during non-measurement periods. Implementation of this feature set an effective read range of the system governed by the write sensitivity of the RFID tag chip (the enhanced read range achieved by construction material mountable tag antenna in Chapter 4 cannot be entirely used). However, the 2-m distance between tag antenna integrated acceleration sensors directly mounted on I-beam and reader antenna in which the measurements of I-beam were conducted is 20 times increase when compared with ~0.1-m in Chapter 3.

The measurements conducted with a simply supported steel I-beam showed that the system is capable of acquiring the natural frequency (1^{st} mode). The natural frequency value acquired was in good agreement with the calculated theoretical value and measured values using two other commercially available independent acceleration measurement systems. An experiment based comprehensive analysis of acceleration sensor circuit distortion due to *Watermark interrupt* was performed and wavelet-based denoising was proposed for the removal and peak smoothing. It was shown that low order wavelets such as sym2 and db2 can be used to denoise acceleration signals of tag antenna integrated acceleration sensors adequately (peak smoothing and removal of introduced distortion).

The comparison of the RFID-based wireless system performance with commercial systems in terms of the natural frequency determination and acceleration sensitivity was performed using several measurement trials. The natural frequency determination accuracy of the RFID-based wireless system was in good agreement with both independent commercial systems configured with similar sample rates (commercial wireless accelerometer system had slightly higher sample rate). In fact, it had −0.03 Hz difference with commercial wireless accelerometer system and −0.05 Hz difference with the commercial wired accelerometer system. The maximum possible variation of the natural frequency determination of the RFID-based wireless system was in a range of ~ 0.1 Hz where 93 % of the values showed variation within a range of ~0.05 Hz (i.e. 40 trials, combined comparison with commercial wired and wireless accelerometer systems). This variation range was in good agreement with commercial wireless accelerometer system and better than that of commercial wired accelerometer system operated with similar sampling rates. The acceleration signal sensitivity of the RFID-based wireless system was benchmarked by comparing the amplitude of the determined natural frequency of the spectrum. According to the comparison of sensors which had lower SNR, the sensitivities of the RFID-based wireless system are 61.3 % and 140 % of sensitivities of commercial wireless and wired systems, respectively.

Overall, this chapter has provided a comprehensive enhancement to RFID-based dynamic acceleration monitoring system and proved its capability of acquiring the natural frequency information of full-scale structural members with similar accuracy to commercial measurement systems. The capability of using multiple tag antenna integrated acceleration sensors with enhanced 50-Hz spectral bandwidth was also shown.

Chapter 6 RFID-Based Wireless Multi-Sensor System for Simultaneous Dynamic Acceleration and Strain Measurement of Infrastructure

6.1 Introduction

In this chapter, the enhanced RFID-based wireless multi-sensor system which can simultaneously measure dynamic acceleration and strain of infrastructure is introduced. The system discussed in Chapter 5 is further improved with novel multi-sensor integrated tag antenna. The tag antenna integrated multi-sensor is created out of custom designed tag antenna in Chapter 4 and the developed multi-sensor circuit. The enhancement of the system to measure 3-axis dynamic acceleration and strain with spectral bandwidths of 40 Hz and 26.5 Hz, respectively, is discussed in detail. Additionally, benchmarking of the RFID-based wireless multi-sensor system is provided by comprehensive comparison of the results with measurements from the commercial wireless strain measurement system. Finally, the conclusions were made considering the aforementioned system enhancement efforts and comparisons.

6.2 Background

The importance of the usage of multiple measurands for IHM has been highlighted in [49, 85, 212]. In particular, it has been specified that combined consideration of dynamic responses of both acceleration and strain would provide more accuracy and reliability [49, 99, 213] in IHM applications. The strain is a measurement parameter which can be directly related to deformation of structural members under load [21]. Furthermore, it is highly sensitive to localized damage [99]. The mode curvature acquired by strain dynamic measurements, strain frequency response and strain energy are used to evaluate fault scenarios of structures. Consequently, usage of dynamic strain measurements to derive those features has been performed in [21, 89]. Dynamic strain measurements performed by an optical fiber system (i.e. a wired system) were proposed for infrastructure health monitoring in [214]. The method was justified by determining natural frequencies using measured dynamic strain of a cantilever beam. The Same method was used to identify damage of a steel I-beam in [215] using frequency of the 1st mode to derive necessary identifiers. Features extracted from shifts of natural frequencies acquired dynamic strain monitoring of aerospace structure in [216] was used for damage identification.

However, when considering strain measurements for IHM, both static and dynamic measurements are important. Electrical strain gauges were used in [217] to monitor deboning of a composite cantilever structural element. Static strain measurements were used extensively in this investigation. Differences of acquired strain measurement from adjacent strain gauges have been used in [218] reliably to detect a crack at the base of a wind tower. Static strain and temperature were simultaneously measured by optical fiber based sensor system in [20].

In addition to the aforementioned advantages of strain measurements, the strain gauges (in particular, the conventional electrical strain gauges) are inexpensive and can cater for a dense population of sensors required in IHM [9]. Furthermore, the measurement techniques with strain gauges [219] and interpreting strain data in IHM have already been developed. The Wheatstone bridge-based resistor arrangements are ubiquitously employed in the instrumentation interface of electrical strain gauges in different configurations such as quarter bridge, half bridge and full bridge [9, 220]. The relationship between strain (ϵ) and quarter bridge output (V_B in V) which can be derived by applying Kirchhoff's circuit laws is given by

$$\frac{V_B}{V_I} = \frac{K\epsilon}{4}\left(\frac{1}{1 + K\frac{\epsilon}{2}}\right) \tag{6.1}$$

where K is the gauge factor and V_I is quarter bridge input voltage (V) . The portion within brackets accounts for the non-linearity between V_B and ϵ of quarter bridge configuration.

Electrical strain gauge integration to active wireless nodes has been commonly put into practice for IHM. However, in a majority of the occasions, strain and acceleration were measured by dedicated systems [9, 78, 92, 213]. However, there are instances in which multiple measurands were performed using same active sensor node. The active sensor node presented in [83] is capable of acquiring dynamic acceleration, strain, and electromechanical impedance. Active platform detailed in [221] could integrate multiple sensor systems of inclinometers and potentiometric crack meters to monitor infrastructure along with environmental changes of temperature and humidity. This was actually a higher level active platform as it integrates sensor systems rather than sensors themselves.

Strain measurements related to IHM by RFID tag antenna integrated strain gauges were previously reported in [133, 134]. However, the capability of continuous monitoring for dynamic information acquisition was not shown. A semi-passive RFID-based strain sensor presented in [136] for wireless IHM had the capability of measuring dynamic strain. The strain gauge sensor consisted of resistance to frequency conversion electronics and two dipole antennas. One antenna is used for modulated backscattering of identification information and for the waking up the sensor. The other antenna is used for backscattering of the output from resistance to frequency conversion electronics. The sensor has shown good read range. A commercial RFID-based strain measurement system with battery-assisted sensors is presented in [222]. The multiple sensor integrations with RFID tag antenna was presented with an augmented module for environmental monitoring in [48] which had acceleration, light and temperature sensors. However, the possibilities of measuring dynamic acceleration or its mounting capability on metal structures were not shown. Therefore, RFID-based wireless systems which can measure simultaneous dynamic acceleration and strain of infrastructure are unprecedented. The work presented in this chapter is predominantly concentrated on filling this gap by introducing multi-sensor integrated semi-passive tag antenna for the developed RFID-based wireless system in previous chapters.

6.3 RFID-Based Multi-sensor System

The enhanced system measuring dynamic acceleration and strain simultaneously, of a cantilever steel beam, is shown in Figure 6.1(a). The major enhancement compared to what presented in Chapter 5 was the novel multi-sensor integrated tag antenna (MSITA) which is capable of acquiring dynamic acceleration and strain. This is shown in Figure 6.1(b) and detailed in Figure 6.3. The MSITA includes the construction material mountable RFID tag antenna designed in Chapter 4 and a custom designed multi-sensor circuit which has a 3-axis accelerometer and a strain gauge as shown in Figure 6.3(a). The tag antenna is integrated with the multi-sensor circuit via I^2C interface. All other system components used in Chapter 5 were unchanged.

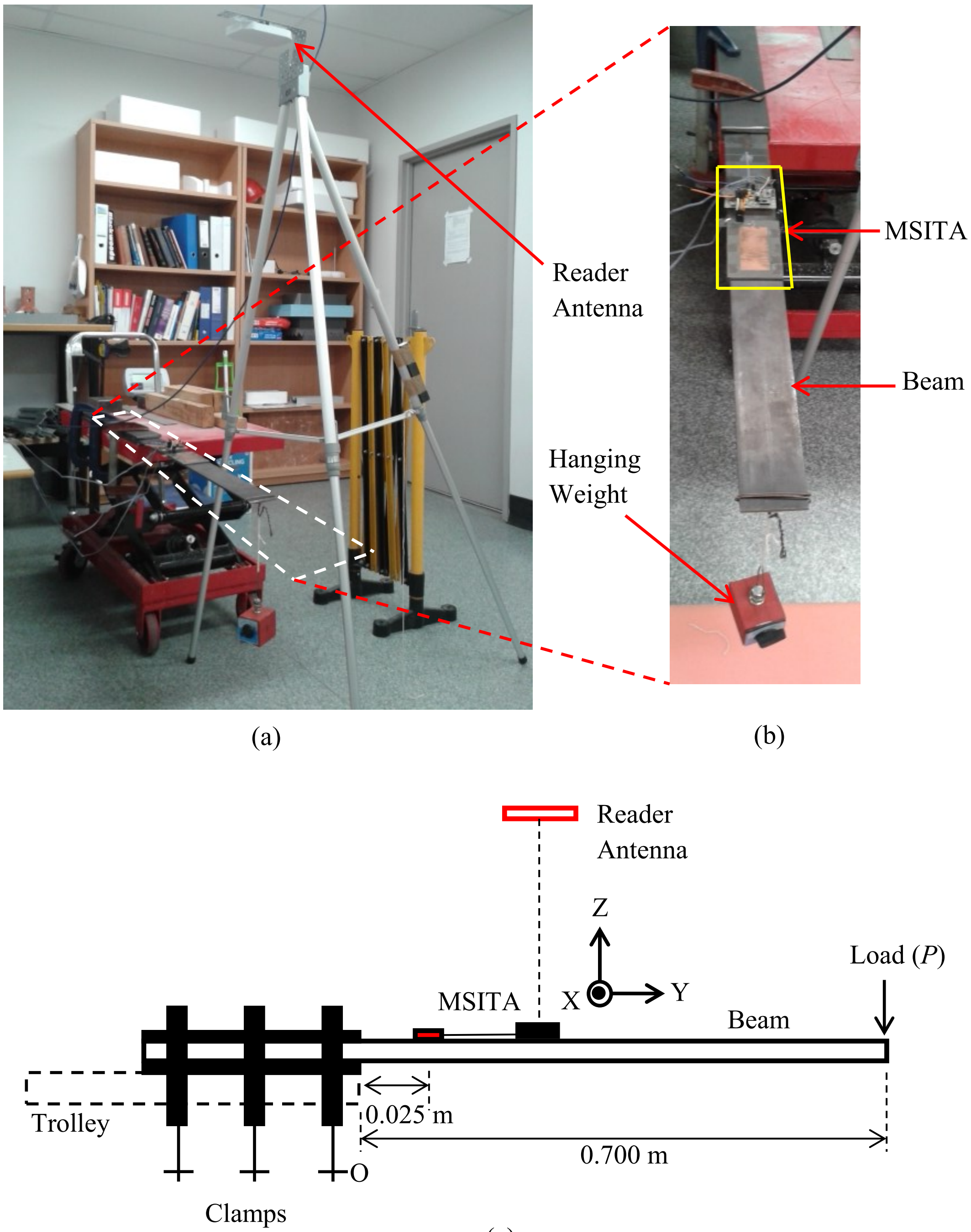

(a) (b)

(c)

Figure 6.1: RFID-based wireless multi-sensor system measuring dynamic acceleration and strain of cantilever steel beam: (a) laboratory setup (b) enlarged view of mounted MSITA on beam and (c) schematic.

6.3.1 Hardware Design of Multi-Sensor Integrated Tag Antenna

Figure 6.2 and Figure 6.3(b) depict the multi-sensor circuit in detail. This was a custom designed expanded version of the acceleration sensor circuit presented in Chapter 5. Therefore, the hardware portion related to acceleration sensing presented in Chapter 5 was unchanged. Additional hardware listed in Table 6.1 required to interface a commercial 120-Ω strain gauge [223] in 3-wire quarter bridge configuration was provided in design and fabrication. In the current design, the strain gauge is wired to the circuit taking into account the general concept that it is less probable to sense both dynamic acceleration and strain at the same position of a structure. Therefore, the 3-wire configuration was provided as it introduces any resistance related to lead wires to both sides of the Wheatstone bridge (onboard with 120-Ω precision resistors with low-temperature coefficient [224], see Figure 6.3(b)). Therefore, the lead wire resistance perturbation influence on bridge output voltage (V_B) is minimum [220].

It is an established and proven practice to use differential amplifiers to amplify analog signals with minor perturbations connected through Wheatstone bridge interfaces as voltage difference should be amplified. In this regard, a Texas Instruments INA333 instrumentation amplifier was used as it provides low power, low noise package with high common-mode rejection ratio (CMRR) [225]. Furthermore, it has inbuilt radio frequency interference (RFI) filters for each input which would help to filter noise induced by RF interference (in particular when strain gauge is used with lead wires).

The programmable gain amplifier (PGA) was introduced for two purposes. One is to increase the maximum gain of the strain gauge interface of the multi-sensor circuit. The aforementioned differential amplifier has a maximum gain of 1000. With the introduction of Microchip MCP6S91 programmable gain amplifier [226], a maximum gain of 32,000 can be reached (both the differential amplifier and PGA combined). The second reason is to provide gain changing flexibility to the multi-sensor circuit without having to do any hardware alterations. Differential amplifier gain could only be altered by changing the gain resistor (RG, see Figure 6.2) [225]. Therefore the introduction of PGA provides convenience in altering gain (in discrete levels given in Table 6.1) of the strain gauge interface of the MSITA by the firmware whenever necessary. The alteration can be performed by configuring PGA via 3-wire SPI bus. The same SPI bus provided for TAIAS in Chapter 5 was extended as shown in Figure 6.2 for this purpose.

The filter was designed as a single pole unity gain low pass filter which has 50-Hz cut-off frequency (50-Hz spectral bandwidth was achieved for 3-axis acceleration measurements in Chapter 5 and it was taken as the specification for the cut-off frequency of the filter) to filter out high-frequency noise. This was designed using Texas instruments low power single supply OPA333 operational amplifier [227] as specified in Table 6.1.

The PIC24F16KA102 microcontroller used in the multi-sensor circuit has built-in 10-bit analog to digital conversion (ADC) module with 9 number of channels [198]. One of these can be directly used for ADC of strain signal. Since the strain signals related to infrastructure are proven and expected to be small in magnitude, an extra 16-bit ADC channel also provided to acquire higher resolution to strain interface of the multi-sensor circuit. This was done by introducing Analog Devices AD7680 16-bit low power ADC integrated circuit [228]. The extended SPI bus in 3-wire mode was used to acquire 16-bit ADC strain data to the microcontroller as depicted in Figure 6.2.

Consequently, the multi-sensor circuit can be used in different configurations due to different stages of amplification, filtering and ADC. Each of these levels was isolated in hardware as such multi-sensor circuit can be used in different configurations which provide dedicated capabilities as listed in Table 6.2. The provision for this was provided by selection switches (SSW, see Figure 6.2) introduced in the multi-sensor circuit. This was predominantly done to provide full configuration flexibility for the circuit when it is being used with different scenarios to measure dynamic acceleration and strain of structures. Additionally, it has provided convenience in testing the circuit in advance to measurements.

Table 6.1: Additional components used in the design of the multi-sensor circuit.

Schematic Description	**Hardware**	**Features**
Differential Amplifier	Texas Instruments INA333 [225]	• Low power consumption and low voltage operation (down to 1.8 V) • Precision instrumentation amplifier • High CMRR (100 dB minimum for Gain ≥ 10) • Low noise (50 nV/Hz$^{-1/2}$ for Gain ≥ 100) • Radio frequency interference (RFI) filtered inputs • Maximum Gain = 1000 (Gain can be set by a single resistor RG)
PGA	Microchip MCP6S91 [226]	• 8 discrete Gain levels (1,2,4,5,8,10,16 and 32) • Low voltage single supply operation (down to 2.5 V) • SPI configuration interface (up to 10 MHz) • Low noise (10 nV/Hz$^{-1/2}$)
Filter	Single-pole unity gain with Texas Instruments OPA333*	• Low power consumption and low voltage operation (down to 1.8 V) • Single supply operation • Low noise • High CMRR (130 dB typical)
16-bit ADC	Analog Devices AD7680 [228]	• Low power and low voltage operation (3 mW consumption at 2.5 V minimum supply for 100 ksps maximum throughput) • 16-bit ADC • SPI data output interface (250 kHz to 2.5 MHz)
Strain gauge**	TML PFL-30-11 [223]	• Gauge factor (K = 2.13) • Suitable for both concrete and metal structures • Coefficient of thermal expansion = 11.8 × 10^{-6}℃$^{-1}$ • Temperature coefficient of K = +0.08 ± 0.05 % per 10℃

* datasheet of Texas Instruments OPA333 [227].
** not shown in Figure 6.2.

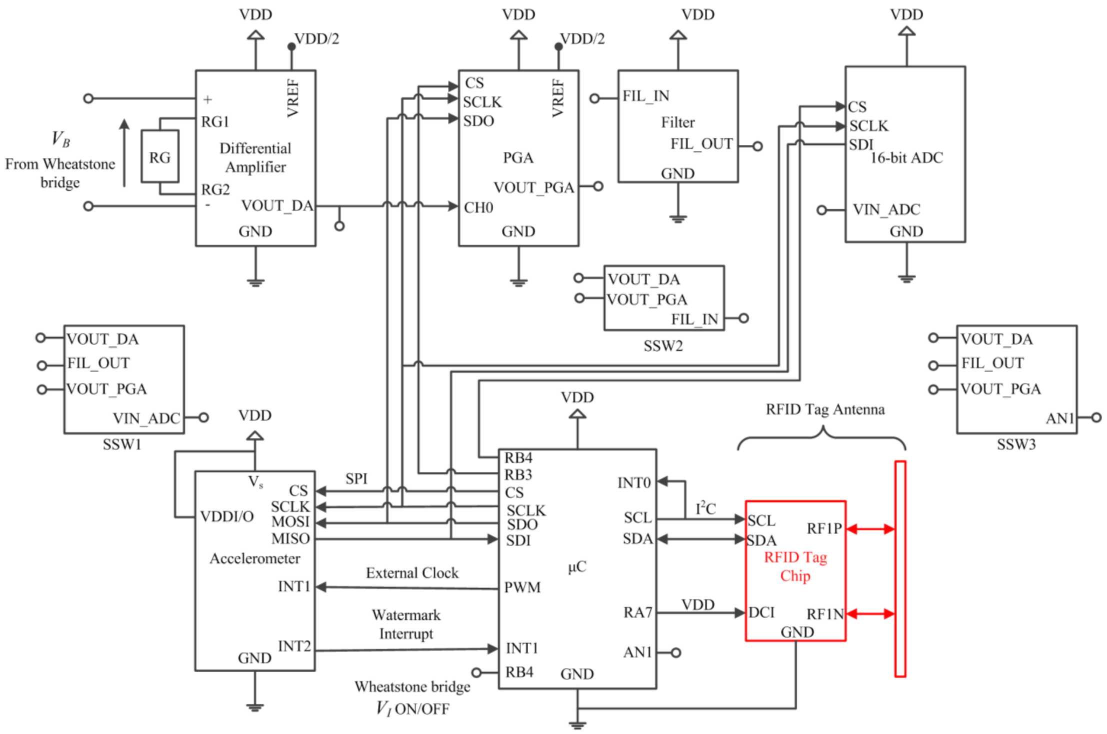

Figure 6.2: Schematic of the multi-sensor integrated tag antenna (V_B - bridge voltage, RG - gain resistor, PGA - programmable gain amplifier, ADC - analog to digital converter, µC - microcontroller, SSW - selection switch and other notations are in accordance with datasheets [135, 179, 198, 225, 226, 228]): VDD = V_I = 2.5 V.

Table 6.2: Possible configurations of strain interface of the multisensor circuit.

Configuration*	Levels Involved
1	Differential amplifier
2	Differential amplifier and PGA
3	Differential amplifier, PGA and filter
4	Differential amplifier and filter

* each can be used with 10-bit or 16-bit ADC.

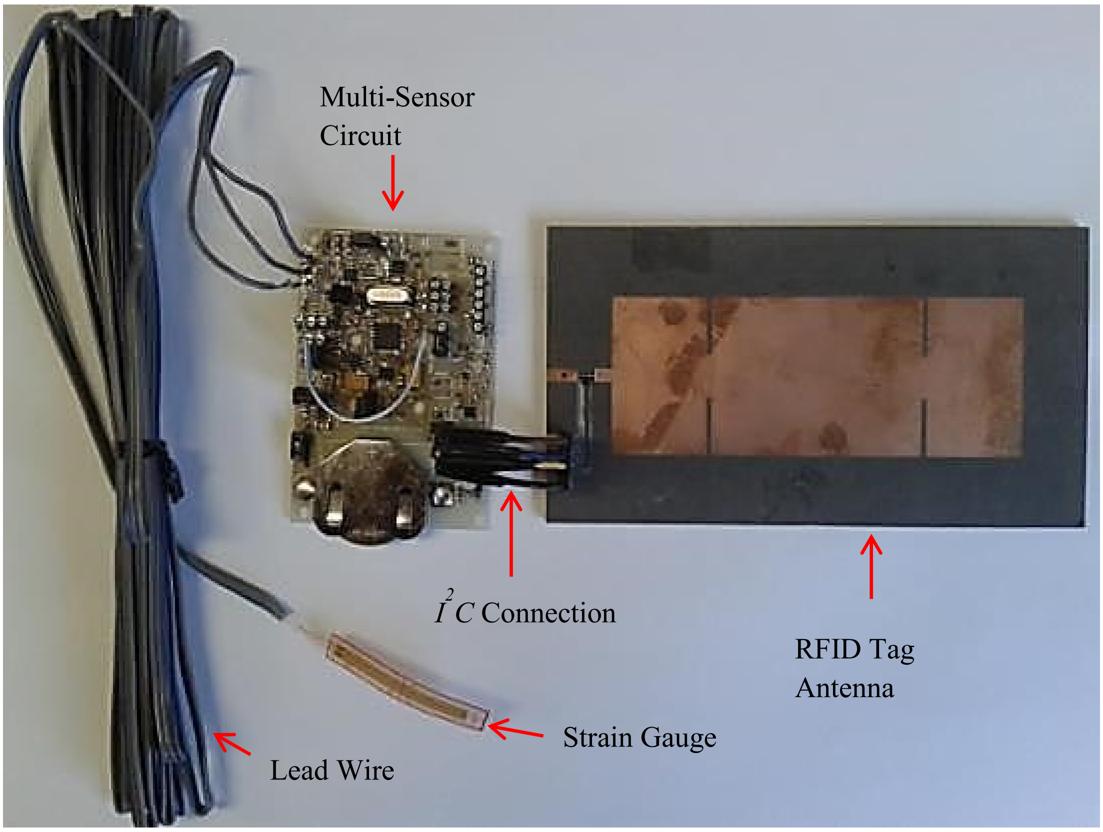

(a)

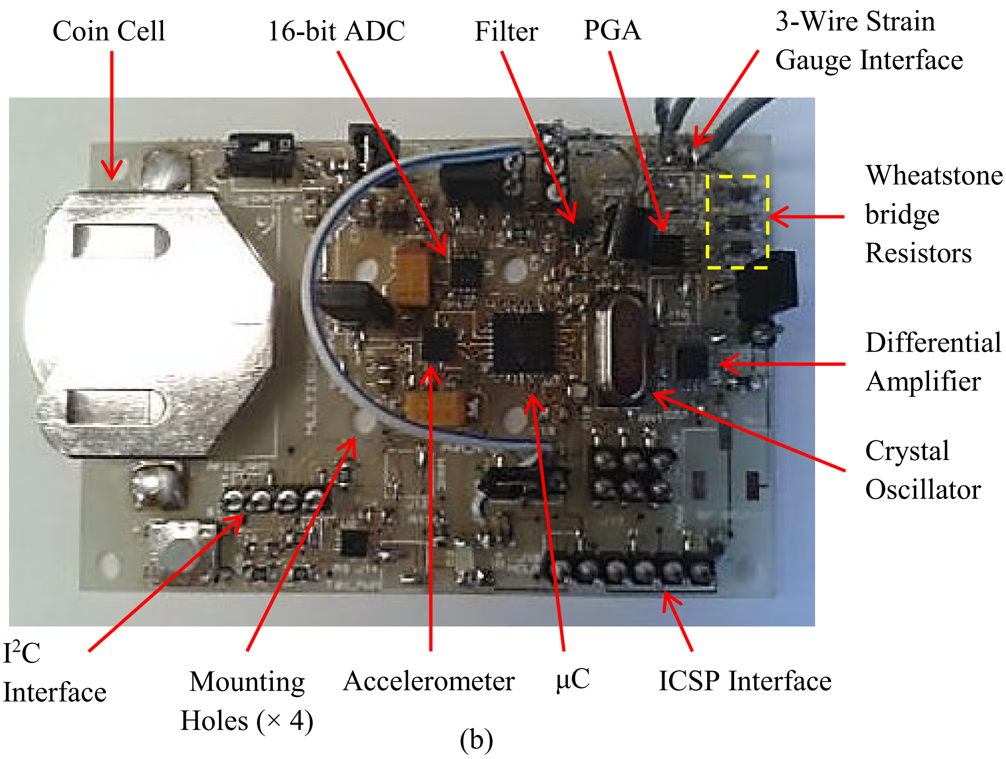

(b)

Figure 6.3: Multi-sensor integrated tag antenna: (a) picture of implementation and (b) enlarged view of the multi-sensor circuit (ICSP - in circuit serial programming).

6.3.2 Firmware Design of Multi-Sensor Integrated Tag Antenna

In the process of firmware design for MSITA, the firmware design presented in Chapter 5 for TAIAS was upgraded with necessary requirements to acquire strain and 3-axis acceleration measurements simultaneously. Figure 6.4 is a part of Figure 5.7 replicated to discuss the firmware update of MSITA. It depicts the timing diagram for the acquisition of 60 acceleration samples (i = 60, 20 each from 3-axis) for firmware configuration provided in Table 5.1 (see Chapter 5). The firmware update was done following the same principle of keeping adequate t_{RF} window to acquire both dynamic acceleration and strain measurements via air interface. It has been implemented and proved in Chapter 5 that t_{RF} shown in Figure 6.4 is adequate acquire 60 number of acceleration measurements (since multiple acquisitions occurred for single acquisition cycle at the reader for two TAIASs which were filtered out using T_w). Under the firmware enhancement in Section 5.2.2 (see Chapter 5), the RF port configuration words were introduced. Therefore, the possibility of widening the t_{RF} window by increasing i, diminishes, since RF port configuration words has be added to every $(i + 1) \times (t_{I2C} + t_{NVM})$ transaction under the constraint of number of maximum word acquisition (i.e. 64) by of "*Optimized tag read*" method used in the measurement acquisition application of the reader. Due to this reason, increasing i beyond 60 was not considered.

Acquisition of strain measurement is now an extra burden to the timing diagram. This is predominantly due to the sequential instruction execution of the microcontroller (which is the general case of all microcontroller families). In the case of MSITA, if microcontroller acquires a strain sample in a single acquisition cycle from 16-bit ADC, it will add one t_{SPI}, t_f, t_{I2C} and t_{NVM} to the timing diagram (t_{SPI} is not there for acquisition from 10-bit built-in ADC). Consequently this reduces t_{RF}. However, it does not have a major influence to the data acquisition by the reader within available t_{RF} window. The firmware of the MSITA was implemented in the aforementioned manner for simultaneous dynamic acceleration and static strain measurements since it provides strain ODR of ~5 Hz.

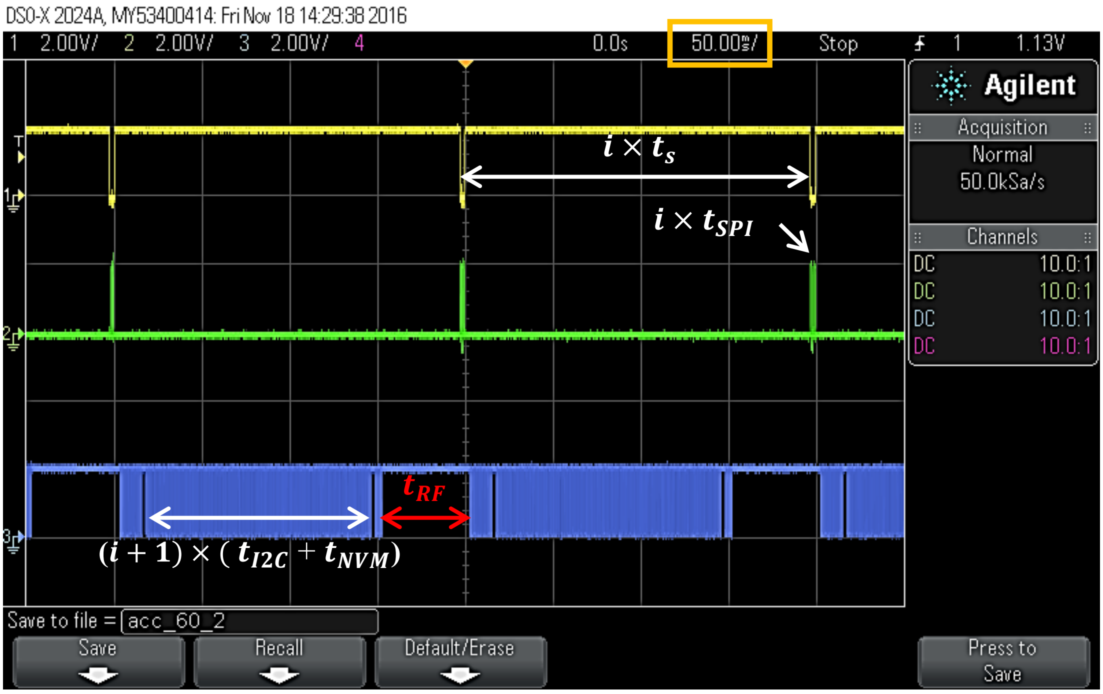

Figure 6.4: Timing diagram of *Watermark interrupt* (yellow), *SPI* receive (green) and I^2C write (blue) of a TAIAS with *two word-NVM writes* for $i = 60$ (t_{I2C} and t_{NVM} for $i + 1$ due to additional T_W and t_f not visible).

However, for dynamic strain measurement, the output data rate should be made higher by acquiring more strain samples within $i \times t_s$. With $i = 60$, maximum strain samples that can be acquired is 3 as the combination of 3-axis acceleration, strain and T_W accounts for the maximum acquisition capacity of "*Optimized tag read*" method of the reader application. When acquiring multiple strain samples, it consumes somewhat more time due to bridge switching. A normal bridge circuitry is a clear current path which will drain the battery at an increased rate if connected continuously during measurement. Hence, the bridge circuitry was switched by the microcontroller as shown in Figure 6.2 (Wheatstone bridge V_I ON/OFF) only when the strain measurement is needed to be acquired. In this process an extra spare time should be provided after the bridge switching to let the bridge voltage settle prior to acquiring the strain reading. This settling time accumulates in the timing diagram with each strain measurement acquired. Therefore, increasing ODR of strain measurement could not be possible without curtailing the ODR of 3-axis acceleration as shown in Figure 6.5.

Figure 6.5 depicts the timing diagram of acquiring 45 number of 3-axis acceleration samples (15 for each axis) and 10 number of strain samples within a single acquisition cycle with accelerometer ODR_{Actual} of 80-Hz. The ODR_{Actual} of the accelerometer was lowered by reducing the frequency of the PWM (50 %) to 41 kHz for $ODR_{Selected}$ 100 Hz according to Equation 5.1 (as there is no discrete 80-Hz ODR configuration of the accelerometer [179]). Since strain readings had to be acquired at equally spaced intervals, the I^2C transaction was discretized as shown in Figure 6.5(a). The acquisition of a single 16-bit strain data is a 3-byte consecutive *SPI* transaction between 16-bit ADC and microcontroller [228]. Therefore, the time consumed is negligible and at some instances, it is not being picked by the oscilloscope as seen in Figure 6.5(a). However, they are being picked in the enlarged view. The gap provided between RF port configuration words and data in Chapter 5 is eliminated in the current firmware design. The powered-on duration of the bridge had to be extended at a single instance as depicted in Figure 6.5(b) to cater for an unavoidable circumstance in firmware coding. The default output of the differential amplifier (VOUT_DA) was tested to be ~1.00 V even though it was designed to be 1.25 V (50 % of the VDD). This has occurred due to a drop of the common-mode voltage at the input of the differential amplifier and it has led to lower the effective symmetric dynamic range of the MSITA strain measurement. Figure 6.5 depicts a strained instance of the cantilever beam as VOUT_DA has increased higher than 1.25 V. The alteration of the firmware provided 80-Hz ODR measurement of 3-axis acceleration (for each axis) and ~53-Hz ODR measurement of strain. The configuration settings of the firmware are given in Table 6.3 and the updated flow diagram is shown in Figure 6.6 and Figure 6.7.

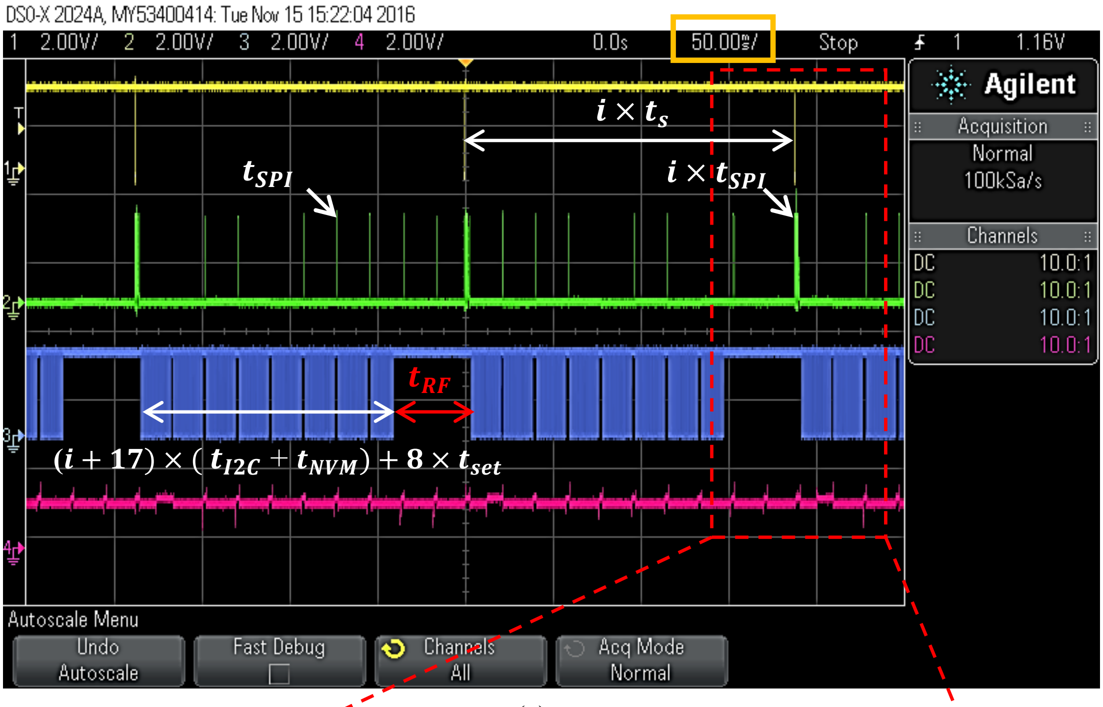

(a)

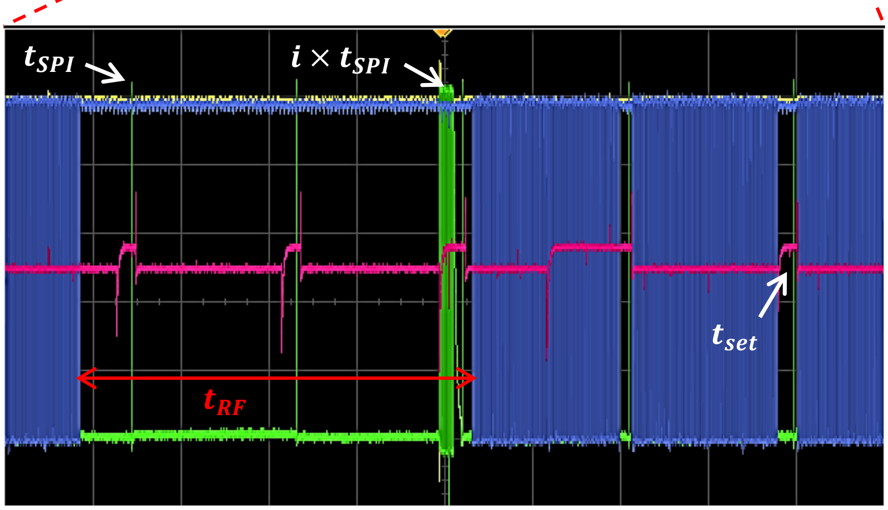

(b)

Figure 6.5: (a) Timing diagram of *Watermark interrupt* (yellow), *SPI* receive (green), I^2C write (blue) and differential amplifier output (magenta) of the MSITA *with two word-NVM writes* for $i = 45$ (t_{I2C} and t_{NVM} for $i + 17$ due to additional 1 ×T_W, 10 × strain acquisitions and 3 × RF port configuration words which consumes 2 × ($t_{I2C} + t_{NVM}$) each ; t_f not visible) and (b) enlarged overlapped view (t_{set} - provided time duration in firmware between bridge power on instance and strain data acquisition).

Table 6.3: Configuration of multi-sensor integrated tag antenna.

Component	**Configuration**
Accelerometer	Acceleration level: ± 2 g Clock: External (41.0 kHz) Output data rate (selected): 100 Hz Output data rate (actual): 80 Hz Noise mode: ultra-low noise Interface: 4-wire SPI (slave) Anti-aliasing filter: Output data rate/2 Interrupt: Watermark configured at 45 acceleration samples
RFID tag antenna	RF ports: 1 blocked, 2 in use (blocked when necessary) Interface: I^2C (slave)
Microcontroller	Interface: I^2C (master) 400 kbps, SPI (master) 2 MHz Oscillator: Primary (4 MHz crystal oscillator) 10-bit ADC: AN1*
Differential amplifier	Gain resistance (RG): 200 Ω**(Gain = 500) Reference voltage: 1.25 V
PGA	Gain: 1*** Interface: 3-wire SPI (slave)
Filter**	Type: Low pass Number of poles: Single Gain: Unity Cut-off frequency: 50 Hz
16-bit ADC	Interface: 3-wire SPI (slave)

* in accordance with [198].
** predominantly a hardware configuration / design.
*** Further amplification by PGA was not needed as differential amplifier provided adequate amplification for experimental case.

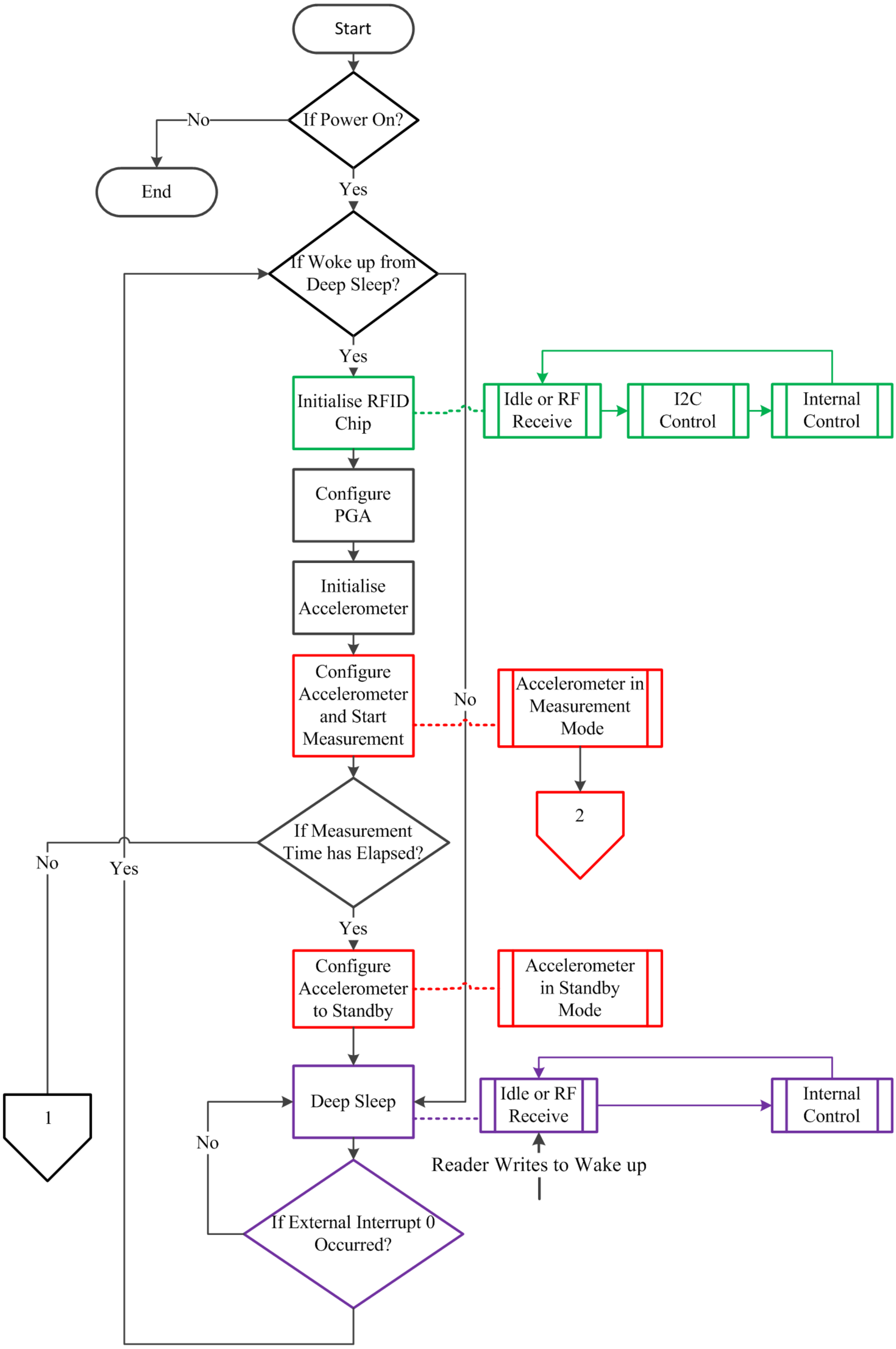

Figure 6.6: Flow diagram of multi-sensor integrated tag antenna firmware.

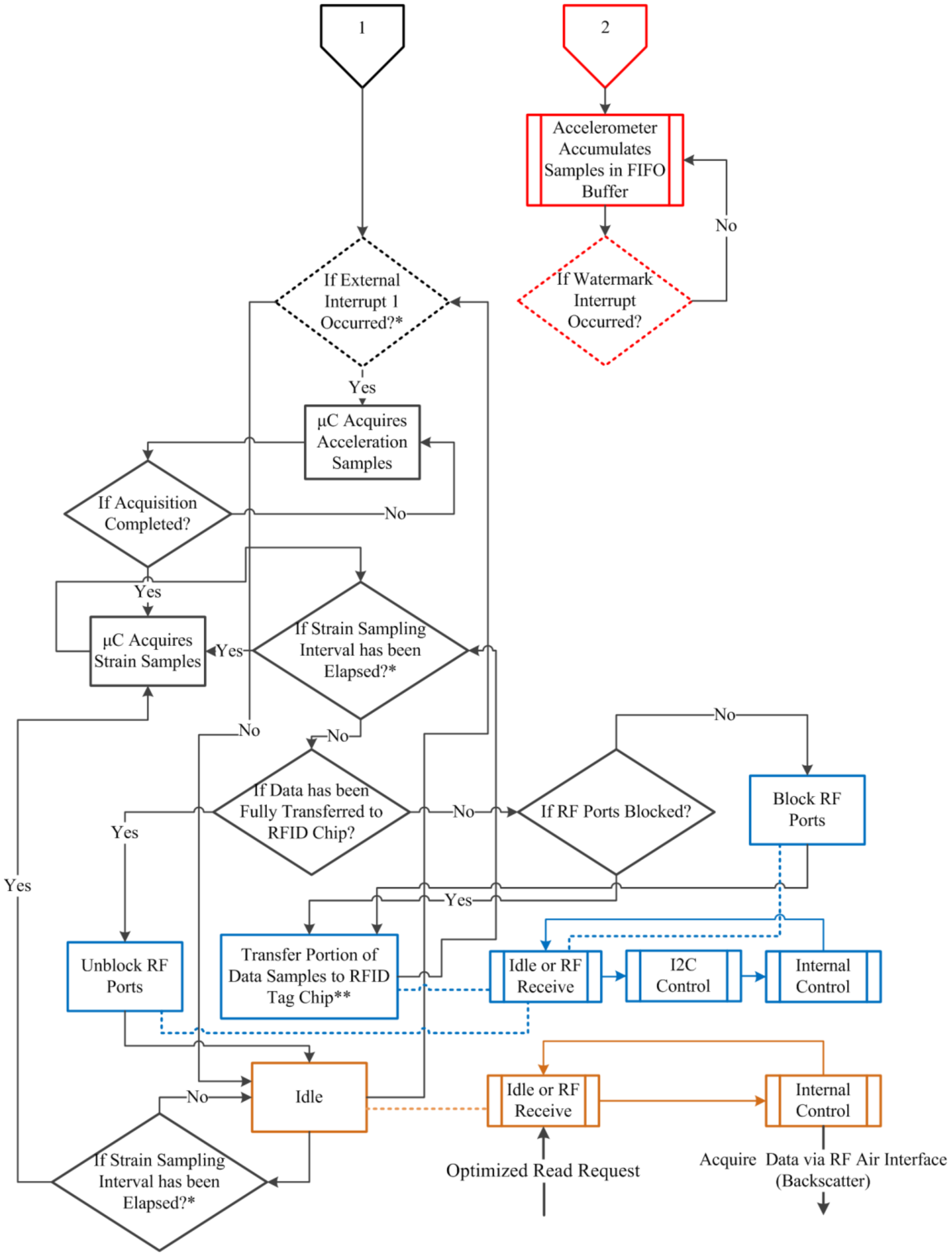

Figure 6.7: Continuation of the flow diagram of multi-sensor integrated tag antenna firmware (* the External interrupt 1 and strain sampling instance do not coincide and **strain data are transferred after finishing the transfer of all acceleration data).

6.4 Measurement Results

The enhanced RFID-based wireless multi-sensor system is applied to measure dynamic acceleration and strain of a cantilever steel beam as shown in Figure 6.1(a). The cantilever portion of the beam has a length (l) of 0.700 m, width (b) of 0.065 m and height (h) of 0.005 m. The MSITA is mounted on the beam as depicted in Figure 6.1(b). The strain gauge is installed following a standard attachment method for metal surfaces at a distance (x) of 0.025 m from O. Figure 6.1(c) provides the schematic of the cantilever arrangement of the beam. The loading of the beam is done at the free end of the beam with hanging weights as shown in Figure 6.1(b).

6.4.1 Static Strain Measurements and Results Comparison with Commercial Systems

In this experiment, the strain measurement of the position shown in Figure 6.1(c) was acquired by discretely increasing the load in similar amounts (~10 N). Additionally to MSITA, a commercial wireless strain sensor system (CWLSS) and a standard wired strain measurement instrument (DSM) listed in Table 6.4 were used to conduct the same measurement. These systems were used with the same strain gauge. Figure 6.8 depicts the measurement results along with the theoretically calculated strain by

$$\epsilon = \frac{6P(l-x)}{Ebh^2}, \qquad 6.2$$

where P is the load (N). The default offset of each system was removed from the measurement results. The root mean square error (RMSE) values were calculated for 1st order polynomial best-fits for the measurement results from each system. According to Figure 6.8, the DSM has the highest strain sensitivity as it provides results almost equal to the theoretical values. The strain sensitivity of MSITA is close to that of DSM. The CWLSS has the highest linearity (comparing RMSE) in the tested loading range mostly due to the low sensitivity shown than other systems. The measurement results from MSITA are non-linear than others, but close to the linearity of the results from DSM. It has to be noted that the relationship between quarter bridge output voltage and strain itself is non-linear as given in Equation 6.1. Since DSM strain values are almost equal to the theoretical strain values, it was chosen as the benchmark to calibrate both MSITA and CWLSS systems. The compensated gauge factor values for each system in calibration are given in Table 6.5. The average of compensated *K* is used with each system in measurements results presented in following sections.

Table 6.4: Systems used in the comparison.

System	Components
CWLSS	• LORD Microstrain SG-Link –LXRS wireless analog 2-channel sensor node [77] • LORD Microstrain WSDA® -Base-104 -LXRS® base station
DSM	• TC-31K Digital Strain Meter [229]

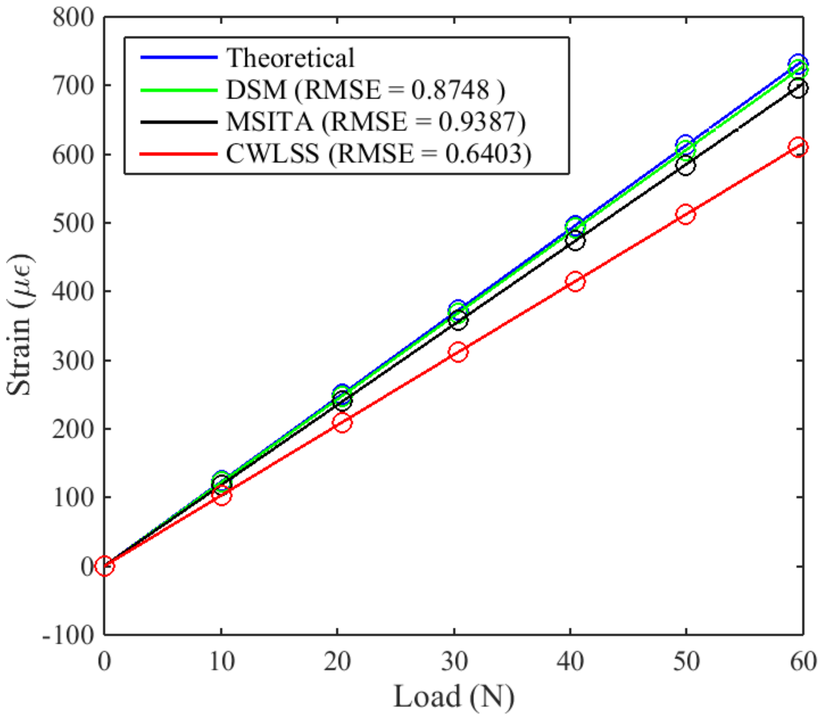

Figure 6.8: Static strain measurement results (RMSE - root mean square error).

Table 6.5: Calibration with gauge factor compensation.

Load* (N)	Strain** ($\mu\epsilon$)	Compensated Gauge Factor (K)	
		MSITA	CWLSS
10.10	123	2.02	1.80
20.40	247	2.04	1.82
30.41	369	2.04	1.83
40.42	492	2.02	1.82
49.93	605	2.02	1.84
59.55	723	2.02	1.83
Average		2.03	1.82

*each increase of load is ≈ 10 N.
**by DSM.

6.4.2 Simultaneous Measurement of 3-Axis Dynamic Acceleration and Strain by MSITA

After calibrating the MSITA, simultaneous measurements of 3-axis dynamic acceleration and strain were conducted upon the same cantilever beam shown in Figure 6.1. A hanging load of 10.10 N was released to induce vibrations of the beam. Figure 6.9 to Figure 6.11

depict the dynamic acceleration measurement results of X, Y, and Z axes, respectively. The related dynamic strain measurement is shown in Figure 6.12. Z- axis has the highest acceleration as the vibration induced force was in the same direction. Both X and Y axes also show acceleration where X-axis has higher magnitude. Figures 6.9 and 6.11 show default offset removed acceleration values. Since Y-axis has initial static acceleration due to the deformation of the beam under load, the default offset was not removed to depict the stabilization of the signal after vibration at default offset. Figure 6.13(a) and Figure 6.13(b) provide the single-sided amplitude spectra calculated from 3-axis dynamic acceleration measurement and strain measurement, respectively.

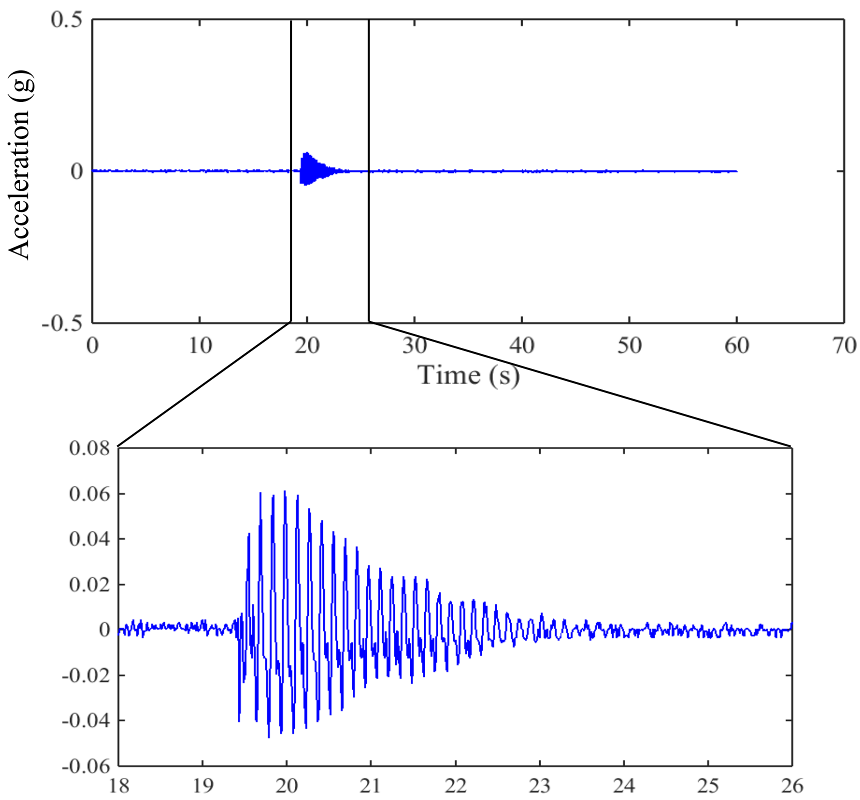

Figure 6.9: X-axis acceleration measurement.

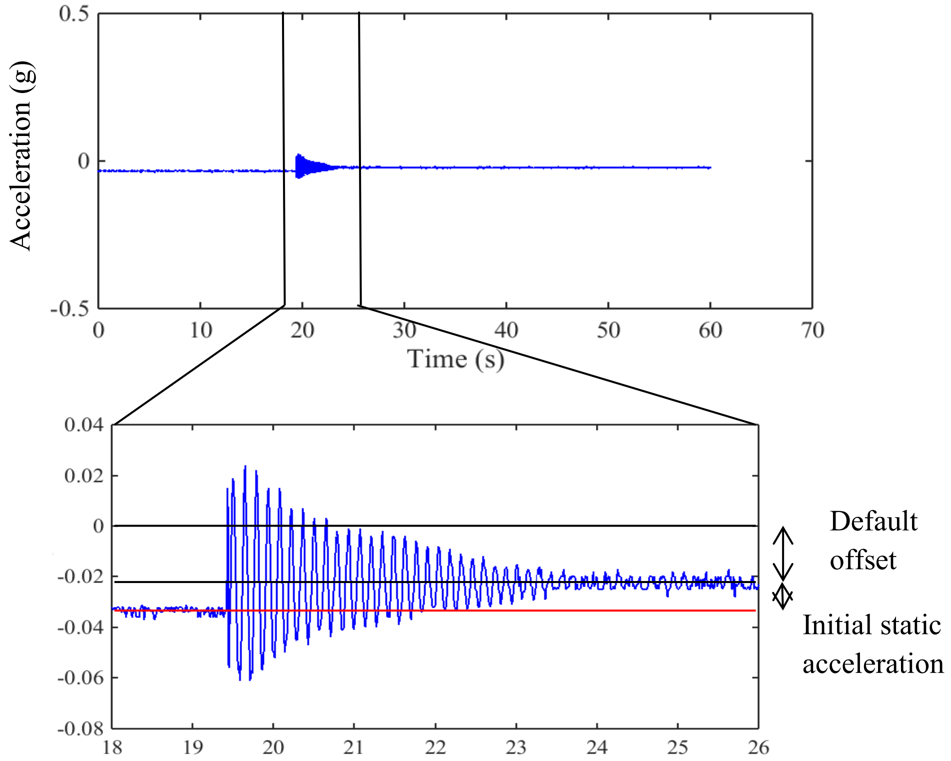

Figure 6.10: Y-axis acceleration measurement.

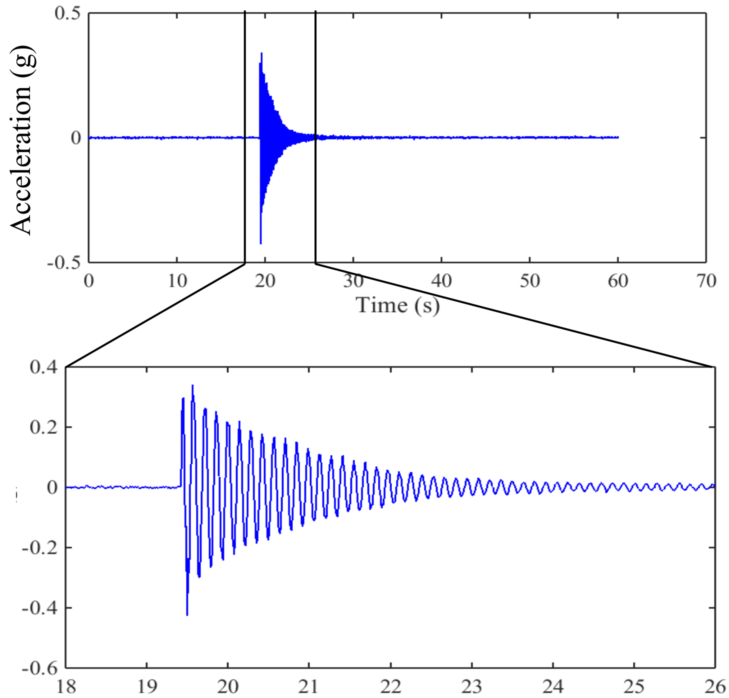

Figure 6.11: Z-axis acceleration measurement.

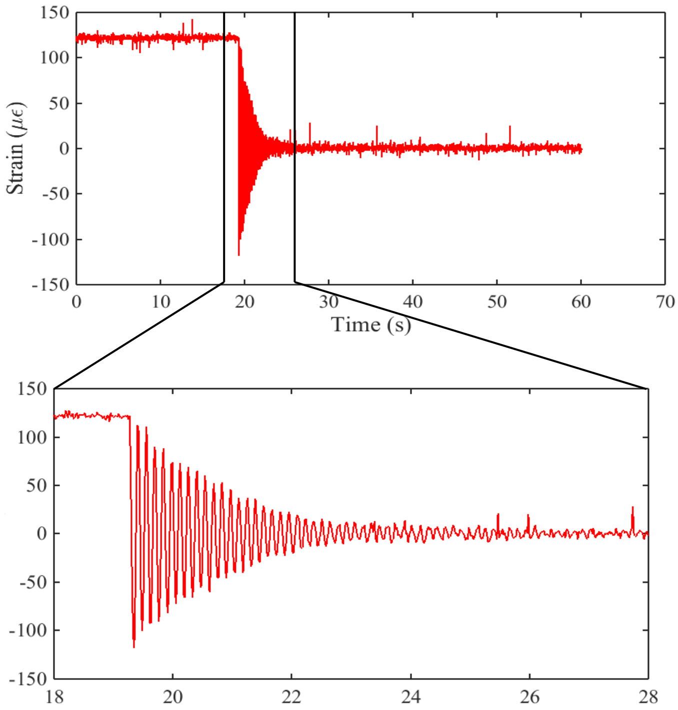

Figure 6.12: Strain measurement.

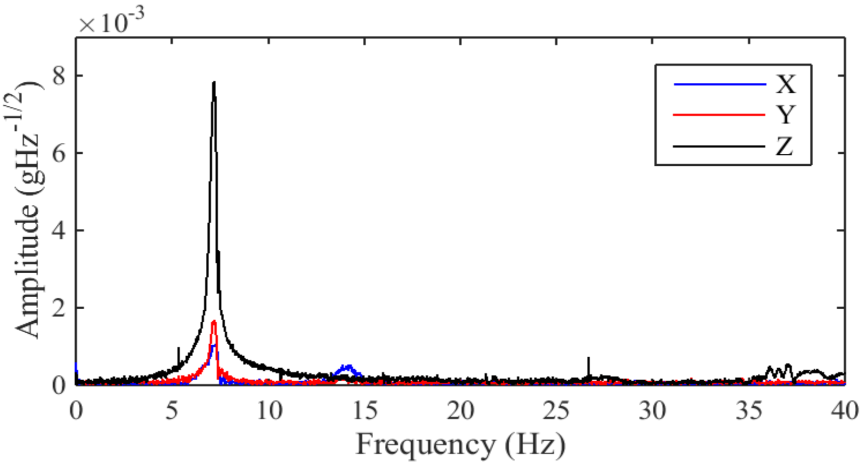

(a)

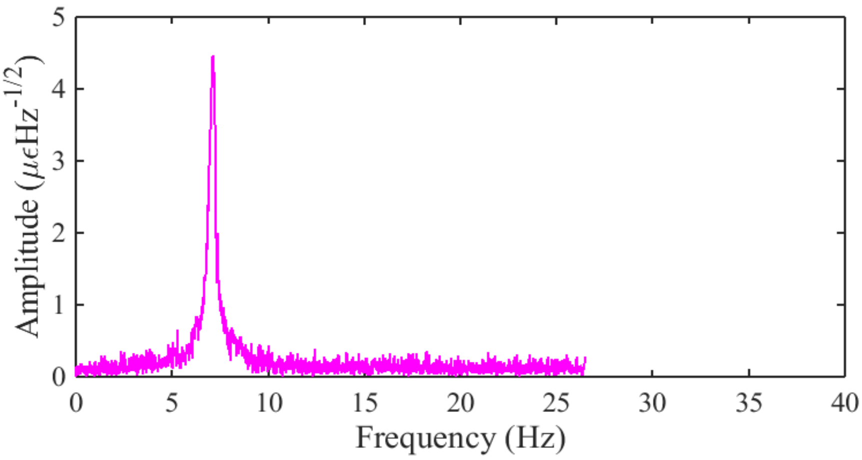

(b)

Figure 6.13: Single-sided amplitude spectra from simultaneous (a) 3-axis dynamic acceleration measurement and (b) strain measurement.

According to Figure 6.13, the prominent peaks have occurred at 7.17 Hz and 7.14 Hz in the amplitude spectra of dynamic acceleration and strain measurement results, respectively. This value is close to the calculated 1st mode (i.e. n = 1) natural frequency of 8.35 Hz for the cantilever beam by Equation 2.1 in which $\kappa \approx \frac{(2n-1)\pi}{2l}$ [90]. The parameters of structural steel A36 were assumed for the natural frequency calculation of the beam since exact parameters were unknown. The existing gap between theoretical and measured values might be due to an error in the assumption. In this experiment, all axes of acceleration are carrying the natural frequency information as can be seen from Figure 6.13(a). This can be due to imperfections of the releasing the hanging load in the process of inducing vibrations. The noise floor of the amplitude spectra of strain measurement result is predominantly due to the noise present in the default portion of the acquired signal (see Figure 6.12). Figure 6.14 shows, time history of Z- axis acceleration and strain for 120-s measurement duration. This figure demonstrates the distortion introduced by accelerometer *Watermark interrupt* signal which was addressed in Chapter 5 (at 5.33-Hz fundamental frequency for current setting). Since, strain measurement result was also acquired from same extended *SPI* bus the effect is present even in the strain measurement (microcontroller acquires both acceleration and the strain data by same SDI input of the *SPI* bus).

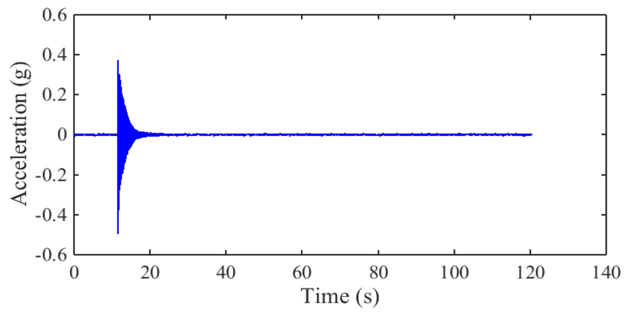

(a)

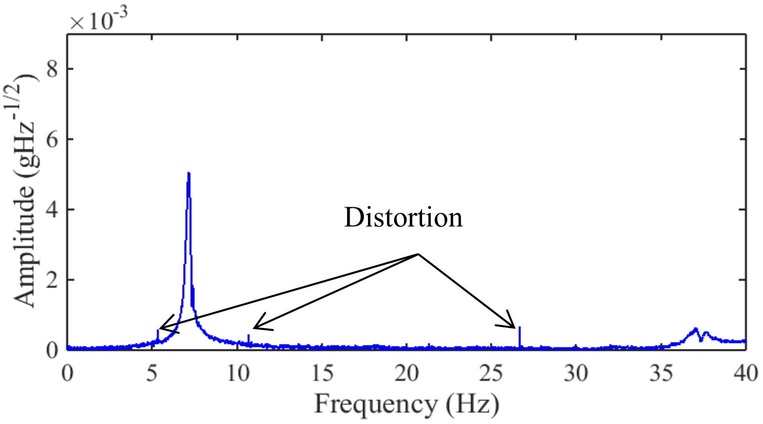

(b)

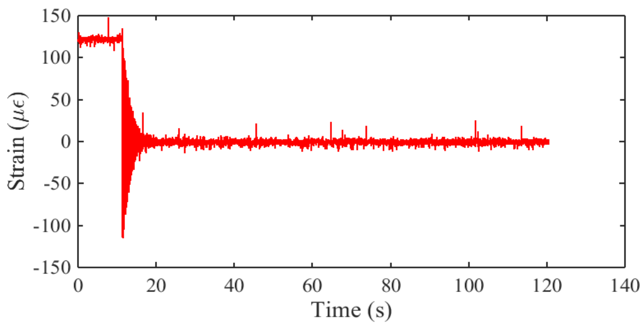

(c)

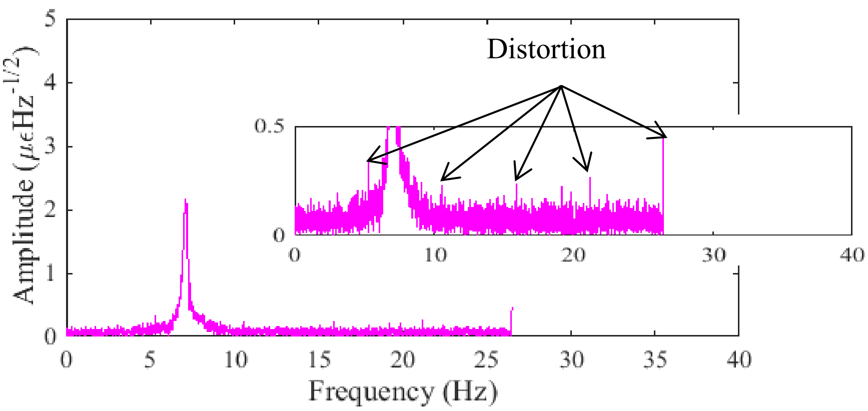

(d)

Figure 6.14: Simultaneous 120-s measurements: (a) time history of Z-axis acceleration, (b) single-sided amplitude spectrum from Z-axis acceleration, (c) time history of strain and (d) single-sided amplitude spectrum from strain.

6.4.3 Comparison with Commercial Wireless Strain Measurement System

Simultaneous measurements were conducted with both MSITA and CWLSS systems upon cantilever beam predominantly to determine the natural frequency detection accuracy of MSITA strain measurement results. The strain gauge for CWLSS was attached on the bottom surface at a same 0.675-m distance from O (according to Equation 6.2 this should provide same strain value as when the strain gauge attached to the same place on top surface). The sampling rate of CWLSS was set to 64-Hz which was the nearest for the ODR of ~53-Hz achieved for MSITA strain interface. Figure 6.15 and Figure 6.16 depict the time history and the amplitude spectra, respectively, of an example simultaneous strain measurement result acquired. The dynamic strain signal of MSITA is almost equal to the signal acquired from the commercial system. The main difference which can be seen in both time history and amplitude spectra of systems is the default noise. This is due to two main reasons. One is the higher ADC resolution of 16 bit in the strain interface of MSITA than that 12 bit of CWLSS. Therefore, MSITA tends to pick-up noise than CWLSS system. Another reason is the failure of the filter of the MSITA to provide the expected design outcome of filtering out high-frequency components. Therefore, the filter of the MSITA should be reconsidered in a future design.

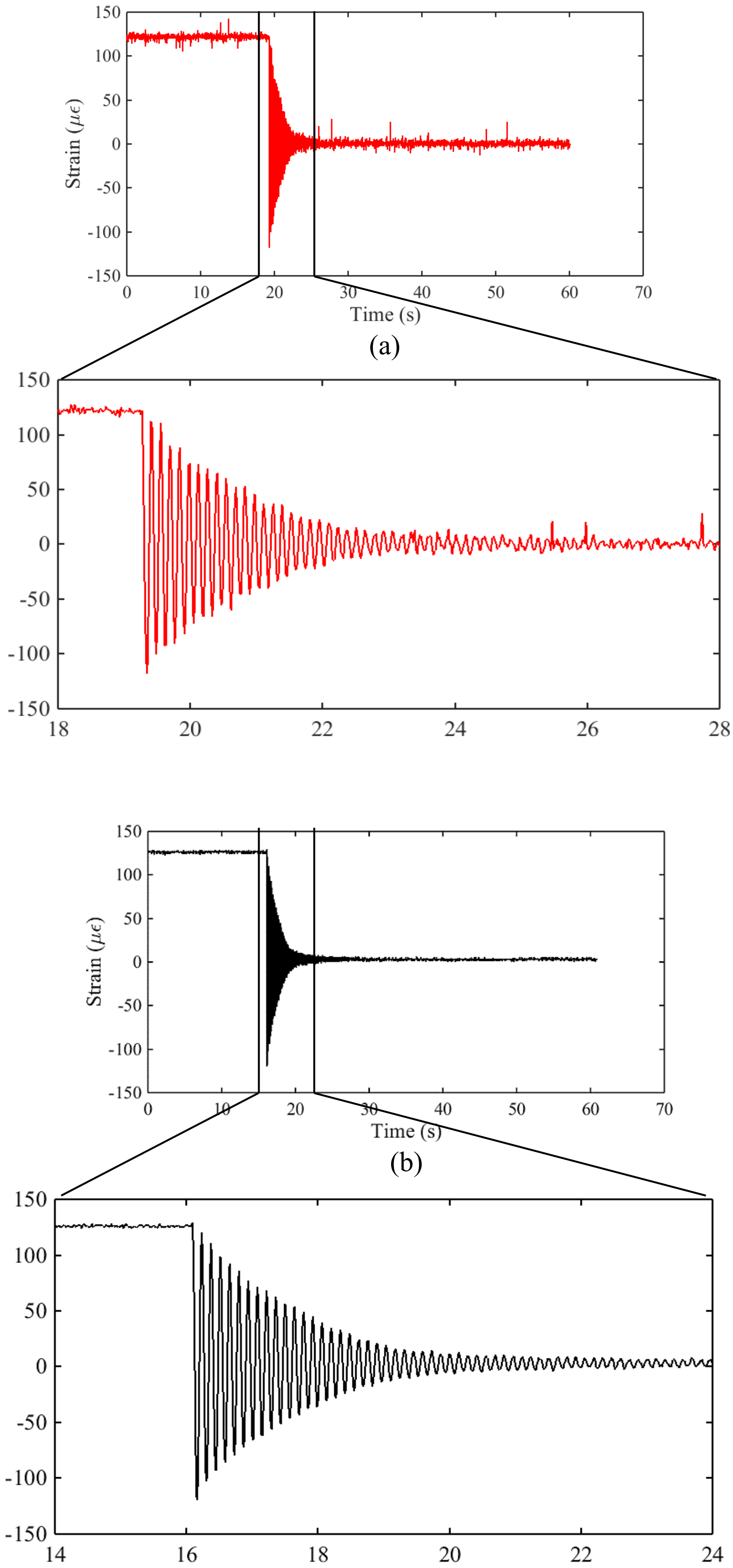

Figure 6.15: Time history of simultaneous strain measurement results from: (a) MSITA and (b) CWLSS.

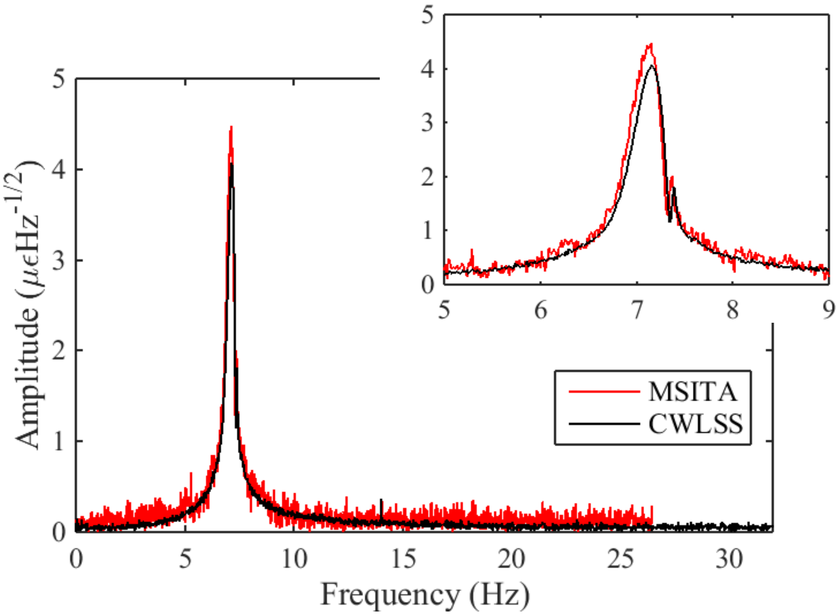

Figure 6.16: Single-sided amplitude spectra of simultaneous strain measurement results from MSITA and CWLSS.

Consequently, the natural frequency determination from dynamic strain measurement results of 20 number of vibration trials of the beam was compared. In the case of MSITA, the Z-axis acceleration results were also considered as it provided the opportunity to compare the natural frequency determination between simultaneously measured acceleration and strain. The denoised results of the both systems (as done in Chapter 5) were considered predominantly to achieve the prominent peak smoothing of amplitude spectrum of MSITA (even though denoising is necessary to remove the introduced distortion from *Watermark interrupt*, the distortion can be disregarded as they are low in amplitude due to high SNR of both acceleration and strain measurements acquired in this experiment). The denoising of the measurements from CWLSS was done only to achieve fair comparison (not necessary as it demonstrates negligible peak distortion, see Figure 6.16).

Figure 6.17 shows natural frequency determination of both original and denoised signals from MSITA and CWLSS systems (dashed lines denote maximum variation range). The advantage of denoising can be seen as the variation of the natural frequency representation has been reduced mostly to one frequency resolution due to the reduction of peak ambiguity. Even the variation of the majority of trials (18 out of 20) seen in natural frequency determination from the strain measurement of MSITA is within one frequency resolution of 0.0129 Hz. The maximum variation ranges of the determined natural frequency values are listed in Table 6.6 for both original and denoised measurements.

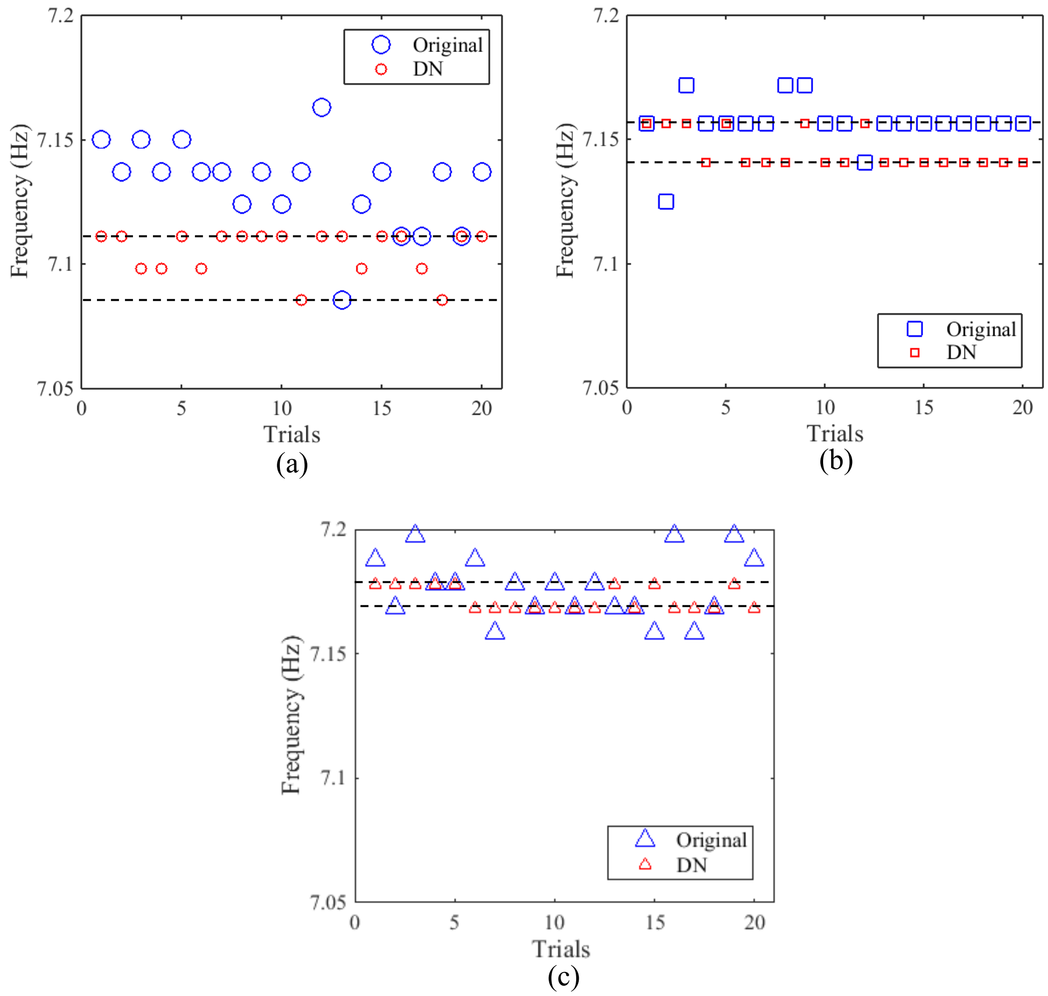

Figure 6.17: Natural frequency determination by (a) strain measurement results of MSITA, (b) strain measurement results of CWLSS and (c) acceleration measurement results of MSITA (DN - denoised).

Table 6.6: Maximum variation range of the determined natural frequency.

System	Measurement	Max. Variation Range(Hz)	
		Original	DN
MSITA	Acceleration*	0.0388	0.0097
	Strain**	0.0774	0.0258
CWLSS	Strain***	0.0468	0.0156

* at a frequency resolution of 0.0097 Hz (80-Hz output data rate and 8192 data points).
** at a frequency resolution of 0.0129 Hz (53-Hz output data rate and 4096 data points).
*** at a frequency resolution of 0.0156 Hz (64-Hz output data rate and 4096 data points).

The mode of the determined natural frequency values of denoised measurements was considered as it provides the ability of the systems to repeat the information. Table 6.7 provides this information in relation to Figure 6.17. Even though proper tallying of the natural frequency results are not possible due to different ODRs of systems (even between simultaneous acceleration and strain measurements of MSITA), they have close values. The natural frequency determination by strain measurement of MSITA is 0.06 Hz less than that by the acceleration measurement from the same. The difference between ODRs of acceleration (80 Hz) and strain measurements (53 Hz) has an influence on this variation. However, when considering the repetition of the natural frequency determination (c.f. Figure 6.17(a) and 6.17(c)) this value can be stated as MSITA system quality for the current configuration given in Table 6.3. The natural frequency determination from the strain measurement of MSITA has a −0.03-Hz error when benchmarked with CWLSS system.

Table 6.7: Natural frequency determination by MSITA and CWLSS.

Frequency Determination	MSITA		CWLSS
	Acceleration	Strain	
Mode (Hz)	7.17	7.11	7.14
Difference (Hz)	−0.06* / −0.03**		

* depending upon acceleration measurement of MSITA.
** benchmarking with strain measurement of CWLSS.

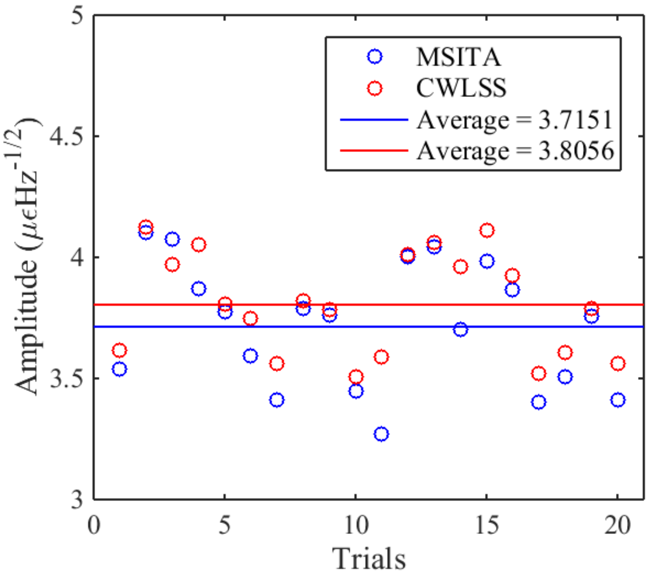

Figure 6.18: Amplitude comparison of the determined natural frequency between MSITA and CWLSS.

Figure 6.18 provides the comparison of the amplitude of the determined natural frequency in the spectra from simultaneous strain measurement results of the cantilever beam by the commercial and RFID-based wireless systems. The amplitudes of the single-sided amplitude spectra of strain measurement results by MSITA for each trial have good agreement with those from CWLSS (since calibrated in advance against DSM and gains of the strain interfaces of both systems were kept nearly the same). According to Figure 6.18, the strain sensitivity of the RFID-based wireless system is 97.6 % (considering average amplitude values of all trials) of that of CWLSS system. This can be visualized also in Figure 6.16 in which both systems show almost the same dynamic strain signal amplitude (The less sensitivity of MSITA shown in the amplitude comparison is predominantly due to default noise present which tends to suppress the peak amplitude).

6.5 Conclusion

This chapter presented the developed RFID-based wireless multi-sensor system for measurement of dynamic acceleration and strain of infrastructure simultaneously. The semi-passive tag antenna integrated acceleration sensor (TAIAS) introduced in Chapter 5 was enhanced to a multi-sensor integrated tag antenna (MSITA) with additional dynamic strain measurement capability. This was accomplished by a custom designed miniature multi-sensor circuit which is compatible to be integrated with the tag antenna. Essentially, the performance of the enhanced system was investigated by applying it to monitor a cantilever steel beam. Static strain, simultaneous dynamic acceleration, and strain measurements were conducted upon the cantilever beam and the results were presented. Finally, the acquired static and dynamic strain measurement results were compared with measurement results from a commercial system (CWLSS).

The firmware designed for the TAIASs in Chapter 5 was enhanced to acquire dynamic strain measurements simultaneously with dynamic acceleration in MSITA. Under the combined constraints of time consumed for *non-volatile memory writes* of RFID tag chip and the capability of the data acquisition application the MSITA could achieve 40-Hz and 26.5-Hz spectral bandwidth for 3-axis acceleration (for each axis) and strain measurements, respectively. The possibility of determining the natural frequency (1st mode) of the cantilever beam with nearly the same accuracy from both acceleration and strain measurements from MSITA was experimentally proven. The experimentally acquired natural frequency value was almost equal to the calculated theoretical value.

The comparison of the RFID-based wireless multi-sensor system performance with CWLSS in terms of the natural frequency determination and strain sensitivity has been done by performing a number of measurement trials. The natural frequency determination accuracy of the strain measurements of the RFID system was in good agreement with CWLSS configured with the nearest sample rates (CWLSS has slightly higher sample rate). In fact, it had −0.03 Hz difference with CWLSS system and −0.06 Hz difference with the natural frequency determination from its own acceleration measurement. The maximum possible natural frequency determination variation of MSITA was within ~0.0258-Hz range where 90 % of the values showed variation within ~0.0129 Hz. This variation was in good agreement with CWLSS system operated with close sampling rate. The strain signal sensitivity of the MSITA was benchmarked by comparing the amplitude of the determined natural frequency within the single-sided spectrum. According to the comparison, the sensitivity of the RFID-based wireless system is 97.6 % of the sensitivity of CWLSS system.

Chapter 7 Passive Mode Investigation of Wireless Power Flow in the Vicinity of a Steel I-Beam and Phase-Based Structural Displacement Measurement Using an RFID Antenna System

7.1 Introduction

In this chapter, UHF power flow in the vicinity of a steel I-beam illuminated by a reader has been studied at different orientations of the beam with respect to the reader antenna. Furthermore, an investigation of phase angle-based structural displacement sensing has been performed. Both investigations have been carried out using an RFID antenna system operated in passive mode. Following sections of the chapter discuss the background leading to the studies, methodologies of the investigations, the computer simulation, and the measurement results. Finally, the conclusions are given based on the results of performed simulations and measurements.

7.2 Background for Wireless Power Flow Investigation

The developed RFID-based wireless IHM system in previous chapters of the thesis had semi-passive UHF RFID tag antenna integrated sensors (i.e. TAIASs and MSITA) which could operate in P and BAP communication modes. The system proposed in Chapter 3 was enhanced by designing a construction material mountable UHF RFID tag antenna (see Chapter 4) providing the possibility of directly mounting the tag antenna integrated sensors on structures made out of concrete or metal (overcoming the tag antenna detuning due to materials of concrete and metal). However, an infrastructure under test can be made out of structural members of different shapes in different orientations (with respect to reader antenna of the developed system). The performance of a wireless system, in particular, the developed system which operates with passive backscatter communication (i.e. wireless interrogation signals from the reader should have a threshold power level at the tag antenna integrated sensors) can be influenced by these shapes and orientations.

The electromagnetic power flow (as power density in Wm^{-2}) is given by the time averaged value of instantaneous Poynting vector (S_{av}) [230, 231]. According to complex Pointing theorem this average power density is given by,

$$S_{av} = \frac{1}{2} Re\{\boldsymbol{E} \times \boldsymbol{H}^*\}, \qquad 7.1$$

where $\boldsymbol{E}$ and $\boldsymbol{H}$ represent the phasors of electric (Vm^{-1}) and magnetic (Am^{-1}) quantities respectively and * represent the complex conjugate. This average power density has been used in [232] to deduce energy streamlines to identify the backward radiation of horn antennas. The same approach was used in [158] where RF energy transmission in metallic environment has been studied with simulated energy flow stream lines. The simulation studies conducted in free space, in metal chamber and with various shapes of metal obstacles have shown that multi-layer antennas perform better than dipole antennas in terms of RF energy reception in metallic environments. A global view of possible variations of the energy flow has been observed in particular with the study which involved metal obstacles. Electromagnetic simulations have been performed in [233] for 5.2-GHz wireless signal propagation in an indoor office environment with visualised Poynting vectors. The simulations have shown clear influence from the reinforced concrete walls upon global signal power flow in considered indoor environment. Furthermore, the performance of selected commercially available RFID tag antennas was studied in [234] for tagging purpose of hollow steel beams used in construction industry. The study has been carried out using read range as the performance indicator where tag antennas were mounted both inside and outside of the hollow steel beams. Subsequently it was concluded that a careful investigation is needed to acquire adequate performance from commercial RFID tag antennas used in such applications. However, when considering the RFID-based wireless sensor system for IHM, the wireless signal power incident on RFID tag antenna integrated sensors is critical. Furthermore, both global signal power flow towards the structural member (upon which the tag antenna integrated sensors are mounted on) and local signal power flow in the vicinity of the structural member are equally important to make decisions on the system setup (e.g., placement of reader antenna and tag antenna integrated sensors). Previous studies of investigating signal power flow of such nature using RFID antenna systems are limited.

7.3 Methodology of Wireless Power Flow Investigation in the Vicinity of Steel I-Beam

Modern electromagnetic simulation tool CST Microwave Studio [160] is capable of spatially simulating the maximum value of the power flow density within a single time period given by Equation 7.1. Therefore, in this investigation, a standard 4-m long steel I-beam (100UC14.8) was modeled with a reader antenna (simulated in transmitting mode at 923 MHz) as shown in Figure 7.1. The I-beam was chosen due to the fact that the performance and applicability of the developed RFID-based wireless dynamic acceleration measurement system were tested using it (see Chapter 5). Identical RFID tag antennas designed in Chapter 4 were mounted on the I-beam as shown in Figure 7.1(a) and at different distances (*d*) for two orientations as shown in Figure 7.1(b). Each of those orientations had two scenarios as given in Table 7.1. These tag antennas were loaded with lumped elements (according to the

RFID chip frontend model [188]) and simulated in the receiving mode. Therefore, in addition to the visualization of the power flow, the voltage across the lumped elements could be monitored. If this voltage is denoted by v, the relationship between it and the incident power density on the tag antenna can be given by [235]:

$$S_{av} \propto |v|^2 \tag{7.2}$$

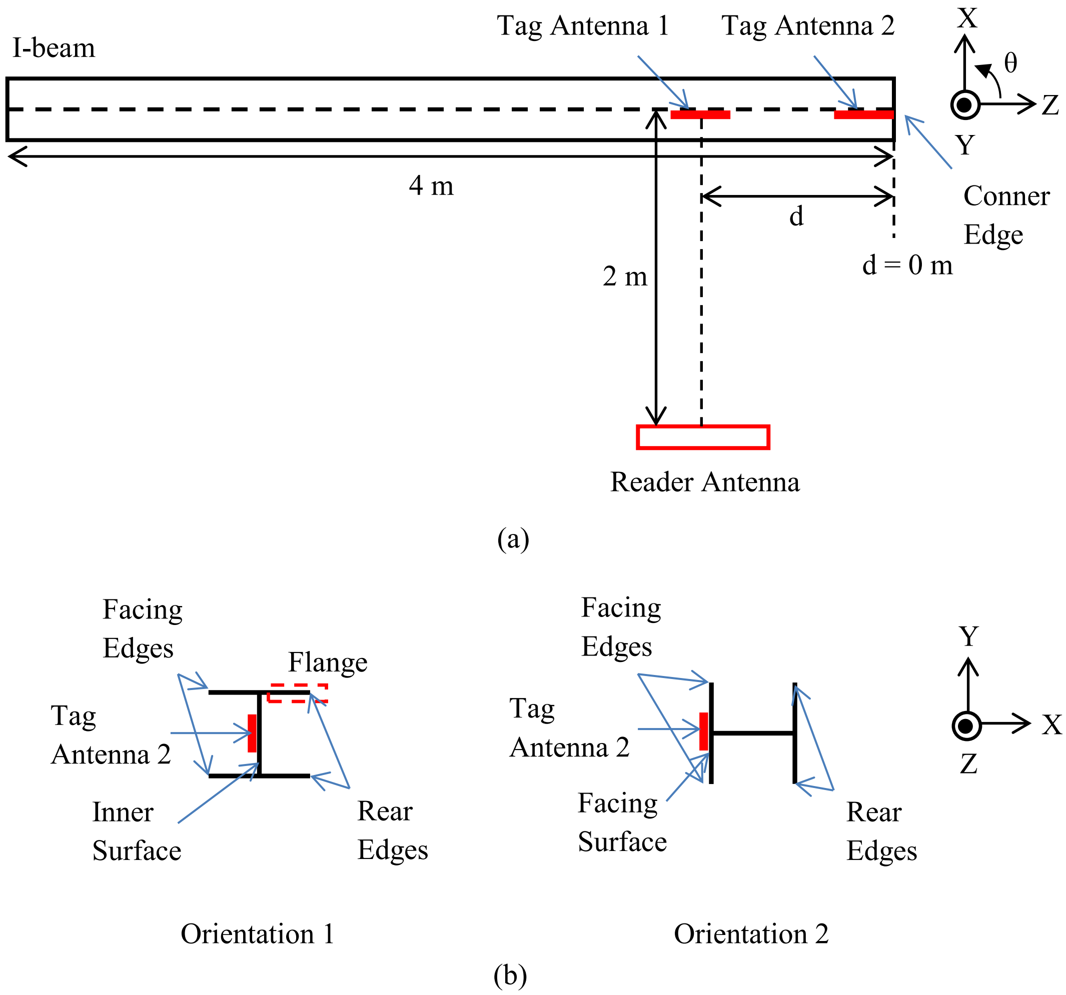

Figure 7.1: Schematic of the simulation and measurement setup: (a) top view of I-beam orientation 1 and (b) side view with different orientations of I-beam for scenario 1.

Table 7.1: Tag antenna positioning.

d (m)	Scenario	
	1	*2*
0.061	Tag antenna 2	−
0.500	Tag antenna 1	Tag antenna 1
0.950	−	Tag antenna 2

The illumination source (reader antenna) is a key component in the simulation model. The UHF RFID tag antennas used in this investigation have linear polarization and this is a general case for RFID systems. The use of a circularly polarized reader antenna is an established practice (followed in previous chapters) to eliminate higher polarization mismatch which is possible even with the slightest misalignment of antennas if linear polarized reader antenna is used. Owing to this, a circularly polarized reader antenna was incorporated in the simulation model as an illumination source.

The experimental case was formed using the RFID wireless link budget. An RFID tag antenna should have a minimum incident power (P_i) to successfully respond to an interrogation from the reader given by [194]:

$$P_i = P_{th} - G_t - 10\log(\tau), \qquad 7.3$$

where P_{th} is the sensitivity of RFID tag chip (dBm), G_t is the gain of RFID tag antenna (dBi) and τ is the power transmission coefficient between tag antenna and tag chip. According to Equation 7.3, unless the tag antenna characteristics change due to location on the I-beam, P_i should be same for identical tag antennas and it is directly proportional to the power density at the tag antenna locations. P_i can be related to minimum transmitted power from the reader (P_r) to receive tag antenna response according to wireless link budget given by [194]:

$$P_r = P_i - G_r - L - 10\log(p), \qquad 7.4$$

where G_r is the gain of the reader antenna (dBi), L is the path loss (dB) and p is the polarization efficiency. Therefore, P_r which is a measurable parameter by the RFID system becomes an indicator of P_i given that the orientation of the tag and reader antennas is being kept the same within the same distance. Consequently, if tag antenna 1 has higher P_r than tag antenna 2 (see Figure 7.1) it indicates that the location of the tag antenna 1 receives less power ($< P_i$) for a given power transmitted by the RFID reader.

7.4 Simulation

7.4.1 Adaptation of Illumination Source

An adapted model of the circularly polarized patch antenna given in [236] was used in the simulation model. The parametric size adaptation of ground plane and the substrate of the initial antenna model were done in CST Microwave Studio to achieve its performances closer to the Laird Technologies® S9025PR reader antenna [176] used in the experiment. In this process, efforts were made to keep the axial ratio of the antenna ≤ 2 dB at 923 MHz. Table 7.2 provides the achieved performance parameters for adapted antenna for simulation model and the antenna used in the experiment. Figure 7.2 depicts the far-field gain pattern of the reader antenna after adaptation. According to it, the adapted reader antenna has a symmetric gain pattern on *XZ* plane while it has an approximately symmetric gain pattern on *YZ* plane.

Table 7.2: Reader antenna performance parameters.

Parameters	**Antenna**	
	Simulation	***Experiment****
Gain (dBi)	5.78	5.50
Angular width (degrees)	94.70	100.00
Total efficiency	0.87	NA
Axial ratio (dB)	3.00	2.00

* the information is from the datasheet [176].

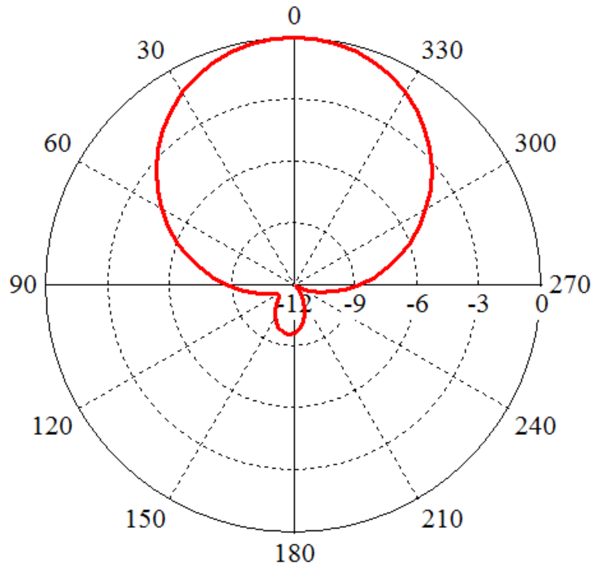

Theta (deg) vs dBi

(a)

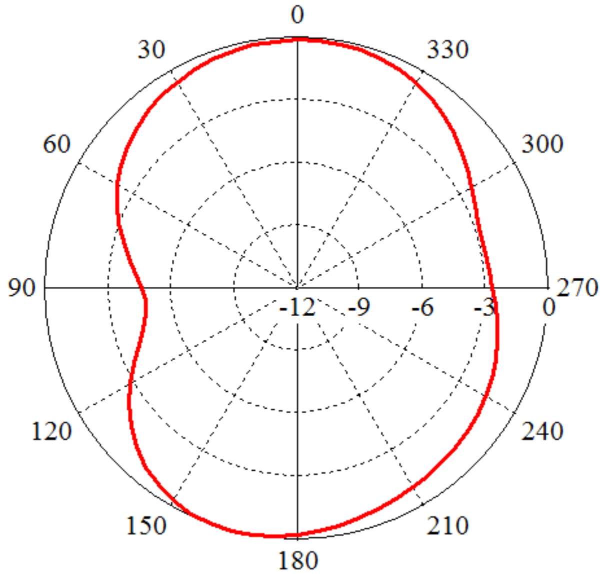

Phi (deg) vs dBi

(b)

Figure 7.2: Normalized far-field gain pattern of simulated reader antenna at 923 MHz: (a) *XZ* plane and (b) *YZ* plane.

7.4.2 Simulation Results

Figure 7.3 shows the power flow towards the tag antenna positioned at line-of-sight to the reader antenna. Approximate equal power flow deviation away from the I-beam can be seen when power flow approaches it at orientation 1 as seen in Figure 7.3(a). The pattern of deviation has created a shadow with low power density at the rear side of the cross section. Furthermore, power density is higher near facing edges than near inner surface. The incident power has concentrated near the facing surface at orientation 2 as seen in Figure 7.3(b). The center of the surface has low power density due to high power concentration near the facing edges. Additionally, high power density has occurred even at the rear edges of the beam. Overall the results show that power flow near the I-beam is influenced significantly by the orientation of the I-beam.

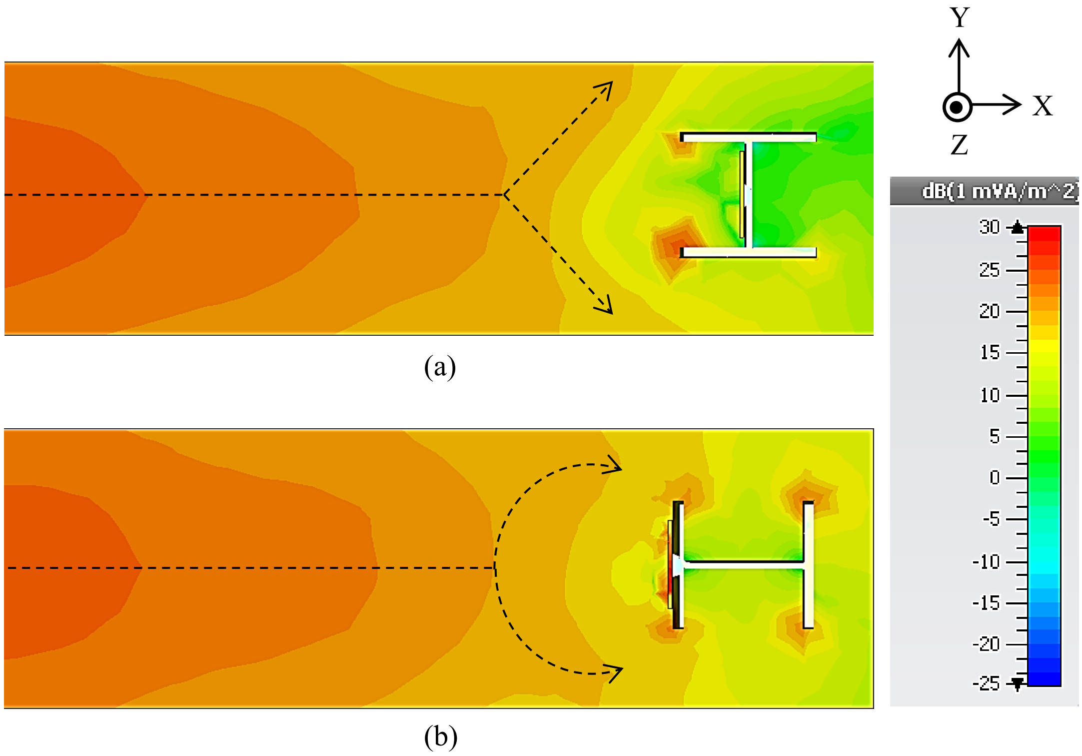

Figure 7.3: Cross-sectional side view of power flow towards I-beam at (a) orientation 1 and (b) orientation 2 at 923 MHz.

Figure 7.4 provides a detailed power density distribution in the vicinity of the I-beam in orientation 1. Tag antenna 2 has higher incident power density than tag antenna 1 (which is at line-of-sight with reader antenna) in scenario 1 and it is mostly influenced by the increased power concentration around the lower facing edge and the flange of the I-beam. In scenario 2, tag antenna 2 has higher incident power density than tag antenna 1 due to increased power concentration on upper facing edge and the flange of the I-beam. Tag antenna 1 in scenario 2 seems to have slightly higher incident power density than the same in scenario 1 which may be due to the difference in coupling effect caused by the variability of the distance between tag antenna placements.

Figure 7.5 depicts the power density distribution in the vicinity of I-beam at orientation 2. It can be seen from Figure 7.5 that tag antenna 2 in scenario 1 has higher incident power density than tag antenna 1. The effect of the corner edge on power density distribution can be highlighted here as there is increased power concentration near all the edges of the I-beam at d = 0.061 m (the scenario 1 at orientation 1 has the same effect which could not be highlighted due to the use of a different scale). In scenario 2, tag antenna 2 has less incident power density than tag antenna 1 due to more power flow deviation towards lower edges of the I-beam.

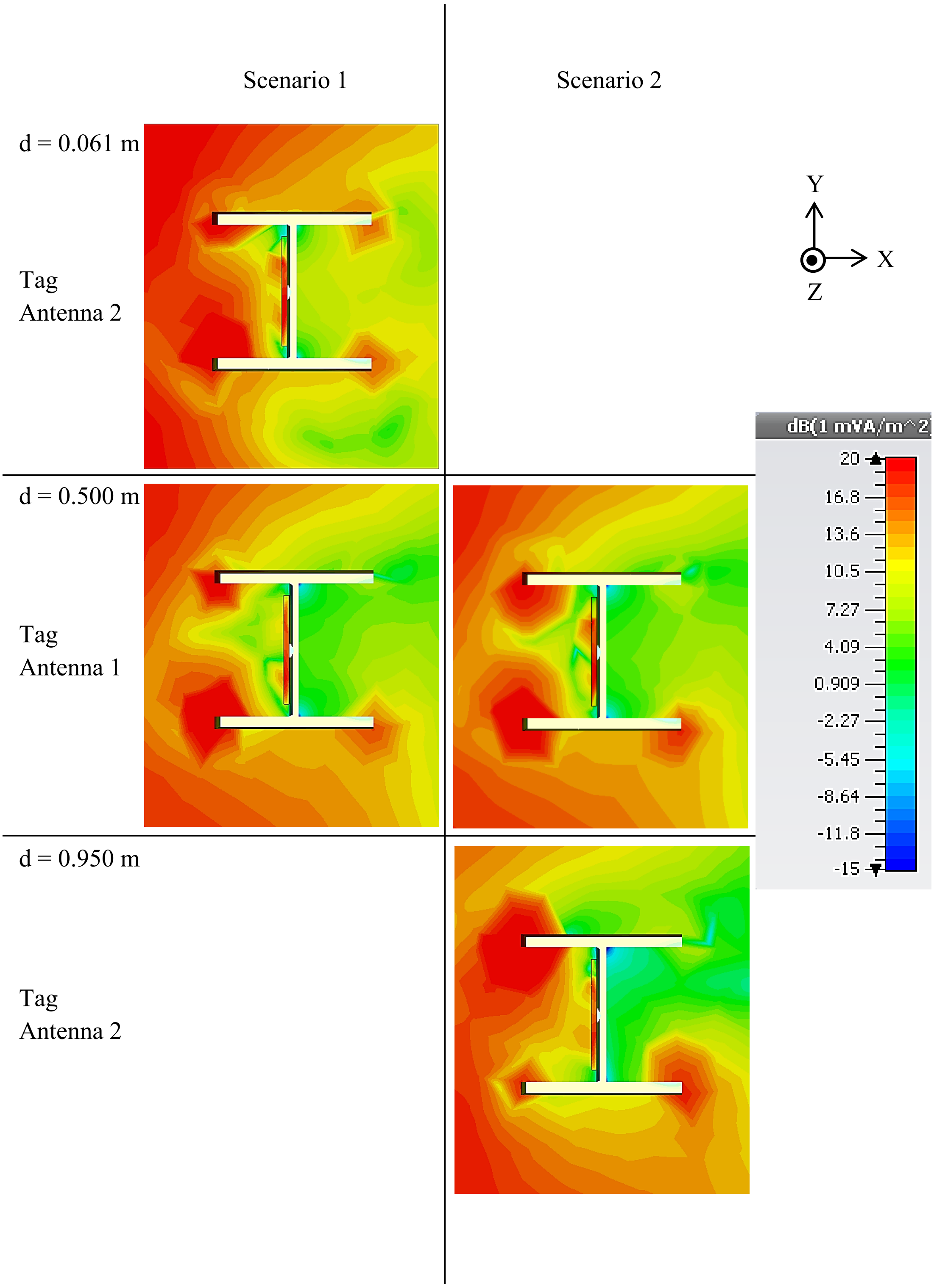

Figure 7.4: Power density distribution in the vicinity of I-beam at orientation 1 at 923 MHz.

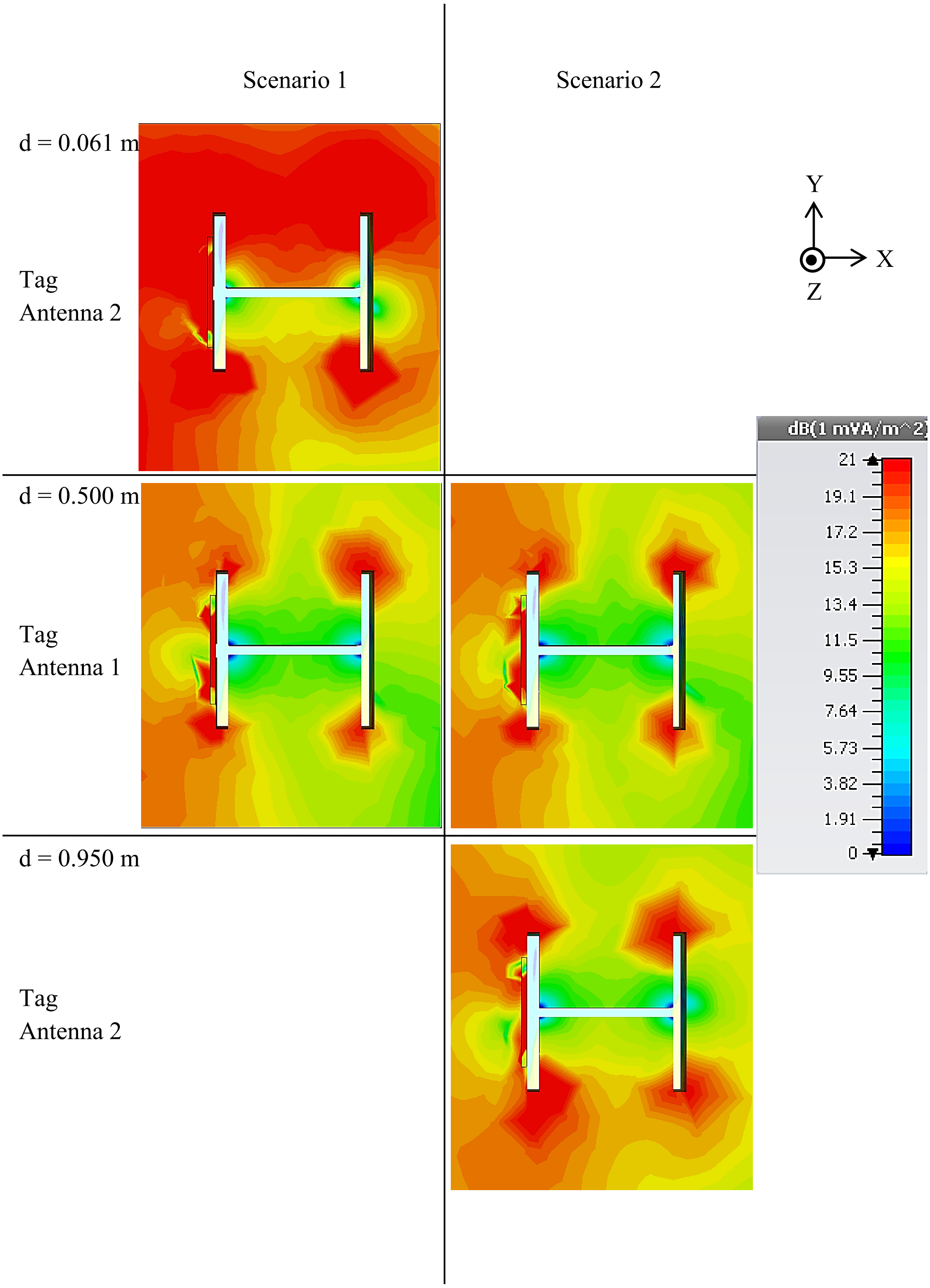

Figure 7.5: Power density distribution in the vicinity of I-beam at orientation 2 at 923 MHz.

Figure 7.6 and Figure 7.7 show the power density distribution in the vicinity of the I-beam on the same scale for scenario 1 and scenario 2, respectively (a different scale has been previously used to highlight the power density at the inner surface in Figure 7.4). Additionally, the Figure 7.6 and Figure 7.7 have the simulation results in which the I-beam was illuminated without tag antenna placement. According to those figures, there is higher power density in the vicinity of I-beam at orientation 2 than at orientation 1. The placement of the tag antennas has increased the incident power density at studied locations. Furthermore, it can be confirmed that the shape of the I-beam has a major contribution to the power density distribution in its vicinity with and without tag antenna placement.

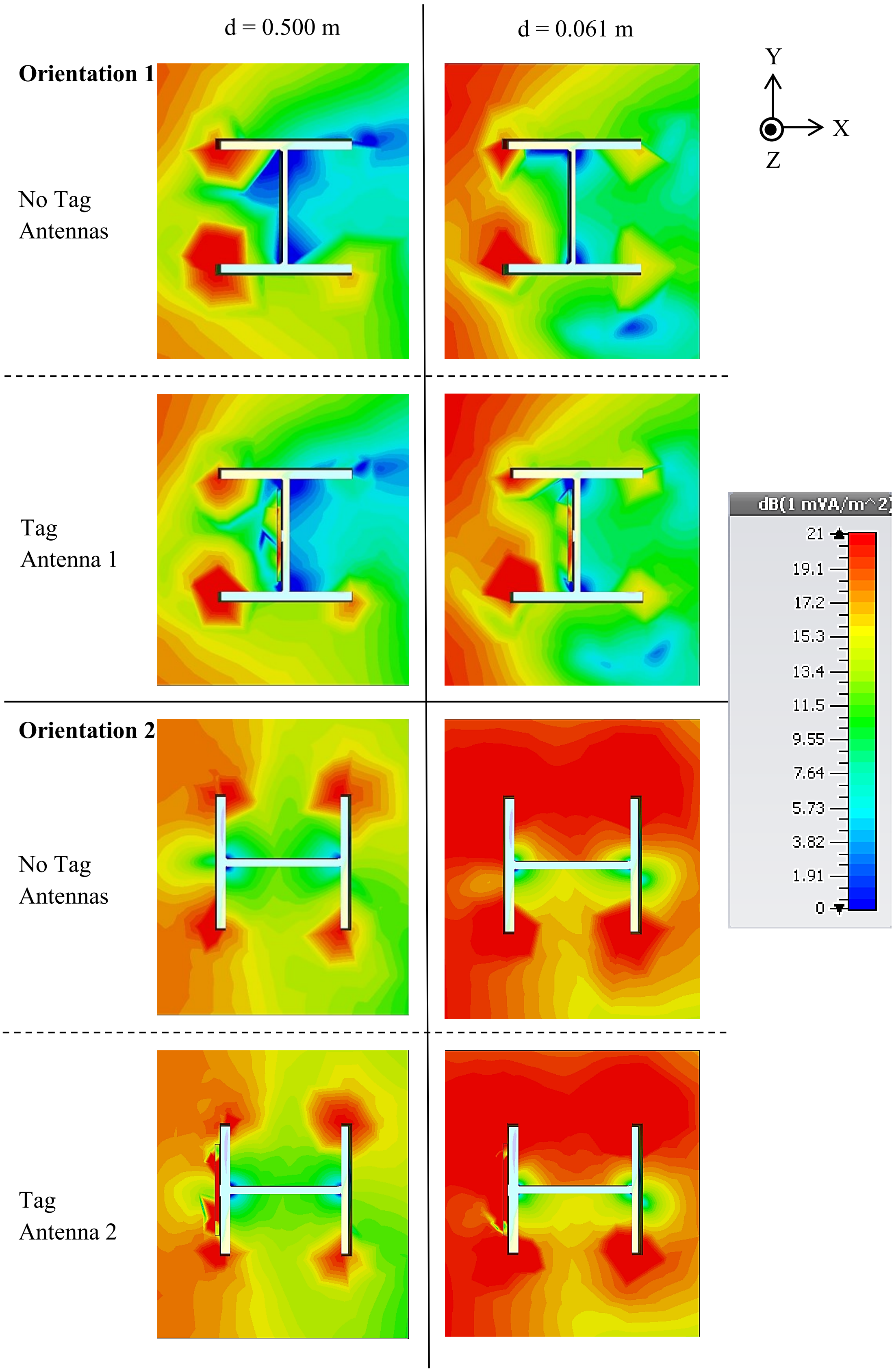

Figure 7.6: Power density distribution in the vicinity of I-beam for scenario 1 in the same scale including I-beam only (without tag antenna placement) simulation for two orientations at 923 MHz.

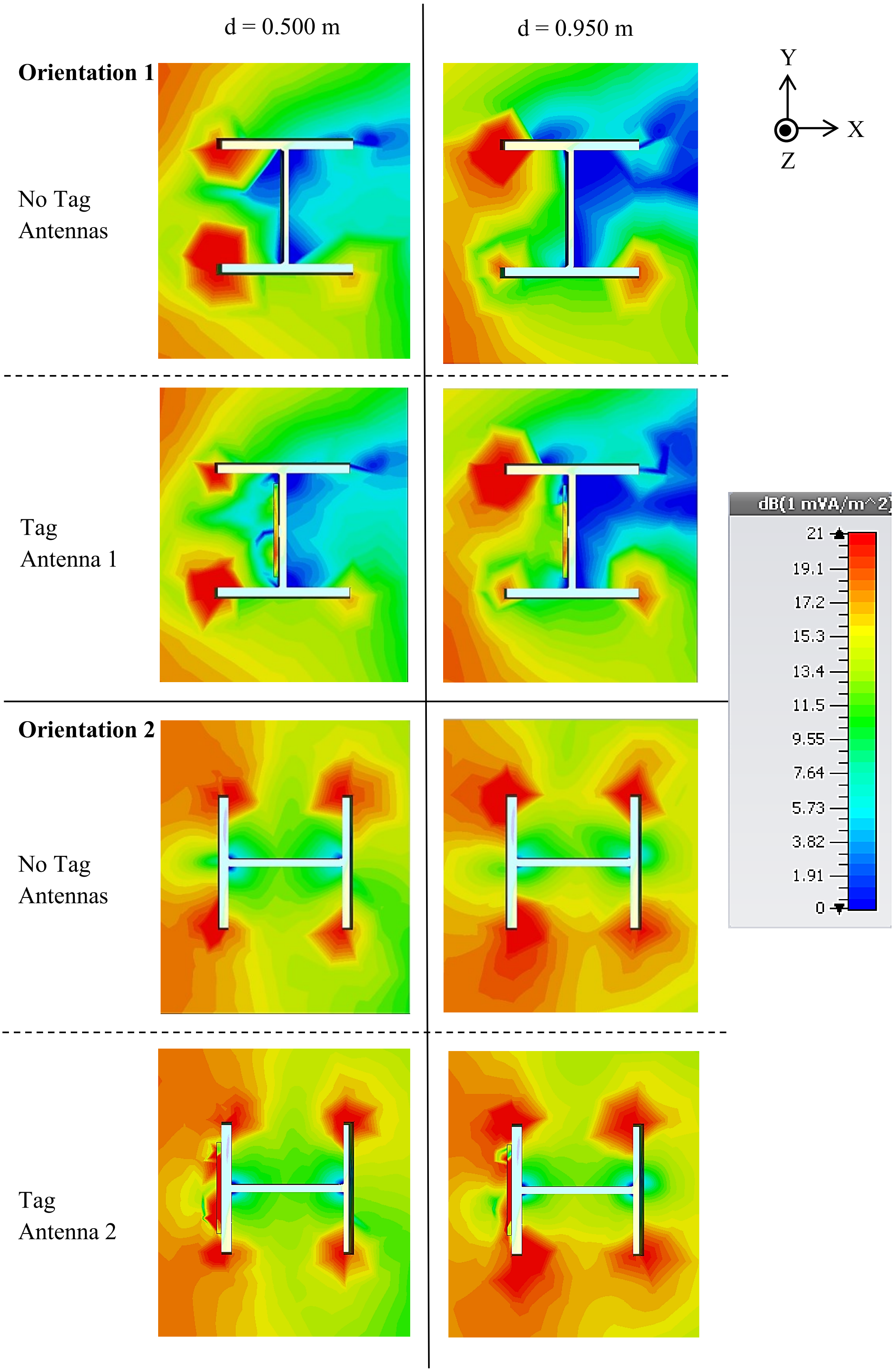

Figure 7.7: Power density distribution in the vicinity of I-beam for scenario 2 in the same scale including I-beam only (without tag antenna placement) simulation for two orientations at 923 MHz.

Simulation of transmitting mode of tag antennas has also been conducted to investigate tag antenna performance in different locations on the I-beam. Figure 7.8 shows the far-field gain pattern of the tag antennas in *XZ* plane for the investigated scenarios. According to Figure 7.8, the tag antennas have higher gain in the placement of orientation 2 than orientation 1 for both scenarios. This shows the influence of the flange of the I-beam on tag antenna gain when mounted on the inner surface. When considering Figure 7.8(a), the gain pattern of the tag antenna 2 has been affected by the placement at the corner edge in both orientations. However, both gain patterns (tag antenna 1 and 2) are approximately identical in the direction of interest (towards the reader antenna) where it would provide a minimal effect on the wireless link budget for each orientation of I-beam. Figure 7.8 (b) confirms that both tag antennas have identical performance as the placement environment on the I-beam are identical for each orientation in scenario 2.

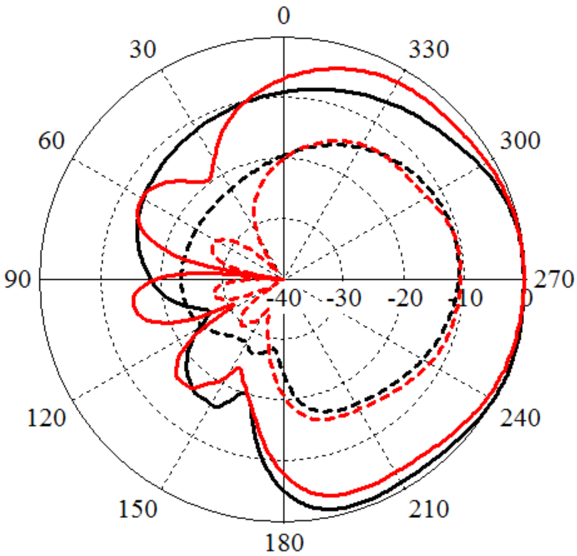

Theta (deg) vs dBi
(a)

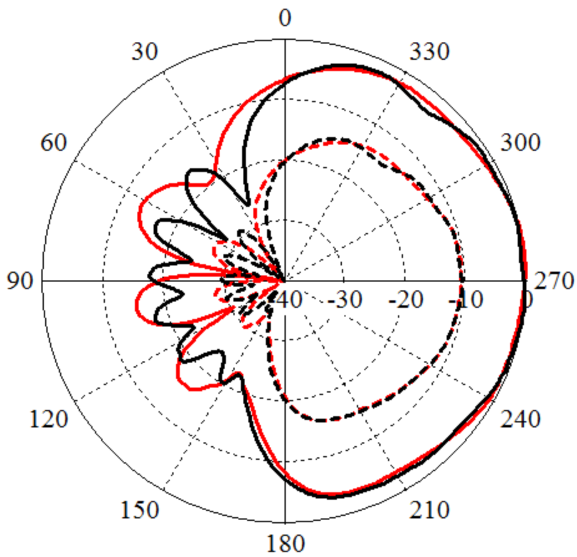

Theta (deg) vs dBi
(b)

Figure 7.8: Normalized far-field gain patterns for tag antennas on *XZ* plane for I-beam at different locations and beam orientations at 923 MHz: (a) scenario 1 and (b) scenario 2 (red - tag antenna 1, dashed - orientation 1).

Figure 7.9 shows the simulated magnitude of the voltages across the lumped elements of tag antennas at 923 MHz when the I-beam was illuminated by the reader antenna. The voltages for orientation 2 is considerably higher than that of orientation 1 which is evident to be influenced by both factors of higher gain demonstrated by tag antennas (see Figure 7.8) and higher power density distribution in the vicinity of the I-beam (see Figure 7.6 and 7.7) in orientation 2. According to Figure 7.9, the lumped element of tag antenna 1 has lower voltage across it than tag antenna 2 for both scenarios at orientation 1 which tallies with the observation made in Figure 7.4 where the inner surface of the I-beam had higher power density at tag antenna 2. The simulated voltage levels across lumped elements of tag antennas with I-beam orientation 2 also tallies with the observation made in Figure 7.5 where tag antenna 2 had higher power density in the vicinity than tag antenna 1 in scenario 1 and otherwise in scenario 2.

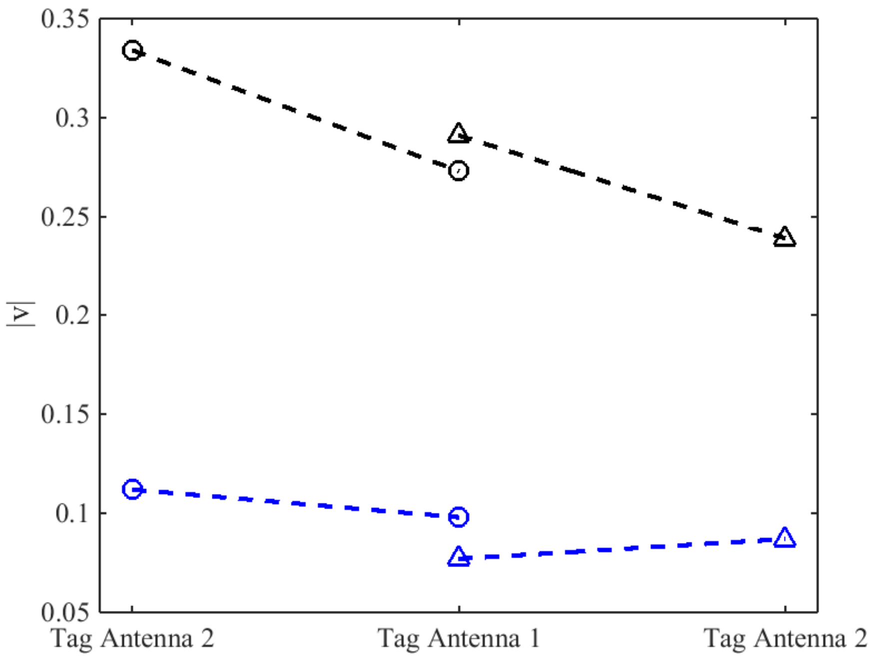

Figure 7.9: Magnitude of the maximum voltage across lumped elements of tag antennas at 923 MHz (blue - orientation 1, black - orientation 2, o - scenario 1 and Δ - scenario 2; the points are connected only for illustrative purpose).

7.5 Measurement Approach

The measurement setup was arranged as shown in Figure 7.1. Two identical tag antennas designed in Chapter 4 were positioned on the I-beam in two orientations at selected locations according to Table 7.1. A picture of the measurement setup is shown in Figure 7.10. The reader antenna was kept 1-m above ground with line-of-sight to tag antenna 1. As described in Section 7.2, P_r was measured using Impinj Speedway Revolution Generation 2 UHF RFID reader [164]. The transmit power was increased by 0.25-dBm steps using Impinj Multireader software [193] during the measurement until the reader receives responses from each tag antenna. The software is capable of recording P_r of the first received response from the tag antennas. Figure 7.11 provides the average P_r measurement for 10 numbers of trials in each scenario.

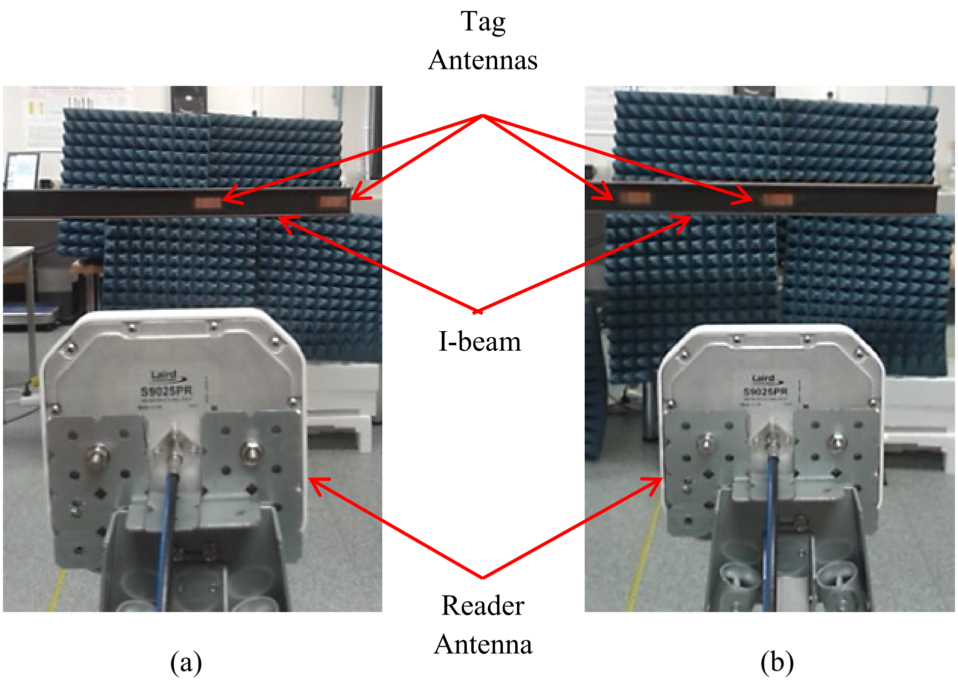

Figure 7.10: Picture of the measurement setup with I-beam orientation 1: (a) scenario 1 and (b) scenario 2.

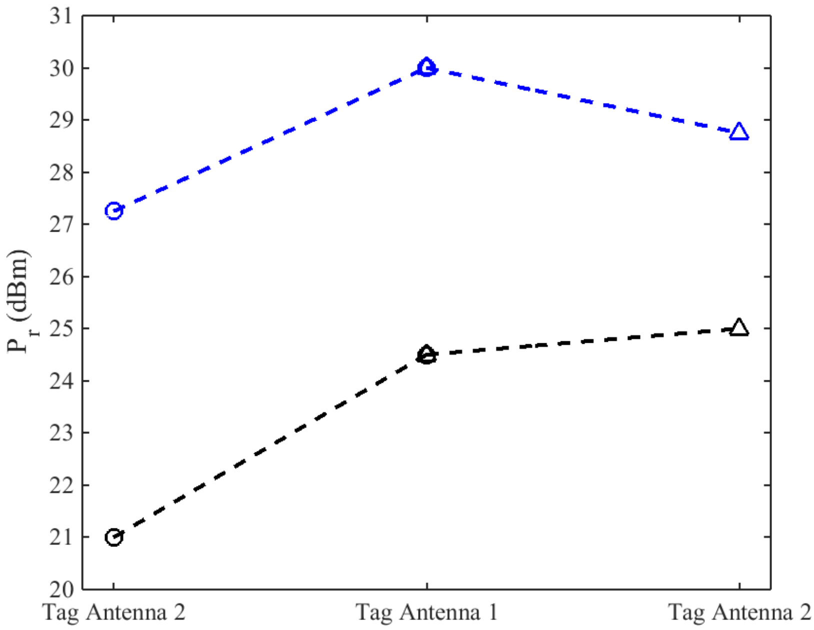

Figure 7.11: Minimum transmit power needed to receive a response from tag antennas (blue - orientation 1, black – orientation 2, o - scenario 1 and Δ - scenario 2; the points are connected only for illustrative purpose).

According to Figure 7.11, P_r for orientation 2 is less than the orientation1 for both scenarios. This is due to the combined effect of higher gain that the tag antennas demonstrate and the higher power density distribution in the vicinity of I-beam in orientation 2 (see Figure 7.6, Figure 7.7 and Figure 7.8). This is also in accordance with the simulated magnitude of the voltage observed across lumped elements of the tag antennas in Figure 7.9. P_r for tag antenna 2 is less than that for tag antenna 1 in both scenarios with orientation 1 (tag antenna 2 always responded earlier than tag antenna 1). This confirms that the line-of-sight location has low incident power density than other studied locations of the I-beam at orientation 1. Tag antenna 2 had lower P_r than tag antenna 1 in scenario 1 for both orientations. This confirms the effect of corner edge of the I-beam where higher power density was observed (see Figure 7.4 and Figure 7.5). Furthermore, tag antenna 2 showed a slightly higher P_r in scenario 2 for orientation 1 which is also in accordance with the observed voltage trend in

Figure 7.9 (even though the measured P_r value difference is less, tag antenna 1 responded earlier than tag antenna 2).

Therefore, measurement results agree well with the simulation results for the investigated scenarios of both I-beam orientations. Based on this observation, the I-beam only simulation can also be justified by the measurement considering the similar power density distributions observed in Figure 7.6 and Figure 7.7 to the simulation with tag antennas. Experimental results may have added uncertainty due to multiple signal reflections. However, the experiment was conducted keeping a considerable volume of open space to other obstacles in the laboratory so that these unwanted effects are minimized. The power density levels in the simulation results depend upon constant input power of 0.5 W (~27 dBm) to reader antenna port and the free space path loss. Due to this reason, power density levels of the simulation results are always higher than that of same experimental scenarios.

7.6 Background on RFID-Based Displacement Sensing and Distance Estimation

RFID-based passive mode displacement sensing for IHM has been introduced in [40] by exploiting the reduction of performance of RFID tag antennas in the vicinity of metallic environments. The possibilities of using backscattered signal power and minimum transmitted signal power to receive a RFID tag antenna response as indicators of structural displacement were examined using a metal plate attached simply supported beam. The deformed beam leads the metal plate towards the tag antenna kept at an initial distance. The changes in backscattered signal power and minimum transmitted power (due to tag antenna detune) were correlated to the displacement of the beam. However, this method has a practical problem of holding (or attachment of) the RFID tag antenna since it has to be at some distance from the structure under test. An RFID-based system which can measure structural displacement with tag antennas which can be mounted on structures may be a solution for the aforementioned issue. In this context, the distance estimation techniques introduced in [237] can be useful. The frequency domain phase difference of arrival (FD-PDoA) principle is used in these applications to acquire the distance estimate [237-239]. The phase of a received tag antenna signal (ϕ in radians) is given by [237]:

$$\phi = \phi_p + \phi_o + \phi_{bs}, \tag{7.5}$$

$$\phi_p = -\frac{4\pi f d}{c}, \tag{7.6}$$

where ϕ_p is the phase rotation due to electromagnetic wave propagation (rad), ϕ_o is the phase offset introduced by RFID reader and reader antenna related components (e.g., cables and connectors), ϕ_{bs} is the phase rotation due to backscatter modulation at the tag antenna, f is the frequency (Hz), c is the velocity of wave propagation (ms^{-1}) and d is the distance between RFID reader antenna and tag antenna (m) [237]. Consequently, the estimated distance $\hat{d}$ (m) can be derived from Equation 7.5 [237]:

$$\hat{d} = -\frac{c}{4\pi}\frac{\partial\phi}{\partial f} \quad 7.7$$

for a continuous spectrum of transmitted frequencies and

$$\hat{d} = d + d_e \quad 7.8$$

where d_e(m) is the distance error related to ϕ_o and ϕ_{bs}. According to Equation 7.8, any change in d (i.e. true displacement Δd in m) is equal to estimated displacement ($\widehat{\Delta d}$ in m) assuming that variation of d_e is small (since ϕ_o and ϕ_{bs} are predominantly system dependent parameters).

The application of FD-PDoA technique with RFID technology in passive mode to sense displacement of structures is attractive as only the RFID tag antenna has to be mounted on the structure. The reported displacement measurement of infrastructure; in particular the deflection of bridge deck (depending upon the type of the bridge) and displacement of expansion joints of bridges are in the order of 4 to 20 mm and 0 to 20 cm, respectively [15, 240-243]. Since FD-PDoA principle with RFID technology in structural displacement measurements is unprecedented, substantial experimental work is needed to investigate the capability of the RFID system with designed tag antenna for such measurement.

Furthermore, due to wrapping nature of ϕ (∈ [0, 2π] radians), theoretically it will be repeated for each frequency after every change of 0.5λ-distance between reader antenna and the tag antenna. When considering the Australian UHF RFID frequency band this distance is ~0.162 m (minimum related to 925.75 MHz). The possibility of directly relating the phase change to displacement can also be investigated within this wrapping distance since it is substantial when comparing to aforementioned ranges of structural displacement.

7.7 Methodology

In this investigation, the RFID tag antenna is mounted on the structure and the reader antenna is attached to the reference point related to which the displacement of the structure has to be measured as shown in Figure 7.12. Then the phase angle of the received signal of tag antenna response is measured by the Impinj Speedway Revolution Generation 2 UHF RFID reader.

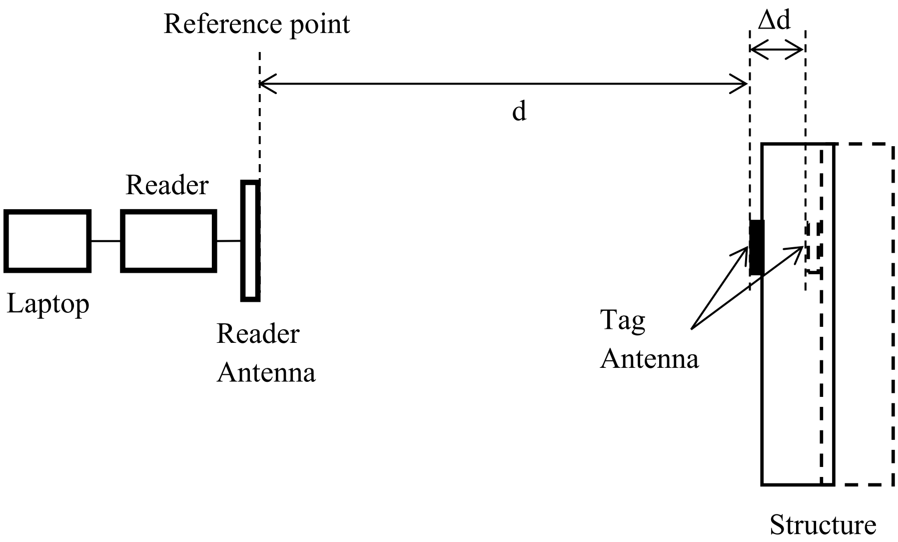

Figure 7.12: Schematic of the RFID-based structural displacement measurement setup.

When considering the Equation 7.5 in relation to Impinj Speedway Revolution Generation 2 UHF RFID reader, the ϕ_o consists of phase rotation introduced by transmitter and receiver circuits apart from reader antenna and cable components [244]. In particular, the phase rotation introduced by the receiver circuits depends upon signal to noise ratio (SNR) of the received tag antenna response which adds the influence of environment to the phase reading. Additionally, it depends upon and the thermal noise of the receiver. The portion of $d_e$subjected to ϕ_{bs} (d_{bs} in m) is given by [245]:

$$d_{bs} = \frac{Q_L \lambda_{res}}{\pi}, \tag{7.9}$$

$$Q_L = \frac{1}{2\pi f_{res} C(R_a + R_c)}, \tag{7.10}$$

where Q_L is the loaded quality factor of RFID tag antenna (when mounted or attached), λ_{res} is the wavelength at the resonant frequency (m), f_{res} is the resonant frequency of the tag antenna (Hz), C is the capacitance of RFID tag chip (F), R_a is resistance of RFID tag antenna (Ω) and R_c is the resistance of RFID tag chip (Ω). Therefore, d_{bs} can be variable due to changes in R_a depending on the environment in which the tag antenna is being used (e.g., influence of mounted material). However, this variation should not be prominent with the use of especially designed RFID tag antennas tolerant to mounting material.

Normally the commercial RFID readers, which cover the dedicated UHF RFID frequency bands, operate with modulated discretely spaced baseband signals defined in regulations [113]. In relation to this, the aforementioned UHF RFID reader which support Australian UHF RFID frequency band has 12 number of discrete baseband transmit frequencies starting from 920.25 MHz to 925.75 MHz with 0.5-MHz spacing. Hence the discrete version of Equation 7.7 given by [239]:

$$\hat{d} = -\frac{c}{4\pi}\frac{\Delta\phi_{1,2}}{\Delta f_{1,2}}, \tag{7.11}$$

can be used in the estimation of distance. Here the $\Delta f_{1,2}$ is the difference between any two discrete base band transmit frequencies within the regulated frequency band and $\Delta\phi_{1,2}$ is the phase difference of received signals related to those two frequencies.

7.8 Measurements

7.8.1 Measurement Setup

The laboratory measurement setup is shown in Figure 7.13. It consists of the Laird Technologies S9025PR circularly polarised reader antenna [176] attached to Z-axis of the 3-axis multifunctional scanner system [246], Impinj Speedway Revolution Generation 2 UHF RFID Reader, a 3-m long coaxial cable which connects the reader antenna and the reader [247], a laptop and the RFID tag antenna (designed in Chapter 4) mounted on a metal plate. The antennas were arranged in line-of-sight and the displacement between antennas was generated by moving the reader antenna along Z-axis automatically by the scanning system for the experimental convenience. The scanner system has the resolution of 0.01 mm where the minimum displacement examined in the experiment was 1 mm.

An application program which is capable of acquiring the phase data of each tag antenna read was created since this information is not directly available to the users of commercial RFID readers (readily available inventory software of the reader is not capable of acquiring phase information). This was done using Octane SDK [163]. The created reader application is capable of producing data which includes the phase of the received signal (in radians with 12-bit resolution), transmit baseband frequency and time stamp for each tag antenna read within specified time period in text file format.

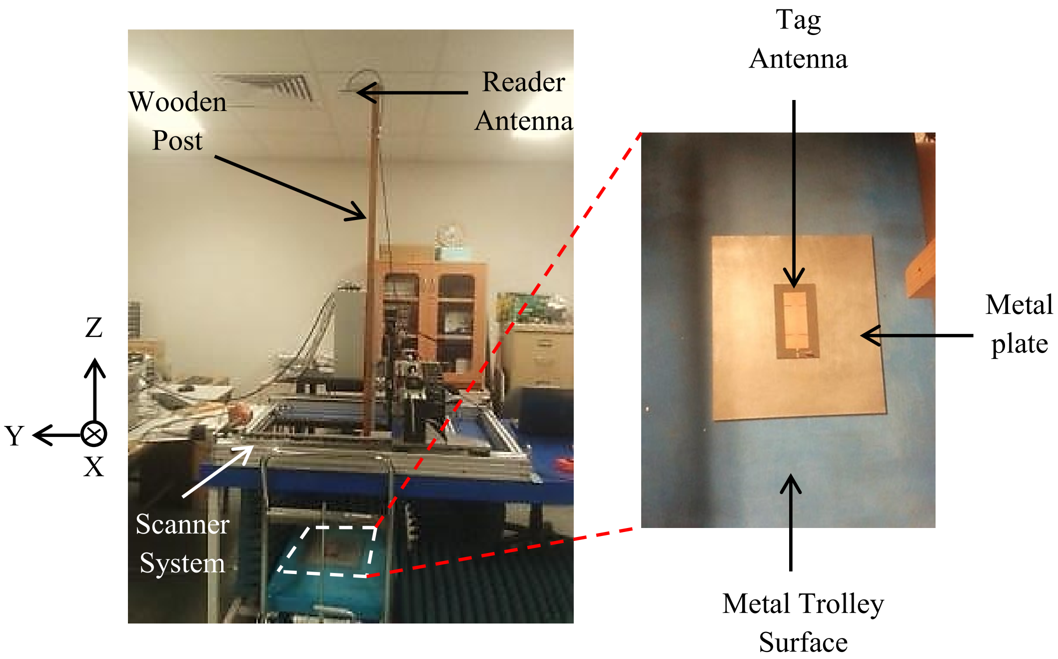

Figure 7.13: Measurement setup (at the ~6λ-starting distance between antennas).

7.8.2 Results and Discussion.

Figure 7.14 shows a 60-s measurement of ϕ verses transmitted base band frequencies of reader interrogation signal for a selected distance between reader and tag antennas. It clearly shows that the designed RFID tag antenna covers the Australian UHF RFID frequency band as ϕ values are acquired for all transmitted frequencies within that frequency band. The clear pattern of ϕ (highlighted in red in Figure 7.14) is related to Equation 7.11. Furthermore, it shows the ambiguity of π radians which is possible with the signal processing of the reader equipment [244]. The amount of variability of ϕ between different tag antenna reads (highlighted in the enlarged view) is due to low SNR of the received signals at the reader at this distance. Furthermore, imprecision of the ϕ measurement caused by frequency hopping technique of the reader is also a factor for this variability.

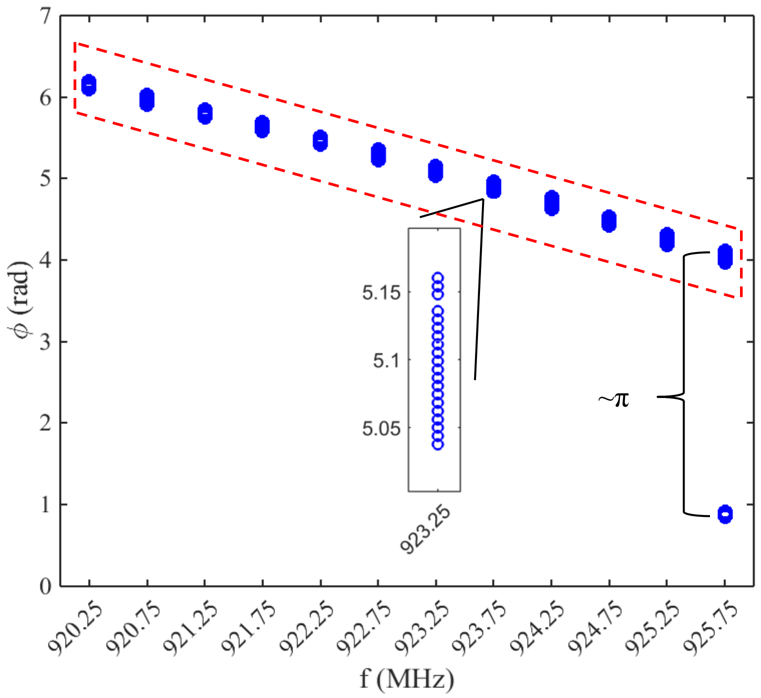

Figure 7.14: Measured phase vs frequency (o - represents a phase value of a single tag antenna response).

Figure 7.15 shows some selected possibilities from conducted measurement results (not within same distance). Figure 7.15(a) and Figure 7.15(b) indicate the wrapping nature where the measured ϕ values have shown transition within [0, 2π] range at different frequencies. The frequency of 920.25 MHz is in the transition boundary separating distinct groups of phase values. Furthermore, the measured ϕ values shown in Figure 7.15(b) (the smallest starting distance between antennas ~λ) have lower variability between tag antenna reads than those shown in the rest (the highest starting distance between antennas ~6λ). This is due to reduced variability of ϕ_o in relation to increased SNR of received tag antenna response signal at the reader within shorter distance. An example where the ambiguity has been increased is shown in Figure 7.15(c) in which the correct value for ϕ at 925.75 MHz has not been acquired and two groups of phase values have been acquired from 922.25 MHz to 925.25 MHz. Figure 7.15(d) shows two 60-s measurements within 6λ starting distance between reader antenna and the tag antenna. The variability between the results of two measurements is due to imprecise phase readings. However, it can be confirmed that a recognisable pattern of ϕ vs frequency retains at every instance.

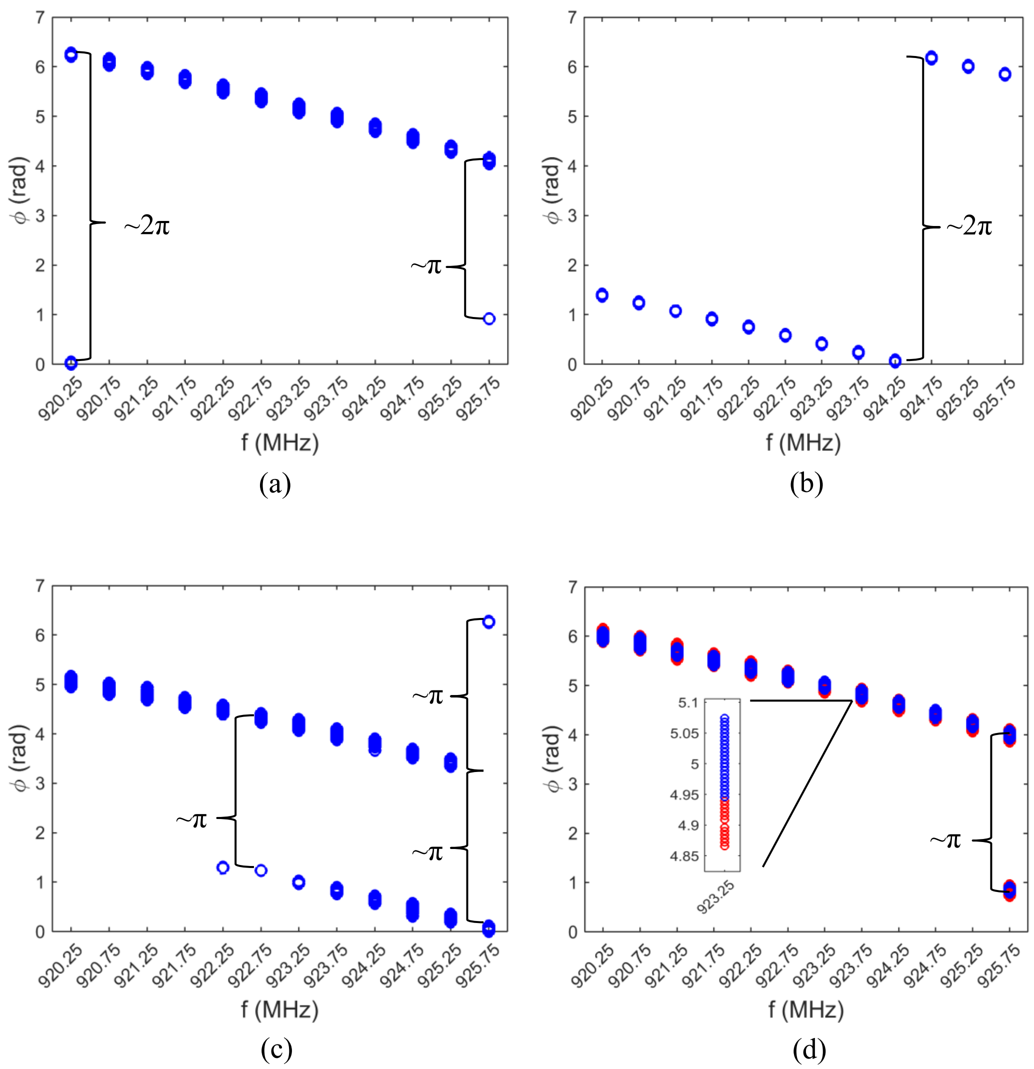

Figure 7.15: Selected examples of 60-s phase measurements by the RFID system: (a) within ~6λ-starting distance with phase wrap and ambiguity, (b) within ~λ-starting distance with phase wrap, (c) within ~6λ-starting distance with high ambiguity and (d) two measurements within ~6λ-starting distance (different colors represent the two measurements).

In the experimental procedure, the reader antenna was moved away in 1-mm intervals from initial starting distances of ~λ and ~6λ between antennas. At each displacement, 10 number of 60-s phase measurements have been acquired considering the variability in Figure 7.15(d).

7.8.2.1 Direct analysis by the Change in Received Phase

Initially, the phase measurement was analyzed directly to investigate the relationship of the phase value change to the displacement. Figure 7.16 shows the changing trend of average ϕ value according to displacement for each frequency (excluding wrapped frequencies) from starting distance of ~λ (0.322 m) between antennas. The average ϕ values are shown with 95 % confidence interval for the 10 number of measurements at each displacement. According to the Figure 7.16 the average ϕ decreases with added displacement for all frequencies. The maximum possible variability of average ϕ is ± 0.009 radians and the minimum gap between two average ϕ values of 1-mm displacement is 0.032 radians. Therefore, 1-mm displacement is distinguishable directly from the change of phase of the received signal within ~λ starting distance between antennas.

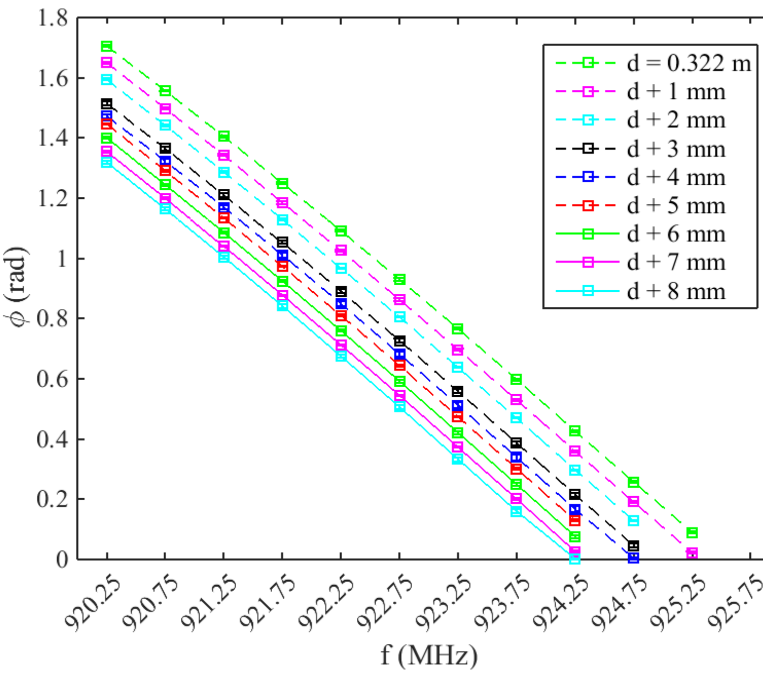

Figure 7.16: Average phase change with displacement for each frequency at 0.322-m starting distance between antennas (points are connected only for illustrative purpose).

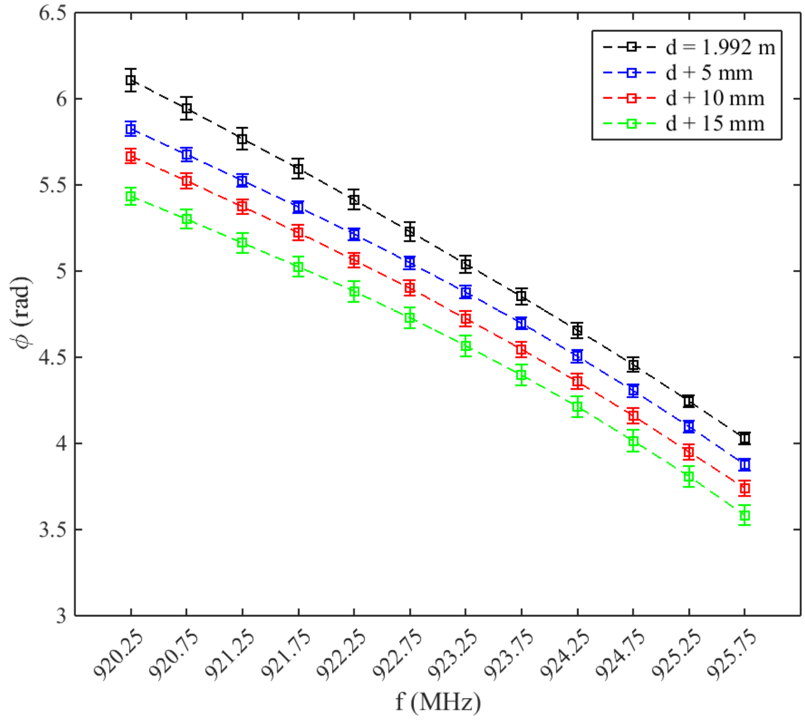

Figure 7.17: Average phase change with displacement for each frequency at 1.992-m starting distance between antennas (points are connected only for illustrative purpose).

Figure 7.17 depicts average phase change for starting distance of ~6λ (1.992-m) between antennas. A recognizable non-linearity of average ϕ against frequency is there in comparison to the shorter starting distance analysed previously. The detectable unambiguous displacement is 5 mm due to imprecision and low SNR (c.f. Figure 7.15(b) and Figure 7.15(d)). Consequently, the value of distinguishable displacement is dependent upon the environment where the RFID setup is being used. Electromagnetically harsh environments would increase the distinguishable displacement value due to increase of imprecation of the measured phase of the received signal. The environment of the measurement setup was considerably harsh due to metal mount of the tag antenna, metal trolley, the wooden post, parts of the 3-axis scanner system (metal, rubber and plastic) and rest of the surrounding objects (see Figure 7.13). The maximum error found out of the average ϕ values is ± 0.065 radians which is clear evidence of increased environmental effect with ~6λ starting distance between antennas. However, this method is theoretically bound by maximum displacement of ~0.162 m due to the wrapping nature of ϕ within Australian UHF RFID frequency band. Additionally, the measured ϕ values of a single frequency are sufficient to use this method. Furthermore when considering Equations 7.7 and 7.11, the distance estimate is proportional to $-\frac{\partial \phi}{\partial f}$ or $-\frac{\Delta\phi_{1,2}}{\Delta f_{1,2}}$. Therefore, probability of detecting unambiguous displacement directly by phase value should be high with higher frequencies of the frequency band. However Figure 7.17 shows otherwise due to increased non-linearity between phase vs frequency caused by low SNR of received tag antenna response signal.

7.8.2.2 Analysis by FD-PDoA

The average ϕ values for a single 60-s measurement (neglecting the ambiguity and wrapped frequencies) at d = 0.322-m distance are shown in Figure 7.18 with 1st order linear best-fit. There is a slight non-linearity of the measured phase vs frequency as seen in the Figure 7.18. This non-linearity imposes a constraint in selecting phase values of two frequencies for $\hat{d}$ calculation using to Equation 7.11. Owing to this, the calculation of $\hat{d}$ has been done by three different ways of phase value selection upon frequencies in order to find displacement estimate. First, all the phase values belong to the range of frequencies from 920.25 MHz to 923.75 MHz were considered with 1st order linear best-fit which would incur the non-linearity of phase vs frequency (this relates to Equation 7.7). The possibility of phase wrapping in higher frequencies of the frequency band due to added displacement was considered in the selection of frequencies (see Figure 7.16). Then, the two phase values of 920.25 MHz and 923.75 MHz were considered according to Equation 7.11 ($\Delta f_{1,2}$ = 3.50 MHz). Finally, the estimate was done using two phase values at 923.25 MHz and 923.75 MHz where the frequency gap is at minimum ($\Delta f_{1,2}$ = 0.50 MHz).

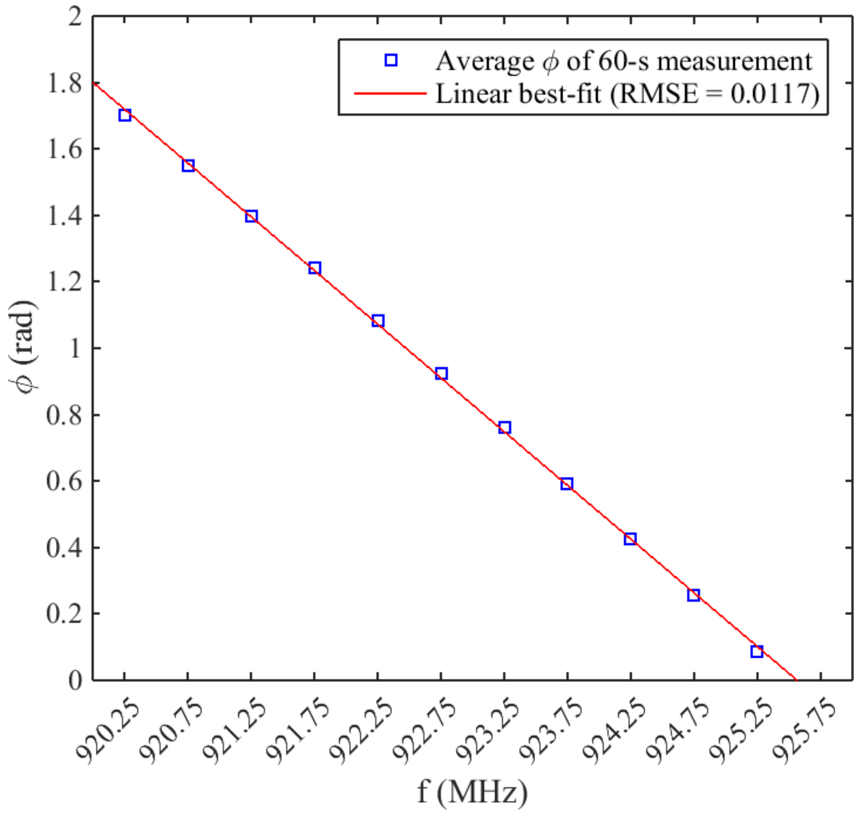

Figure 7.18: Average phase vs frequency at 0.322-m starting distance and the 1st order linear best-fit.

Figure 7.19 and Figure 7.20 show the estimated displacement ($\widehat{\Delta d}$) vs true displacement (Δd) for the first two aforementioned phase value selection methods. According to Figure 7.19 and Figure 7.20, the displacement estimates and the errors are exaggerated due to inaccuracy shown in phase measurement by the reader (the measurements has higher $\frac{\partial \phi}{\partial f}$ or $\frac{\Delta \phi_{1,2}}{\Delta f_{1,2}}$ than they should be). A linearly increasing trend could be found between estimated displacement and the true displacement as approximated with linear best-fit in Figure 7.19 and Figure 7.20. However, displacement estimate from the phase value selection of two consecutive frequencies (923.25 MHz and 923.75 MHz) did not provide such linear relationship with true displacement.

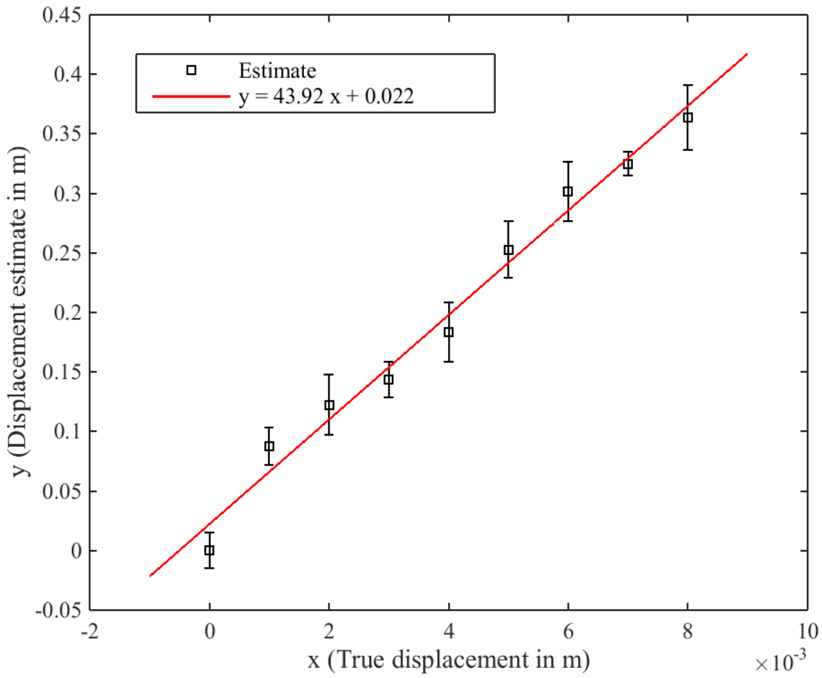

Figure 7.19: Displacement estimate vs true displacement considering the phase values from 920.25 MHz to 923.75 MHz at starting distance of 0.322 m.

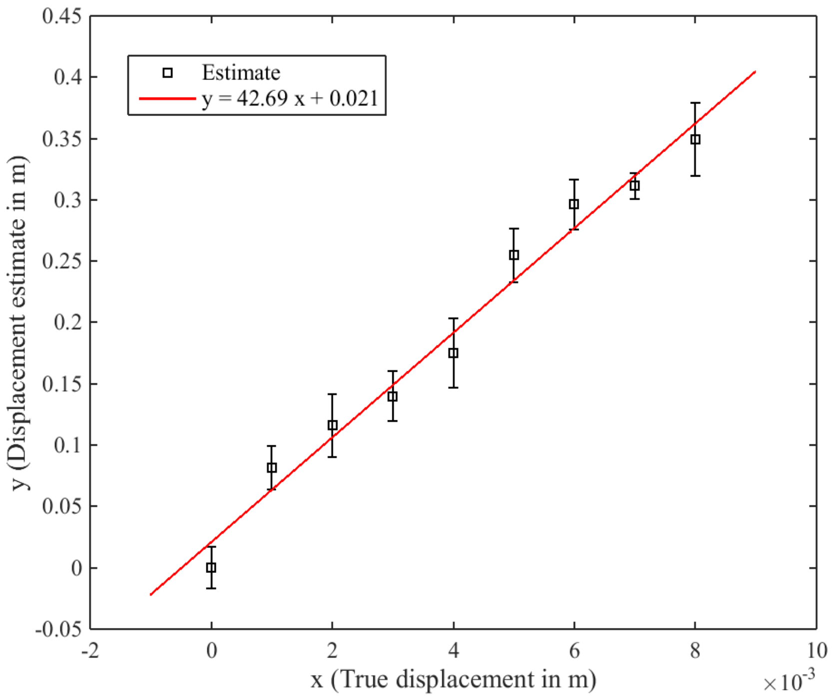

Figure 7.20: Displacement estimate vs true displacement considering the phase values of 920.25 MHz and 923.75 MHz at starting distance of 0.322 m.

The exaggeration of displacement estimates due to reader inaccuracy can be compensated using the 1st order linear best-fit parameters given in Figure 7.19 and Figure 7.20. The compensated displacement estimate ($\frac{\widehat{\Delta d}-0.022}{43.92}$) vs true displacement is shown in Figure 7.21. According to Figure 7.21, there is only a minor difference between compensated displacement estimates between the first two ways of phase value selection. This shows that the non-linearity added by the imprecision of phase values measured with ~λ starting distance has only a minor effect on the displacement estimate. Furthermore, phase values of the frequencies having relatively high separation between them should be selected to avoid non-linearity influence on the displacement estimate.

The estimated displacements for two other trials with starting distance of 0.325 m (has an initial displacement of 0.003 m compared to 0.322 m starting distance) between antennas are shown in Figure 7.22. The linear 1st order linear best-fit parameters used in the initial estimation (see Figure 7.19) were used in the displacement estimate compensation of these additional trials. Except for the noticeable outlier of additional trail 2 at 0.003 m displacement, the additional trails show a good agreement. Therefore a distinguishable displacement measurement of 1-mm is possible within ~λ starting distance between antennas even with the inherent inaccuracy of the reader. This displacement measurement resolution accounts for ± 0.31 % related to 0.322-m starting distance between antennas. The maximum compensated displacement estimate error (95 % confidence interval) was ± 0.0003 m within the measurements excluding the outlier.

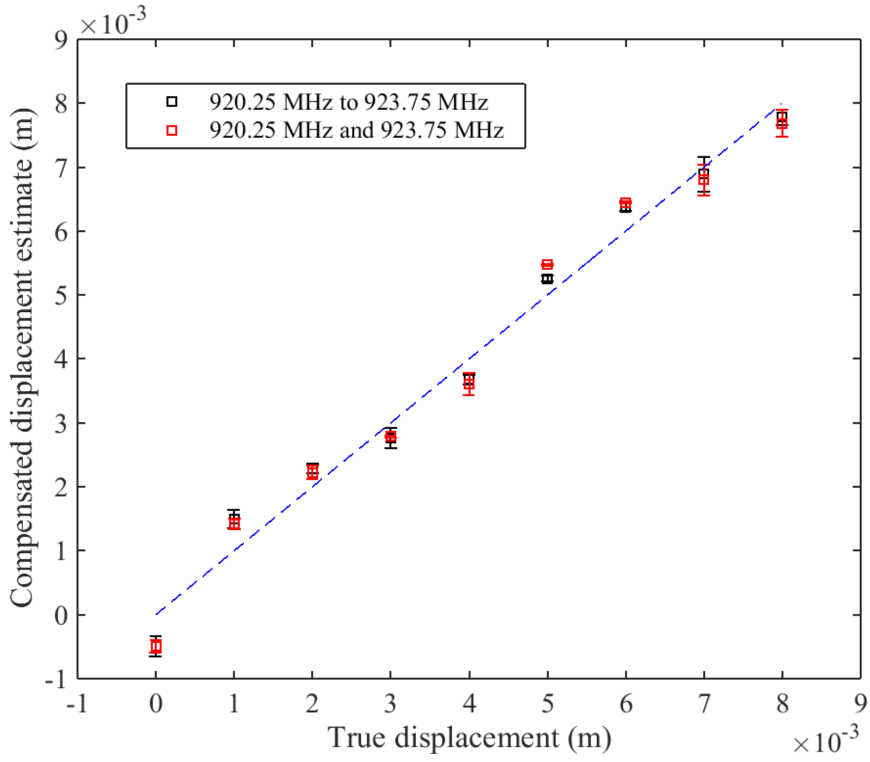

Figure 7.21: Compensated displacement estimate vs true displacement at starting distance of 0.322 m.

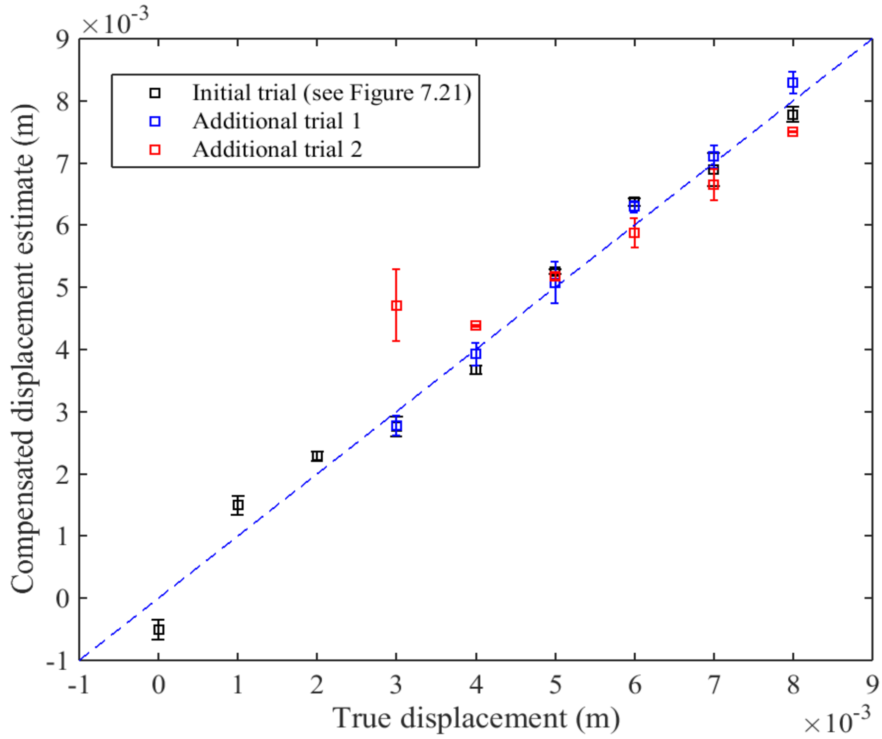

Figure 7.22: Compensated displacement estimate vs true displacement for additional trials at starting distance of 0.325 m (phase value selection from 920.25 MHz to 923.75 MHz).

However, conclusive displacement estimates could not be acquired for 1-mm true displacement intervals with FD-PDoA method for ~6λ (1.992 m) starting distance between antennas. The determination of frequencies for phase value selection was more difficult than previous due to an increase of non-linearity (higher RMSE than in Figure 7.18) of phase vs frequency as shown in Figure 7.23 (Figure 7.17 also shows this non-linearity). The exaggeration of estimated displacement and errors were higher than those found for ~λ starting distance. A proper linear relationship between estimated displacement and true displacement could not be found to compensate for the inaccuracy related to higher $\frac{\partial\phi}{\partial f}$ or $\frac{\Delta\phi_{1,2}}{\Delta f_{1,2}}$.

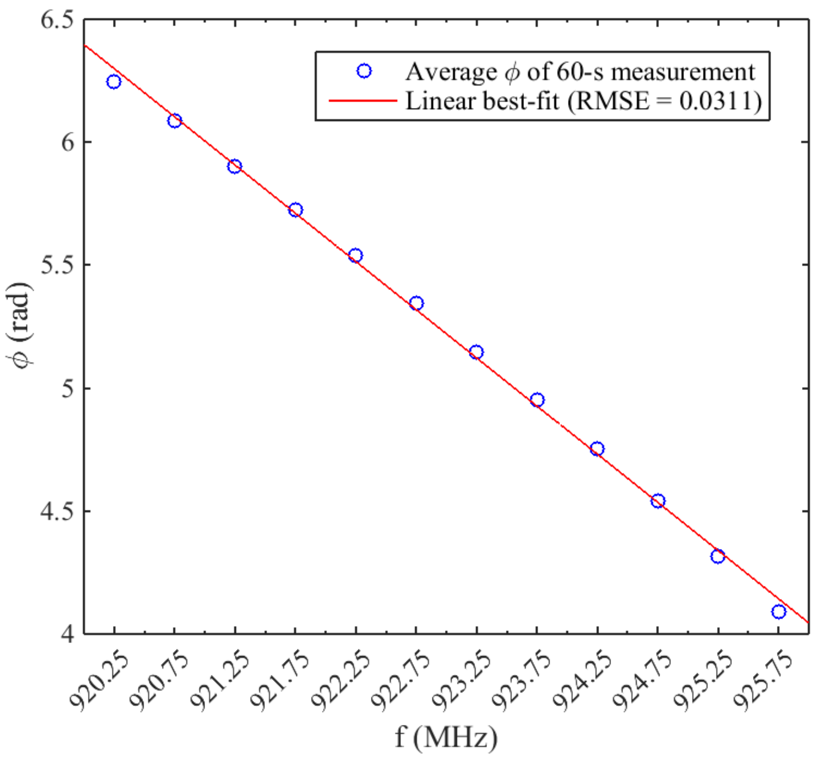

Figure 7.23: Average phase vs frequency at 1.992-m starting distance and the 1st order linear best-fit.

7.9 Conclusion

The results of wireless power flow distribution at 923 MHz frequency in the vicinity of a steel I-beam were presented in the first part of this chapter. An RFID antenna system with designed tag antenna (in Chapter 4) was used in simulations to make the investigation experimentally viable by measurements of minimum transmitting power. According to power density simulations, this distribution depends on the I-beam orientation with respect to the direction of illumination. The I-beam at orientation 2 with respect to reader antenna (i.e. illumination source) had higher power density distribution in the vicinity of it than orientation 1. The detailed investigation has proved that both I-beam orientation and shape have an influence upon the amount of UHF power incident on the tag antennas positioned at its different locations. In particular, the line-of-sight location of the I-beam at orientation 1 had lower power density than other studied locations. In both investigated orientations, the corner edge of the I-beam had higher power density. These differences observed in simulated power density distribution were in accordance with the simulated voltage levels across the lumped elements of tag antennas. The minimum transmitting power measurement results correlated well with simulation results. This investigation is useful in aligning the reader antenna with respect to the orientation of the I-beam and positioning multiple tag antenna integrated sensors on the I-beam to monitor its health by developed RFID-based wireless IHM system.

In the second part of the chapter, the viability of phase-based structural displacement measurement using RFID tag antenna system in passive mode was investigated. It was shown that measurement of 1-mm and 5-mm structural displacement is possible with a change in phase values of received tag antenna responses within ~λ and ~6λ starting distance between antennas, respectively. There was increased imprecision of phase measurement due to low SNR of received tag antenna responses at ~6λ starting distance than ~λ starting distance. It has also been shown that 1-mm structural displacement can be measured using FD-PDoA principle for ~λ starting distance between antennas. The displacement estimates had to be compensated for the exaggeration generated by the phase measurements of the reader. The maximum compensated displacement estimated error was ±0.0003 m. However, the application of the same principle to measure small structural displacements at ~6λ starting distance was negatively affected by increased non-linearity of measured phase vs frequency. The phase-based structural displacement measurement method studied in this chapter is primarily a reference-based method where reader antenna should be attached to a reference position. The construction material mountable tag antenna was an added advantage in the system setup for structural displacement measurement where extra arrangement to hold the tag antenna was not needed.

Chapter 8 Conclusion

8.1 Summary

In this thesis, a semi-passive RFID-based wireless sensor system was developed to measure dynamic acceleration and strain of infrastructure through the design of tunable construction material mountable RFID semi-passive tag antenna and custom designed miniature sensor circuits. The system's ability to measure dynamic responses from mounted tag antenna integrated sensors with enhanced communication range and wider spectral bandwidth is experimentally proven with different structural members. The influence of the orientation and shape of structural members on wireless power delivery to mounted sensors was studied using an RFID antenna system in passive mode. The system's ability in passive mode structural displacement measurement was also investigated.

The major investigations and outcomes are outlined as follows:

- In Chapter 3, the prototype RFID-based wireless dynamic acceleration system with tag antenna integrated acceleration sensor for wireless IHM was developed. The specific firmware design to achieve the capability of measuring dynamic acceleration using tag antenna integrated acceleration sensor was introduced. The non-volatile memory write latency of RFID tag chip and inadequacy of data acquisition technique were highlighted as constraints to achieve higher spectral bandwidth. It was shown that the prototype system is capable of acquiring the natural frequency information of a structural member. Furthermore, it was also shown that the system is capable of identifying the loaded and unloaded states of the structural member with determination of natural frequency shift.

- A novel tunable construction material mountable UHF RFID tag antenna which can be used as I^2C slave component for the creation of tag antenna integrated sensors was developed in Chapter 4. Antenna design and the creation of an electromagnetic simulation model were also carried out. It was shown that the slit-based miniaturization method can be simultaneously used for impedance matching and parametric optimization of the tag antenna to acquire higher performance in several UHF RFID frequency bands. It was also shown that mounting material of concrete and metal has a minor negative influence on maximum gain and size of the metal mounts has no influence upon reflection characteristics of the antenna through comprehensive electromagnetic simulation. Furthermore, the use of local mesh properties around tiny features of the antenna to retain similar simulation accuracy with increased simulation volume was also shown. In addition, antenna fabrication and essential laboratory measurements of the resonant frequency, maximum gain, read range and readability were conducted. The measurement results were found to be in good agreement with simulation results.

- In Chapter 5, the RFID-based dynamic acceleration measurement system was improved by introducing novel tag antenna integrated acceleration sensors directly mountable on structures. A miniaturized acceleration sensor circuit which can be integrated with the developed construction material mountable tag antenna was designed. The spectral bandwidth of 3-axis dynamic acceleration measurement of the system was enhanced to 50-Hz with improved firmware and data acquisition. The feasibility of the system to handle multiple tag antenna integrated acceleration sensors mounted on different locations was shown by conducting measurements upon a full-scale steel I-beam. The ability of the system in determining the natural frequency of the I-beam and the acceleration sensitivity were benchmarked against independent commercial wired and wireless measurement systems.

- The RFID-based dynamic acceleration measurement system was further enhanced for measurement of dynamic acceleration and strain, simultaneously, in Chapter 6. A miniaturized multi-sensor sensor circuit which can be integrated with the developed construction material mountable tag antenna was designed. The firmware was improved to measure 3-axis acceleration and strain with spectral bandwidths of 40 Hz and 26.5 Hz, respectively. The calibration of the strain interface is performed against a standard strain measurement instrument by conducting static train measurements upon a cantilever steel beam. The feasibility of the system to acquire natural frequency information of the beam from both dynamic acceleration and strain measurements (simultaneous measurements) was shown. The ability of the system in determining the natural frequency of the cantilever beam and the strain sensitivity of the system were benchmarked against a commercial wireless strain measurement system.

- An investigation of wireless power flow in the vicinity of a steel I-beam was performed using RFID reader-tag antenna system in Chapter 7. The simulation model was created using reader antenna and tag antennas with lumped elements mounted on a steel I-beam. It was shown that the power flow towards the I-beam is influenced by its orientation with respect to reader antenna and the power flow in the vicinity is influenced by its shape. It was also shown that at some orientation of the I-beam, the line-of-sight location has less incident power influenced by its shape. The experimental method was formulated using the RFID wireless link budget to relate minimum reader transmits power to incident power and the simulation results were justified by experimental results. The passive mode investigation of the ability of the RFID system to measure structural displacement was performed using the acquisition of phase angle-of-arrival of the received signal at the reader. It was shown that displacement of 1-mm can be measured directly by the change in phase angle-of-arrival or frequency domain phase difference of arrival within starting distance of a single wavelength (λ) related to Australian UHF RFID frequencies. It was also shown that 5-mm displacement can be measured directly by the change in phase angle-of-arrival within a 6-λ initial distance within the phase angle measurement accuracy of the RFID reader equipment.

8.2 Conclusion

An RFID-based wireless system was proposed and designed with structure mountable semi-passive tag antenna integrated sensors for IHM. The system could measure 3-axis dynamic acceleration and both dynamic and static strain of infrastructure. Furthermore, it could measure structural displacement in passive mode. The hardware and firmware-based improvements of the system were gradually performed to enhance the read range in infrastructure environments, the spectral bandwidth of dynamic response measurements and the capability of performing multiple dynamic measurements simultaneously. The optimization of the system operating in infrastructure environments was carried out by comprehensive simulations consisting of performance analysis of tag antenna mounted on concrete and metal members and essential laboratory measurements. The abilities of the enhanced system in measuring dynamic responses of infrastructure, the natural frequency determination and state change identification of infrastructure was shown by conducting measurements with three structural members that had different dimensions, shapes, and boundary conditions. It was shown that the non-volatile memory write latency of the RFID chip imposes a major constraint on the enhancement of the spectral bandwidth of dynamic response measurements.

Moreover, the results obtained by the developed system were in good agreement with the results obtained from the commercially available wired and wireless measurement systems. The natural frequency determination errors of the developed system by dynamic acceleration measurements were −0.05 Hz and −0.03 Hz when benchmarked against commercial wired and wireless acceleration measurement systems operated with close sampling rates, respectively. Almost 93 % of the measurement results had a maximum variation of the determined natural frequency values within ~0.05-Hz range (it was shown that this range depends upon SNR and it would be narrowed with increased SNR in Chapter 7). The acceleration sensitivity of the developed system was 140 % and 61.3 % when benchmarked against the sensitivities of the commercial wired and wireless acceleration measurement systems, respectively. The natural frequency determination by the dynamic strain measurements of the developed system had an error of −0.06 Hz when compared with the natural frequency determination of the simultaneous dynamic acceleration measurement (subjected to different sample rates of dynamic acceleration and strain measurements). This error was −0.03 Hz when benchmarked against a commercial wireless strain measurement system (subjected to different sample rates of the systems). Almost 90 % of the measurement results had a maximum variation of the determined natural frequency values within ~0.01 Hz range. The strain sensitivity of the developed system was 97.6 % of the sensitivity of the commercial wireless strain measurement system.

Additionally, the wireless power flow simulations in the vicinity of tag antenna mounted structural members were conducted. The simulation results were consistent with the conducted laboratory measurements. Is was also shown that both size and shape of the mount affects the readability of tag antenna due to the variation of antenna gain pattern and incident wireless signal power. Furthermore, the investigations have shown that the reader antenna orientation can be adjusted with respect to the structural member to achieve a higher amount of wireless power delivery to mounted sensors (i.e., in the vicinity of the structure). The investigation with the phase angle-of-arrival measurements proved that the system can be used to detect structural displacement accurately within an initial short distance between the reader antenna and tag antenna mounted on structures (subjected to the accuracy of the phase angle measurement of the reader). Finally, the measurements conducted with a steel I-beam confirmed the ability of the developed RFID-based system to handle multiple semi-passive tag antenna integrated sensors measuring dynamic responses enabling fulfillment of the highly demanded necessity of IHM.

8.3 Future Work

The recommendations for future research are as follows:

- One future work suggestion is the optimization of sensor circuits using the following steps. Firstly, the PCB layout routing optimization could be used to isolate the SPI bus from the *Watermark interrupt* route to remove existing distortion in measurement data. Next is the optimization of the DC power supply section. The power supply section can be optimized as a battery backup supply with the introduction of either vibration-based or solar energy harvesting. Since the semi-passive RFID tag antenna integrated sensors were developed with circuits having low power electronic components, the energy harvested from both ambient and induced vibrations of structures or from a miniature solar panel may easily increase the lifetime of them.

- Determining the maximum number of RFID tag antenna integrated sensors which can be interrogated by a single reader antenna would be important. The selected commercial UHF RFID reader (from Chapter 4 onwards) has the capability of supporting multiple reader antennas. Therefore, flexibility is there to configure the system either as single reader antenna or multiple reader antennas covering a single cluster of the wireless IHM system. Furthermore, the type of the reader antenna can also be altered to have extra coverage. The reader scans between antenna ports when multiple reader antennas are configured. Also, when the tag antenna integrated sensor population grows, data acquisition duration allocated to a single tag antenna integrated sensor will be decreased. Consequently, the complexity of this task increases. The maximum number of tag antenna integrated sensors which can accommodate a single cluster is important in the perspective of informative data acquisition of IHM.

- Enhancing of developed semi-passive tag antenna integrated sensors to measure environmental temperature and humidity is another suggestion for future work. These measurements will be helpful in removing the environmental factor associated with raw dynamic acceleration and strain measurements. As highlighted in Chapters 5 and 6, the non-volatile memory latency of the RFID tag chip will not allow measuring temperature and humidity for each and every data point of dynamic acceleration and strain. However, acquiring an average temperature and humidity measurement for a single reader acquisition cycle may be a possibility. The acquisition of average values can be justified given that the fluctuations of environmental temperature and humidity are less within the measurement duration of acceleration and strain.

- The next suggestion is the extension of the system with integrated long range wireless capability. The reader used in the system development can support the integration of wireless nodes which provides the capability of accessing it from a distant location through a wireless link. This capability can be exploited in developing the higher tier inter-cluster wireless communication equipped with reader integrated wireless nodes as cluster heads. The data acquisition application shall also be enhanced depending on the number of readers. This work will also lead to identifying the maximum amount of reader integrated wireless nodes that the RFID-based wireless IHM system can accommodate when monitoring dynamic responses.

References

[1] T. Chan and D. P. Thambiratnam, *Engineering Tools, Techniques and Tables : Structural Health Monitoring in Australia*. Hauppauge, US: Nova, 2011.

[2] B. Turner, S. J. Brandenberg, and J. P. Stewart. (2014). *Evaluation of collapse and non-collapse of parallel bridges affected by liquefaction and lateral spreading*. Available: http://peer.berkeley.edu/publications/peer_reports/reports_2014/webPEER-2014-10-Brandenberg.pdf

[3] G. A. Christian. (2010). *Bridge failures -lessons learned*. Available: http://mceer.buffalo.edu/education/bridge_speaker_series/2009-2010/presentations/P1%20Lessons%20learned%20from%20Bridge%20Failures_FINAL.pdf

[4] (2008). *Collapse of I-35W highway bridge, Minneapolis, Minnesota, August 1, 2007*. Available: http://www.ntsb.gov/investigations/AccidentReports/Reports/HAR0803.pdf

[5] D. Huston, *Structural sensing, health monitoring and performance evaluation*. Boca Raton: Taylor & Francis.

[6] S. C. Mukhopadhyay, *New development in sensing technology for structural health monitoring*. Verlag Berlin Heidelberg: Springer, 2011.

[7] J. P. Lynch, A. Partridge, K. H. Law, T. W. Kenny, A. S. Kiremidjian, and E. Carryer, "Design of piezoresistive MEMS-based accelerometer for integration with wireless sensing unit for structural monitoring," *Journal of Aerospace Engineering,* vol. 16, no. 3, pp. 108-114, 2003.

[8] H. Liu, R. Han, Y. Wei, and X. Zhao, "Displacement monitoring of structures using laser image displacement method," in *Earth and Space 2014*, ed, pp. 589-599.

[9] C. Haksoo, C. Sukwon, and C. Hojung, "Structural health monitoring system based on strain gauge enabled wireless sensor nodes," in *5th International Conference on Networked Sensing Systems*, 2008, pp. 211-214.

[10] A. Morassi, "Identification of a crack in a rod based on changes in a pair of natural frequencies," *Journal of Sound and Vibration,* vol. 242, no. 4, pp. 577-596, 2001.

[11] P. C. Chang, A. Flatau, and S. C. Liu, "Review paper: health monitoring of civil infrastructure," *Structural Health Monitoring 2.3,* pp. 257-267, 2003.

[12] M. N. Cerri, M. Dilena, and G. C. Ruta, "Vibration and damage detection in undamaged and cracked circular arches: Experimental and analytical results," *Journal of Sound and Vibration,* vol. 314, no. 1–2, pp. 83-94, 2008.

[13] I. Trendafilova, M. P. Cartmell, and W. Ostachowicz, "Vibration-based damage detection in an aircraft wing scaled model using principal component analysis and pattern recognition," *Journal of Sound and Vibration,* vol. 313, no. 3–5, pp. 560-566, 2008.

[14] A. Sang, K. Marsden, M. Wolfe, D. Gifford, M. Froggatt, and B. Soller, "High resolution, dynamic strain measurements with continuous fiber Bragg gratings for structural health monitoring," in *IEEE Avionics, Fiber-Optics and Photonics Technology Conference*, 2009, pp. 29-31.

[15] G. Moor, N. Meng, and C. O'Suilleabhain, "Remote structural health monitoring systems for bridge expansion joints and bearings," in *Proceedings of 2nd Conference on Smart Monitoring, Assessment and Rehabilitation of Civil Structures*, Istanbul, Turkey, 2013.

[16] Y. Q. Ni, B. S. Wang, and J. Ko, "Simulation studies of damage location in Tsing Ma Bridge deck," in *In Proceedings of Nondestructive Evaluation of Highways, Utilities and Pipelines IV, SPIE*, 2001, pp. 312-323.

[17] M. Çelebi, "Seismic instrumentation of buildings," Report 2000-157, 2000.

[18] H.-J. Park, K.-Y. Koo, and C.-B. Yun, "Modal flexibility-based damage detection technique of steel beam by dynamic strain measurements using FBG sensors," *International Journal of Steel Structures,* vol. 7, no. 1, pp. 11-18, 2007.

[19] M. Q. Feng and D.-H. Kim, "Novel fiber optic accelerometer system using geometric moiré fringe," *Sensors and Actuators A: Physical,* vol. 128, no. 1, pp. 37-42, 2006.

[20] C. L. W. Allan, A. C. Paul, and P. Gang-Ding, "Multiplexed fibre Fizeau interferometer and fibre Bragg grating sensor system for simultaneous measurement of quasi-static strain and temperature using discrete wavelet transform," *Measurement Science and Technology,* vol. 17, no. 2, p. 384, 2006.

[21] H. Murayama, D. Wada, and H. Igawa, "Structural health monitoring by using fiber-optic distributed strain sensors with high spatial resolution," *Photonic Sensors,* vol. 3, no. 4, pp. 355-376, 2013.

[22] K.-S. Kim, Y.-C. Song, G.-S. Pang, and D.-J. Yoon, "Study on the application of fiber Bragg grating sensors for the containment structures of nuclear power plants," in *Smart Structures and Materials*, 2005, pp. 584-590.

[23] J. A. Rice and B. F. Spencer Jr, "Flexible smart sensor framework for autonomous full-scale structural health monitoring," Newmark Structural Engineering Laboratory. University of Illinois at Urbana-Champaign. 1940-9826, 2009.

[24] J. M. Rybak, "Remote condition monitoring using open-system wireless technologies," *Sound and Vibration,* vol. 40, no. 2, p. 16, 2006.

[25] J. P. Lynch and K. J. Loh, "A summary review of wireless sensors and sensor networks for structural health monitoring," *Shock and Vibration Digest,* vol. 38, no. 2, pp. 91-130, 2006.

[26] S. Park, H.-H. Shin, and C.-B. Yun, "Wireless impedance sensor nodes for functions of structural damage identification and sensor self-diagnosis," *Smart Materials and Structures,* vol. 18, no. 5, p. 055001, 2009.

[27] J. Kim and J. P. Lynch, "Experimental analysis of vehicle–bridge interaction using a wireless monitoring system and a two-stage system identification technique," *Mechanical Systems and Signal Processing,* vol. 28, pp. 3-19, 2012.

[28] S. Jang, H. Jo, S. Cho, K. Mechitov, J. A. Rice, S. H. Sim*, et al.*, "Structural health monitoring of a cable-stayed bridge using smart sensor technology: deployment and evaluation," *Smart Structures and Systems,* vol. 6, no. 5-6, pp. 439-459, 2010.

[29] M. Jayawardhana, X. Zhu, R. Liyanapathirana, and U. Gunawardana, "An experimental study for decentralized damage detection of beam structures using wireless sensor networks," *Structural Monitoring and Maintenance,* vol. 2, no. 3, pp. 237-252, 2015.

[30] S. Cho, H. Jo, S. Jang, J. Park, H.-J. Jung, C.-B. Yun*, et al.*, "Structural health monitoring of a cable-stayed bridge using wireless smart sensor technology: data analyses," *Smart Structures and Systems,* vol. 6, no. 5-6, pp. 461-480, 2010.

[31] G. J. Pottie and W. J. Kaiser, "Wireless integrated network sensors," *Commun. ACM,* vol. 43, no. 5, pp. 51-58, 2000.

[32] G. Anastasi, M. Conti, M. Di Francesco, and A. Passarella, "Energy conservation in wireless sensor networks: A survey," *Ad Hoc Networks,* vol. 7, no. 3, pp. 537-568, 2009.

[33] A. Deraemaeker, "Vibration based structural health monitoring using large sensor arrays: Overview of instrumentation and feature extraction based on modal filters," in *New Trends in Vibration Based Structural Health Monitoring*, A. Deraemaeker and A. Worden, Eds., ed New York, NY, USA: Springer, 2010, pp. 19-32.

[34] W. Bajwa, J. Haupt, A. Sayeed, and R. Nowak, "Compressive wireless sensing," in *5th International Conference on Information Processing in Sensor Networks*, 2006, pp. 134-142.

[35] Q. Ling and Z. Tian, "Decentralized sparse signal recovery for compressive sleeping wireless sensor networks," *IEEE Transactions on Signal Processing,* vol. 58, no. 7, pp. 3816-3827, 2010.

[36] Y. Lu, A. Savvaris, A. Tsourdos, and M. Bevilacqua, "Vibration energy harvesters for wireless sensor networks for aircraft health monitoring," in *IEEE Metrology for Aerospace (MetroAeroSpace)*, 2016, pp. 25-32.

[37] T. T. Thai, H. Aubert, P. Pons, R. Plana, M. M. Tentzeris, and G. R. DeJean, "A newly developed radio frequency wireless passive highly sensitive strain transducer," in *in Proceedings of IEEE Sensors* 2011, pp. 211-214.

[38] A. Daliri, A. Galehdar, W. S. Rowe, K. Ghorbani, and S. John, "Utilising microstrip patch antenna strain sensors for structural health monitoring," *Journal of Intelligent Material Systems and Structures,* vol. 23, no. 2, pp. 169-182, 2012.

[39] S. Bhadra, D. J. Thomson, and G. E. Bridges, "A wireless embedded passive sensor for monitoring the corrosion potential of reinforcing steel," *Smart materials and structures,* vol. 22, no. 7, p. 075019, 2013.

[40] R. Bhattacharyya, C. Floerkemeier, and S. Sarma, "Towards tag antenna based sensing - An RFID displacement sensor," in *IEEE International Conference on RFID*, 2009, pp. 95-102.

[41] X. Yi, T. Wu, Y. Wang, R. T. Leon, M. M. Tentzeris, and G. Lantz, "Passive wireless smart-skin sensor using RFID-based folded patch antennas," *International Journal of Smart and Nano Materials,* vol. 2, no. 1, pp. 22-38, 2011.

[42] W. Leon-Salas, S. Kanneganti, and C. Halmen, "Development of a smart RFID-based corrosion sensor," in *IEEE Sensors*, 2011, pp. 534-537.

[43] D. G. Watters, A. J. Bahr, P. Jayaweera, and D. L. Huestis, "Smart pebbles: Passive embeddable wireless sensors for chloride ingress monitoring in bridge decks," 2003.

[44] P. Pursula, I. Marttila, K. Nummila, and H. Seppä, "High frequency and ultrahigh frequency radio frequency identification passive sensor transponders for humidity and temperature measurement within building structures," *IEEE Transactions on Instrumentation and Measurement,* vol. 62, no. 9, pp. 2559-2566, 2013.

[45] A. Deivasigamani, A. Daliri, C. H. Wang, and S. John, "A review of passive wireless sensors for structural health monitoring," *Modern Applied Science,* vol. 7, no. 2, p. 57, 2013.

[46] T. Bjorninen, L. Sydanheimo, L. Ukkonen, and Y. Rahmat-Samii, "Advances in antenna designs for UHF RFID tags mountable on conductive items," *IEEE Antennas and Propagation Magazine,* vol. 56, no. 1, pp. 79-103, 2014.

[47] K. Finkenzeller, "Differentiation Features of RFID Systems," in *RFID Handbook*, ed: John Wiley & Sons, Ltd, 2003, pp. 11-28.

[48] D. D. Donno, L. Catarinucci, and L. Tarricone, "RAMSES: RFID augmented module for smart environmental sensing," *IEEE Transactions on Instrumentation and Measurement,* vol. 63, no. 7, pp. 1701-1708, 2014.

[49] S. H. Sim, B. F. S. Jr., and T. Nagayama, "Multimetric sensing for structural damage detection," *Journal of Engineering Mechanics,* vol. 137, no. 1, pp. 22-30, 2011.

[50] J. Min, S. Park, C.-B. Yun, and B. Song, "Development of a low-cost multifunctional wireless impedance sensor node," *Smart Structures and Systems,* vol. 6, no. 5-6, pp. 689-709, 2010.

[51] Y. Liang and C. Hwu, "On-line identification of holes/cracks in composite structures," *Smart Materials and Structures,* vol. 10, no. 4, p. 599, 2001.

[52] H. Gu, P. Jin, Y. Zhao, G. M. Lloyd, and M. L. Wang, "Design and experimental validation of a wireless PVDF displacement sensor for structure monitoring," in *NDE for Health Monitoring and Diagnostics*, 2004, pp. 91-99.

[53] F. Casciati, S. Casciati, L. Faravelli, and R. Rossi, "Hybrid wireless sensor network," in *Smart Structures and Materials*, 2004, pp. 308-313.

[54] E. Sazonov, K. Janoyan, and R. Jha, "Wireless intelligent sensor network for autonomous structural health monitoring," *Smart Structures/NDE,* pp. 305-314, 2004.

[55] C. R. Farrar, D. W. Allen, G. Park, S. Ball, and M. P. Masquelier, "Coupling sensing hardware with data interrogation software for structural health monitoring," *Shock and Vibration,* vol. 13, no. 4-5, pp. 519-530, 2006.

[56] J. P. Lynch, K. H. Law, A. S. Kiremidjian, E. Carryer, C. R. Farrar, H. Sohn*, et al.*, "Design and performance validation of a wireless sensing unit for structural monitoring applications," *Structural Engineering and Mechanics,* vol. 17, no. 3-4, pp. 393-408, 2004.

[57] X. Hanxing, Y. Jun, and X. Mingge, "The application of wavelet transform in the processing of low frequency distortion of pyrotechnic shock signal," in *2nd International Conference on Mechanic Automation and Control Engineering*, 2011, pp. 1728-1731.

[58] J. Niu, Z. Deng, F. Zhou, Z. Cao, Z. Liu, and F. Zhu, "A Structural Health Monitoring System Using Wireless Sensor Network," in *5th International Conference on Wireless Communications, Networking and Mobile Computing*, 2009, pp. 1-4.

[59] M. J. Whelan, M. V. Gangone, and K. D. Janoyan, "Highway bridge assessment using an adaptive real-time wireless sensor network," *IEEE Sensors Journal,* vol. 9, no. 11, pp. 1405-1413, 2009.

[60] S. Kim, S. Pakzad, D. Culler, J. Demmel, G. Fenves, S. Glaser*, et al.*, "Health monitoring of civil infrastructures using wireless sensor networks," in *Proceedings of the 6th international conference on Information processing in sensor networks*, 2007, pp. 254-263.

[61] (2007). *Wireless sensor networks product reference guide*. Available: http://www.investigacion.frc.utn.edu.ar/sensores/Equipamiento/Wireless/Crossbow_Wireless_2007_Catalog.pdf, accessed: 15 August 2014.

[62] R. M. Kling, "Intel motes: advanced sensor network platforms and applications," in *MTT-S International Microwave Symposium Digest, MWSYM*, 2005, p. 4.

[63] E. G. Straser, A. S. Kiremidjian, and T. H. Meng, "Modular, wireless damage monitoring system for structures," ed: Google Patents, 2001.

[64] T. Nagayama, M. Ruiz-Sandoval, B. F. Spencer Jr, K. A. Mechitov, and G. Agha, "Wireless strain sensor development for civil infrastructure," in *Proceedings of 1st International Workshop on Networked Sensing Systems*, 2004, p. 97.

[65] S. Pakzad and G. Fenves, "Structural health monitoring applications using MEMS sensor networks," in *Proceedings of the 4th International Workshop on Structural Control*, 2004, pp. 47-56.

[66] M. Ruiz-Sandoval, B. Spencer Jr, and N. Kurata, "Development of a high sensitivity accelerometer for the Mica platform," in *Proceedings of the 4th International Workshop on Structural Health Monitoring*, 2003, pp. 1027-1034.

[67] J. A. Rice and B. Spencer Jr, "Structural health monitoring sensor development for the Imote2 platform," in *The 15th International Symposium on: Smart Structures and Materials & Nondestructive Evaluation and Health Monitoring*, 2008, pp. 693234-693234-12.

[68] T. Nagayama and B. F. Spencer Jr, "Structural health monitoring using smart sensors," Newmark Structural Engineering Laboratory. University of Illinois at Urbana-Champaign. 1940-9826, 2007.

[69] Y. Wang, J. P. Lynch, and K. H. Law, "Wireless structural sensors using reliable communication protocols for data acquisition and interrogation," in *Proceedings of 23rd International Modal Analysis Conference (IMAC XXIII)*, Orlando, FL, USA, 2005.

[70] R. Rolfes, S. Zerbst, G. Haake, J. Reetz, and J. P. Lynch, "Integral SHM-system for offshore wind turbines using smart wireless sensors," in *6th International Workshop on Structural Health Monitoring*, Stanford, CA, USA, 2007.

[71] A. T. Zimmerman, M. Shiraishi, R. A. Swartz, and J. P. Lynch, "Automated Modal Parameter Estimation by Parallel Processing within Wireless Monitoring Systems," *Journal of Infrastructure Systems,* vol. 14, no. 1, pp. 102-113, 2008.

[72] J. P. Lynch, Y. Wang, K. H. Law, J. H. Yi, C. G. Lee, and C. B. Yun, "Validation of a large-scale wireless structural monitoring system on the Geumdang Bridge," in *Proceedings of 9th International Conference on Structural Safety and Reliability*, 2005, pp. 19-23.

[73] S. Zerbst, G. Haake, J. Reetz, J. Lynch, and R. Rolfes, "Integral SHM-system for offshore wind turbines using smart wireless sensors," in *Proceedings of the 6th International Workshop of Structural Health Monitoring*, 2007, pp. 1889-1896.

[74] N. Kurata, B. Spencer Jr, and M. Ruiz-Sandoval, "Risk monitoring of buildings using wireless sensor network," in *Proceedings of the International Workshop on Advanced Sensors, Structural Health Monitoring, and Smart Structures*, 2003, pp. 10-11.

[75] B. Spencer, "A study on building risk monitoring using wireless sensor network MICA mote," in *1st International Conference on Structural Health Monitoring and Intelligent Infrastructure*, 2003, pp. 353-363.

[76] Á. Lédeczi, T. Hay, P. Volgyesi, D. R. Hay, A. Nádas, and S. Jayaraman, "Wireless acoustic emission sensor network for structural monitoring," *IEEE Sensors Journal,* vol. 9, no. 11, pp. 1370-1377, 2009.

[77] LORD MicroStrain. *Wireless Nodes*. Available: http://www.microstrain.com/wireless/sensors, accessed: 9 October 2015.

[78] LORD MicroStrain. *Wireless gateways*. Available: http://www.microstrain.com/wireless/gateways, accessed: 9 October 2015.

[79] *Wireless sensors*. Available: http://www.beanair.com/wireless-sensors.html, accessed: 15 April 2016.

[80] *A multi-protocol wireless sensor networks coordinator*. Available: http://www.beanair.com/wireless-coordinator.html, accessed: 15 April 2016.

[81] A. Tani, M. Ugaji, and Y. Yamabe, "A building structural-performance monitoring system using RFID tag with sensors," in *Proceedings of the International Conference on Computing in Civil and Building Engineering*, 2010, p. 441.

[82] A. Tani, Y. Yamabe, M. Murakami, and M. UGAJI, "Fundamental tests on structural health monitoring systems by using RFID tag with sensors," in *Proceedings of 14th World Conference on Earthquake Engineering*, 2008, pp. 1-8.

[83] D.-D. Ho, K.-D. Nguyen, H.-S. Yoon, and J.-T. Kim, "Multiscale acceleration-dynamic strain-impedance sensor system for structural health monitoring," *International Journal of Distributed Sensor Networks,* vol. 8, no. 10, 2012.

[84] X. Liu and J. Cao, *Wireless Sensor Networks for Structural Health Monitoring*. Cham, Switzerland: Springer International Publishing, 2016.

[85] T. Kijewski-Correa, S. Su, E. Abittan, and P. J. Antsaklis, "On the use of heterogeneous, wireless sensor networks for damage assessment in bridges under known excitations," in *Proceedings of 4th World Conference on Structural Control and Monitoring*, International Association for Structural Control and Monitoring, Los Angeles, 2006.

[86] T. Kijewski-Correa, M. Haenggi, and P. Antsaklis, "Multi-scale wireless sensor networks for structural health monitoring," *Proceedings of SHM-II'05,* pp. 16-18, 2005.

[87] J. H. Weng and C. H. Loh, "Structural health monitoring of arch dam from dynamic measurements," in *Earth and Space 2010: Engineering, Science, Construction, and Operations in Challenging Environments*, G. Song and R. B. Malla, Eds., ed: American Society of Civil Engineers, pp. 2518-2534.

[88] G. De Roeck, B. Peeters, and J. Maeck, "Dynamic monitoring of civil engineering structures," *Proceedings of IASS-IACM 2000, Computational Methods for Shell and Spatial Structures, Chania, Greece,* 2000.

[89] A. Philips Adewuyi, Z. Wu, and N. H. M. Kammrujaman Serker, "Assessment of vibration-based damage identification methods using displacement and distributed strain measurements," *Structural Health Monitoring,* vol. 8, no. 6, pp. 443-461, 2009.

[90] R. G. Merritt, "Vibration of systems having distributed mass and elasticity," in *Harris' Shock and Vibration Handbook*, A. G. Piersol and T. L. Paez, Eds., 6th ed New York, NY, USA: McGraw-Hill, 2010, pp. 19-25.

[91] J. Maeck, G. Feltrin, and G. De Roeck, "Vibration based damage identification on a concrete highway bridge," in *1st European Workshop on Structural Health Monitoring*, 2002.

[92] P. L. Jerome, W. Yang, J. L. Kenneth, Y. Jin-Hak, and Y. Chung-Bang, "Performance monitoring of the Geumdang Bridge using a dense network of high-resolution wireless sensors," *Smart Materials and Structures,* vol. 15, no. 6, pp. 1561-1575, 2006.

[93] E. Caetano, Cunha, C. Moutinho, and W. Hu, "Dynamic monitoring of civil engineering structures," in *3rd Experiment International Conference (exp.at'15)*, 2015, pp. 79-85.

[94] S. S. Kessler, S. M. Spearing, M. J. Atalla, C. E. S. Cesnik, and C. Soutis, "Damage detection in composite materials using frequency response methods," *Composites Part B: Engineering,* vol. 33, no. 1, pp. 87-95, 2002.

[95] S. Chinchalkar, "Determination of crack location in beams using natural frequencies," *Journal of Sound and Vibration,* vol. 247, no. 3, pp. 417-429, 2001.

[96] M. N. Cerri and F. Vestroni, "Detection of damage in beams subjected to diffused cracking," *Journal of Sound and Vibration,* vol. 234, no. 2, pp. 259-276, 2000.

[97] M. N. Cerri and G. C. Ruta, "Detection of localised damage in plane circular arches by frequency data," *Journal of Sound and Vibration,* vol. 270, no. 1–2, pp. 39-59, 2004.

[98] S. P. Shah, J. S. Popovics, K. V. Subramaniam, and C.-M. Aldea, "New directions in concrete health monitoring technology," *Journal of Engineering Mechanics,* vol. 126, no. 7, pp. 754-760, 2000.

[99] S. Fabio Luis Marques dos, P. Bart, L. Jenny, D. Wim, and G. Luiz Carlos Sandoval, "The use of strain gauges in vibration-based damage detection," *Journal of Physics: Conference Series,* vol. 628, no. 1, p. 012119, 2015.

[100] S. Deshmukh, I. Mohammad, M. Tentzeris, T. Wu, and H. Huang, "Crack detection and monitoring using passive wireless sensor," in *ASME Conference on Smart Materials, Adaptive Structures and Intelligent Systems*, 2009, pp. 511-516.

[101] J. Erdmann, S. Deshmukh, and H. Huang, "Microwave antenna sensors for fatigue crack monitoring under lap joints," in *ASME Conference on Smart Materials, Adaptive Structures and Intelligent Systems*, 2010, pp. 619-625.

[102] I. Mohammad and H. Huang, "Monitoring fatigue crack growth and opening using antenna sensors," *Smart Materials and Structures,* vol. 19, no. 5, p. 055023, 2010.

[103] A. Daliri, C. H. Wang, S. John, A. Galehdar, W. S. Rowe, and K. Ghorbani, "Multidirectional circular microstrip patch antenna strain sensor," in *ASME Conference on Smart Materials, Adaptive Structures and Intelligent Systems*, 2011, pp. 481-487.

[104] A. Daliri, A. Galehdar, S. John, W. Rowe, and K. Ghorbani, "Circular microstrip patch antenna strain sensor for wireless structural health monitoring," in *Proceedings of the World Congress on Engineering*, 2010, p. 1173.

[105] A. Daliri, A. Galehdar, S. John, W. S. Rowe, and K. Ghorbani, "Slotted circular microstrip patch antenna application in strain based structural health monitoring," in *Proceedings of the 7th DSTO International Conference on Health and Usage Monitoring (HUMS), Melbourne, Australia*, 2011.

[106] R. Matsuzaki, M. Melnykowycz, and A. Todoroki, "Antenna/sensor multifunctional composites for the wireless detection of damage," *Composites Science and Technology,* vol. 69, no. 15–16, pp. 2507-2513, 2009.

[107] S.-D. Jang and J. Kim, "Passive wireless structural health monitoring sensor made with a flexible planar dipole antenna," *Smart Materials and Structures,* vol. 21, no. 2, p. 027001, 2012.

[108] J. Chuang, D. Thomson, and G. Bridges, "Embeddable wireless strain sensor based on resonant RF cavities," *Review of Scientific Instruments,* vol. 76, no. 9, p. 094703, 2005.

[109] J. C. Butler, A. J. Vigliotti, F. W. Verdi, and S. M. Walsh, "Wireless, passive, resonant-circuit, inductively coupled, inductive strain sensor," *Sensors and Actuators A: Physical,* vol. 102, no. 1, pp. 61-66, 2002.

[110] B. Carkhuff and R. Cain, "Corrosion sensors for concrete bridges," *IEEE instrumentation & measurement magazine,* vol. 6, no. 2, pp. 19-24, 2003.

[111] J. Yi, S. Ke, A. Fredrick Just, and Q. Manuel Toledo, "Design and characterization of a passive wireless strain sensor," *Measurement Science and Technology,* vol. 17, no. 11, pp. 2869-2876, 2006.

[112] G. Marrocco, "The art of UHF RFID antenna design: impedance-matching and size-reduction techniques," *IEEE Antennas and Propagation Magazine,* vol. 50, no. 1, pp. 66-79, 2008.

[113] GS1, (2014). *Regulatory status for using RFID in the EPC Gen 2 band (860 to 960 MHz) of the UHF Spectrum*. Available: http://www.gs1.org/docs/epc/UHF_Regulations.pdf, accessed: 15 March 2015.

[114] P. V. Nikitin and K. V. S. Rao, "Theory and measurement of backscattering from RFID tags," *IEEE Antennas and Propagation Magazine,* vol. 48, no. 6, pp. 212-218, 2006.

[115] A. Ruhanen, M. Hanhikorpi, F. Bertuccelli, A. Colonna, W. Malik, D. Ranasinghe*, et al.*, "Sensor-enabled RFID tag handbook," *BRIDGE, IST-2005-033546, January,* 2008.

[116] S. Preradovic, I. Balbin, and N. C. Karmakar, "Development of a low-cost semi-passive transponder for sensor applications at 2.4GHz," in *International Symposium on Communications and Information Technologies*, 2007, pp. 131-135.

[117] N. C. Karmakar, S. M. Roy, S. Jenvey, S. Preradovic, T. D. Vo, and G. F. Swiegers, "Development of a low-cost backscattered semi-active RFID tag at 2.4 GHz," *International Journal of RF and Microwave Computer-Aided Engineering,* vol. 17, no. 6, pp. 574-582, 2007.

[118] C. Occhiuzzi, C. Paggi, and G. Marrocco, "Passive RFID strain-sensor based on meander-line antennas," *IEEE Transactions on Antennas and Propagation,* vol. 59, no. 12, pp. 4836-4840, 2011.

[119] S. Caizzone, E. DiGiampaolo, and G. Marrocco, "Wireless crack monitoring by stationary phase measurements from coupled RFID tags," *IEEE Transactions on Antennas and Propagation,* vol. 62, no. 12, pp. 6412-6419, 2014.

[120] S. Capdevila, G. Roqueta, M. Guardiola, L. Jofre, J. Romeu, and J. C. Bolomey, "Water infiltration detection in civil engineering structures using RFID," in *6th European Conference on Antennas and Propagation (EUCAP)*, 2012, pp. 2505-2509.

[121] T. J. Lesthaeghe, S. Frishman, S. D. Holland, and T. J. Wipf, "RFID tags for detecting concrete degradation in bridge decks," presented at the InTrans Project Reports, Paper 70, 2013.

[122] K. J. Loh, J. P. Lynch, and N. A. Kotov, "Passive wireless strain and pH sensing using carbon nanotube-gold nanocomposite thin films," in *The 14th International*

Symposium on: Smart Structures and Materials & Nondestructive Evaluation and Health Monitoring, 2007, pp. 652919-652919-12.

[123] S. Preradovic and N. C. Karmakar, "Chipless RFID: bar code of the future," *IEEE Microwave Magazine,* vol. 11, no. 7, pp. 87-97, 2010.

[124] E. M. Amin and N. Karmakar, "Development of a chipless RFID temperature sensor using cascaded spiral resonators," in *Proceedings of IEEE Sensors* 2011, pp. 554-557.

[125] S. Preradovic and N. Karmakar, "Chipless RFID tag with integrated sensor," in *IEEE Sensors*, 2010, pp. 1277-1281.

[126] E. M. Amin, M. S. Bhuiyan, N. C. Karmakar, and B. Winther-Jensen, "Development of a low cost printable chipless RFID humidity sensor," *IEEE Sensors Journal,* vol. 14, no. 1, pp. 140-149, 2014.

[127] S. Dey, J. K. Saha, and N. C. Karmakar, "Smart sensing: chipless RFID solutions for the internet of everything," *IEEE Microwave Magazine,* vol. 16, no. 10, pp. 26-39, 2015.

[128] C. Mandel, M. Schüßler, and R. Jakoby, "A wireless passive strain sensor," in *IEEE Sensors*, 2011, pp. 207-210.

[129] P. Kalansuriya, R. Bhattacharyya, S. Sarma, and N. Karmakar, "Towards chipless RFID-based sensing for pervasive surface crack detection," in *IEEE International Conference on RFID-Technologies and Applications (RFID-TA)*, 2012, pp. 46-51.

[130] S. Dey, P. Kalansuriya, and N. C. Karmakar, "Chipless RFID based high resolution crack sensing through SWB technology," in *IEEE International Microwave and RF Conference (IMaRC)*, 2014, pp. 330-333.

[131] S. Manzari, T. Musa, M. Randazzo, Z. Rinaldi, A. Meda, and G. Marrocco, "A passive temperature radio-sensor for concrete maturation monitoring," in *IEEE RFID Technology and Applications Conference (RFID-TA)* 2014, pp. 121-126.

[132] D. Watters, P. Jayaweera, A. Bahr, and D. Huestis, "Design and performance of wireless sensors for structural health monitoring," in *AIP Conference Proceedings*, 2002, pp. 969-976.

[133] S. Ogawa and T. Sato, "Monitoring of concrete structures using passive type RFID tags with sensory functions," presented at the The International Conference on Electrical Engineering, , Okinawa, Japan, 2008.

[134] Y. Ikemoto, S. Suzuki, H. Okamoto, H. Murakami, X. Lin, H. Itoh*, et al.*, "Force sensor system for structural health monitoring using passive RFID tags for structural health monitoring," in *PORTABLE-POLYTRONIC 2008 - 2nd IEEE International Interdisciplinary Conference on Portable Information Devices and the 2008 7th IEEE Conference on Polymers and Adhesives in Microelectronics and Photonics*, 2008, pp. 1-6.

[135] Impinj, (2013). *Monza X-8K Dura Datasheet, [Revision 1.1]*. Available: https://support.impinj.com/hc/en-us/articles/202756868-Monza-X-8K-Dura-Datasheet, accessed: 1 May 2014.

[136] E. D. Giampaolo, A. DiCarlofelice, and A. Gregori, "An RFID-enabled wireless strain gauge sensor for static and dynamic structural monitoring," *IEEE Sensors Journal,* vol. 17, no. 2, pp. 286-294, 2016.

[137] B. Pátkai and D. McFarlane, "RFID-based sensor integration in aerospace," *Integration,* vol. 2, p. 1, 2006.

[138] P. Mirmobin and A. J. Brackenbury, "Sensor system including multiple radio frequency identification tags," ed: Google Patents, 2009.

[139] J. D. Griffin, G. D. Durgin, A. Haldi, and B. Kippelen, "RF tag antenna performance on various materials using radio link budgets," *IEEE Antennas and Wireless Propagation Letters,* vol. 5, no. 1, pp. 247-250, 2006.

[140] D. M. Dobkin and S. M. Weigand, "Environmental effects on RFID tag antennas," in *IEEE MTT-S International Microwave Symposium Digest*, 2005, pp. 135-138.

[141] G. Manzi and M. Feliziani, "Impact of UHF RFID IC impedance on the RFID system performances in presence of dielectric materials," in *International Symposium on Electromagnetic Compatibility-EMC Europe*, 2008, pp. 1-6.

[142] T. Deleruyelle, P. Pannier, M. Egels, and E. Bergeret, "An RFID tag antenna tolerant to mounting on materials," *IEEE Antennas and Propagation Magazine,* vol. 52, no. 4, pp. 14-19, 2010.

[143] P. Raumonen, L. Sydanheimo, L. Ukkonen, M. Keskilammi, and M. Kivikoski, "Folded dipole antenna near metal plate," in *IEEE Antennas and Propagation Society International Symposium* 2003, pp. 848-851.

[144] M. S. Hasan and H. Yu, "Design and simulation of UHF RFID tag antennas and performance evaluation in presence of a metallic surface," in *5th International Conference on Software, Knowledge Information, Industrial Management and Applications (SKIMA)* 2011, pp. 1-5.

[145] T. Bjorninen, K. E. Delzo, L. Ukkonen, A. Z. Elsherbeni, and L. Sydnheimo, "Long range metal mountable tag antenna for passive UHF RFID systems," in *IEEE International Conference on RFID-Technologies and Applications (RFID-TA)*, 2011, pp. 202-206.

[146] Y. M. Um, U. Kim, W. Seong, and J. Choi, "A novel antenna design for UHF RFID tag on metallic objects," in *Progress In Electromagnetics Research Symposium (PIERS)* 2007, pp. 158-161.

[147] S. L. Chen and K. H. Lin, "A slim RFID tag antenna design for metallic object applications," *IEEE Antennas and Wireless Propagation Letters,* vol. 7, pp. 729-732, 2008.

[148] S. L. Chen, "A miniature RFID tag antenna design for metallic objects application," *IEEE Antennas and Wireless Propagation Letters,* vol. 8, pp. 1043-1045, 2009.

[149] H.-D. Chen, Y.-H. Tsao, and C.-Y. Kuo, "Low-profile radio frequency identification tag antenna using a trapezoid patch mountable on metallic surfaces," *Microwave and Optical Technology Letters,* vol. 52, no. 8, pp. 1697-1700, 2010.

[150] B. Lee and B. Yu, "Compact structure of UHF band RFID tag antenna mountable on metallic objects," *Microwave and Optical Technology Letters,* vol. 50, no. 1, pp. 232-234, 2008.

[151] L. Mo and C. Qin, "Planar UHF RFID tag antenna with open stub feed for metallic objects," *IEEE Transactions on Antennas and Propagation,* vol. 58, no. 9, pp. 3037-3043, 2010.

[152] H. W. Son and S. H. Jeong, "Wideband RFID tag antenna for metallic surfaces using proximity-coupled feed," *IEEE Antennas and Wireless Propagation Letters,* vol. 10, pp. 377-380, 2011.

[153] T. Bjorninen and L. Ukkonen, "Small slot antenna for metal mountable UHF RFID tags," in *Proceedings of the IEEE International Symposium on Antennas and Propagation*, 2012, pp. 1-2.

[154] R. Kanan and A. Azizi, "UHF RFID transponders antenna design for metal and wood surfaces," in *IEEE International Conference on RFID*, 2009, pp. 270-277.

[155] C. Mariotti, G. Orecchini, M. Virili, F. Alimenti, and L. Roselli, "RFID tag antenna embedded in concrete structures for construction industry," in *6th European Conference on Antennas and Propagation (EUCAP)*, 2012, pp. 3469-3472.

[156] D. Daly, T. Melia, and G. Baldwin, "Concrete embedded RFID for way-point positioning," in *International Conference on Indoor Positioning and Indoor Navigation (IPIN)*, 2010, pp. 1-10.

[157] S. H. Jeong and H. W. Son, "UHF RFID tag antenna for embedded use in a concrete floor," *IEEE Antennas and Wireless Propagation Letters,* vol. 10, pp. 1158-1161, 2011.

[158] G. Liu, N. Mrad, G. Xiao, Z. Li, and D. Ban, "Metallic environmental effect on RF-based energy transmission," *IEEE Antennas and Wireless Propagation Letters,* vol. 11, pp. 925-928, 2012.

[159] A. Mitrokotsa and C. Douligeris, "Integrated RFID and sensor networks: architectures and applications," *RFID and sensor networks: Architectures, protocols, security and integrations,* pp. 511-535, 2009.

[160] CST. (2014). *CST Studio Suite*. Available: http://www.cst.com/Products/CSTS2, accessed: 21 January 2014.

[161] Microchip. *MPLAB X integrated development environment (IDE)*. Available: http://www.microchip.com/mplab/mplab-x-ide, accessed: 5 July 2014.

[162] *Visual studio 2012*. Available: https://msdn.microsoft.com/en-us/library/dd831853(v=vs.110).aspx, accessed: 10 March 2015.

[163] Impinj. *Octane SDK*. Available: https://support.impinj.com/hc/en-us/articles/202755268-Octane-SDK, accessed: 15 August 2015.

[164] Impinj. *Speedway Readers*. Available: https://support.impinj.com/hc/en-us/articles/202755388-Speedway-Reader-Product-Brief-Datasheet, accessed: 20 September 2016.

[165] *Model: 086C04*. Available: http://www.pcb.com/Products.aspx?m=086C04, accessed: 10 February 2015.

[166] PCB Group, Inc. *Accelerometers-sensors for shock, vibration and acceleration*. Available: http://www.pcb.com/TestMeasurement/Accelerometers, accessed: 9 October 2015.

[167] National Instruments. *Data acquisition (DAQ)-National Instruments*. Available: http://www.ni.com/data-acquisition, accessed: 9 October 2015.

[168] EPCglobal Inc., (2005). *EPC Radio-Frequency Identity Protocols Class-1 Generation-2 UHF RFID Protocol for Communication at 860 MHz - 960 MHz Version 1.0.9*. accessed: 10 March 2014.

[169] A. P. Sample, D. J. Yeager, P. S. Powledge, A. V. Mamishev, and J. R. Smith, "Design of an RFID-based battery-free programmable sensing platform," *IEEE Transactions on Instrumentation and Measurement,* vol. 57, no. 11, pp. 2608-2615, 2008.

[170] A. P. Sample and J. R. Smith, "The wireless identification and sensing platform," in *Wirelessly Powered Sensor Networks and Computational RFID*, J. R. Smith, Ed., ed New York, NY, USA: Springer Science + Business Media, 2013, pp. 33-56.

[171] Bisa Technologies (Hong Kong) Ltd. (2008). *Vibration Sensor Tag*. Available: http://bisa.com.hk/VibrationSensorTag_e.html, accessed: 15 May 2014.

[172] W. Zhou and S. Piramuthu, *RFID and Sensor Network Automation in the Food Industry*. Chicester, West Sussex, PO19 8SQ, UK: John Wiley & Sons Ltd, 2016.

[173] evigia. (2014). *Evigia EV3 Active RFID Tags with Integrated Sensing*. Available: http://www.evigia.com/wireless-tracking-technologies/active-rfid-tags/, accessed: 12 June 2014.

[174] WAVETREND. (2011). *Activ Tags*. Available: http://www.wavetrend.net/activ-tags.php, accessed: 15 June 2014.

[175] farsens. *Kineo-A3DH*. Available: http://www.farsens.com/en/products/kineo-a3dh, accessed: 15 March 2015.

[176] Laird Technologies. *S9025P Mini RFID Panel Antenna*. Available: http://cdn.lairdtech.com/home/brandworld/files/ANT-DS-S9025P-1115.pdf, accessed: 15 September 2014.

[177] Impinj, (2014). *IPJ-RS500-GX, IPJ-RS500-EU Electrical, Mechanical & Thermal Specification*. Available: https://support.impinj.com/hc/en-us/categories/200156278-Indy-Reader-Chip-Products, accessed: 5 August 2014.

[178] *900-1114_Monza_X_demo_board_PCBA_schematic*. Available: https://support.impinj.com/hc/en-us/article_attachments/201113673/900-1114_Monza_X_Demo_Board_PCBA_Schematic_v1.5.pdf., accessed: 10 January 2015.

[179] ANALOG DEVICES, (2012-2013). *ADXL362 Datasheet*. Available: http://www.analog.com/en/products/mems/accelerometers/adxl362.html#product-overview, accessed: 21 May 2014.

[180] Microchip, (2005-2014). *Explorer 16 development board user's guide*. Available: http://ww1.microchip.com/downloads/en/DeviceDoc/50001589b.pdf, accessed: 10 July 2014.

[181] ANALOG DEVICES. *Evaluation board user guide*. Available: http://www.analog.com/media/en/technical-documentation/user-guides/UG-351.pdf, accessed: 10 August 2014.

[182] Microchip, (2005-2012). *PIC24FJ128GA010 Family Datasheet*. Available: http://ww1.microchip.com/downloads/en/DeviceDoc/39747F.pdf, accessed: 10 July 2014.

[183] K. H. Low, "Letter to the editor: closed-form formulas for fundamental vibration frequency of beams under off-centre load," *Journal of Sound and Vibration,* vol. 201, no. 4, pp. 528-533, 1997.

[184] D. Deavours and D. Dobkin, "UHF passive RFID tag antennas," in *Microstrip and Printed Antennas*, ed: John Wiley & Sons, Ltd, 2010, pp. 263-303.

[185] D. C. Ranasinghe and P. H. Cole, "Far-field tag antenna design methodology," in *RFID handbook : applications, technology, security, and privacy*, ed: Boca Raton : Taylor & Francis, 2008, pp. 65-91.

[186] J. Z. Huang, P. H. Yang, W. C. Chew, and T. T. Ye, "A novel broadband patch antenna for universal UHF RFID tags," *Microwave and Optical Technology Letters,* vol. 52, no. 12, pp. 2653-2657, 2010.

[187] T. V. Koskinen, H. Rajagopalan, and Y. Rahmat-Samii, "A thin multi-slotted dual patch UHF-band metal-mountable RFID tag antenna," *Microwave and Optical Technology Letters,* vol. 53, no. 1, pp. 40-47, 2011.

[188] Impinj, (2013). *Monza X Antenna Design Note, [Revision 2.1]*. Available: https://support.impinj.com/hc/en-us/articles/202756888-Monza-X-Antenna-Design-Application-Note, accessed: 5 August 2014.

[189] J. Huang, "Microstrip antennas: analysis, design, and application," in *Modern Antenna Handbook*, C. A. Balanis, Ed., ed: Hoboken, NJ : J. Wiley & Sons, 2008 pp. 157-200.

[190] D. Pena, R. Feick, H. D. Hristov, and W. Grote, "Measurement and modeling of propagation losses in brick and concrete walls for the 900-MHz band," *IEEE Transactions on Antennas and Propagation,* vol. 51, no. 1, pp. 31-39, 2003.

[191] A. Robert, "Dielectric permittivity of concrete between 50 Mhz and 1 Ghz and GPR measurements for building materials evaluation," *Journal of Applied Geophysics,* vol. 40, no. 1–3, pp. 89-94, 1998.

[192] AINFO Inc. *LB-880 0.8-8.0 GHz Broadband Horn Antenna*. Available: http://www.ainfoinc.com/en/p_ant_h_brd.asp, accessed: 10 September 2015.

[193] Impinj. *Impinj MultiReader Software*. Available: https://support.impinj.com/hc/en-us/articles/202755258-Impinj-Multi-Reader-Software, accessed: 9 October 2015.

[194] L. Catarinucci, D. D. Donno, R. Colella, F. Ricciato, and L. Tarricone, "A cost-effective SDR platform for performance characterization of RFID tags," *IEEE*

Transactions on Instrumentation and Measurement, vol. 61, no. 4, pp. 903-911, 2012.

[195] K. S. Rao, P. V. Nikitin, and S. F. Lam, "Antenna design for UHF RFID tags: a review and a practical application," *IEEE Transactions on antennas and propagation,* vol. 53, no. 12, pp. 3870-3876, 2005.

[196] Modern STEEL CONSTRUCTION, (2007). *Evaluation of existing structures*. Available: http://msc.aisc.org/globalassets/modern-steel/steelwise/30762_steelwise_reno.pdf, accessed: 15 May, 2016.

[197] K. Ward-Harvey, *Fundamental Building Materials*, 4th ed. Boca Raton, Florida, USA: Universal-Publishers, 2009.

[198] Microchip, (2008-2011). *PIC24F16KA102 family data sheet*. Available: http://ww1.microchip.com/downloads/en/DeviceDoc/39927c.pdf, accessed: 15 July 2015.

[199] Microchip, (2009). *nanoWatt XLP eXtreme Low Power MCUs*. Available: http://www.es.co.th/Schemetic/PDF/DM240311.PDF, accessed: 15 May 2015.

[200] Microchip. *Practical applications of low-power design with nanoWatt XLP™*. Available: http://ww1.microchip.com/downloads/en/DeviceDoc/Future%20XLP%20Article.pdf , accessed: 10 August 2015.

[201] R. Colella, D. D. Donno, L. Tarricone, and L. Catarinucci, "Advances in the design of smart, multi-function, RFID-enabled devices," in *IEEE Antennas and Propagation Society International Symposium (APSURSI)*, 2014, pp. 1678-1679.

[202] Microchip, (2006). *Power saving features*. Available: http://ww1.microchip.com/downloads/en/devicedoc/39698a.pdf, accessed: 10 July 2015.

[203] Microchip, (2009). *Power saving features with deep sleep*. Available: http://ww1.microchip.com/downloads/en/DeviceDoc/39727a.pdf, accessed: 10 July 2015.

[204] *Understanding EPC Gen2 Search Modes and Sessions*. Available: https://support.impinj.com/hc/en-us/articles/202756158-Understanding-EPC-Gen2-Search-Modes-and-Sessions, accessed: 20 May 2015.

[205] S. W. Smith, *The Scientist and Engineer's Guide to Digital Signal Processing*: California Technical Pub., 1997.

[206] Z. K. Peng and F. L. Chu, "Application of the wavelet transform in machine condition monitoring and fault diagnostics: a review with bibliography," *Journal of Mechanical Systems and Signal Processing,* vol. 18, no. 2, pp. 199-221, 2004.

[207] L. Wang, L. Ma, and Y. Huang, "The application of lifting wavelet transform in the fault diagnosis of reciprocating air compressor," in *International Conference on Intelligent System Design and Engineering Application*, 2010, pp. 574-576.

[208] X. Zhou, C. Zhou, and I. J. Kemp, "An improved methodology for application of wavelet transform to partial discharge measurement denoising," *IEEE Transactions on Dielectrics and Electrical Insulation,* vol. 12, no. 3, pp. 586-594, 2005.

[209] J. Li, C. Cheng, T. Jiang, and S. Grzybowski, "Wavelet de-noising of partial discharge signals based on genetic adaptive threshold estimation," *IEEE Transactions on Dielectrics and Electrical Insulation,* vol. 19, no. 2, pp. 543-549, 2012.

[210] X. Ma, C. Zhou, and I. J. Kemp, "Automated wavelet selection and thresholding for PD detection," *IEEE Electrical Insulation Magazine,* vol. 18, no. 2, pp. 37-45, 2002.

[211] (2016). *Wavelet toolbox*. Available: https://au.mathworks.com/help/wavelet/index.html?s_cid=doc_ftr, accessed: 15 May 2016.

[212] E. M. Mugambi, K. Kwan, B. C. Laskowski, T. K. Ooi, and A. Corder, "MEMS-based strain and corrosion sensors for structural health monitoring," in *Proceedings of 6th International Workshop on Structural Health Monitoring*, Stanford University, Stanford, Calif., 2007.

[213] S. H. Sim and J. B. F. Spencer. (2015). *Combined use of acceleration and strain in damage detection*. Available: https://www.researchgate.net/publication/266587628

[214] M. Aldo, C. Agnese, P. Salvatore, B. Romeo, and Z. Luigi, "Modal analysis of a cantilever beam by use of Brillouin based distributed dynamic strain measurements," *Smart Materials and Structures,* vol. 21, no. 12, p. 125022, 2012.

[215] Y. Tang, Z. Wu, C. Yang, G. Wu, and C. Wan, "A model-free damage identification method for flexural structures using dynamic measurements from distributed long-gage macro-strain sensors," *Journal of Intelligent Material Systems and Structures,* vol. 25, no. 13, pp. 1614-1630, September, 2014.

[216] A. Panopoulou, D. Roulias, T. H. Loutas, and V. Kostopoulos, "Health monitoring of aerospace structures using fibre Bragg gratings combined with advanced signal processing and pattern recognition techniques," *Strain,* vol. 48, no. 3, pp. 267-277, 2012.

[217] G. M. Kamath, R. Sundaram, N. Gupta, and M. Subba Rao, "Damage studies in composite structures for structural health monitoring using strain sensors," *Structural Health Monitoring,* vol. 9, no. 6, pp. 497-512, 2010.

[218] M. Benedetti, V. Fontanari, and D. Zonta, "Structural health monitoring of wind towers: remote damage detection using strain sensors," *Smart Materials and Structures,* vol. 20, no. 5, p. 055009, 2011.

[219] K. Scott and A. Owens, "Instrumentation," in *Strain gauge technology*, A. L. Window, Ed., 2nd ed Crown House, Linton Road, Barking, Essex IG11 8JU, England: Elsevier Science Publishers Ltd, pp. 151-216.

[220] J. Pople, "Errors and uncertainties of strain measurement," in *Strain gauge technology*, A. L. Window, Ed., 2nd ed Crown House, Linton Road, Barking, Essex IG118JU, England: Elsevier Science Publishers LTD, pp. 217-272.

[221] F. Federici, R. Alesii, A. Colarieti, F. Graziosi, and M. Faccio, "Design and validation of a wireless sensor node for long term structural health monitoring," in *IEEE Sensors*, 2013, pp. 1-4.

[222] RFID Journal, (2015). *RFID helps contractors to measure strain during construction of Seattle rail tunnels*. Available: http://www.rfidjournal.com/articles/view?12913, accessed: 10 September 2015.

[223] TML Tokyo Sokki Kenkyujo Co., Ltd. *Polyester strain gauges - series P/PF*. Available: http://www.tml.jp/e/product/strain_gauge/gauge_list/pf_list.html, accessed: 10 August 2015.

[224] VISHAY, (2012). *Precision MELF resistors*. 41-49. Available: http://docs-asia.electrocomponents.com/webdocs/112f/0900766b8112fab1.pdf, accessed: 10 September 2015.

[225] Texas Instruments, (2015). *INA333 micro-power (50uA), zero-drift, rail-to-rail out instrumentation amplifier*. Available: http://www.ti.com/product/INA333, accessed: 10 September 2015.

[226] Microchip, (2004). *Single-ended, rail-to-rail I/O, low-rain PGA*. Available: http://www.microchip.com/wwwproducts/en/MCP6S91, accessed: 20 September 2015.

[227] Texas Instruments, (2015). *OPAx333 1.8-V, micropower, CMOS operational amplifiers, zero-drift series (Rev. E)* Available: http://www.ti.com/product/opa333?keyMatch=opa333&tisearch=Search-EN-Everything, accessed: 20 September 2015.

[228] ANALOG DEVICES. *AD7680*. Available: http://www.analog.com/en/products/analog-to-digital-converters/ad-converters/ad7680.html, accessed: 20 August 2015.

[229] TML Tokyo Sokki Kenkyujo Co., Ltd. *Digital strainmeter*. Available: http://www.proact-tools.com/instrument/instrument_sub/tc31k.html, accessed: 5 September 2016.

[230] U. S. Inan, A. S. Inan, and R. K. Said, *Engineering electromagnetics and waves*, 2 ed. Prentice Hall, 1 Lake Street, Upper Saddle River, NJ 07485: Pearson Education, Inc., 2006.

[231] C. A. Balanis, "Fundamental parameters and definitions for antennas," in *Modern Antenna Handbook*, C. A. Balanis, Ed., ed: Hoboken, NJ : J. Wiley & Sons, 2008, pp. 3-56.

[232] J. F. Nye, G. Hygate, and W. Liang, "Energy streamlines: a way of understanding how horns radiate backwards," *IEEE Transactions on Antennas and Propagation,* vol. 42, no. 9, pp. 1250-1256, 1994.

[233] A. Kyoya and M. Omiya, "Electromagnetic simulations and numerical models for an accurate prediction of indoor radio wave propagation in an office environment," in *IEEE International Conference on Computational Electromagnetics (ICCEM)*, 2016, pp. 152-154.

[234] A. Happonen, H. Hamalainen, and J. Ikonen, "Radio identification in construction industry case: Tagging hollow steel beams," in *16th International Conference on Software, Telecommunications and Computer Networks (SoftCOM 2008)* 2008, pp. 233-237.

[235] D. M. Pozar, *Microwave Engineering*: Wiley, 2012.

[236] CST, (2013). *Design of circularly-polarized patch antennas using CST Microwave Studio*. Available: https://www.cst.com/Applications/Article/Design-Of-Circularly-Polarized-Patch-Antennas-Using-CST-MICROWAVE-STUDIOReg, accessed: 15 January 2016.

[237] P. V. Nikitin, R. Martinez, S. Ramamurthy, H. Leland, G. Spiess, and K. V. S. Rao, "Phase based spatial identification of UHF RFID tags," in *IEEE International Conference on RFID (IEEE RFID 2010)*, 2010, pp. 102-109.

[238] L. Xin, Y. Zhang, and M. G. Amin, "Multifrequency-based range estimation of RFID Tags," in *IEEE International Conference on RFID*, 2009, pp. 147-154.

[239] A. Povalac and J. Sebesta, "Phase difference of arrival distance estimation for RFID tags in frequency domain," in *IEEE International Conference on RFID-Technologies and Applications (RFID-TA)*, 2011, pp. 188-193.

[240] X. Hou, X. Yang, and Q. Huang, "Using inclinometers to measure bridge deflection," *Journal of Bridge Engineering,* vol. 10, no. 5, pp. 564-569, 2005.

[241] F. Moreu, H. Jo, J. Li, R. E. Kim, S. Cho, A. Kimmle*, et al.*, "Dynamic assessment of timber railroad bridges using displacements," *Journal of Bridge Engineering,* vol. 20, no. 10, p. 04014114, 2015.

[242] F. Moreu, J. Li, M. A. H. Jo, R. E. Kim, S. Scola, J. B. F. Spencer*, et al.*, "Reference-free displacements for condition assessment of timber railroad bridges," *Journal of Bridge Engineering,* vol. 21, no. 2, p. 04015052, 2016.

[243] J. W. Park, S. H. Sim, and H. J. Jung, "Displacement estimation using multimetric data fusion," *IEEE/ASME Transactions on Mechatronics,* vol. 18, no. 6, pp. 1675-1682, 2013.

[244] Impinj, (2013). *Speedway revolution reader application note - Low level user data support*. Available: https://support.impinj.com/hc/en-us/articles/202755318-Application-Note-Low-Level-User-Data-Support, accessed: 15 January 2016.

[245] V. Viikari, P. Pursula, and K. Jaakkola, "Ranging of UHF RFID tag using stepped frequency read-out," *IEEE Sensors Journal,* vol. 10, no. 9, pp. 1535-1539, 2010.

[246] S. Kharkovsky, P. Giri, and B. Samali, "Non-contact inspection of construction materials using 3-axis multifunctional imaging system with microwave and laser sensing techniques," *IEEE Instrumentation & Measurement Magazine,* vol. 19, no. 2, pp. 6-12, 2016.

[247] *HUBER+SUHNER® DATA SHEET Coaxial Cable: ENVIROFLEX_142*. Available: http://www.commswestdistribution.com.au/wp-content/uploads/2015/07/HUBER-SUHNER_ENVIROFLEX_142_dataSheet.pdf, accessed: 15 March 2016.